UNIVERSITE MONTPELLIER II SCIENCES
ET TECHNIQUES DU LANGUEDOC

THÈSE

présenté pour obtenir
LE TITRE DE DOCTEUR
DE L'UNIVERSITE DE MONTPELLIER II

Ecole doctorale: I2S
Laboratoire d'accueil: IFPEN
Spécialité : Mathématiques et modélisation
Directeur de thèse: Franck Nicoud

Par Hubert BAYA TODA

SIMULATION AUX GRANDES ECHELLES ET ETUDE EXPERIMENTALE DES ECOULEMENTS PARIETAUX EN GEOMETRIES COMPLEXES

LES modeling and experimental study of wall-bounded flows in complex geometries

---

Soutenance le 29 novembre 2011 devant le jury composé de:

M. Franck Nicoud	Professeur à l'université de Montepllier II	Directeur de thèse
M. Thierry Poinsot	Directeur de recherche IMFT, Toulouse	Examinateur
M. Pierre Sagaut	Professeur à l' université Pierre et Marie Curie, Paris 6	Rapporteur
M. Marc Bellenoue	Professeur à l'ENSMA, Poitiers	Rapporteur
M. Benoist Thirouard	Chef de département à l'IFPEN	Membre invité
Mme. Karine Truffin	Ingénieur de recherche à l'IFPEN	Encadrant IFP E.n.
M. Gilles Bruneaux	Expert à l'IFPEN	Encadrant IFP E.n.

ABSTRACT

The increase of supercomputer capacities is currently opening the road of complex geometry to Large Eddy Simulations. This modeling approach allows to take into account directly the largest scales of the flows and gives information not accessible so far with the usual Reynolds-Averaged-Navier-Stokes modeling based on the temporal averaging. Although accurate models have been developed in an academic framework with good results, their extension to complex geometries in particular to Internal Combustion (IC) engines remains an open question. This is notably the case for the Dynamic Smagorinsky model since the complexity of the flows involved in such configurations (combustion, spray atomization, multiphase flows, wall interaction...) prevents the use of averaging over homogeneous directions, leading to the necessity to clip negative values of the subgrid-scale (SGS) viscosity and to an overestimation of the global dissipation. Moreover, the lack of experimental data where complex effects such as unsteadiness, vortex convection and vortex wall-interaction are present, restricts the assessment of SGS viscosity models to academic test cases such as Homogeneous Isotropic Turbulence and Turbulent Channel. The objectives of this thesis were then three fold: to construct an experimental database relevant to the aforementioned phenomena usually encountered in IC engines flows, to assess the performances of existing SGS models and to develop a new SGS model that better reproduces those effects without ad hoc procedure.
The database corresponds to an unsteady hot impinging jet in turbulent cross flow with a strong interaction between the induced vortex ring and the impingement surface. Different optical diagnostics such as PIV (particle Image Velocimetry for velocity measurements), LIF (Laser Induced Fluorescence for gas temperature measurements) and LIPT (Laser Induced Phosphorescence Thermography for surface temperature measurements) were used for generating a complete database. Concerning, the SGS model referred to as the "SIGMA" model (σ-model), it was designed to automatically vanish in different canonical laminar flows (pure shear, pure rotation, isotropic expansion and contraction, stagnation points ...) for which no SGS activity is expected. LES simulations of the experimental set-up lead to an accurate estimation of the propagation velocity of the vortex along the wall and thus heat transfer at the solid boundary. Finally, a discussion about a procedure for the dynamical evaluation of the model constant is presented which is another step for completely extending the model to more complex cases and for reducing the gap between academic and industrial-like LES simulations.

ACKNOWLEDGEMENTS

I first want to thank IFPEN for having financed this thesis and also CINES for the available computer resources needed for achieving these results.

It is a real honor for me to have in my jury Professor Thierry Poinsot, Professor Pierre Sagaut and Professor Marc Bellenoue. They are source of inspiration for young researchers and I specially want to thanks them for having accepted to evaluate my thesis.

I am particularly thankful to my thesis advisor Professor Franck Nicoud who introduced me to the world of research, turbulence and computer simulations. Results obtained during this work would not have been possible without his permanent commitment and useful advices.

A special thanks also to my two IFPEN supervisors Karine Truffin and Gilles Bruneaux, not only for their permanent scientific advices but also for the moral support during the difficult periods of this thesis. I thank Karine for having taught me the mandatory requirements of rigor and precision in Computational Science. Thank you to Gilles for having introduce me to the exciting and interesting field of optical diagnostics and also for having done his best to make me feel comfortable during these three years.

This thesis work would not have been possible without the support and the interesting discussions with all my colleagues from R102 departement and R106 as well. I want to thank them all through the head of these departements: Antonio Pires Da Cruz, Benoist Thirouard and the head of the division Stephane Henriot. A particular thanks to Christian Angelberger for his very useful support and advice during this last three years and for having noticeably contributed to my participation to the CTR summer program 2010 at Stanford University. Olivier Cabrit who I appreciated to work with during this summer program is also warmly acknowledged for helping me and providing me advices throughout this thesis.

I would also like to acknowledge the many friends and colleagues who have generously shared their time and knowledge with me during the past three years: Gabrielle, Sabre, Emre C., Tatyana, Yohan, Zakaria, Guillaume Bernard, Haifa, El Abchi, Lionel Martinez, Hedi, Benedicte, Bejoy, Julien Bohbot, Nikola, Carlo, Kirsten, Stavros, May-Carle, Stephane, Anthony, Sullivan, Emre O., Damien Kah, Pauline, Aymeric, Alessio, Jorg, Damien Peyresaubes, Jerome Cherel, Thomas, Clement, David, Laurent, Vincent, Mathieu Andre, Mathieu Le Comte, Loic, Louis-Marie, Guillaume, Sylvie, Djamela, Christine Lemenand and Amel Boukra.

I dedicate this thesis work to my family who has always supported and encouraged me: my two sisters Athalie and Diane, my two brothers Valery and Duclos, and of course my mother Cecilia. I also dedicate it to my father TODA who I hope would have been proud of this work.

Contents

INTRODUCTION

Context of the thesis

The environmental concern is imposing severe constraints to the transport industry. In terms of local pollutant emission this concern has led to the definition of more and more stringent environmental norms for the regulation of carbon monoxide, nitrogen oxide, particles matter and unburned hydrocarbons: for instance from 1992 (Euro I) to 2009 (Euro V), the permitted CO level has decreased by 83% for diesel engines (passenger cars). Moreover, the future restrictions (Euro VI in 2014) should reduce the NOx levels by up to 55%. More recently, the global warming concern has led to more constraints on the green house gases emission of vehicles so that it is becoming the major concern taken into account in the development of new technologies.

In order to respond to these challenges, several paths are actually considered, the main being:

1. Using electric or hybrid vehicles: full electric cars provide the advantage of reducing to negligible levels the local pollutants and green house gases emissions, but the question of life cycle emission is still raised when considering the energy generation; hybrid vehicles take advantage of improved energy management since they allow for instance energy recovery during braking or engine stop at idle, or even a more efficient use of the IC engine.
2. Alternative fuel such as biofuels have gained a growing scientific attention thanks to their good field to wheel balance. Also they raise interest in the context of fuel price increase and risk of shortage of conventional fuels. However they also raise questions regarding the definition/evaluation of their total pollutant emission and also world food, deforestation, water consumption ...etc
3. The improvement of combustion efficiency remains a key lever in the race for reducing green gas emission levels. Indeed it has a positive effect on all sides and although engine technologies have been continuously improved in the last decades, the progress of technology enables more gain to be expected in the future. Current research in this field focuses on clean combustion modes and high efficient technologies such as downsizing, combined with systemic optimization of the engine and the after treatment system (particle filters and catalytic converters).

In all cases, the optimization of combustion efficiency appears to be a key lever since combustion remains one of the most interesting energy converter for the transport application. This can only be achieved by a thorough understanding of the phenomena that control the combustion in order to provide pertinent guidelines for the design of efficient engine technologies. This understanding can be provided by advanced experimental and numerical tools. These advanced tools are both required since they give complementary information on the processes involved. Indeed, advanced experimental tools provide in-situ information but are limited by implementation issues, while numerical tools can provide extensive information but require to be validated against experimental data to ensure that the provided results are predictive enough to be representative of the real processes. The context of this thesis work lies in the development of such predictive numerical tools for efficient engine design.

Objectives of the thesis

Computational Fluid Dynamics (CFD) tools used for engine development mainly rely on three different methods: Reynolds-Averaged-Navier-Stokes (RANS), Large Eddy Simulation (LES) and Direct Numerical Simulation (DNS). They are ranked here in terms of increasing complexity, predictive capability but also computational cost. For this last reason, RANS have been extensively used in engine development, even though it is limited in terms of precision and predictive capability. While DNS is still not affordable in terms of computational costs, thanks to the increase of computers/super computers capacities, LES is becoming an affordable tool for engine design and is rising more and more interest for its predictive capabilities. Recent applications show that LES can provide very detailed and precise information on the flow and combustion processes inside the engine. It has the advantage of providing a precise characterization of the bigger scales of the flow that control most of the dynamics. Modeling of the behavior of the small scales is still required but their characteristics are usually assumed to be universal and less dependent on the geometry.

This modeling process requires a theoretical knowledge of the phenomena of interest as well as validation against experimental data. In terms of turbulence predictions, probably one of the main parameter influencing combustion in IC engines, validations of LES models are generally performed on simple academics cases. Indeed, most of the LES turbulence models are validated on Homogeneous Isotropic Turbulence and Turbulence Channel. This latter case is used for testing the properties of the model in wall-bounded flows. Those cases are certainly important for the assessment of the basics properties of the models but are not always relevant in the case of complex geometries such as the ones encountered in IC engines.

Figure 1: Artistic image of an IC engine combustion chamber. It illustrates the complexity of the flows : sprays atomization, multi-phases flows, combustions, wall-bounded flows

The processes involved in IC engines are very complex as illustrated in Fig. 1; they involve multiphase flows, turbulent flows, combustion processes, wall-bounded flows. Therefore, generating a database that account for all the physical phenomena involved would be a very difficult task. In addition, the presence of solid boundaries is a main issue for LES. Near a solid boundary, the hypothesis of the isotropy of the small scales under which LES models are developed is no longer valid. Moreover, combustion is also strongly quenched near solid boundary and the boundary layers existing in the combustion chamber are not systematically well established as it is the case in the Turbulent Channel cases used for validation.
These considerations show that the use of LES for predictive engine simulations require a specific development work in order to improve the models performance in such complex geometries. Also, the validation of these improved models requires the design of specific experiments that are simple enough to allow detailed validation but are also representative enough to catch the most important processes that are occurring in the combustion chamber.

The improvement of LES models in complex geometries and the design of specific validation experiments for these models are the global objectives of this PhD work. When considering aerothermal effects, flows in IC engines can be simplified to the following processes: hot vortices formations during combustion, convections in a turbulent environment of those vortices enhanced by piston movements and intake/exhaust valves flows, and finally impingement of the vortices with the combustion chamber walls. Designing a dedicated experiment taking into account the main feature of these processes will therefore be the objective of the PhD work. This experiment should provide the condition for accurate and detailed experimental measurements as well as good conditions for reliable LES simulations, in terms of mesh size for instance. The choice of the experimental techniques for the measurement of the parameters of interest (velocity, temperature) is also a key issue. Optical diagnostics techniques are the most appropriate since they provide accurate and non intrusive measurements of several parameters.

The objectives of this PhD work is therefore to develop a dedicated experimental set up reproducing the complexity of the flows in IC engines and to generate a reliable database with advanced optical diagnostic methods. This database should lead to the assessment of existing LES models and to the improvement of new models with better performances in complex geometries. The experimental set-up is designed as the best compromise between the requirements of fast and accurate LES simulations and detailed and accurate measurements. This experiment should take into consideration the vortices-wall interaction in a turbulent environment. More generally, it should mimic the vortices formation, convection and impingement inside the combustion chamber in a turbulent environment.

Organization of the manuscript

The manuscript is organized as follows:

- In **Chapter 1**, the governing equations and the LES formalism is introduced.
- In **Chapter 2**, the experimental set-up and the optical diagnostics (Particle Image Velocimetry, Laser Induced Fluorescence and Laser Induced Phosphorescence Thermography) used are presented.
- In **Chapter 3**, the academic test cases used for preliminary tests and the implementation performed in the main solver used during this thesis are presented. The σ-model is also introduced with a procedure for dynamically evaluating the model constant.
- In **Chapter 4**, LES simulations of the experimental set-up are compared with experimental results. Sensitivity tests are performed for identifying the key parameters that can impact the quality of the LES simulations.
- Finally, some proposals on improvement strategy of the model and the experimental set-up are suggested.

Chapter 1

Governing Equations and Literature survey

It must be admitted that the principal result of fifty years of turbulence research is the recognition of the profound difficulties of the subject.

S.A. Orszag (1970)[1]

[1]Taken from the book Turbulence: An Introduction for Scientists and Engineer of P.A. Davidson. (Oxford University Press 2004)

1.1 Governing Equations and Simplifying assumptions

In this section, the governing equations and the simplifying assumptions on which the work performed in this thesis is based on are presented. The Einsteins's rule of summation is used over repeated indices except for the index k refers to the k^{th} species. Summation for species will be explicitly represented with the $\sum$ symbol.
The set of conservation equations describing the evolution of a compressible flow with chemical reactions of thermodynamically active scalars are well known and available in different books [115, 154]. These are the continuity equations Eq.(1.1), mass species conservation Eq.(1.2), momentum conservation Eq.(1.3), total non-chemical energy conservation Eq.(1.4) and perfect gas equation of state Eq.(1.5) expressed as follows:

$$\frac{\partial \rho}{\partial t} + \frac{\partial (\rho u_i)}{\partial x_i} = 0 \tag{1.1}$$

$$\frac{\partial \rho Y_k}{\partial t} + \frac{\partial (\rho (u_i + V_{k,i}) Y_k}{\partial x_i} = \mathcal{W}_k \tag{1.2}$$

where $V_{k,i}$ is the diffusive velocity of species k in the i^{th}-direction.

$$\frac{\partial (\rho u_i)}{\partial t} + \frac{\partial (\rho u_i u_j)}{\partial x_j} = -\frac{\partial p}{x_i} + \frac{\partial \tau_{ij}}{\partial x_j} + \mathcal{S}_i \tag{1.3}$$

$$\frac{\partial (\rho e_t)}{\partial t} + \frac{\partial (\rho e_t u_i)}{\partial x_i} = -\frac{\partial q_i}{\partial x_i} + \frac{\partial (\tau_{ij} u_i)}{\partial x_j} - \frac{\partial (p u_i)}{\partial x_i} + \mathcal{Q}^{rad} + \mathcal{Q} + u_i \mathcal{S}_i \tag{1.4}$$

$$\frac{p}{\rho} = rT \tag{1.5}$$

where $\mathcal{W}_k$ is the mass production or consumption of the species k governed by the different chemical reactions, $\mathcal{Q}^{rad}$ is the radiative source term, $\mathcal{S}_i$ is the momentum source term acting in the i^{th}-direction and $\mathcal{Q}$ is the energy source term. τ_{ij} is the viscous stress tensor expressed as follows:

$$\tau_{ij} = 2\mu \left(S_{ij} - \frac{1}{3} \delta_{ij} S_{ll} \right) \text{ with } S_{ij} = \frac{1}{2} \left(\frac{\partial u_j}{\partial x_i} + \frac{\partial u_i}{\partial x_j} \right) \tag{1.6}$$

In what follows, some simplifying hypothesis are presented. They are actually the one considered in the main solver AVBP [1] used during this thesis. As it is shared by a large community of researchers, most of these hypothesis are taken from the AVBP HandBook or from similar research projects [5, 21, 104].

- **Simplifying hypothesis**

  Throughout this thesis work, the following hypothesis are considered:

  1. no external forces
  2. effects of volume viscosity are null
  3. no Dufour effect for the heat flux
  4. radiation heat transfer is negligible
  5. the gas mixture is supposed to be perfect
  6. no chemical reactions

- **Thermodynamical parameters:**

  The reference state is considered at the temperature $T_o = 0\ K$ and the pressure $P_o = 1\ bar$. The sensible enthalpies $h^T_{s,k}$, enstropies s^T_k and sensible energies $e^T_{s,k}$ are constant every 100 K and are tabulated from 0 to 5000 K. They are respectively defined by Eq.(1.7), Eq.(1.8) and Eq.(1.9):

$$h^T_{s,k}(T_i) = \int_{T_o=0K}^{T_i} C_{p,k}dT = \frac{h^{T,m}_{s,k}(T_i) - h^{T,m}_{s,k}(0)}{W_k}, \quad i = 1, 51 \tag{1.7}$$

$$s^T_k(T_i) = \frac{s^{T,m}_k(T_i) - s^{T,m}_k(T_0)}{W_k}, \quad i = 1, 51 \tag{1.8}$$

$$e^T_{s,k} = \int_{T_o=0K}^{T_i} C_{v,k}dT = h^T_{s,k}(T_i) - r_k T_i, \quad i = 1, 51 \tag{1.9}$$

The superscript $()^T$ stand for the tabulated variable at temperature T_i and the superscript $()^m$ for the molar variable. $h^T_{s,k}$, s^T_k and the molar weight W_k are taken from the JANAF [141] tables. Heat capacities at constant pressure $C_{p,k}$ and constant volume $C_{v,k}$ are considered constant between T_i and $T_{i+1} = T_i + 100\ K$ and are expressed as follows:

$$C_{p,k} = \frac{\partial h_{s,k}}{\partial T} \tag{1.10}$$

$$C_{v,k} = \frac{\partial e_{s,k}}{\partial T} \tag{1.11}$$

The sensible enthalpy of species k is obtained through a linear interpolation based on the temperature.

$$e_{s,k}(T) = e^T_{s,k} + (T - T_i)\frac{e^T_{s,k}(T_{i+1}) - e^T_{s,k}(T_i)}{T_{i+1} - T_i} \tag{1.12}$$

The sensible energy and sensible enthalpy of the mixing are expressed as follows:

$$\rho e_s = \sum_{k=1}^{N} \rho_k e_{s,k} = \rho \sum_{k=1}^{N} Y_k e_{s,k} \tag{1.13}$$

$$\rho h_s = \sum_{k=1}^{N} \rho_k h_{s,k} = \rho \sum_{k=1}^{N} Y_k h_{s,k} \tag{1.14}$$

- **Equation of state of the mixing of perfect gases:**

The state equation of the mixing of perfect gas is expressed as follows:

$$P = \rho \frac{\mathcal{R}}{W} T \tag{1.15}$$

where W is the molar mass of the mixing expressed following:

$$\frac{1}{W} = \sum_{k=1}^{N} \frac{Y_k}{W_k} \tag{1.16}$$

The constant r and the heat capacities C_p and C_v of the mixing are expressed with respect to the mass fraction of the different species:

$$r = \frac{\mathcal{R}}{W} = \sum_{k=1}^{N} \frac{Y_k}{W_k} \mathcal{R} = \sum_{k=1}^{N} Y_k r_k \tag{1.17}$$

$$C_p = \sum_{k=1}^{N} Y_k C_{p,k} \tag{1.18}$$

$$C_v = \sum_{k=1}^{N} Y_k C_{v,k} \tag{1.19}$$

$\mathcal{R} = 8.3143\ J.mol^{-1}.K^{-1}$ is the universal perfect gas constant. The polytropic exponant of the mixing is given by $\gamma = C_p/C_v$. The constant of the mixing, the heat capacities and the polytropic constant depend on the local composition of the mixing given by the molar fraction $Y_k(x,t)$. They can vary in space and also evolve in time:

$$r = r(x,t), \quad C_p = C_p(x,t), \quad C_v = C_v(x,t) \ \text{ and } \ \gamma = \gamma(x,t) \tag{1.20}$$

The temperature is deduced from the sensible energy using Eq. (1.12) and Eq. (1.13). The sound speed velocity of the mixing useful for defining the boundary conditions is given by the following expression:

$$c^2 = \gamma r T \tag{1.21}$$

- **Multi-species molecular diffusion:**

When external forces acting on the species are neglected, the exact expression of the diffusion velocity is reduced to:

$$V_{k,i} = \underbrace{-\sum_{l} D_{kl} \frac{\partial X_l}{\partial x_i}}_{mixture\ effect} \underbrace{- \sum_{l} D_{kl} \left(X_l - Y_l\right) \frac{1}{p} \frac{\partial p}{\partial x_i}}_{pressure\ gradient\ effect} \underbrace{- \sum_{l} D_{kl} \mathcal{X}_l \frac{\partial ln T}{\partial x_i}}_{Soret\ effect} \tag{1.22}$$

where D_{kl} are the multicomponent diffusion coefficients of the diffusion matrix and $\mathcal{X}_l$ the thermal diffusion ratio of species l. Solving the transport system Eq.(1.22) is an expensive task for CFD codes and this is why the system is often simplified in practice. First of all, the pressure gradient effect is neglected because the pressure variations are weak in most practical combustion systems. The Soret effect is also neglected and the simplification of Eq.(1.22) is achieved by the use of the Hirschfelder-Curtis approximation [60] with correction velocity. As mentioned by Giovangigli [54] this is the best possible first-order model for estimating diffusion velocities of a multicomponent mixture. It consists in replacing the rigorous mixture effect part of the diffusion system by a simpler one:

$$V_{k,i}^{hc} X_k = -D_k \frac{\partial X_k}{\partial x_i} \tag{1.23}$$

where the $V_{k,i}^{hc}$ denotes the Hirschfelder and Curtis diffusion velocity, and D_k an equivalent diffusion coefficient of species k into the rest of the mixture. The latter coefficient is built from the binary diffusion coefficients D_{ij} which can be assessed from the gas kinetic theory in [54]:

$$D_k = \frac{1 - Y_k}{\sum_{j \neq k} X_j / Djk} \tag{1.24}$$

The mass conservation is ensured by the system of the following two equations:

$$\sum_{k}^{N} Y_k = 1 \tag{1.25}$$

$$\sum_{k}^{N} Y_k V_{k,i} = 0 \tag{1.26}$$

In order to satisfy those two constraints, a correction velocity V_i^{cor} is added to the Hirschfelder and Curtis diffusion velocity. V_i^{cor} is expressed as :

$$V_i^c = \sum_{k=1}^{N} D_k \frac{W_k}{W} \frac{\partial X_k}{\partial x_i} \tag{1.27}$$

The diffusion velocities for each species k is then given by the following expression:

$$V_{k,i} = V_{k,i}^{hc} + V_i^{cor} \tag{1.28}$$

The diffusion species flux J_k that accounts for this corrective velocity is defined by the following expression:

$$J_{i,k} = \rho Y_k \left(V_i^{hc} + V_i^c \right) = -\rho \left(D_k \frac{W_k}{W} \frac{\partial X_k}{\partial x_i} - Y_k V_i^c \right) \tag{1.29}$$

Combined with the assumption of constant Schmidt numbers, the Hirschfelder and Curtis approximation is very convenient because the equivalent diffusion coefficients can be easily related to the kinematic viscosity according to: $D_k = \nu / Sc_k$. The problem is then efficiently closed by imposing the Schmidt numbers and it is not necessary to compute the D_{ij} coefficients which are complex functions of the collision integrals and thermodynamics variables. Finally the dynamic viscosity is modeled by a power law-expression:

$$\mu = \mu_{ref} \left(\frac{T}{T_{ref}} \right)^c \tag{1.30}$$

where typical values are $\mu_{ref} = 1.7 \times 10^{-5}$ Pa.s, $T_{ref} = 300$ K and $c = 0.76$.

- **Heat Diffusion term:**

  The total heat flux is the sum of the conduction heat flux expressed with the Fourier law and the diffusion heat flux of the species:

$$q_i = -\lambda \frac{\partial T}{\partial x_i} - \rho \sum_{k=1}^{N} \left(D_k \frac{W_k}{W} \frac{\partial X_k}{\partial x_i} - Y_k V_i^c \right) h_{s,k} \tag{1.31}$$

  where λ is the thermal conductivity of the mixing defined by assuming a constant Prandtl number:

$$\lambda = \frac{\mu C_p}{Pr} \tag{1.32}$$

1.2 Turbulence modeling and Large Eddy Simulation:

1.2.1 Turbulence modelling

Turbulence modeling is a very challenging and fascinating issue in an engineering point of view. Specially because of the complexity of the nature of the turbulence and the wide range of domain that it can affect. As described in several books available in the literature [7, 27, 117] turbulent flows are characterized by strong velocity fluctuations both in space and time resulting in a chaotic, diffusive, dissipative and intermittent flow motion (see Fig.1.1). As a consequence, turbulence can be a desirable phenomena that can increase performances in some industrial applications such as heat exchanger design, combustion, mixing process ...etc At the same time, it can alter the performances in other applications such as in pipe lines by enhancing the pressure loss, in aeroacoustic by altering the combustion stability in turbines for instance, or in the aeronautic sector. We all have in mind safety advices of the cabin crew during a flight when going through a turbulent environment.

Figure 1.1: Turbulence created by the eruption of the Mt.Spurr near Anchorage in 1992

In all cases, it is important for engineers to have reliable numerical models able to accurately predict its effects. A main characteristic of turbulent flows is the well known Reynolds number that expresses the ratio between the forces of inertia and the molecular viscosity effect:

$$Re \approx \frac{(U \cdot \triangle U)}{(\nu \cdot \triangle^2 U)} \tag{1.33}$$

where U is a characteristic velocity, ν the kinematic viscosity of the fluid. First attempt for understanding the complete dynamics of turbulent flows was provided by Kolmogorov who characterized them through a given spectrum and the energy cascade[2]. To this respect the most energetic eddies that provide the energy to the flow are of size L (integral length) and the smallest eddies where the energy is dissipated by viscous effects are of size η also known as the Kolmogorov length scale. The ratio of these two parameters is an indicator of the size of the spectrum or more specifically the number of degrees of freedom of the flow in one direction. It is approximated as follows:

[2]The forward energy cascade concept of Kolmorogov only holds for 3D turbulence which is the case throughout our study and implies the development of turbulence due to the vortex stretching motion. The stretching of the vortex in a plan leads to fluctuations in the direction perpendicular to that plan. In 2D turbulence, such as in oceanographic and atmospheric flows, the concept of forward energy cascade is no longer valid. Instead, there is an hypothesis of double cascade process [76] that consists in a forward enstrophy cascade and in an inverse energy cascade. The enstrophy is driven from the biggest scales to the smallest ones and the energy injected at a given scale is driven back to bigger scales through an inverse energy cascade process. More about 2D turbulence can be found in [78, 142]

$$\frac{L}{\eta} \approx Re^{3/4} \tag{1.34}$$

It means that for a 3D turbulent flow, the number of nodes required to fully characterize the flows would be around $Re^{9/4}$.
There are actually three main methods for predicting numerically turbulent flows. They can all be defined by their ability to reproduce the Kolmogorov spectrum:

- **Direct Numerical Simulation (DNS):**

  As its name implies, it consists in completely considering the Kolmogorov spectrum at each time step. Its application requires very accurate numerical schemes and well defined boundary conditions. It is sometimes referred to in the literature as a numerical experiment. In this approach, no model is required since all the scales of the flows are directly resolved meaning that all the $Re^{9/4}$ degrees of freedom should be considered in the DNS of a 3D flow. Recalling the order of magnitude of the integral length $L \approx 2 - 10$ mm and the Kolmogorov length $\eta \approx 10$ μm for an IC engine [59], the number of nodes that would be required to perform a DNS of an IC engines is roughly 10^{12}. Moreover the ratio of characteristics times also varies as $Re^{3/4}$ meaning that the Navier-Stokes equation have to be solved Re^3 (10^{16}) times if we want to calculate the evolution of the solution of volume L^3 for a duration equal to the characteristics time of the most energetic scale.(It is important to emphasize that this consideration does not take into consideration phenomena such as combustion, fuel atomization that will lead to a refinement of the size of the mesh). Compared to the current number of nodes used for IC engine simulations, it is obvious that performing DNS of IC engines is not affordable. Although DNS in complex geometries [100] have been recently performed, the use of DNS is mostly restricted to fundamental studies in simple configurations that aim at developping model for alternative methods such as RANS and LES described latter on.

- **Reynolds-Averaged Navier-Stokes (RANS):**

  The equations resolved in RANS simulations are obtained through a statistical averaging of the Navier-Stokes equations. It is only the spectrum of the mean flow that is partially resolved and all the turbulent structures are completely modeled. This is achieved by modeling the terms that appear in the averaged Navier-Stokes equations. The RANS approach allows to use coarse meshes which lead to fast computation times. It is widely used in the industry and can give very good results as long as the simulated flows are statistically steady. This method was extended to unsteady flows through the U-RANS (Unsteady-Reynolds-Averaged Navier-Stokes) modeling method.

- **Large Eddy Simulations (LES):**

  Large Eddy Simulation can be seen as a compromise between the extracted informations and the computational cost. It consists in spatially filtering the Navier-Stokes equations and to take into account only the biggest structures of the flows. The latter in most cases[3] control the dynamics of the flows. In LES simulations, the spectrum of turbulence is partially resolved at each time step under the assumption that the non resolved scales referred to as the Subgrid-Scale terms have an universal behavior no matter the geometry and the initial conditions. It is generally assumed that the subgrid scales of the energy spectrum have a dissipative behavior. It means that for a lower CPU time cost compared with DNS simulations (which is still important compared with RANS), one has access to more information than in a RANS simulation. Moreover, for a perfect LES, the increase of the mesh resolution should lead to a DNS simulation which is not the case for RANS. Coming back to the simulation of the IC engine, one can decide to accelerate the running time by simulating the flow with a lower spatial resolution while keeping the biggest structures of the flow. It remains "only" to well express the non resolved terms presented in the next section.

[3]The problem is more complex in combustion because chemical reactions take place at very small scales, still the use of LES for combustion prediction leads generally to better prediction compared to RANS [95].

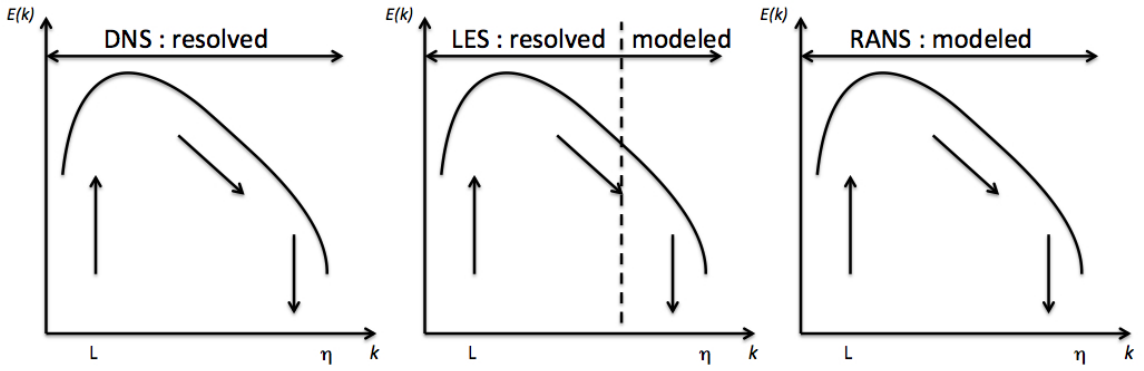

Figure 1.2: Comparison of the three main technique for numerically modeling the turbulence.

Fig. 1.2 summarizes how the three mentioned simulation methods handle the Kolmogorov energy spectrum. It confirms the fact that the modeling requirement in RANS simulations are more important although the scales that they should reproduce strongly depends on the configuration. Concerning the LES methods, the modeling effort focuses on reproducing the dissipative behavior of the small scales which can be achieved either numerically or physically.

1.2.2 Large Eddy Simulation formalism:

Length-scale separation on a generic function f in compressible turbulent flows is achieved with the spatial Favre filtering operation [2, 150] (it allows to avoid unclosed terms in the continuity equation) that reads :

$$\widetilde{f(\mathbf{x},t)} = \frac{1}{\overline{\rho(\mathbf{x},t)}} \int_{-\infty}^{+\infty} \rho(\zeta,t)\ f(\zeta,t)\ G_\Delta(\zeta-\mathbf{x})d\zeta, \tag{1.35}$$

where G_Δ denotes the filter function and the over bar symbol denotes the non mass weighted filtering operator:

$$\overline{f(\mathbf{x},t)} = \int_{-\infty}^{+\infty} f(\zeta,t) G_\Delta(\zeta-\mathbf{x})d\zeta, \tag{1.36}$$

Properties of the filters:

In order to ensure that the filtered Navier-Stokes equations are tractable, the chosen filter G_Δ has to meet the following properties:

- **P1** It must conserve constant values, which is equivalent to the normalization condition

$$\int_{-\infty}^{+\infty} G_\Delta(\zeta)d^3\zeta = 1; \tag{1.37}$$

- **P2** G_Δ has to be linear

$$\overline{f+g} = \bar{f} + \bar{g} \tag{1.38}$$

- **P3** It should commute with the derivation in space and time:

$$\overline{\frac{\partial f}{\partial t}} = \frac{\partial \bar{f}}{\partial t}, \quad \overline{\frac{\partial f}{\partial x_i}} = \frac{\partial \bar{f}}{\partial x_i}. \tag{1.39}$$

  This second property which is important to derive LES equations is not always verified specially on unstructured meshes where a second order commutation error can arise.

The function f can then be decomposed, based on the Favre-filter operator as:

$$f = \tilde{f} + f' \tag{1.40}$$

where $\tilde{f}$ is the resolved part of f and f' is the SGS part.
It is important to emphasize that in contrary to the traditional time averaging the Favre averaging leads to the following inequalities:

$$\bar{\rho}\tilde{\bar{f}} = \overline{\rho\tilde{f}} \neq \bar{\rho}\tilde{f} \tag{1.41}$$

$$\tilde{\bar{f}} \neq f \; and \; \tilde{f}' \neq 0 \tag{1.42}$$

Finally, it can be verified that the Favre-filter operator does not commute with the derivative:

$$\frac{\partial \tilde{f}}{\partial x_i} = \widetilde{\frac{\partial f}{\partial x_i}} + \frac{1}{\bar{\rho}}\overline{f\frac{\partial \rho}{\partial x_i}} - \frac{\tilde{f}}{\bar{\rho}}\frac{\partial \bar{\rho}}{\partial x_i} \tag{1.43}$$

This results is not incompatible with the property **P3** because it is not the Favre-filter which is applied to the Navier-Stokes equation but the non mass weighted filter operator which theoretically verifies the property **P3**.

Most common filters:

The most common filters used are:

- Top - Hat filter

$$G_\Delta(x_i - \zeta_i) = \begin{cases} \frac{1}{\Delta} & \text{for } |x_i - \zeta_i| \leq \frac{\Delta}{2} \\ 0 & \text{otherwise} \end{cases} \tag{1.44}$$

- Gaussian filter

$$G_\Delta(x_i - \zeta_i) = \sqrt{\frac{\Gamma}{\pi\Delta^2}} exp\left(\frac{-\Gamma|x_i - \zeta_i|^2}{\Delta^2}\right) \tag{1.45}$$

- Cutoff filter

$$G_\Delta(x_i - \zeta_i) = \frac{sin(k_c(x_i - \zeta_i))}{k_c(x_i - \zeta_i)} \tag{1.46}$$

where $k_c = 2\pi/\Delta$ is the wavenumber and $\Gamma \approx 6$ a parameter of the Gaussian filter [126].

More about the properties of the different filters can be found in the literature ([117, 126, 148]). It is worth noting that when dealing with general purpose solvers and complex geometries, the filtered operation is most of the time implicitly assumed and the filter width is equal to the local mesh size Δ.

Filtered Navier-Stokes equation and SGS terms: (see AVBP Handbook [1] for more details)

The application of the filtering operation to the instantaneous set of compressible Navier-Stokes equations presented in 1.1 leads to the following equations which contain the SGS quantities that need modeling [48, 126] :

$$\frac{\partial \bar{\rho}\widetilde{Y_k}}{\partial t} + \frac{\partial}{\partial x_i}(\bar{\rho}\widetilde{Y_k}\widetilde{u_i}) = -\frac{\partial}{\partial x_i}(\overline{J_{k,i}} + J_{k,i}^{SGS}) \tag{1.47}$$

$$\frac{\partial \bar{\rho}\tilde{u_i}}{\partial t} + \frac{\partial}{\partial x_j}(\bar{\rho}\tilde{u_i}\tilde{u_j}) = -\frac{\partial}{\partial x_j}(\bar{P}\delta_{ij} - \overline{\tau_{ij}} - \tau_{ij}^{SGS}) \tag{1.48}$$

$$\frac{\partial \bar{\rho}\tilde{e}_t}{\partial t} + \frac{\partial}{\partial x_j}(\bar{\rho}\tilde{e}_t\tilde{u}_j) = -\frac{\partial}{\partial x_i}(\overline{u_i(P\delta_{ij} - \tau_{ij})} + \overline{q_{ij}} + q_{ij}^{SGS}) \tag{1.49}$$

where $J_{k,i} = \rho Y_k V_{k,j}$ is the diffusive flux of species k in the j^{th}-direction and the superscript SGS denotes sub-grid scales contributions which must be modeled. Besides, filtered version of the viscous fluxes must be assessed from the known, filtered variables.
The diffusive species flux vector is computed from Eq.(1.30):

$$\overline{J_{k,i}} = -\overline{\rho\left(D_k\frac{W_k}{W}\frac{\partial X_k}{\partial x_i} - Y_k V_i^c\right)} \tag{1.50}$$

$$\approx -\bar{\rho}\left(\bar{D_k}\frac{W_k}{\overline{W}}\frac{\partial \tilde{X}_k}{\partial x_i} - \tilde{Y}_k\tilde{V}_i^c\right), \tag{1.51}$$

where higher order correlations between the different variables of the expression are assumed negligible. Similarly, the filtered heat flux is :

$$\overline{q_i} = -\overline{\lambda\frac{\partial T}{\partial x_i}} + \sum_{k=1}^{N}\overline{J_{k,i}h_{s,k}} \tag{1.52}$$

$$\approx -\bar{\lambda}\frac{\partial \tilde{T}}{\partial x_i} + \sum_{k=1}^{N}\overline{J_{k,i}}\tilde{h}_{s,k} \tag{1.53}$$

and the laminar filtered stress tensor $\overline{\tau_{ij}}$ is given by the following relations:

$$\overline{\tau_{ij}} = \overline{2\mu(S_{ij} - \frac{1}{3}\delta_{ij}S_{ll})}, \tag{1.54}$$

$$\approx 2\bar{\mu}(\tilde{S}_{ij} - \frac{1}{3}\delta_{ij}\tilde{S}_{ll}), \tag{1.55}$$

and

$$\tilde{S}_{ij} = \frac{1}{2}(\tilde{g}_{ij} + \tilde{g}_{ji}), \tag{1.56}$$

where $\tilde{g}_{ij} = \frac{\partial \tilde{u}_j}{\partial x_i}$ is the velocity gradient tensor of the resolved scales.

Finally, for the system to be solved numerically, closures need to be supplied for the remaining SGS terms:

- **the SGS stress tensor**

$$\tau_{ij}^{SGS} = -\bar{\rho}(\widetilde{u_i u_j} - \tilde{u}_i \tilde{u}_j), \tag{1.57}$$

  An eddy viscosity assumption is supposed for modeling the effect of the unresolved scales and the subgrid-scale stress tensor reads:

$$\tau_{ij}^{SGS} - \frac{1}{3}\tau_{kk}^{SGS}\delta_{ij} = 2\rho\nu_{sgs}\widetilde{S}_{ij} \tag{1.58}$$

  where ν_{sgs} is the subgrid-scale viscosity.

- **the SGS heat flux vector**

$$q_i^{SGS} = \bar{\rho}(\widetilde{u_i e_t} - \tilde{u}_i \widetilde{e_t}), \tag{1.59}$$

  The SGS heat flux is simplified as follows:

$$q_i^{SGS} = -\lambda^{SGS}\frac{\partial \tilde{T}}{\partial x_i} + \sum_{k=1}^{N} J_{k,i}^{SGS}\tilde{h}_{s,k} \tag{1.60}$$

  where λ^{SGS} is the subgrid-scale conductivity and $J_{k,i}^{SGS}$ the SGS diffusive species vector. Besides $\tilde{T}$ is the Favre filtered temperature which satisfies the modified filtered state equation $\bar{p} = \bar{\rho} r \tilde{T}$ [39, 97].

- **the SGS diffusive species vector**

$$J_{k,i}^{SGS} = -\bar{\rho}\left(D_k^{SGS}\frac{W_k}{\overline{W}}\frac{\partial \tilde{X}_k}{\partial x_i} - \tilde{Y}_k\tilde{V}_i^{c,SGS}\right) \tag{1.61}$$

  with

$$D_k^t = \frac{\nu^{SGS}}{S_{c,k}^{SGS}} \tag{1.62}$$

  where $S_{c,k}^{SGS}$ is the turbulent Schmidt number that will remain constant for all the species during this study: $S_{c,k}^{SGS} = 0.7$. In addition, $\tilde{V}_i^{c,SGS}$ is a correction velocity defines in such a way (see Eq.(1.63)) that the SGS diffusion species is coherent with mass conservation which requires $\sum_k J_{k,j}^{SGS} = 0$

$$\widetilde{V}_i^c + \widetilde{V}_i^{c,SGS} = \sum_{k=1}^{N}\left(\frac{\bar{\nu}}{S_{c,k}} + \frac{\nu_{sgs}}{S_{c,k}^{SGS}}\right)\frac{W_k}{\overline{W}}\frac{\partial \widetilde{X}_k}{\partial x_i}, \tag{1.63}$$

Throughout this thesis, emphasize will be paid only on the SGS viscosity (SGS stress tensor) and the SGS conductivity (SGS heat flux vector). These two numbers can be linked with the SGS Prandlt number similarly to the molecular Prandlt number: $Pr_{sgs} = \bar{\rho}\nu_{sgs}C_p/\lambda_{sgs}$. The different techniques for modeling those two terms are presented in the next section.

Remark: It is important to highlight that the formalism presented here is no the only one for defining the equations for LES. The one presented here is the most dominant in the literature and is based on the "filtering" so that LES evolutions equations are solved for the spatially filtered velocity field. Alternative formalisms such as the "self-conditioned fields" [116] approach exist that aim to overcome some shortcomings of the filtered based formalism.

1.3 Literature survey

There are three main categories for modeling the subgrid scale stress tensor well summarized by Sagaut [126] and Pope [117]:

- The functional approach which consists in modeling the effect of the unresolved small scales on the large scales without lingering over the structure of the tensor itself. It usually consists in introducing a scalar, the so-called subgrid scale viscosity, in order to reproduce the dissipative character of the small scales. It is probably the most widespread approach for industrial applications since the early works of Smagorinsky [135].
- The structural approach which consists in finding the best approximation of the structure of the SGS tensor using the resolved velocity field. It allows to take into consideration the anisotropy of the tensor and it also helps to reproduce the backscatter that is the energy transfer from the small scales to the bigger scales [77, 85, 113]. The most known of those models are probably the scale similarity model [9] and the Clark model [29]. This approach although suffering from a lack of dissipation is still of interest as shown by recent works of Park and Mahesh [109].
- As it can be difficult to distinguish physical dissipation to numerical errors in LES [105], there is a third category for modeling the SGS tensor effect that is the MILES (Monotonically Integrated LES) or ILES (Implicit LES). It consists as reported by Fernando *et al* [47] in incorporating effects of unresolved scales implicitly through a class of nonoscillatory finite-volume numerical fluids solvers. This class includes methods such as flux-corrected transport, the piece wise parabolic method and total variation dimishing algorithm. More details about ILES algorithms and results are available in the literature [15, 55].

We will focus on the models based on the functional approach (developed in the physical space) in other terms on the SGS viscosity ν^{sgs}. Indeed, one can consider that in combustion chambers, the most dominant effect to be reproduced by the unresolved scales is the dissipative one. The latter is probably more important than the exact knowledge of the structure of the SGS tensor. Moreover, the structural method can be seen as an improvement step of any functional models in order to take into account anisotropy and backscatter. The combination of those two methods leads to mixed models that share the advantages of the two formulations as shown by recent work of Lodato *et al* [87]. Concerning the MILES approach, which is a very interesting and pragmatic alternative, it requires specific algorithms and solver class which are not compatible with the main solver used during this thesis.

1.3.1 SGS viscosity models:

All the models that are presented here were developed in an incompressible framework. But they can be extended to compressible[4] flows under the assumption of low Mach number [42, 130]. In what follows, the initial filter used for incompressible flow $\bar{()}$ is replaced by the favre filter $\tilde{()}$. The following literature survey if of course not an exhaustive one. It intends to give a broad idea of the methodology for modeling the SGS viscosity and the major obstacles for their applications in complex geometries.

Static models:

Static models are model defined with a fix constant. As the value of the constant may vary depending on the configuration, the values of the constant given in what follows are the most used in the literature.

[4]The models can be extended without the necessity to take into account the trace part of the SGS stress tensor as proposed for example by Speziale *et al.* [138] or Zang *et al.* [158]. Indeed, for incompressible flows this term is included in the pressure but for compressible flows, it should also be modeled except for low Mach number flows for which its impact is negligible.

1. **Smagorinsky model [135]**

   The Smagorinsky model was initially developed for weather forecast simulations purposes. It corresponds to the strain rate and is expressed as follows :

$$\nu_{sgs} = (C_s\Delta)^2 D_s(\tilde{\mathbf{u}}) \tag{1.64}$$

   where $C_s = 0.18$ is the model constant Δ the length scale and D_s the time scale. The Smagorinsky model has the advantage that it can be very easily implemented and it is not very demanding in terms of computational time costs. It is also widely used for industrial applications because of its robustness. However, it leads to large over prediction of the SGS viscosity for shear flows and it is not appropriate when dealing with wall bounded flows or transient flows.

2. **Structure function model [94]**
   This model is based on the transposition in the physical space of the model of Métais and Lesieur [94] developed in the spectral space. The viscosity in the spectral space is expressed as follows:

$$\nu_{sgs} = \frac{2}{3} C_k^{-3/2} [\frac{\bar{E}(k,t)}{kc}]^{1/2} \tag{1.65}$$

   where $C_k = 1.4$ is the Kolmogorov constant and k_c the cutt-off wavelength.
   The transposition to the physical space is achieved via a structure function. The SGS viscosity is then expressed as:

$$\nu_{sgs}(x,\Delta,t) = 0.105 C_k^{-3/2} \Delta x [F_2(x,\Delta,t)] \tag{1.66}$$

   The main drawback of this model is that as long as there is no energy at the cutoff wavelength (in case of laminar flows for example) the spectral viscosity is zero. However, the physical viscosity is not zero because the structure function is based on gradient of the mean flow that are not necessarily zero in laminar/transient situation. This can lead to the same problem observed with the Smagorinsky model. More advanced structure functions [33] were developed to overcome those drawbacks but are still difficult to apply in complex configurations.

3. **SGS kinetic equation based model**

   This model is based on the use of the information contained directly in the unresolved scales. It consists in solving a modeled equation for the SGS kinetic energy. The SGS viscosity is expressed as :

$$\nu_{sgs} = C_{keq} \Delta \sqrt{\widetilde{k_{sgs}}} \tag{1.67}$$

   where $C_{keq} \approx 0.1$ and $\widetilde{k_{sgs}}$ is the SGS kinetic energy.
   The advantage of this model is that it is not based on the velocity gradient tensor and can well predict strongly turbulent flows for which velocity gradients are not necessarily very high. However, the choice of the different constants for the SGS kinetic equation can be discussed.

4. **Sagaut and Ta Phuoc Loc model [125]**
   The originality of this model is that it combines the information of the resolved and unresolved scales. Indeed, this model allows to take into consideration interaction between those two scales. It contains an additional parameter α to be properly estimated. The SGS viscosity is expressed as :

$$\nu_{sgs} = C_m |\tilde{S}|^{\alpha} (\widetilde{k_{sgs}})^{\frac{1-\alpha}{2}} \Delta^{1+\alpha} \tag{1.68}$$

Advanced static models

We refer to as "Advanced static models" models with a constant parameter, which have the intrinsically properties through their timescale to vanish in different laminar configurations. This is generally achieved by using invariant of the gradient velocity tensor g_{ij}. The advantage of such models for simulating complex configurations (more precisely IC engines in our case) is that the a priori knowledge of the geometry is not necessary since they automatically identify near wall region and then switch off.

5. **WALE model [106]**

The main objective of the WALE model was to correctly reproduce the correct near wall behavior y^3 [26] (where the $y-$ axis is the direction perpendicular to the solid boundary) of the SGS viscosity without any additional procedure. This model was the first able to meet this property which is important in case of wall bounded flows because it switches off the model in case of pure shear and allows a realistic transition from laminar to turbulent flow. The resulting SGS viscosity is expressed as follows:

$$\nu_{sgs} = (C_w \Delta)^2 D_w(\tilde{\mathbf{u}}) \tag{1.69}$$

where $C_w = 0.5$ is the model constant.

$$D_w(\mathbf{u}) = \frac{(\widetilde{S^d_{ij}}\widetilde{S^d_{ij}})^{3/2}}{(\widetilde{S_{ij}}\widetilde{S_{ij}})^{5/2} + (\widetilde{S^d_{ij}}\widetilde{S^d_{ij}})^{5/4}} \tag{1.70}$$

and $\widetilde{S^d_{ij}}$ is the symmetric part of the square of the velocity gradient tensor.

6. **Vreman model [149]**

This model presents similar advantages as the WALE model but with a different asymptotic behavior y^1. It is also well suitable for wall bounded and shear flows since it was specially design to vanish in those configurations. The SGS viscosity is expressed as :

$$\nu_{sgs} = (C_v \Delta)^2 D_v(\tilde{\mathbf{u}}) \tag{1.71}$$

where $C_v = 0.264$ is the model constant.

$$D_v(\tilde{\mathbf{u}}) = \sqrt{\frac{B_\beta}{\alpha_{kl}\alpha_{kl}}} \tag{1.72}$$

and

$$B_\beta = \beta_{11}\beta_{22} - \beta_{12}\beta_{12} + \beta_{11}\beta_{33} + \beta_{13}\beta_{13} + \beta_{22}\beta_{33} + \beta_{23}\beta_{23}$$

$$\beta_{ij} = \textstyle\sum_{m=1}^{3} \alpha_{mi}\alpha_{mj}$$

$$\alpha_{ij} = \frac{\partial \tilde{u}_j}{\partial x_i} \tag{1.73}$$

Despite the interesting properties of the Vreman and the WALE model, they both share the same drawbacks. Indeed recent studies [18, 40] showed that the WALE model produces viscosity in case of pure rotation thus potentially alter the prediction of vortex motion. It is also the case for the Vreman model. This issue is discussed in the chapter 3 of this manuscript.

Improvement methods:

The development of a SGS model can be divided in two steps: the choice of the time scale and the improvement method in order to compensate some drawbacks of the time scale. The choice of the improvement method is of course as important as the development of the time scale and the resulting model is an entirely new SGS viscosity/tensor. Again the list presented here is not an exhaustive list of the procedures for improving the prediction of eddy-viscosity type models.

1. **Damping functions [35]**

   The damping function was initially introduced by Deardoff in order to overcome the main drawback of the Smagorinsky model in Turbulent Channel. Indeed, a simple diminution of the Smagorinsky constant is not enough in case of wall-bounded flows and it is then necessary when getting close to the solid boundary to damp the viscosity. The resulting SGS viscosity is then expressed as follows:

   $$\nu_{sgs} = (C_s\Delta)^2 f(y^+) D_s(\tilde{\mathbf{u}}) \tag{1.74}$$

   where $f(y^+)$ is the Van-Driest function:

   $$f(y^+) = 1 - exp(-y^+/A^+) \tag{1.75}$$

   with $A^+ = 25$

   The main inconvenient of the Van-Driest function is that it requires the explicit knowledge of y^+ which is straightforward in turbulent channel but a difficult task in an industrial configuration. Alternative damping function like the function proposed by Yoshizawa *et al* [156] are now available to overcome this issue.

2. **Germano-identity and Dynamic Smagorinsky model [52]**

   Among the different improvement methods, the Germano-identity is probably the most popular. Although the hypothesis of local equilibrium on which it is based can be discussed [32], it has the advantage to overcome almost all the drawbacks of the Smagorinsky model: value of the constant, overestimation of the viscosity for non-turbulent flows, near wall damping. The Germano-identity leads to the development of the dynamic Smagorinsky model that has the originality to have a constant that varies both in space and time. The construction of this model consists in using two filters: the initial filter $\tilde{()}$ (filter width Δ) and the test filter $\hat{()}$ (filter width $\hat{\Delta}$). When applying those filters to the NS equations there are two SGS tensors that appear (τ_{ij} and T_{ij}) and which are linked by the Germano-identity as follows:

   $$T_{ij}^{sgs} - \hat{\tau}_{ij}^{sgs} = L_{ij} \tag{1.76}$$

   where L_{ij} is the Leonard term:

   $$L_{ij} = \widehat{\tilde{u}_i\tilde{u}_j} - \widehat{\tilde{u}}_i\widehat{\tilde{u}}_j \tag{1.77}$$

   The same viscosity is used for modeling the two SGS tensors and are rewritten following:

   $$\tau_{ij}^{sgs} = 2C_s^2\gamma_{ij} \tag{1.78}$$

   and

$$T_{ij}^{sgs} = 2C_s^2\beta_{ij} \tag{1.79}$$

the Germano-identity becomes:

$$2C_s^2\beta_{ij} - \widehat{2C_s^2\gamma_{ij}} = L_{ij} \tag{1.80}$$

at this stage, it is assumed that the constant does not vary over a distance equal to the test filter meaning that $\widehat{2C_s^2\gamma_{ij}} = 2C_s^2\widehat{\gamma_{ij}}$. Equation 1.80 becomes:

$$2C_s^2 M_{ij} = L_{ij} \tag{1.81}$$

with

$$M_{ij} = \beta_{ij} - \widehat{\alpha_{ij}} \tag{1.82}$$

Using the least mean square method [84] the final constant of the dynamic constant is expressed as follows:

$$C_s^2 = -\frac{1}{2}\frac{L_{ij}M_{ij}}{M_{ij}M_{ij}} \tag{1.83}$$

The problem with the dynamic Smagorinsky is the stabilization of the value of the constant C_s. Negative values that were considered as "backscatter" prediction can strongly disturb the simulation. The most popular technique is to average the constant over homogeneous directions when they exist. The constant is then expressed as follows:

$$C_s^2 = -\frac{1}{2}\frac{< L_{ij}M_{ij} >_h}{< M_{ij}M_{ij} >_h} \tag{1.84}$$

where $< >_h$ stands for an ensemble average over the homogeneous directions. For example, plans parallel to the wall in a turbulent channel.
Because in most industrial applications it is not easy to identify such homogeneous directions, different more advanced stabilization methods were developped such as the localization methods [53], the lagrangian methods [93] or more recently a method that allows to reduce the error on the dynamic constant [89]. Still, the common practice is to apply the least mean square method over a small volume surrounding the node of interest and to simply set the negative values of the constant to zero (which is the clipping) leading to:

$$C_s^2 = \mathbf{max}\ \left[0, -\frac{1}{2}\frac{< L_{ij}M_{ij} >_{loc}}{< M_{ij}M_{ij} >_{loc}}\right] \tag{1.85}$$

where $< >_{loc}$ stands for an average over a small volume surrounding the node of the current grid point.
The dynamic procedure has always been considered as a standard procedure to improve the prediction of a model. Analytical and numerical results performed in this thesis will show that it can not be successfully applied to all models.

3. **Mixed models**

Mixed models inspired by the Bardina studies [9, 10] come from the decomposition of the SGS tensor:

$$\tau_{ij} = \bar{\rho}(\widehat{u_i u_j} - \tilde{u}_i\tilde{u}_j) = \underbrace{L_{ij} + C_{ij} + R_{ij}}_{Leonard\ decomposition} = \underbrace{\mathcal{L}_{ij} + \mathcal{C}_{ij} + \mathcal{R}_{ij}}_{modified\ Leonard\ decomposition} \tag{1.86}$$

In the Leonard decomposition the velocity $u_j = \tilde{u}_j + u'_j$ is introduced only in the first term of the SGS tensor :

$$L_{ij} = \bar{\rho}(\widetilde{\tilde{u}_i\tilde{u}_j} - \tilde{u}_i\tilde{u}_j) \tag{1.87}$$

$$C_{ij} = \bar{\rho}(\widetilde{\tilde{u}_i u'_j} + \widetilde{u'_i\tilde{u}_j}) \tag{1.88}$$

$$R_{ij} = \bar{\rho}\widetilde{u'_i u'_j} \tag{1.89}$$

In the modified Leonard decomposition the velocity is introduced in the two terms of the SGS tensor:

$$\mathcal{L}_{ij} = \bar{\rho}(\widetilde{\tilde{u}_i\tilde{u}_j} - \tilde{\tilde{u}}_i\tilde{\tilde{u}}_j) \tag{1.90}$$

$$\mathcal{C}_{ij} = \bar{\rho}(\widetilde{\tilde{u}_i u'_j} + \widetilde{u'_i\tilde{u}_j} - \tilde{\tilde{u}}_i\tilde{u'}_j - \tilde{\tilde{u}}_j\tilde{u'}_i) \tag{1.91}$$

$$\mathcal{R}_{ij} = \bar{\rho}(\widetilde{u'_i u'_j} - \tilde{u'}_i\tilde{u'}_j) \tag{1.92}$$

The modified decomposition is interesting because each terms respect the fundamental property of the Galilean invariance and can be modeled separately. Studies of Germano [51] and Speziale [137] have demonstrated the importance of this property and in [107] a more extensive review is done about the invariant modeling in LES of turbulence.

The similarity mixed model is obtained by neglecting $\mathcal{C}_{ij}$ and the second term in $\mathcal{R}_{ij}$. The SGS stress tensor is then modeled as:

$$\tau_{ij}^{sgs} \simeq \bar{\rho}\widetilde{u'_i u'_j} + \mathcal{L}_{ij} \tag{1.93}$$

The first term in Eq.(1.93) is modeled with the SGS viscosity. The final expression of the SGS stress tensor is as follows:

$$\tau_{ij}^{sgs} = -2\bar{\rho}\nu_{sgs}S_{ij} + \bar{\rho}(\widetilde{\tilde{u}_i\tilde{u}_j} - \tilde{\tilde{u}}_i\tilde{\tilde{u}}_j) \tag{1.94}$$

where ν_{sgs} can be either a dynamic model [150, 159] or a static model [87].
Mixed models are very interesting alternative for simulating flows for which the shortcoming of eddy-viscosity models can have an impact.

4. **Variational Multi-Scale methods and filtered models**

VMS methods can be considered as an entirely different formulation of LES. It is sometimes referred to in the literature as VMS-LES. However we made the choice to include this formulation as an improvement methods for existing models. In contrary to the classical LES formulation where the SGS tensor acts on the entire resolved velocity field, the VMS method as describe by Hughes *et al* [61] consists in an a priori separation of scales. It leads to the resolution of two distinct equations: one for the bigger scales $\mathbf{u}$ which do not require any closure and the second for the small-scales $\mathbf{u^s}$ which require a model. The main advantage of the VMS formulation is that the SGS viscosity is a function of the small-scales $\mathbf{u^s}$ which do not exist in laminar flows. Resulting VMS models are then very interesting since they switch on only when the flow is turbulent. More information about VMS methods can be found in the literature [11, 62, 75].
Similar to the VMS approach, another type of improvement strategy also exists that consist in a posteriori filtering (with a high-pass filter) [128] the resolved velocity field u and then to express the SGS viscosity as a function of the filtered velocity. The resulting viscosity is also inactive in case of laminar flows. This property was for example use to overcome the drawback of the WALE model in case of pure rotation [18] while preserving its properties to vanish near walls with the proper asymptotic behavior.

5. **Global dynamic method for the constant**

   The development of advanced time scales (Vreman and WALE) already mentioned above now gives the possibility to evaluate globally rather than locally the coefficient. Indeed, because they meet several local properties, it remains only necessary to evaluate the proper global dissipation. Two global dynamic methods [108, 157] were recently developed and the most efficient according to the study of Lee *et al.* [81] and easy to implement consists in performing a volume weighted averaging of local values that are obtained through the Germano identity. The resulting coefficient homogeneous in space is then expressed as:

$$C_g^2 = -\frac{1}{2}\frac{< L_{ij}M_{ij} >_v}{< M_{ij}M_{ij} >_v} \tag{1.95}$$

   where $< >_v$ stands for the volume weighted averaging performed over the entire geometry.
   The global dynamic procedure presents the advantage that it does not require any homogeneous directions and the issue of negative constant is avoided. Because the dynamic procedure is used only for estimating the overall dissipation, the time scale should be reliable enough to vanish in laminar regions. This is not the case for the Smagorinsky model and neither the two cited advanced models vanish in case of pure rotation.

1.3.2 SGS heat flux:

Similar to the SGS tensor, the SGS heat flux can be modeled using a functional or structural method. First attempts of structural modeling of the SGS heat flux were performed by Calmet [23]. A large review of the structural models (based on the gradient diffusion hypothesis) was recently performed by Wang *et al.*[151].
As for the SGS tensor, we have chosen a functional method for modeling the SGS heat flux. It consists to introduce a SGS conductivity λ_{sgs} that will reproduce the heat transfer induced by the unresolved small scales. The SGS heat flux is then expressed as follows:

$$q_j^{sgs} = -\lambda^{sgs}\frac{\partial \tilde{T}}{\partial x_j} \tag{1.96}$$

Two main formulations are available for modeling the SGS conductivity:

1. **SGS conductivity based on a constant SGS Prandtl number**

   The advantage of this hypothesis is that it is very simple to implement. The SGS conductivity is expressed as follows:

$$\lambda^{sgs} = \frac{\bar{\rho}C_p}{Pr^{sgs}}\nu^{sgs} \tag{1.97}$$

   It remains only necessary to set the value of the SGS Prandtl number. The SGS conductivity shares the same properties and also the drawbacks of the SGS conductivity. But the main problem of such a formulation is near solid boundaries. Indeed, when getting close to walls, the turbulent Prandtl should increase in order to damp the SGS heat flux [68, 69]. Moreover, as for the constant of the SGS viscosity model the SGS Prandt number may vary with the turbulence intensity, mesh resolution and also numerical scheme used.

2. **SGS conductivity inspired from the dynamic Smagorinsky model**

   We can suppose that for non wall-resolved simulation and RANS approaches the hypothesis of a constant turbulent Prandtl number completely makes sense. But in an LES point of view for

which spatial variations are expected it is necessary to account for those variations through the SGS conductivity. One of the best way to achieve that is to use the Germano-identity as done by Moin *et al* [97] for computing the dynamic Prandtl number. In order to avoid numerical issues, we will directly compute the SGS conductivity. In fact, from Eq. 1.97 the SGS conductivity can be expressed as :

$$\lambda^{sgs} = \bar{\rho} C_p \ (C_\lambda \Delta)^2 D_s(\mathbf{u}) \tag{1.98}$$

where $D_s(\mathbf{u})$ is the Smagorinsky time scale and C_λ an unknown constant that will be computed dynamically.

The procedure is similar as for the dynamic Smagorinsky model. The energy equation is filtered using two filters of size Δ and $\hat{\Delta}$. They are two terms that appear: q^{sgs} and Q^{sgs}. The Germano-identity gives the following relationship between the two terms:

$$H_j = Q_j^{sgs} - \hat{q}_j^{sgs} = C_p(\widehat{\bar{\rho}\tilde{u}_j\tilde{T}} - (1/\hat{\bar{\rho}})\widehat{\bar{\rho}\tilde{u}_j}\widehat{\bar{\rho}\tilde{T}}) \tag{1.99}$$

The same conductivity model is used for modeling the two SGS Heat flux tensors following:

$$q_j^{sgs} = C_\lambda^2 \gamma_j^{'} \tag{1.100}$$

and

$$Q_j^{sgs} = C_\lambda^2 \beta_j^{'} \tag{1.101}$$

assuming that the constant does not vary over a distance equal to the test filter Eq.(1.99) reads:

$$C_\lambda^2 N_j = H_j \tag{1.102}$$

where

$$N_j = \beta_j^{'} - \widehat{\gamma_j^{'}} \tag{1.103}$$

using the least square method of Lilly [84] the final expression of the SGS dynamic conductivity constant reads:

$$C_\lambda^2 = \frac{H_j N_j}{N_j N_j} \tag{1.104}$$

As in the case of the dynamic Smagorinsky constant, it is recommended to stabilize this expression by averaging the constant over homogeneous directions. For reasons already mentioned this is not possible in IC engines.

$$C_\lambda^2 = \mathbf{max}\ \left[0, \frac{< H_j N_j >_{loc}}{< N_j N_j >_{loc}}\right] \tag{1.105}$$

We have decided to stabilize with a local averaging over the cells surrounding ($<>_{loc}$) the current node and to clip the negative remaining value of the constant (Eq. 1.105). One could wonder why we do not recommend the clipping of the SGS viscosity while we still use the same procedure for the conductivity. Since it is the velocity that convect the temperature, clipping the SGS viscosity may have a larger impact on the flow while the effect of clipping the SGS conductivity is expected to be minor. Moreover, compared to the constant SGS Prandtl number actually used in the AVBP solver [1], this formulation will allow to take into account regions where the SGS heat flux should vanish. This is a first step before further improvements.

Chapter 2

Experimental set-up and Diagnostics:

The target applications of the models that are developed in the framework of this thesis are Internal Combustion (IC) engines. Academic cases are of course used in a first step to make sure that the models respect the properties that will be enumerated latter on in the third chapter of this manuscript. But in order to make sure that those models would be reliable and predictable enough in complex configurations, it is necessary to compare their predictions against experimental data that are somehow representative of the physics (combustion is considered in this study as an aerothermal effect without species modification) taking place. To this respect, an experiment that consists in a pulsed hot jet that impinges with a cold surface in presence of a cross flow (at ambient temperature) was designed. This experiment was specially set-up for comparison with Large Eddy Simulation results: simple enough to enable accurate model validation, fully controlled boundary conditions (the cross flow profile and injector velocity profile are well-defined) and representative enough to take into account the most important physical phenomena occurring in combustion chambers: unsteadiness and interaction among hot vortices and a developed boundary layer near solid boundaries. Moreover advanced non intrusive optical diagnostics (Particle Image Velocimetry, Laser Induced Fluorescence, Laser Induced Phosphorescence Thermography) are applied in order to extract relevant data such as velocity field, temperature field and wall temperature. Those data will be of particular interest for the assessment of the robustness and predictability of the different models.

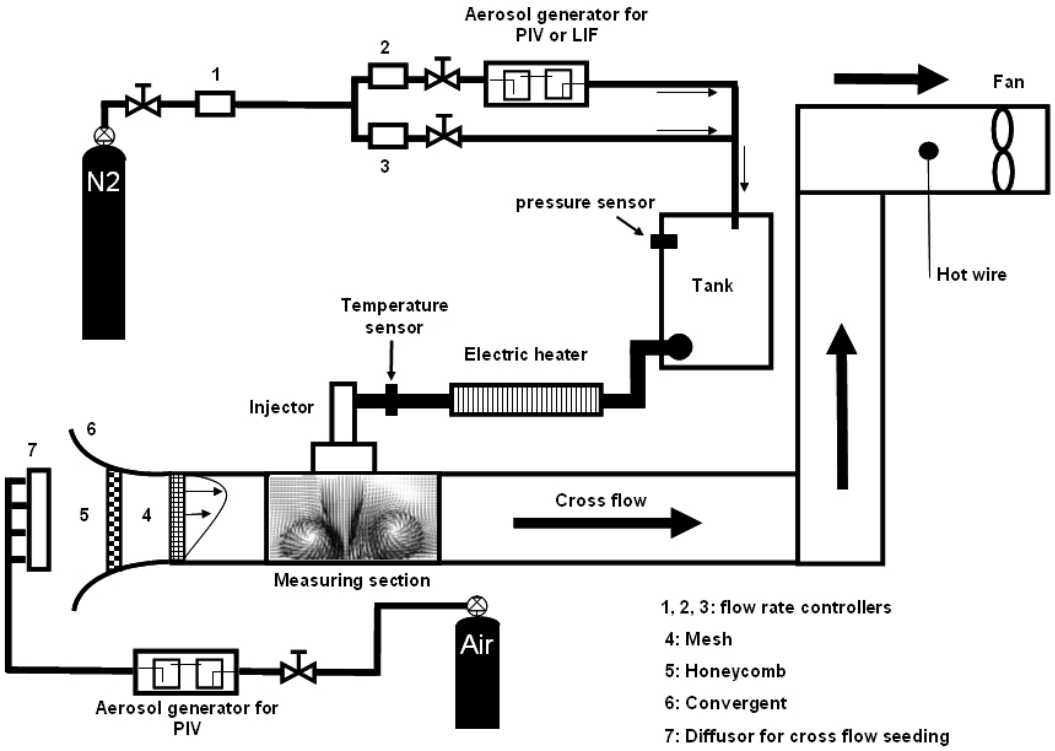

Figure 2.1: Schematic description of the experimental set-up of the hot impinging pulsed jet in presence of a cross flow.

2.1 Experimental set-up

The flow pattern inside a combustion chamber is the result of a combination of interaction between various sources: flow induced by the movement of intakes/exhausts valves, movement of the piston, vaporization of the fuel after injection, wall interaction and of course dilatation of gas after the combustion. Although the recent progress made in the field of optical diagnostics development make it now possible to have a deeper understanding of those combined phenomena through optical IC engines, it is still a challenge today to provide complete validation data in the engine environment. In addition, performing full validation computation in the engine environment is also a major challenge specially in term of computational time cost. The alternative chosen in this work is to reproduce the different cited phenomena in a more simple configuration, simple enough to allow good quality computation and experimental measurements, but complex enough to catch the main important features and therefore provide a good validation platform. A configuration consisting of cycles of interaction between hot irregular vortices and their impingement with solid boundaries in a turbulent and unsteady environment was therefore chosen for this purpose. These guidelines led to the experimental set-up shown in Fig. 2.1 that takes into account the constraints discussed in the next section.

2.1.1 Design guidelines:

The target objective is to reproduce numerically the experimental set-up along with the requirement to provide adequate conditions to the application of optical diagnostics techniques for the data acquisition leaded to some guidelines regarding the characteristics of the experiment. The guidelines listed in what follows are actually the best compromises between the constraints imposed by the modeling issues and those imposed by the application of the measurement techniques:

- **Dimensions and unsteadiness:** Since flows in combustion chambers are highly unsteady, it is important that the models developed account for fast temporal variation (typically of the order of

100μs). At the same time, a good spatial resolution is required within the computational domain. These requirements have been taken into account for the design of the experiment, in particular for the selection of the injector technology as discussed here. Concerning the computational domain, the first parameter that was set was the height of the computational domain H (the distance between the injector exit and the impinging surface) with respect to the injector diameter D. Based on a

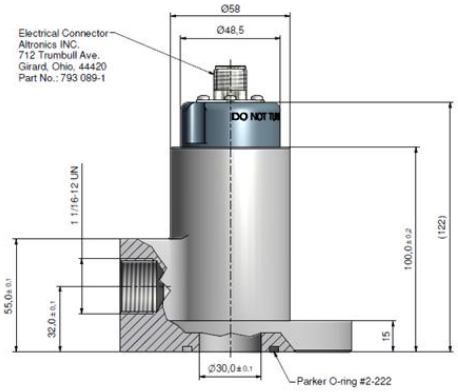

Figure 2.2: Hoerbiger $GV50$ injector.

recent study [86] where similar turbulent impinging jets were simulated, it was decided to keep a constant and refined resolution in the streamwise and spanwise direction corresponding to $5H$. The volume where the mesh is refined corresponds to $V_{mesh} = 25H^3$. Let us consider $H = \beta D$ and N the number of nodes per diameter, the total number of nodes is given by the following expression:

$$Total_{node} \approx 25\beta^3 N^3 \tag{2.1}$$

It is considered here that $N = 30$ is the minimal number of nodes required to correctly describe the velocity profile in the injector exit. Varying β from 2 to 3 would increase the total number of nodes from 5.4 million nodes to more than 18 million nodes only considering the volume of interest around the injector. This result shows that it is necessary to limit the parameter β to a maximum of 2, in order to keep a good resolution and to limit the total number of nodes to a reasonable level considering computational cost. This distance also allows the formation of the vortex ring which is one of the important feature of the experiment. However, this dimension is also constrained by optical diagnostic issues. Indeed, in order to avoid using specific optical elements, the visualization domain is limited to a minimum dimensions of the order of 1 to 2 cm. Selecting a channel height of 2 cm means that the injector diameter is about 1 cm since the simulation constraints impose $\beta = 2$. As a result, the requirements for the injector exit are that the injector diameter is 1 cm and that its temporal response is of the order of 100μs. This shows that typical injector technology used in engine is not adequate since while the typical time response is fast enough, the nozzle hole diameter is much too small (typically lower than 1mm). This would require a visualization domain of the order of 2 mm considering simulation constraints, which is not practical for optical diagnostic application, or a very important number of node which is not practical for simulation when considering computational time. For these reasons, an Hoerbiger GV 50 injector was selected (see Fig. 2.2). It is characterized by a fast response time (100μs) and a large flow area (effective flow area diameter of 1cm, exit diameter of 3 cm). A convergent was used to reduce the exit diameter to the same value than the effective area, $D = 1$cm. This convergent was designed to allow a uniform velocity profile at the injector exit. Its geometry is described in more details later in the manuscript.

- **Low Mach Number flows:** The models developed in the framework of this thesis are done under the important assumption that only low Mach number flows are considered. It typically means $M < 0.2$. Although flows close to the intake and exhaust valves can be at a sonic state, velocities inside combustion chambers are in general small compared to the sound velocity. The maximal temperature ($T_{max} = 393$ K) that the injector can handle leads to a threshold for the velocity around $80 - 95$ m/s. The velocity amplitude is controlled by the pressure in the tank (see Fig. 2.1) that is fixed after preliminaries PIV measurements at $P_{tank} = 200$ mbar (Due to pressure losses

in the pipes between the tank and the injector, the Bernoulli equation did not lead to the correct value of the pressure that corresponds to the target velocity magnitude at the injector exit). For security purposes, the injected gas is nitrogen. It is a neutral gas which will not interact with the particles and fluorescent tracer molecules that will be used for optical diagnostics purposes.

- **Cross Flow:** The presence of the cross flow was necessary to recreate a turbulent environment and the development of a cold boundary layer near walls. It is generated by a fan situated downstream of the experimental set-up. The velocity of the cross flow was monitored with a hot wire and tuned in order to have a deviation of the jet of around 1 cm at the impinging location. This was done qualitatively by visualization at different cross flow rate using Schlieren visualization technique. The turbulent intensity of the cross flow was generated by a grid situated at 10 cm of the centre of the jet. The size of the mesh of the grid was based on works of [7]. Before generating the turbulence, it was necessary to have a flat velocity profile and laminar flow at the entrance of the channel. This was achieved with a combination of a convergent and an honeycomb. The role of the honeycomb is to brake the biggest turbulent structures and laminarize the cross flow before imposing the turbulence with the grid. The shape of the convergent is based on work of [13, 17, 92]. The main difficulty was to avoid any separation of the boundary layer. Detailed on the shape of the convergent, the size of the honeycomb and the grid size are given in the next section.

- **Optical accessibility:** Wide optical accesses were provided by UV quality (Excimer 248 nm) large quartz window in order to optimize the application of advanced optical diagnostics. The advantage of those techniques is that there are non intrusive. The flow is not disturbed during the measurements and the extracted data are more reliable. The final experimental set-up is equipped with 4 wide optical access, two on the sides parallel to the cross flow, one perpendicular to the cross flow and another one on the top.

- **Wall temperature measurement:** Since the injector can not support a gas heated at more than $T_{max} = 400$ K, it was necessary to identify an appropriate material for the impinging surface that could lead to a measurable increase of the wall temperature. The choice was based on a simple 0D model based on the thermal effusivity of two bodies in contact. Indeed, assuming the perfect case of contact between the nitrogen coming from the injector at T_{max} and the impinging surface, the instantaneous temperature (T_I) at the interface is given by the following expression:

$$T_I = \frac{(E_N T_N + E_w T_w)}{(E_N + E_w)} \tag{2.2}$$

where E_N, E_w are respectively the nitrogen and wall thermal effusivity and T_N, T_w are respectively the initial nitrogen and wall temperature.

Table 2.1: Temperature increase for different materials

Material	ρ (Kg/m^3)	C_p $(KJ/Kg/K)$	λ $(W/m/K)$	Effusivity $(J.K^{-1}m^{-2}.s{-}1/2)$	ΔT (K)
nitrogen	0.96	1.012	0.025	0.16	—
Aluminium	2700	0.897	200	695.97	0.02
Copper	8920	0.385	380	1142.36	0.01
Zinc	7135	0.387	1.16	56.60	0.19
Plexiglas	1190	1.47	0.19	18.23	0.58
Balsa	160	2.9	0.055	5.05	2.05
WDS Ultra	2.14	1.05	0.019	2.14	4.65
WDS High	2.34	1.05	0.021	2.35	4.27

Table 2.1 summarizes the different predicted contact temperatures for different materials. We can observe that for aluminum, the temperature increase is not measurable with the technique available. The choice of the material was an important issue for performing wall temperature measurement. Finally the WDS Ultra was chosen because it is a very good thermal insulator material with a low effusivity and that should theoretically leads to a temperature drop of 4 K during the jet impact which was considered to be measurable.

2.1.2 Experimental set-up description:

The experimental set-up is made of four main parts: the admission part, the jet-interaction part, the gas supply part and the extraction part.

Admission part

The admission part situated upstream of the set-up allows to generate a smooth cross flow characterized by a flat velocity profile and a specific turbulent intensity. The cross flow is useful to reproduce the boundary layer interaction with the jet and also clean the jet-interaction part from the seeding particles. This part is composed of: a convergent for accelerating the flow and generating a flat velocity profile, a Honeycomb (the only constraint on the honeycomb design is the length which should be at least eight time bigger than the size of a single cell [12, 91]) for breaking the large turbulent structures thus smoothing the cross flow and finally a grid for imposing the turbulent intensity.

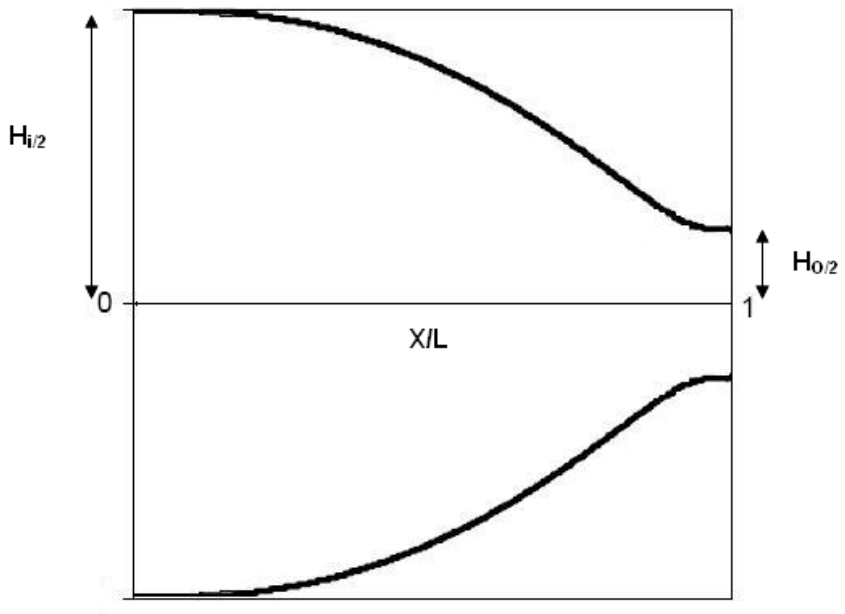

Figure 2.3: Convergent shape: $H_{i/2}$ is the inlet half height , $H_{o/2}$ is the outlet half height, L is the contraction length, X is the horizontal coordinate

The shape of the convergent was designed to avoid boundary layer separation as recommended in previous studies [13, 17, 92]. The main parameters for defining the shape of the convergent are:

- contraction ratio C = inlet-area/outlet-area
- height ratio ϵ_H = inlet-height/outlet-height
- shape parameter θ which is set to 0.4

Table 2.2: Parameters of the convergent

Inlet-height	Outlet-height	Contraction length	Contraction ratio	Height-ratio
200 mm	20 mm	200 mm	10	10

The half-height as indicated in Fig. 2.3 of the convergent is given by the following expression:

$$h_{i/2} = \left[-\eta(H_{i/2}^{1/\theta} - H_{o/2}^{1/\theta}) + H_{i/2}^{1/\theta}\right]^{\theta} \tag{2.3}$$

and

$$\eta = 10\left(\frac{x}{L}\right)^3 - 15\left(\frac{x}{L}\right)^4 + 6\left(\frac{x}{L}\right)^5 \tag{2.4}$$

The grid for imposing the turbulence is characterized by a solidity coefficient of the biggest holes. The diameter of the holes decreases from the top to the bottom. The diameter of the biggest holes is $D_{grid}^{big} = 0.8$ mm and the distance between two holes is around $d_{holes} = 0.2$ mm. The diameter of the smallest holes is $D_{grid}^{small} = 0.5$ mm. (see Fig. 2.4).

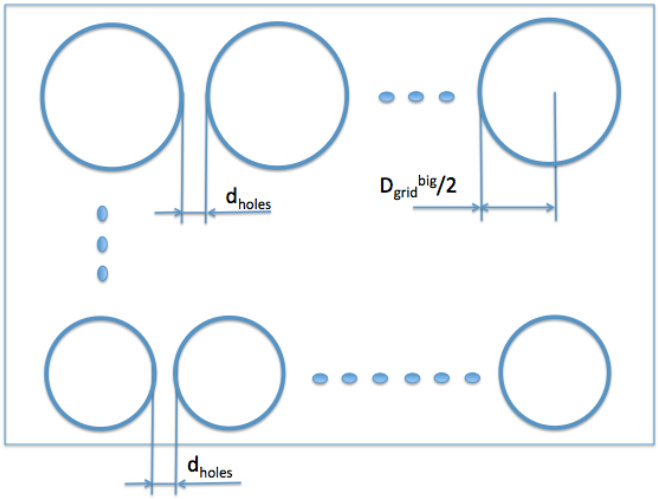

Figure 2.4: Schematic representation of the grid

The solidity factor [7] is defined as follows:

$$\psi = \frac{surface - blocked - by - the - grid}{initial - surface} \tag{2.5}$$

The solidity factor reads:

$$\psi \approx \frac{((D_{grid}^{big}/2 + d_{holes})^2 - (D_{grid}^{big}/2)^2)}{(D_{grid}^{big}/2 + d_{holes})^2} \approx 0.5 \tag{2.6}$$

The grid Mesh size can be approximated to $M \approx D_{grid}^{big} + d_{holes} \approx 1mm$. The position of the injector center was set to $100M$ in order to have a developed turbulence during the injection. This distance is largely higher than the recommended distance $20M$ in [7].

Jet-interaction part

This part corresponds to the zone where the interaction between the jet, the cross flow and the wall takes place. It is a rectangular shape volume. The injector is situated at the center on the top of this part at 100 mm of the grid. This is considered to be a reasonable distance to have a fully developed turbulence

under the injector. The dimensions in the spanwise direction is set to 400 mm (200 mm from the jet center to the edges in each direction). This correspond to 20 D and should allow to avoid any lateral wall effects on the expansion of the vortices after the impingement.

Gas supply part

The Jet supplier part is equipped with a seeding system and the nitrogen source. There is also a heating system to obtain a hot jet. In order to have regular injections of gas during the experiments, a buffer volume (Tank) was mounted between the nitrogen source and the injector. The volume of the tank ($20L$) is sufficiently large compared to a single injection to prevent any impact of the injection on pressure variations from the source of nitrogen and vice versa. Fig. 2.5 shows the different components of the gas supply part.

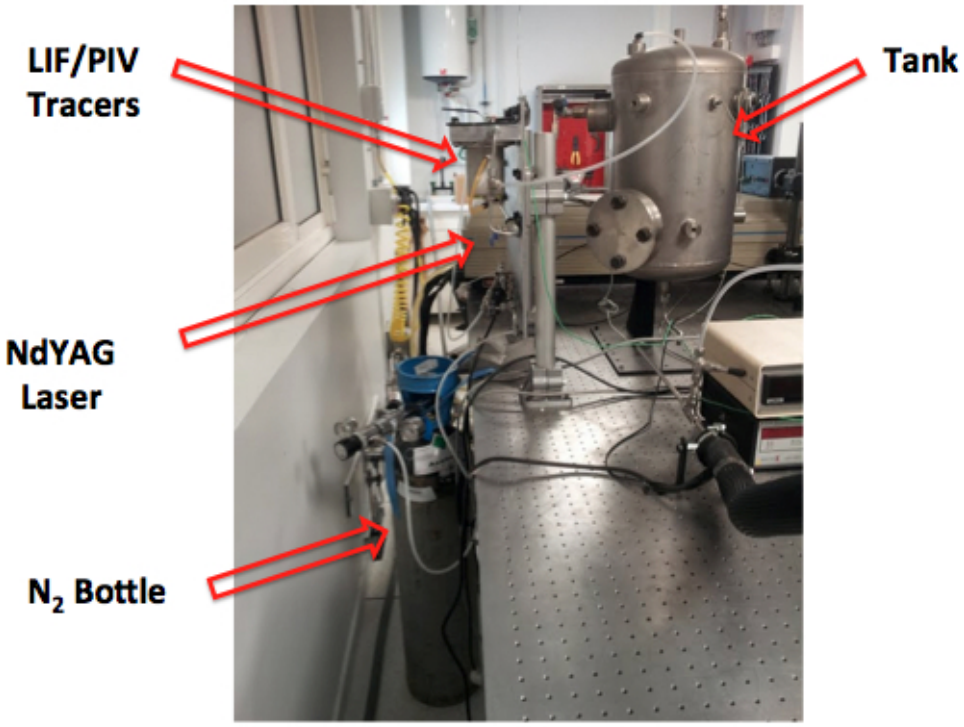

Figure 2.5: Some components of the jet supplier part.

Extraction part

The extraction part is equipped with a fan for generating the cross flow. The intensity of the cross flow can be changed and is measured with a hot wire. The hot-wire gives of course only a local information of the velocity but it allows to make sure that the experiments are performed under the same conditions.

The final experiment set-up is shown in Fig. 2.6.

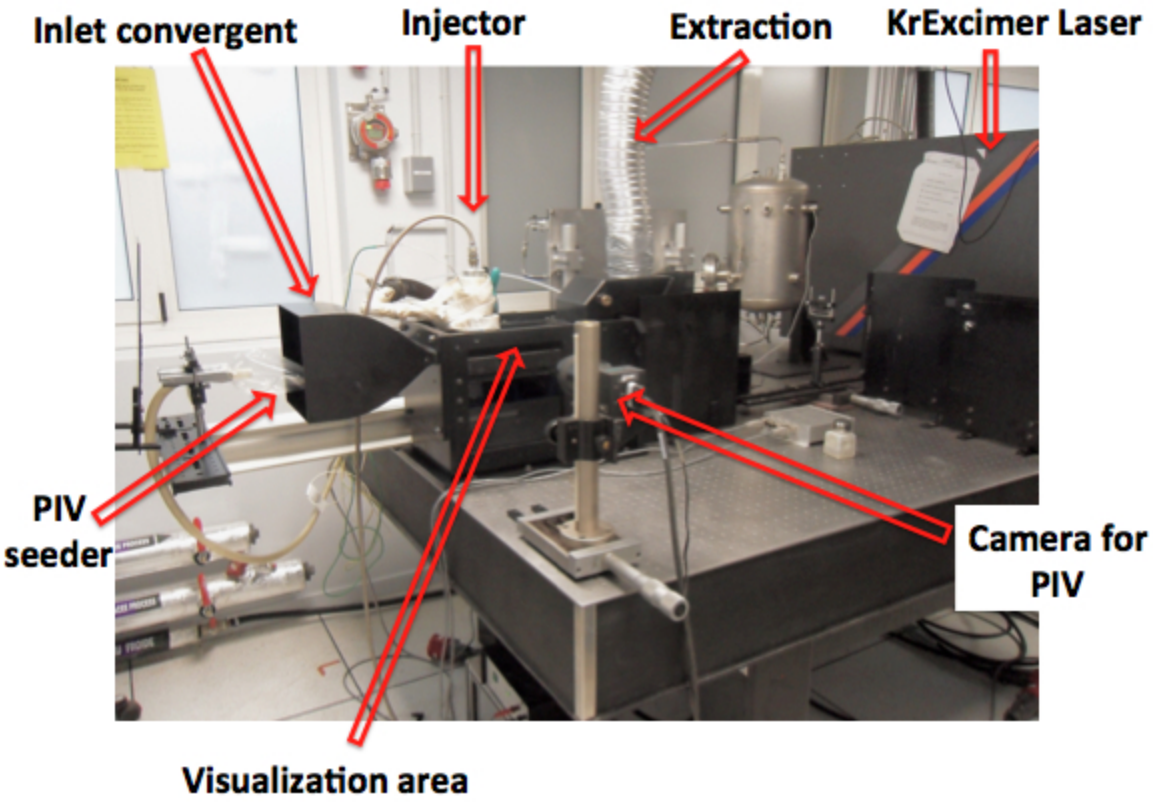

Figure 2.6: Experimental set-up

2.2 Velocity measurements: Particle Image Velocimetry

Along with LDV (Laser Doppler Velocimetry) and PDV (Planar Doppler Velocimetry), PIV is one the most popular non intrusive and particle based technique for velocity measurements. It is widely used in the automotive industry for geometry design or understanding the aerodynamics (swirl/tumble) effects taking place in IC engines for instance.
The PIV was used for two purposes with two different seeding set up. When the seeding was performed in the injected gas it was used for the following objectives:

- To understand the dynamic of the injector and to characterize the flow rate of the injector. The latter will be an important inlet condition for the numerical simulation of the set-up.
- The second objective was to set the pressure in the tank in order to limit the Mach number below 0.2 (which corresponds to $V \approx 80 - 90\ m/s$). The injector was supplied by a pressurized tank (full of nitrogen) whose pressure determines the amplitude velocity of the jet. As emphasized in the literature review, the extension of the SGS models is mostly developed in an incompressible framework, and its extension to compressible flows is possible under the assumption of low Mach number.

Finally, when the seeding was performed upstream of the cross flow (before the convergent) PIV was used to measure the velocity field during jet injection and interaction with the wall. The obtained data will be used in chapter 4 to evaluate the different SGS models.

2.2.1 Principle of PIV:

The PIV principle can be found in several books [4, 119] and it is based on the measurement of the displacements of the tracer particles seeded in a flow in a fixed time interval. It is performed by creating two successive narrow light sheets in the region of interest. Two successive Mie scattering images of particles are recorded. The instantaneous velocity of a fluid is determined by the displacements of particles in the images by a specific processing based on cross correlation estimation knowing the delay between the two images.

2.2.2 Experimental set-up:

The experimental set-up for the PIV measurements is represented in Fig. 2.7

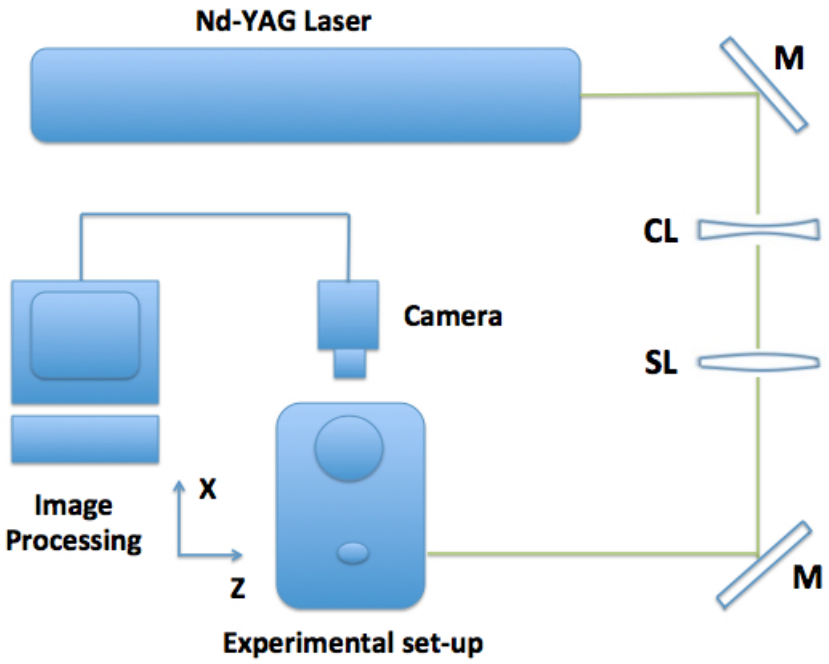

Figure 2.7: Schematic description of the PIV set-up for a plane in the X direction: M stands for mirror, SL the spherical lens and CL the cylindrical lens.

Laser sheet: The laser sheet is generated by a Nd:YAG-laser (Spectra Physics reference: PIV400) working at its second harmonic 532 nm. The time duration between two consecutive pulses is 2 μs. The frequency of the laser is 10 Hz but an external synchronizer was used in order to set the recording frequency to 1 Hz that corresponds to the frequency of the injector. The laser sheet was generated by a combination of a divergent cylindrical lens of 40 mm focal length and a convergent spherical lens of 1000 mm focal length. Different mirrors reflecting at 532 nm were used to orientate the laser depending of the position of the plane. The width of the laser sheet was about 1.5 mm and the height 40 mm.

Seeding system: The flow was seeded with liquid particles of Sebacat oil of size less than 5 μm. For the jet characterization the flow going to the injector was seeded and for the interaction between the jet and the cross-flow study only the cross flow was seeded. Preliminaries analysis confirmed the low value of the Stokes[1] number of the particle insuring that they are controlled only by the aerodynamics effects.

Signal collection and post-processing: The Mie scattering signal originating from the particles was collected with a CCD camera of 2048x2048 pixels^2 resolution equipped with a lens with the following characteristics: $f = 105$ mm and $f_\sharp = 2.8$. The processing of the data was performed with Insight 3G software. Each pair of images was processed using cross correlation based on Fast Fourier Transformation FFT. The size of the interrogation windows varied from 16x16 pixels^2 to 64x64 pixels^2 depending on the velocity of the flow. A local post-processing procedure based on the comparison of the velocity magnitude of the pixel of interest and the median value of the surrounding pixels was used to remove the non physical too high local velocity. No replacements of the removed velocity was applied. More details about the processing techniques can be found in [119].

[1] $S_t = \frac{\rho_p d^2}{18 \mu_g \tau}$
where ρ_p is the particle density of the particles, d the diameter of the particle, μ_g the dynamic viscosity of the ambient gas and τ the characteristic time.

2.2.3 Results and analysis:

Pressure operation point and Flow rate of the injector

After several tests, it was found that in order to limit the mach number below 0.2, the tank pressure had to be set at $P = 200\ mbar$. This is showed by the maximum velocity in Fig. 2.8 to 2.9 which is around 90 m/s. This pressure was kept constant during all the measurement campaign.

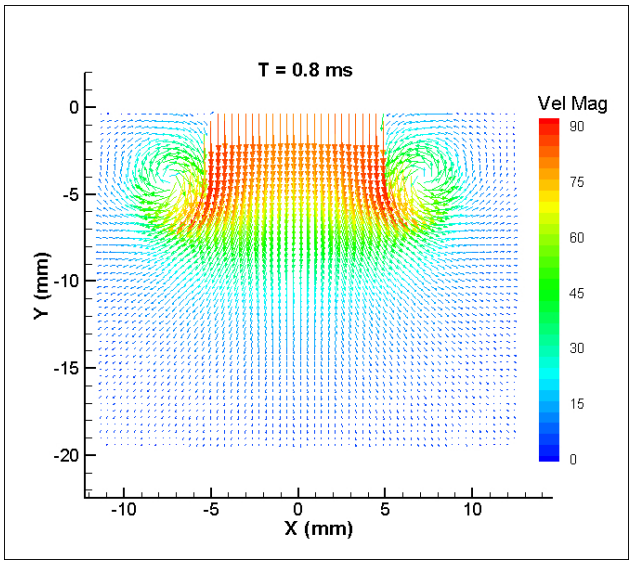

Figure 2.8: Velocity vector field of the jet without impinging surface at time $t = 0.8$ms

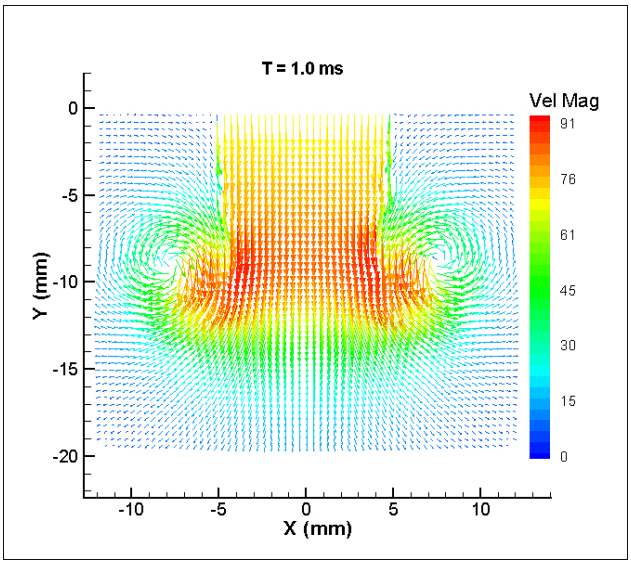

Figure 2.9: Velocity vector field of the jet without impinging surface at time $t = 1.0$ms

PIV results without the impingement surface show that the behavior of the injector can be separated in two distinct phases :

1. **Unsteady phase:** which corresponds to the early injection times from $T = 0.0\ ms$ to $T = 2.8\ ms$ (see Fig. 2.8 to 2.14). This phase is characterized by a strong variation of the velocity and the formation of a ring vortex.
2. **Steady phase:** which corresponds to the times from $T = 3.0\ ms$ to $T = 10\ ms$. During this phase the velocity varies slightly around 20 m/s and 25 m/s. One can also observe the formation of vortices but of small intensities compared with that of the unsteady phase.

This results also indicate that the unsteady phase with the biggest vortex will be very important for the heat transfer during the impingement. We can also forecast that the steady phase will be more easily influenced by the cross flow than the unsteady phase since the velocity in the second phase is not very high.

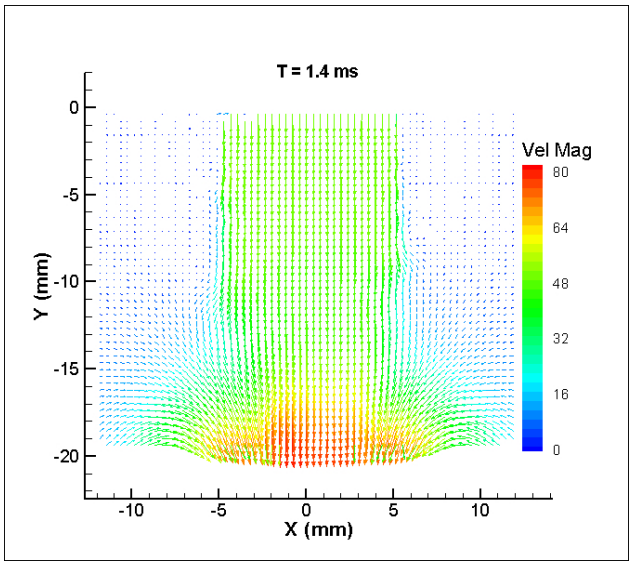

Figure 2.10: Velocity vector field of the jet without impinging surface at time $t = 1.4$ms

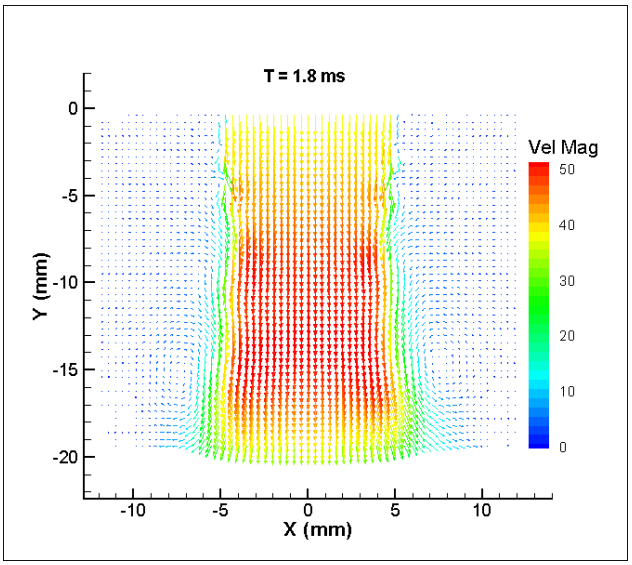

Figure 2.11: Velocity vector field of the jet without impinging surface at time $t = 1.8$ms

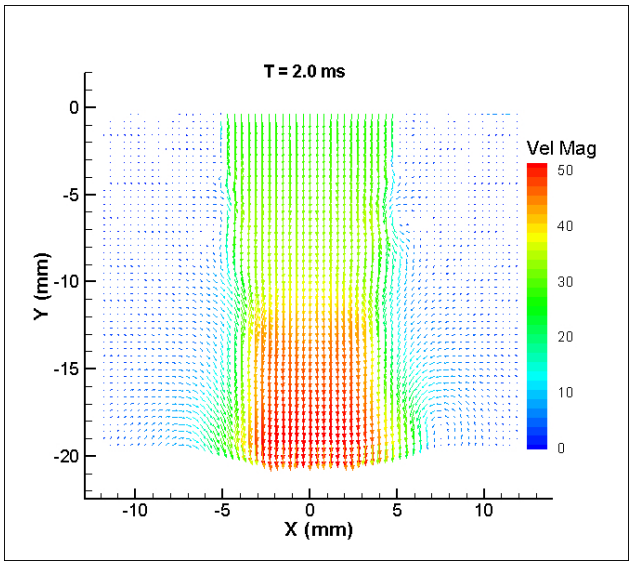

Figure 2.12: Velocity vector field of the jet without impinging surface at time $t = 2.0$ms

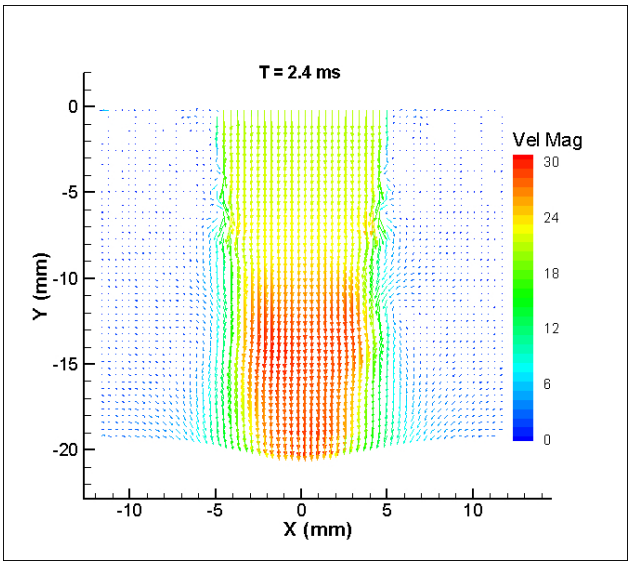

Figure 2.13: Velocity vector field of the jet without impinging surface at time $t = 2.4$ms

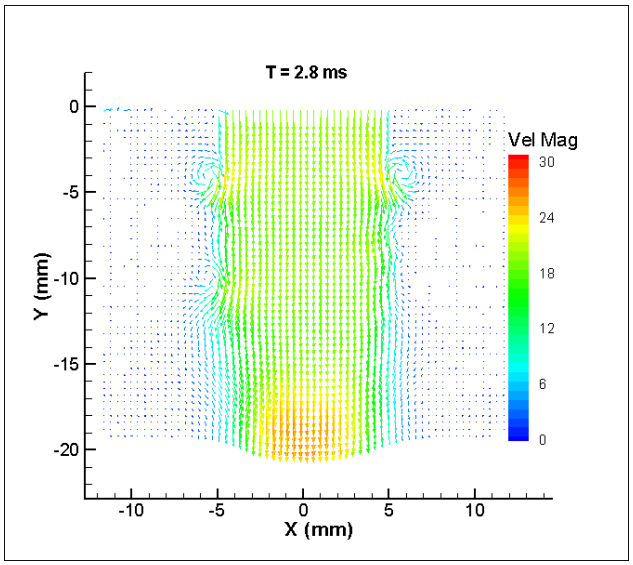

Figure 2.14: Velocity vector field of the jet without impinging surface at time $t = 2.8$ms

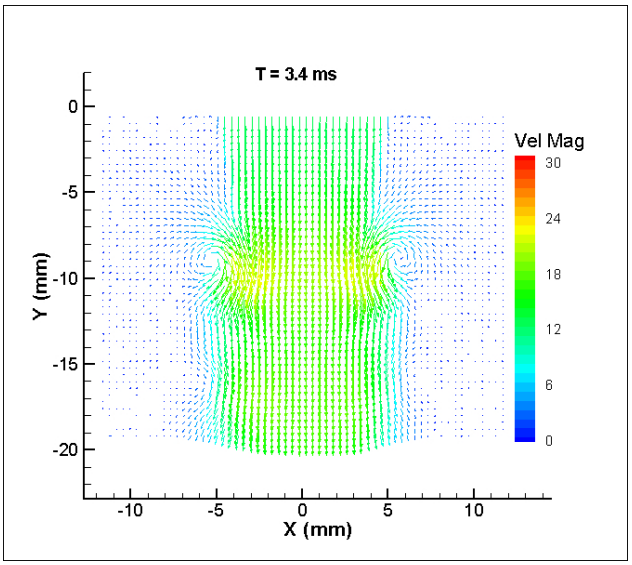

Figure 2.15: Velocity vector field of the jet without impinging surface at time $t = 3.4$ms

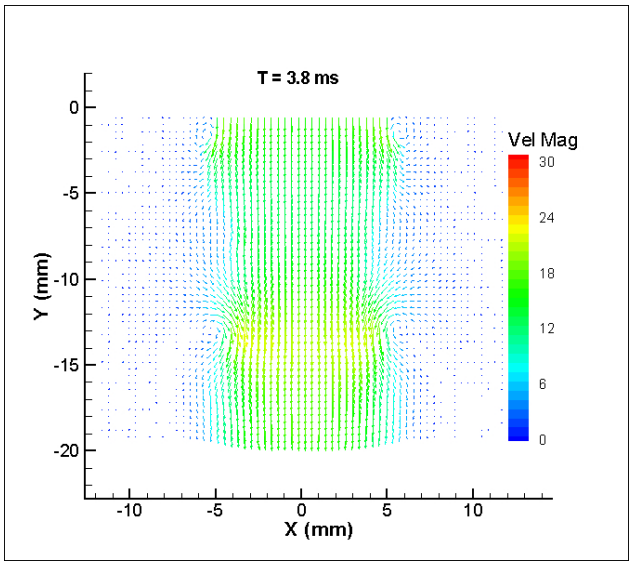

Figure 2.16: Velocity vector field of the jet without impinging surface at time $t = 3.8$ms

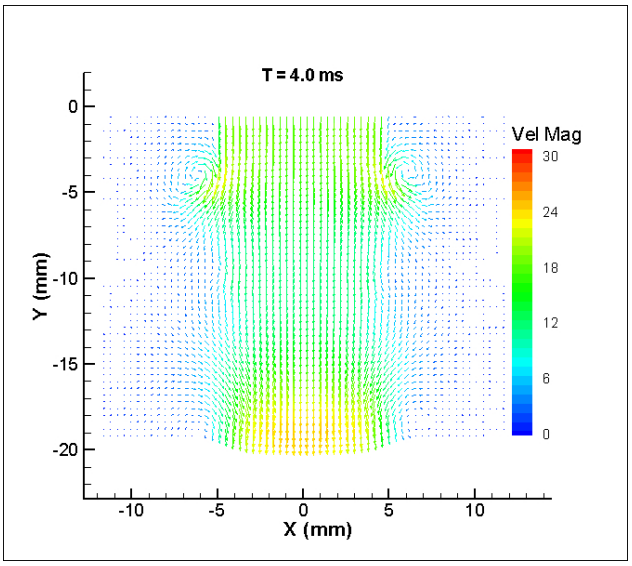

Figure 2.17: Velocity vector field of the jet without impinging surface at time $t = 4.0$ms

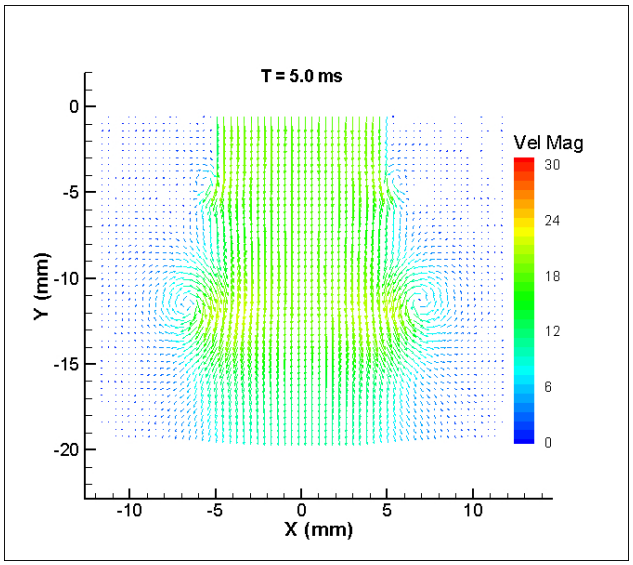

Figure 2.18: Velocity vector field of the jet without impinging surface at time $t = 5.0$ms

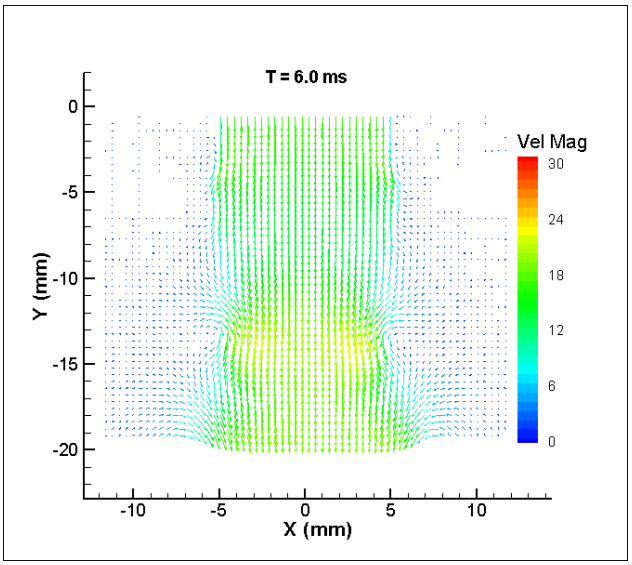

Figure 2.19: Velocity vector field of the jet without impinging surface at time $t = 6.0$ms

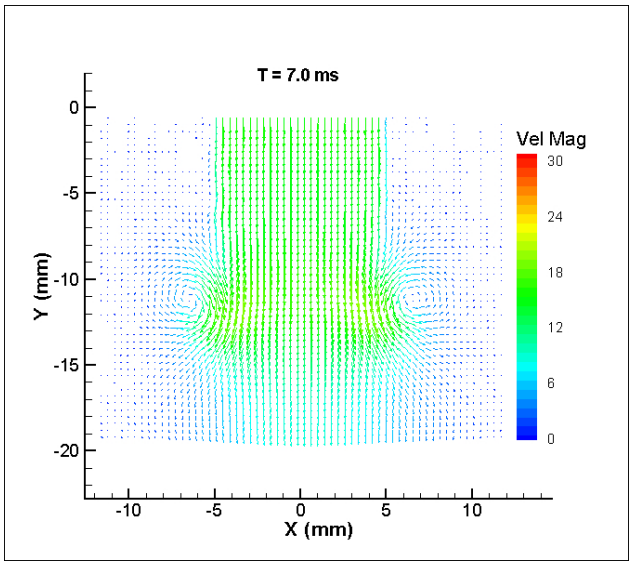

Figure 2.20: Calibration curves

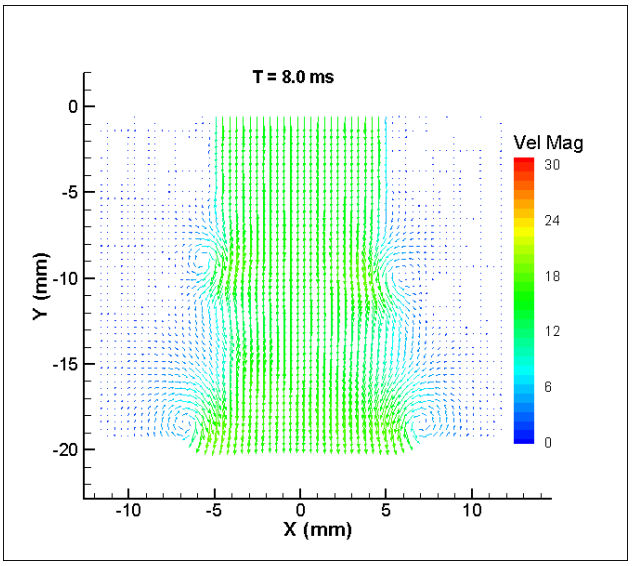

Figure 2.21: Normalized calibration curve

The flow rate was estimated from the PIV measurement assuming that the flow is axy-symetric and that the velocity profile is uniform (this was confirmed by the measurement). A constant value corresponding to the velocity measured along the injector axis at $1mm$ from the exit was multiplied by the exit section. Fig 2.22 shows the corresponding flow rate on which we can distinguish the two operating phases of the injector (unsteady and steady).

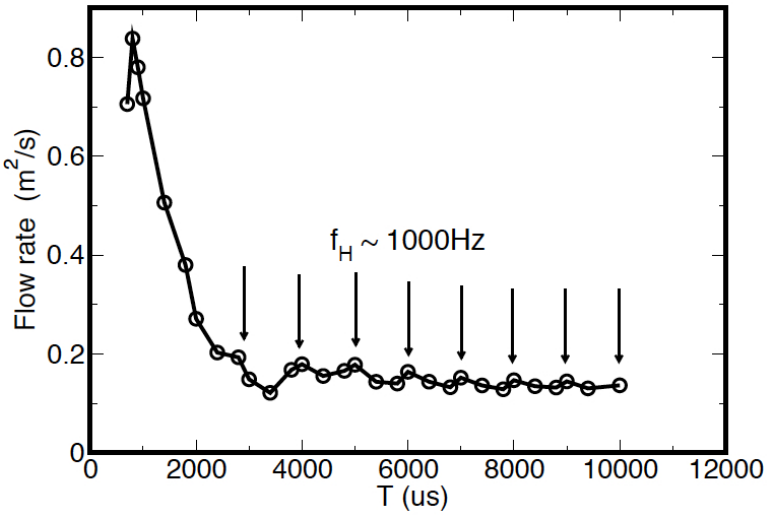

Figure 2.22: Flow rate of the injector

Helmholtz resonator

Fig. 2.22 shows that the steady phase of the injector is governed by oscillations at a specific frequency $f_H = 1000\ Hz$. This is actually due to the strong shape variation at the exit of the injector. As explained in the experimental set-up section, a convergent is fixed at the exit of the injector to reduce the injection diameter from 30 mm to 10 mm as shown in Fig. 2.24. As a consequence, the convergent acts like an Helmholtz resonator well described by Poinsot and Veynante [115].

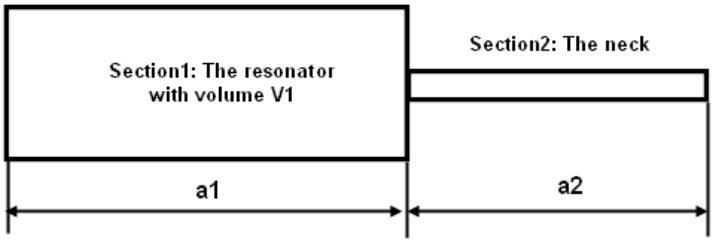

Figure 2.23: Schematic description of an Helmholtz resonator as described by Poinsot and Veynante [115]

The frequency induces by such variation of volume (see Fig. 2.23) can be expressed as follows:

$$f_H = \frac{c_o}{2\pi}\sqrt{\frac{S_2}{a_2 V_1}} \tag{2.7}$$

It is necessary to accurately characterize this frequency in order to provide a full description of the boundary condition for the computation. This requirement is important since the computational domain will not include the whole injection system. Indeed, it was decided for computation time issues to limit the computational domain to the top of the convergent. This decision was reinforced by the fact that the exact geometry of the injector was not known. It is therefore important to provide a good estimation of the height and thus the volume. Simulations will start from the top of the convergent and it will be important to determine accurately the height and thus the volume V_1 of the resonator in order to have the same frequency during the simulation. Indeed, the geometry of the injector is quite complex and the real size of the convergent will not necessarily leads to the expected frequency. Modifications will be made as follows:

$$\Delta V = \frac{S_2 c_o^2}{4\pi^2 a_2}\left(\frac{1}{f_H^2} - \frac{1}{f_{num}^2}\right) \tag{2.8}$$

where f_{num} is the frequency obtained in the simulation when the convergent has exactly the same size as in the experiment. ΔV corresponds to the increase or reduction of the volume of the convergent in order to reach the target observed frequency f_H.

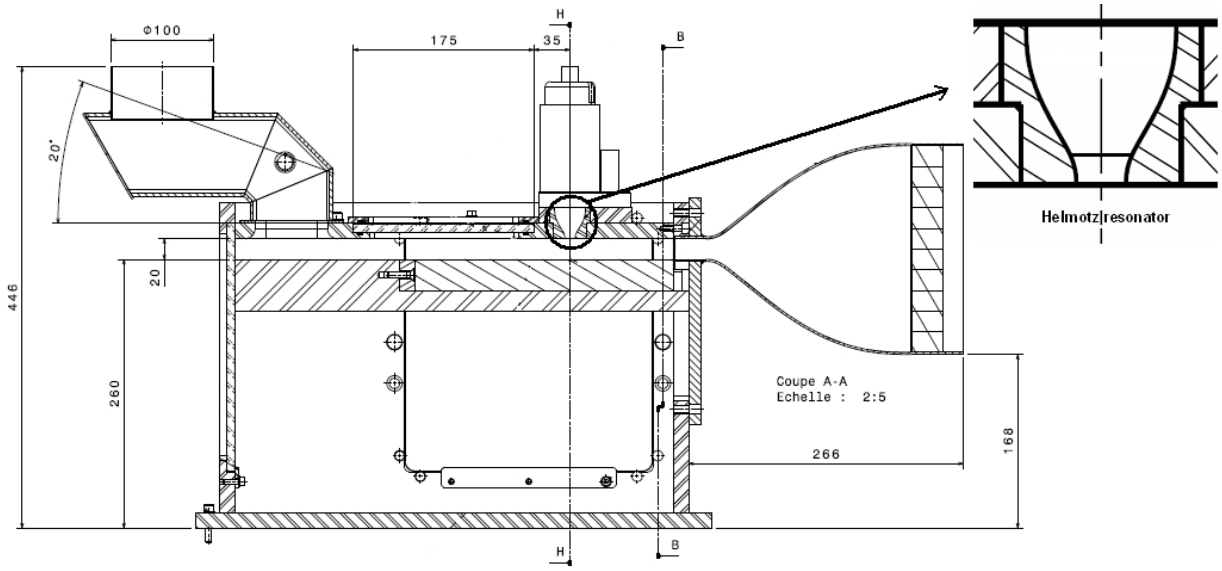

Figure 2.24: Experimental set-up with a zoom in on the convergent that acts as a Helmholtz resonator

2.3 Schlieren visualization for Cross flow rate estimation

The objective of the Schlieren technique was to tune the cross flow rate in order to provide a deviation of about one diameter ($1D$) at the impinging location. The $1D$ deviation was chosen as a reasonable distance for deviating the jet. Although numerous studies on deviation of jet in cross flow are available in the literature [28, 45, 64, 90, 110, 120], we have chosen to use the Schlieren visualization for two main reasons: first most of the studies are based on steady jet which is not the case in this work, second the implementation of the Schlieren technique is relatively fast and easy, so that decisive information can be obtained rapidly. Indeed, it is widely used in IC engines for densities variations observations and sprays investigations [102, 112].

2.3.1 Principle of the Schlieren visualization:

Schlieren visualization is based on the deviation of light by refractive index gradients. The index gradient can be due to temperature gradients, strong velocity gradients (in case of high Mach number flows for instance) or concentration gradients. The index gradients are directly related to flow density gradient. The deflected light is compared to undeflected light on a viewing screen. The undisturbed light is partially blocked by a filter as it will be seen on the experimental set-up. The light that is deflected away from the filter is a representation of the phenomena that leaded to the density gradients. In our case, this light represents the temperature gradients between the jet and the cross flow.

2.3.2 Experimental set-up:

The experimental set-up for the Schlieren visualization is represented in Fig. 2.25.

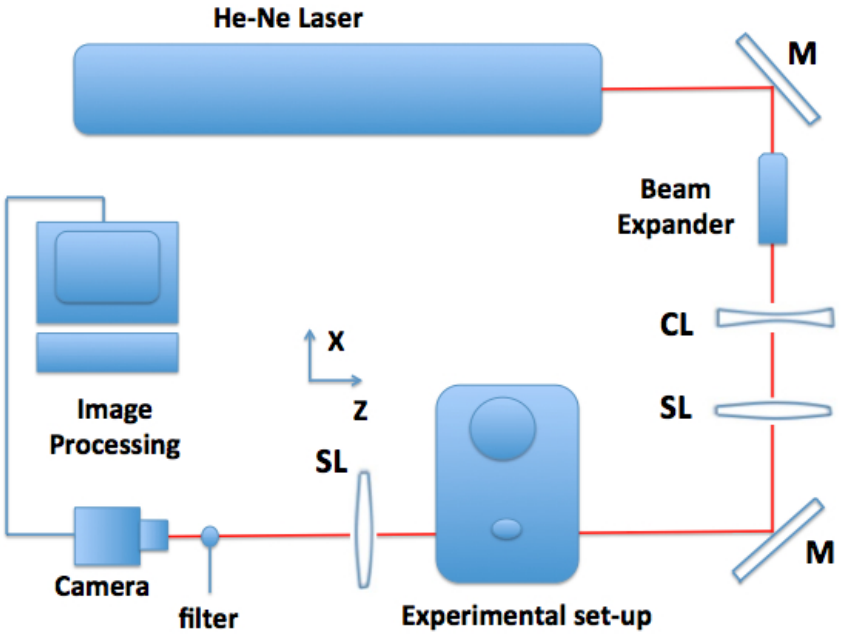

Figure 2.25: Schematic description of the Schlieren set-up: M stands for mirror, SL the spherical lens and CL the cylindrical lens.

Laser illuminator: The laser illumination is generated by a helium-neon laser (HeNe laser) with a red emission at 632 nm combined with a beam expander (to increase the size of the beam), one divergent cylindrical lens of focal length 50.8 mm, 2 convergent lenses of focal length 600 mm.

Signal collection: The non deflected light (where there is no temperature gradients) was filtered with a small spherical ball of tin and the deflected light was recorded with a high speed Photron camera (reference FASTCAM-SA1) equipped with a lens with the following characteristics: $f = 105$ mm and $f_\sharp = 2.8$.

2.3.3 Results: Tuning of the cross flow velocity

Four configurations corresponding to the flow rate given by the hot wire were investigated. For each flow rate, Schlieren visualization were performed in order to visualize the deviation of the jet. It is worth noting that the indicated flow rate does not correspond to the real flow rate in the measuring section part of the experimental set-up. Indeed, some differences may exist due to the pressure losses between the measurement point and the measuring section. Moreover the flow rate is deduced from a single point measurement of the velocity while the velocity profile in the pipe is not known and is probably not homogeneous. Only the PIV measurements without injection with the same cross flow intensity will give more quantitative information about the effective flow rate (velocity profile) inside the modeling part of the set-up. This is provided in the final chapter of this report in which comparisons between experimental data and simulations are performed. Although the hot wire is not used here to provide quantitative information on the effective flow rate, as shown in this section it provides a relative indication useful for the tuning of the experiment and also useful to make sure that the experimental conditions are the same throughout all the measurement campain.

Case A: Measured flow rate with the hot wire 31 m^3/h

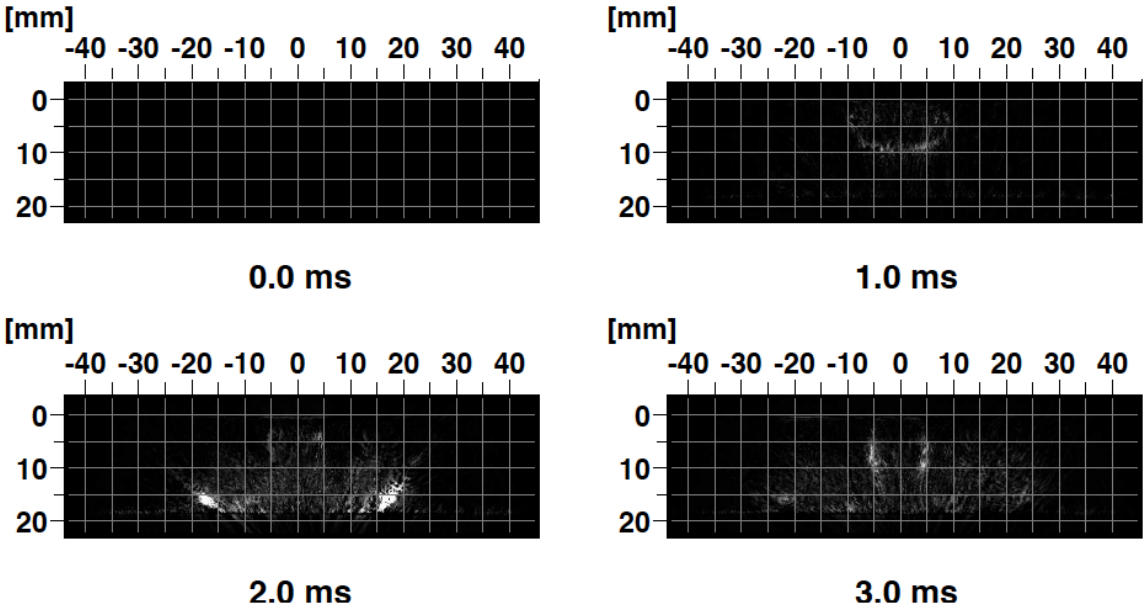

Figure 2.26: Case A: Jet in cross flow visualization from 0 to 3 ms.

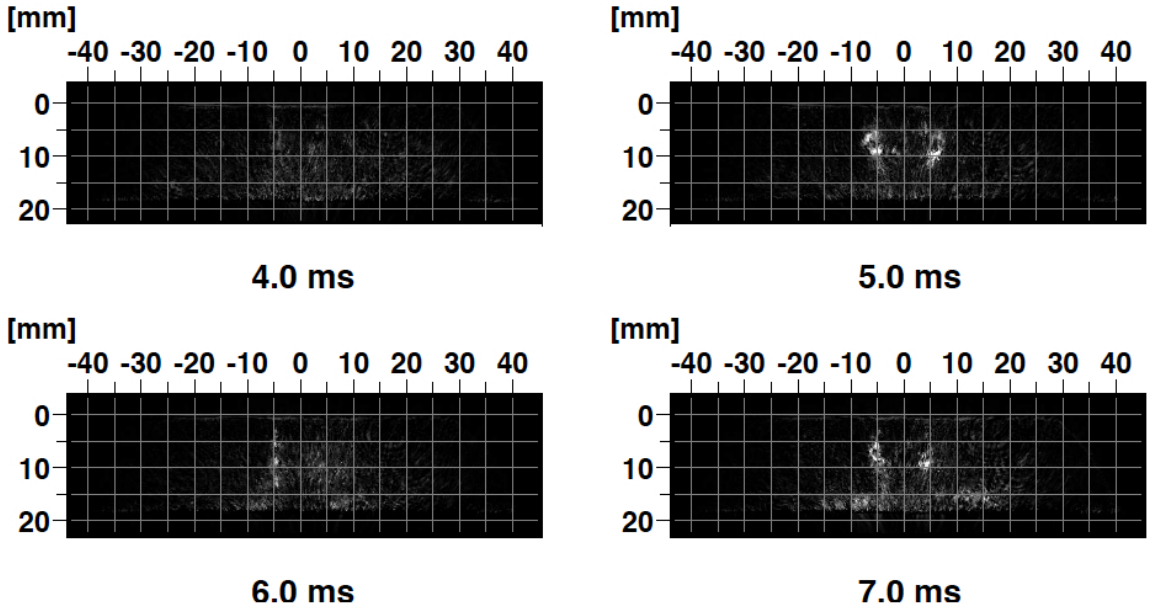

Figure 2.27: Case A: Jet in cross flow visualization from 4 to 7 ms.

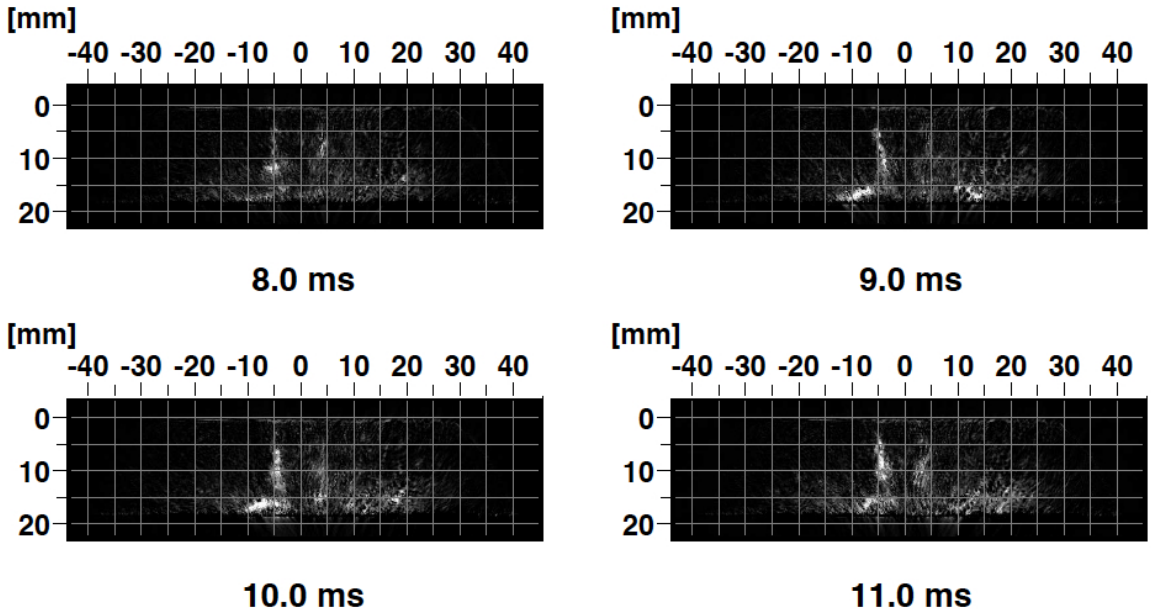

Figure 2.28: Case A: Jet in cross flow visualization from 8 to 11 ms.

Fig 2.26, 2.27, 2.28 show that the cross flow is very low and has almost no impact on the jet.

Case B: Measured flow rate with the hot wire 66 m^3/h

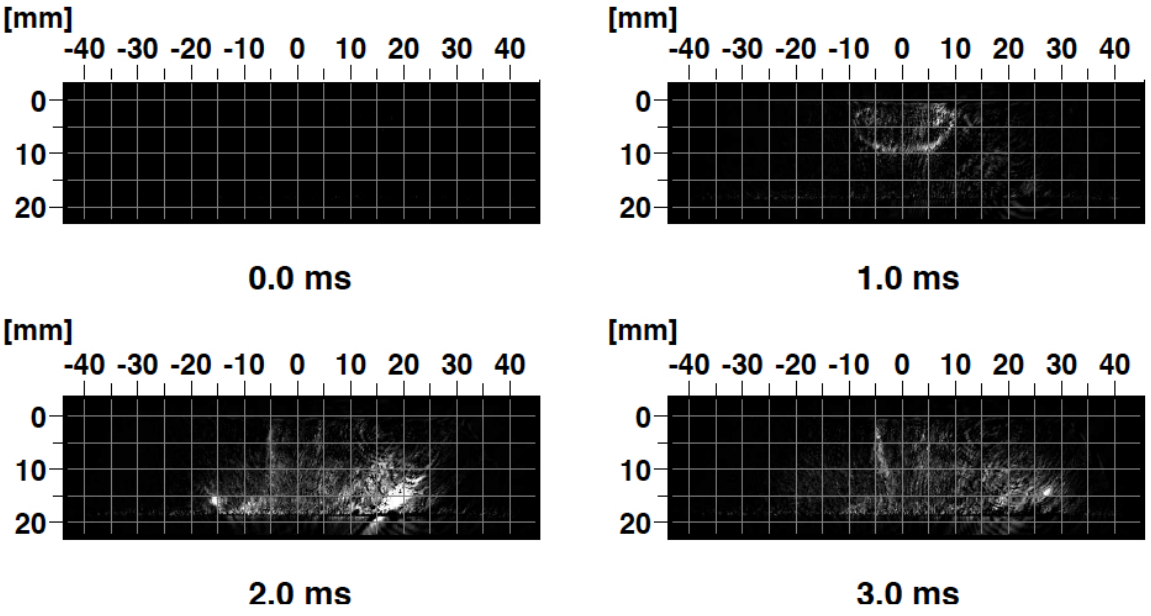

Figure 2.29: Case B: Jet in cross flow visualization from 0 to 3 ms.

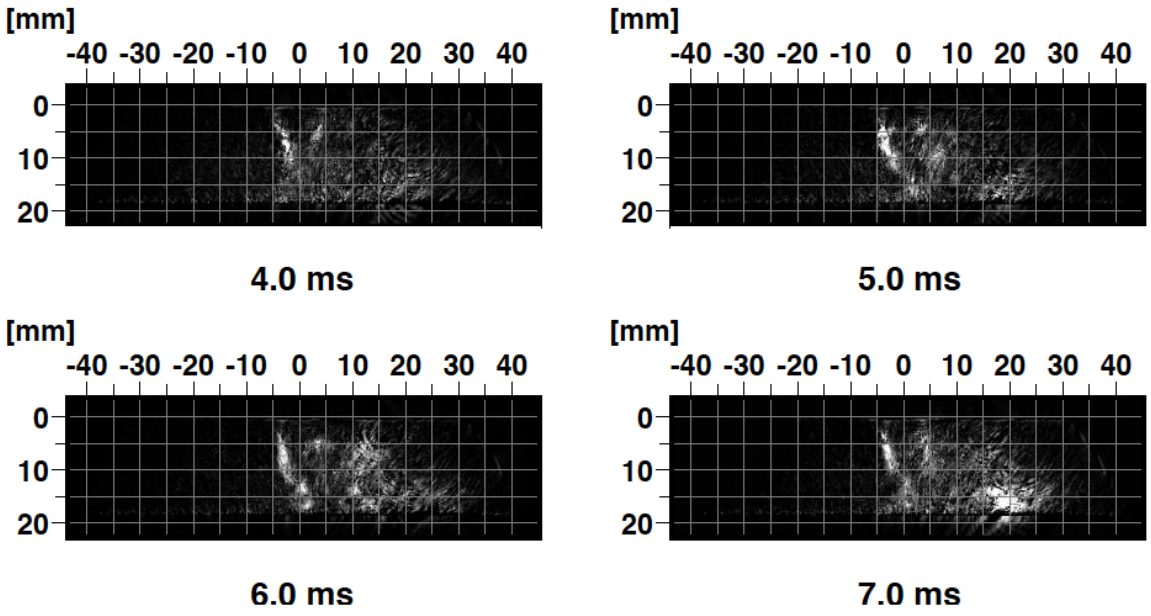

Figure 2.30: Case B: Jet in cross flow visualization from 4 to 7 ms.

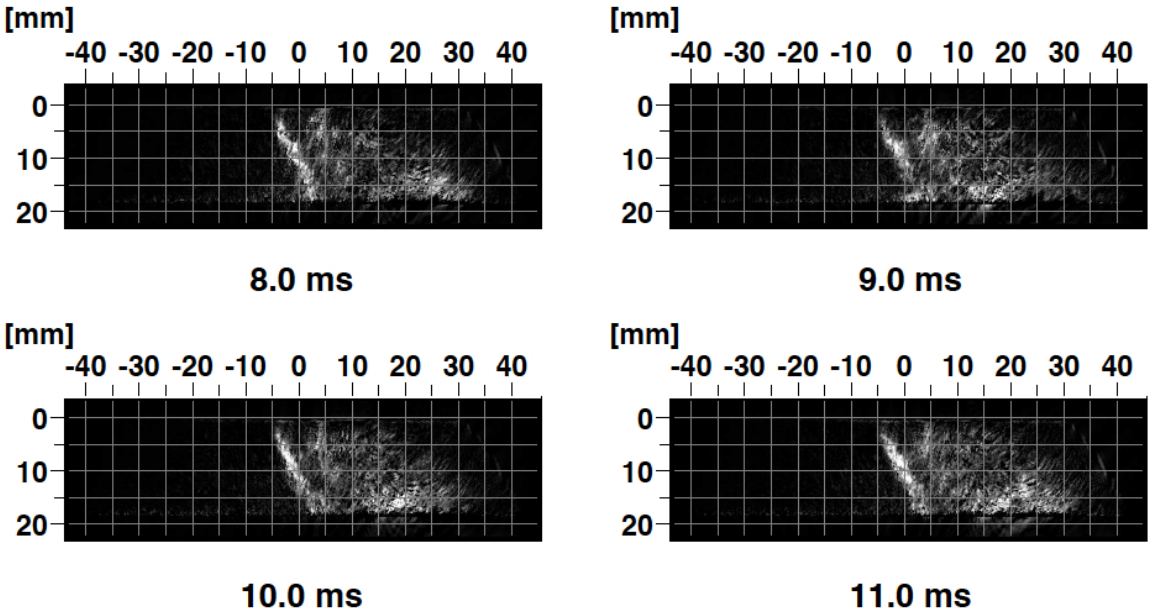

Figure 2.31: Case B: Jet in cross flow visualization from 8 to 11 ms.

Fig 2.29, 2.30, 2.31 show that a slight deviation of the jet can be observed after the impingement but still the deviation is around $0.5D$ which is still lower than the desired deviation of the jet.

Case C: Measured flow rate with the hot wire 96 m^3/h

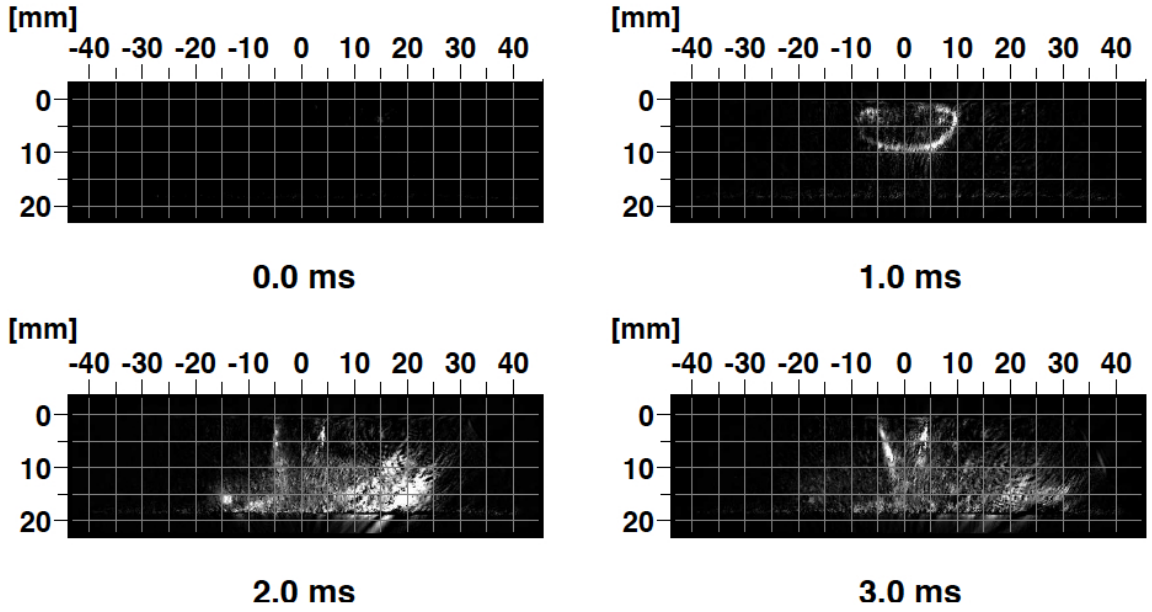

Figure 2.32: Case C: Jet in cross flow visualization from 0 to 3 ms.

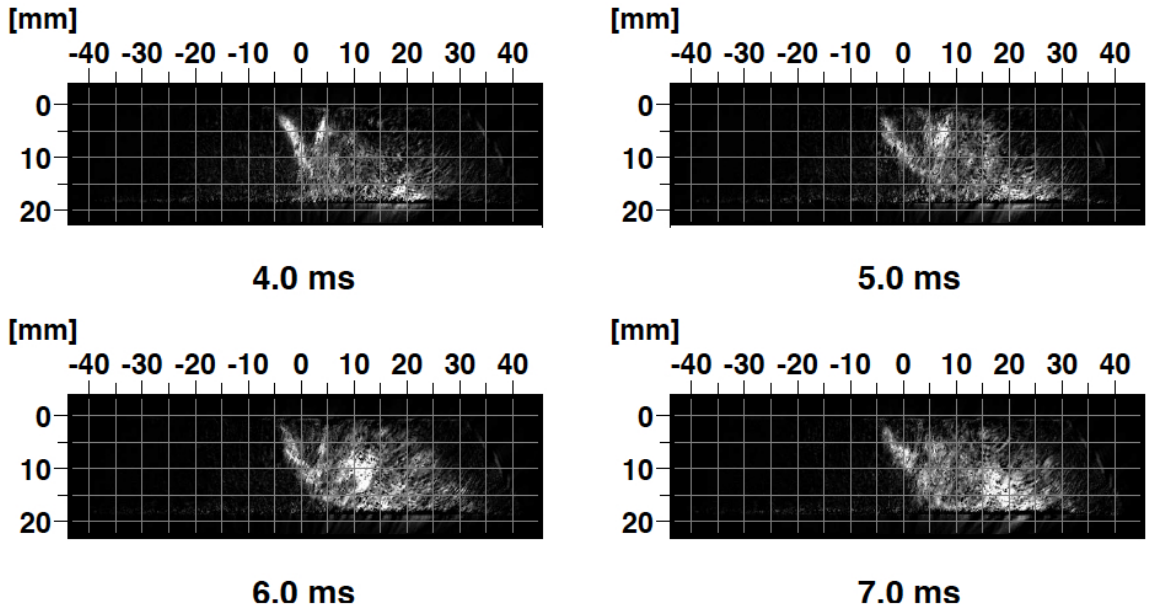

Figure 2.33: Case C: Jet in cross flow visualization from 4 to 7 ms.

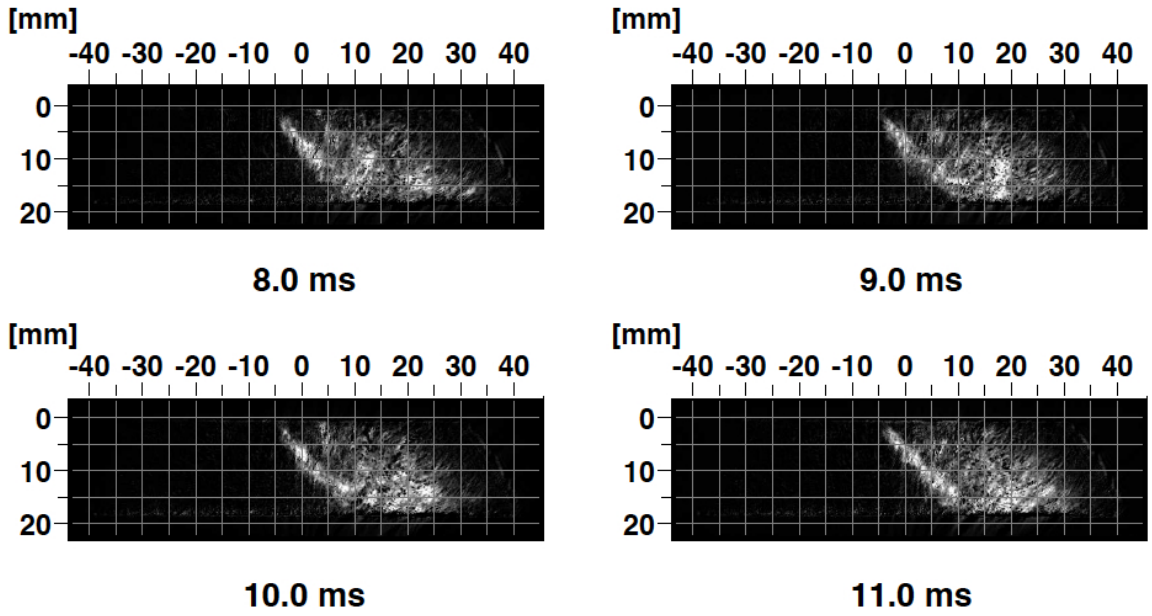

Figure 2.34: Case C: Jet in cross flow visualization from 8 to 11 ms.

For this cross flow intensity, Fig 2.32, 2.33, 2.34 show that the target deviation is achieved. Indeed, the stabilization of the jet correspond to a deviation of about 1D at the impingement surface.

Case D: Measured flow rate with the hot wire 122 m^3/h

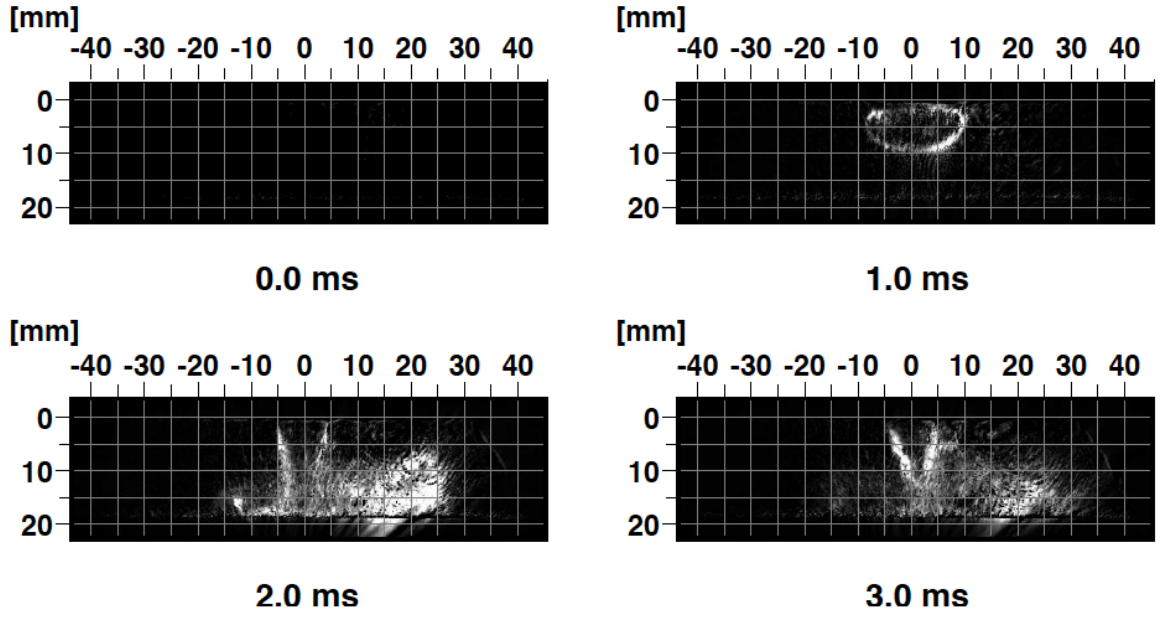

Figure 2.35: Case D: Jet in cross flow visualization from 0 to 3 ms.

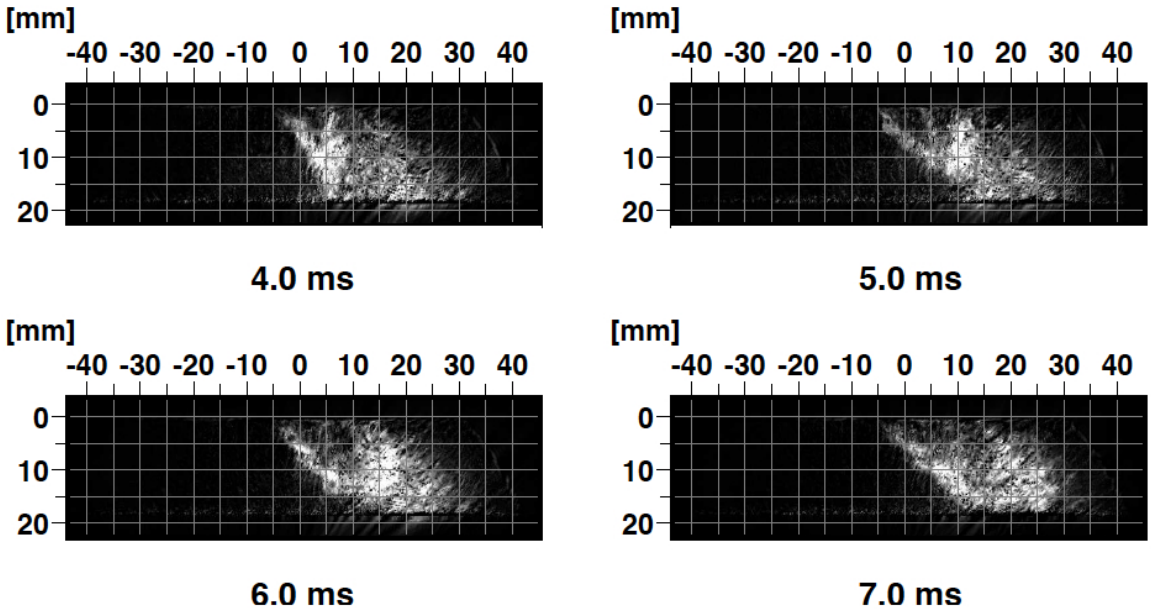

Figure 2.36: Case D: Jet in cross flow visualization from 4 to 7 ms.

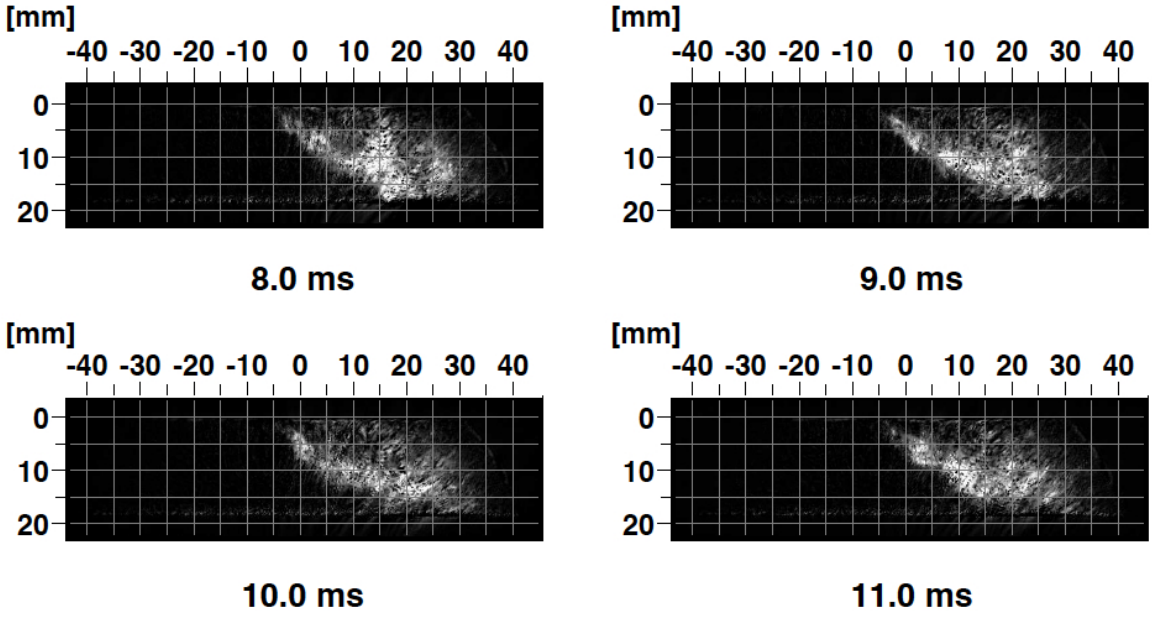

Figure 2.37: Case D: Jet in cross flow visualization from 8 to 11 ms.

Fig 2.32, 2.33, 2.34 show that the cross flow intensity is very high and the deviation is too large. For the late time observation, the jet does not seem to reach the solid surface.

Finally, the cross flow rate indicated by the hot wire which corresponds to one diameter deviation is roughly 96 m^3/s. As already, explained this does not correspond to the flow rate in the measuring section but allows to make sure that all the experiment are performed under the same conditions regarding the cross flow intensity.

2.4 Gas temperature measurement: Laser Induced Fluorescence and the adiabatic-mixing model

Laser Induced Fluorescence was chosen as the measurement technique for gas temperature and mixing. Laser induced fluorescence is mainly proportional to the fluorescent tracer concentration in the flow, but depending on the tracer characteristics it is also affected by temperature gradients, allowing for temperature measurements, as well as oxygen concentration gradients when the tracer is affected by oxygen quenching. More details about the photophysical processes and the characteristics of the commonly used fluorescent tracers can be found in [132]. Because nitrogen had to be used in the injector supply system for security reasons (mainly to avoid inflammable mixture when fluorescent tracer are added to the bath gas), heterogeneities in oxygen concentration were expected in the jet. As a result, fluorescence quenching was expected in the experiment depending on the fluorescent tracer properties. This feature had to be taken into account when selecting the fluorescent tracer, as well as sensitivity of the fluorescence tracer to temperature in the temperature range of the experiments. Considering these issues, the following tracers were selected:

- **Toluene**: It has the advantage to have a good sensitivity to temperature variations so that with an appropriate calibration of the ratio of the fluorescence intensity recorded simultaneously at two spectra bands the temperature can be deduced [74] with good accuracy. However, the fluorescence signal is strongly quenched in presence of oxygen thus limiting the two color LIF-toluene to the oxygen free portion of the jet (the portion close to the injector exit).
- **Diacetyl**: Unlike Toluene, the Diacetyl is only weakly affected by temperature variations (for the temperature range investigated in our study) nor by oxygen variations. It is an interesting tracer for mixing characterization and can directly give the mass fraction of the injected nitrogen. However, it can not be used for temperature measurement. More about diacetyl tracer can be found in [56]

The idea behind the choice of those two tracers is to take advantage of their complementary properties and the adiabatic-mixing model. The adiabatic-mixing model temperature estimation is a data post-processing technique based on the thermodynamical equilibrium between two or more fluids. In an adiabatic mixing process, knowing the mass fraction between two gases the equilibrium temperature depends only on the initial temperatures. In other terms, by measuring the inlet temperature of the jet at the convergent exit (where the flow is homogeneous and does not contain oxygen) using toluene and measuring the mass fraction of the nitrogen using diacetyl (where the flow is heterogeneous), the temperature of the whole domain can be deduced.

2.4.1 Principle of the adiabatic mixing model

This technique was already successfully used in IC engines for temperature measurements knowing the fuel air ratio [41, 43]. The model is actually based on the conservation of energy among the two gases. In [43] for example, the objective was to obtain the temperature after the injection of cold fuel in an hot in-cylinder air environment. The equilibrium temperature is derived from the following expression:

$$\int_{T_{mix}}^{T_{a,i}} c_{p,a} dT = \frac{F}{A} \left[\int_{T_{fl,i}}^{T_{int}} c_{p,fl} dT + h_{\nu,T_{int}} + \int_{T_{int}}^{T_{mix}} c_{p,fv} dT \right] \tag{2.9}$$

where $T_{a,i}$ is the air initial temperature, $T_{fl,i}$ is the initial fuel temperature, T_{mix} the final temperature of the mixing air-fuel, T_{int} the temperature at which the fuel vaporizes from the liquid to the gas state, F the fuel mass fraction, A the air mass fraction, $c_{p,a}$ the heat capacity of the air at constant pressure, $c_{p,fv}$ and $c_{p,fl}$ respectively the heat capacity at constant pressure of the fuel at the vapor and liquid state and $h_{\nu,T_{int}}$ the latent heat of vaporization of the fuel.
The term on the left expresses the decrease of the thermal energy of the air, the first term in the bracket

on the right expresses the increase of the energy of the fuel at the liquid state, the second term (also in the bracket on the right) the energy required to vaporize the fuel from liquid phase to gaseous phase and the last term (in the bracket on the right) the increase of energy of fuel once at the gaseous phase. $\frac{F}{A}$ is the mass fuel air ratio. Finally Eq. 2.9 clearly states the energy balance between the two fluids.
In the case of our experiment, the problem is simpler because the two fluids are in the gaseous phase. In fact, the energy provided by the hot injected nitrogen is decreased by the ambient air cross flow. The final temperature is then deduced from the following expression:

$$N \int_{T_{mix}}^{T_{n,i}} c_{p,n} dT = (1 - N) \int_{T_{a,i}}^{T_{mix}} c_{p,a} dT \tag{2.10}$$

All the terms of expression 2.10 are known except the nitrogen mass fraction N and the initial jet temperature $T_{n,i}$. The injector is heated at $120K$ (see Fig. 2.1) but we can not assume that the injected gas is also at that temperature because of the complex configuration of the injector and the convergent at the exit.

Shortcomings of the adiabatic-mixing model: It is worth noting that the adiabatic mixing model as it will be used here has some limitations. Specially near the impingement wall the system is no longer adiabatic. Moreover, we also assume that the diffusivity of the diacetyl in the air is identical to the diffusivitiy of nitrogen so that the mass fraction given by the LIF measurements corresponds to the mass fraction of the nitrogen.

2.4.2 Jet inlet temperature measurements: LIF Toluene

While single color toluene LIF can be used to measure temperature when the tracer concentration is homogeneous ([36, 140]), this technique can not be used in stratified flows. In such case, 2 line toluene LIF is recommended for determining the inlet jet temperature, since the local tracer concentration cancels out when performing the ratio of the two recorded signals. Moreover, the gas composition at the convergent exit can be considered oxygen-free (only nitrogen) so that the toluene signal will not suffer from oxygen quenching [74] as it would be the case in the remaining part of the jet.
Two-color LIF toluene was initially introduced by Luong *etal.* [88] and more recently studied by Tea *etal.* [144] for IC engines application. It relies on the temperature-dependence of the emission fluorescence spectrum which is red-shifted with increasing temperature as shown in Fig. 2.38.

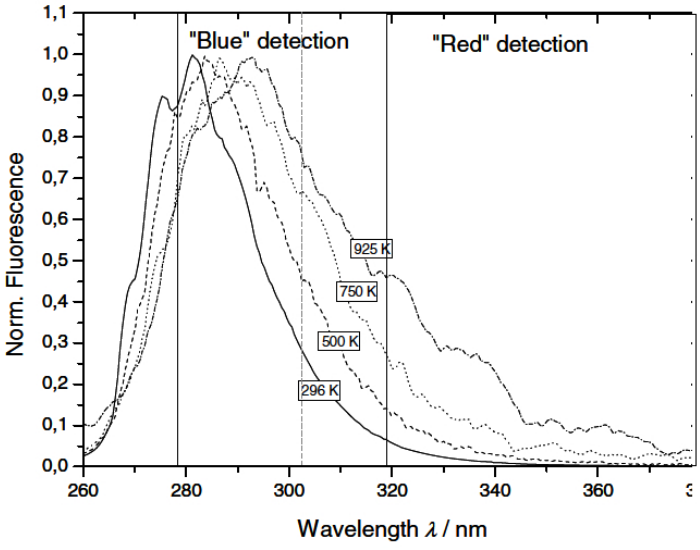

Figure 2.38: Red shift of the emissions spectrum with increasing temperature [88]

The technique consists in measuring the fluorescence signal in two distinct spectral bands. The ratio of the two signals is directly proportional to the temperature. Indeed the fluorescence signal S_{fl} is directly proportional to the toluene number density n_{tot}, the absorption cross section σ_{abs} and the fluorescence quantum yield Φ_{fl} :

$$S_{fl}(T,x,y) = n_{tot}(T,x,y)\sigma_{abs}(T)\Phi_{fl}(T) \tag{2.11}$$

where T is the local temperature and (x,y) the spatial coordinates. The ratio of the fluorescence signal detected in two different spectral bands is given by the following equation:

$$\frac{S_{fl}^{'blue'}}{S_{fl}^{'red'}} = \frac{\eta^{'blue'} E_{laser}(x,y) n_{tot}(x,y)\sigma_{abs}(T(x,y))\Phi_{fl}^{'blue'}(T(x,y))}{\eta^{'red'} E_{laser}(x,y) n_{tot}(x,y)\sigma_{abs}(T(x,y))\Phi_{fl}^{'red'}(T(x,y))} = f(T(x,y)) \tag{2.12}$$

Eq. 2.12 shows that with an appropriate calibration of the fluorescence characteristics for two spectral bands, the temperature can be afterward predicted. Two pass-band filters centered at 320 nm and 280 nm are used during our experiment. As reported in [88] and [144] the two-color LIF toluene has numerous advantages. Indeed, both spatial laser intensity and tracers density variations cancel out with this technique. Moreover the use of a single-wavelength excitation (248 nm for our experiment) also significantly reduce the experimental cost and complexity of the set-up and therefore enable to optimize the measurement accuracy.

Linearity check:

An important step in LIF measurement is to make sure that the fluorescence occurs in the linear regime. Indeed, the 2 line toluene LIF technique relies on photophysical processes occurring in that particular regime in which the fluorescence intensity is directly proportional to the laser intensity. In the saturated regime the photophysical processes are very different and the strategy used to measure temperature is no longer applicable. The linearity test consists in verifying that the fluorescence intensity is directly proportional to laser fluence. Since saturation occurs more rapidly at lower temperature the linearity test is realized at lowest temperature (ambient) of the experimental range. The corresponding set-up is shown in Fig. 2.56.

- **Set-up:**

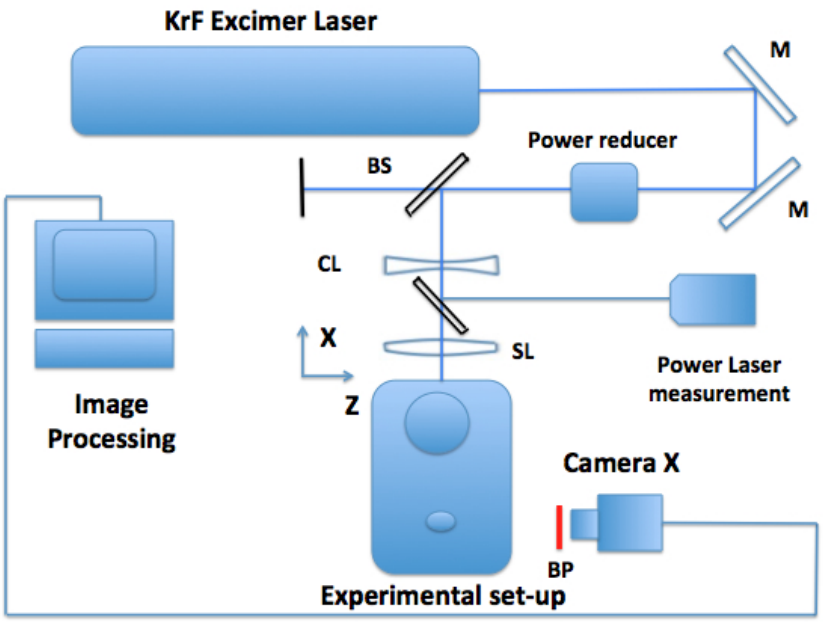

Figure 2.39: Schematic description of the 2 line toluene LIF set-up for the linearity study : M stands for mirror, SL the spherical lens, CL the cylindrical lens, BS the beam splitter and BP the band pass filter

Laser sheet: The laser sheet is generated by a KrF Excimer Laser (Coherent Physics) with a signal at 248 nm. The power intensity of the laser was controlled using a power reducer and measured with a powermeter. Additional beam splitters were used to reduce the intensity of the laser.
Seeding system and signal collection The flow was seeded with toluene by bubbling the toluene flow. The signal was recorded with an intensified CCD camera. A Band Pass filter centered at 280 *nm* was fixed on the camera. Images were post-processed with an In-House software developed at IFPEN (VIM and additional Matlab routines).

- **Results:**

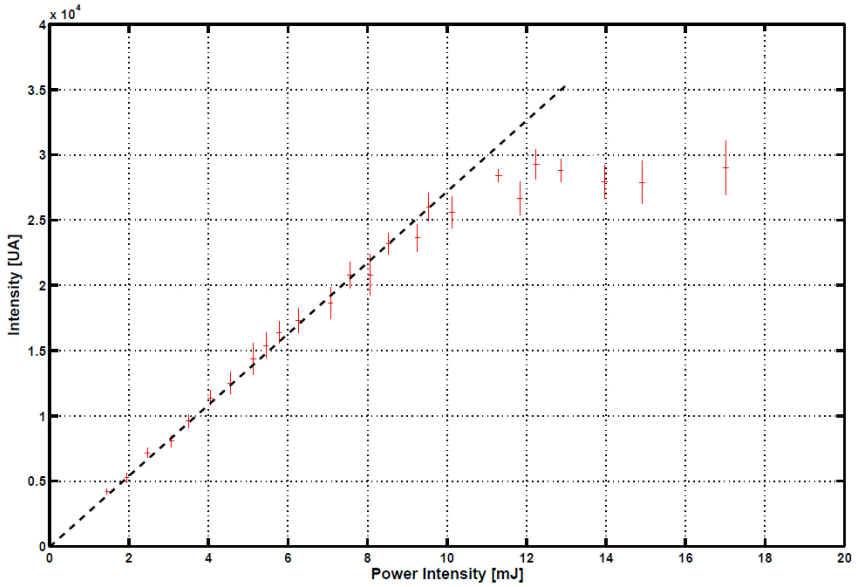

Figure 2.40: Linearity test curve.

The post-processing of images was performed just at the exit of the injector where the seeding is expected to be homogeneous. We can see in Fig. 2.40 that the linear regime is obtained for

power density below 11 mJ. Above that value there is a saturation phase where the LIF-Toluene measurement technique can not be applied. The vertical bars represent the standard deviation on the signal for the 50 recorded images. The horizontal bars correspond to the standard deviation on the measured laser intensity. Because the fluorescence signal is directly proportional to the laser intensity in the linear regime, we have decided to perform the rest of our measurements at the 8 mJ intensity. This ensure that the fluorescence is excited in the linear regime while optimizing signal to noise ratio.

Calibration phase:

As mentioned above the 2 line toluene LIF technique requires a calibration curve that corresponds to the ratio of the signal for two distinct filters band. The normalized calibration curve (see Fig. 2.71) used corresponds to the work of Tea *etal.*. It correspond to the ratio of the fluorescence signal obtained with the band pass filter centered at 280 *nm* (BP 280) and 320 *nm* (BP 320). Each point of the curve is obtained from a given spectrum of the toluene at the corresponding temperature. A complete description of the procedure of the calibration phase can be found in [144].

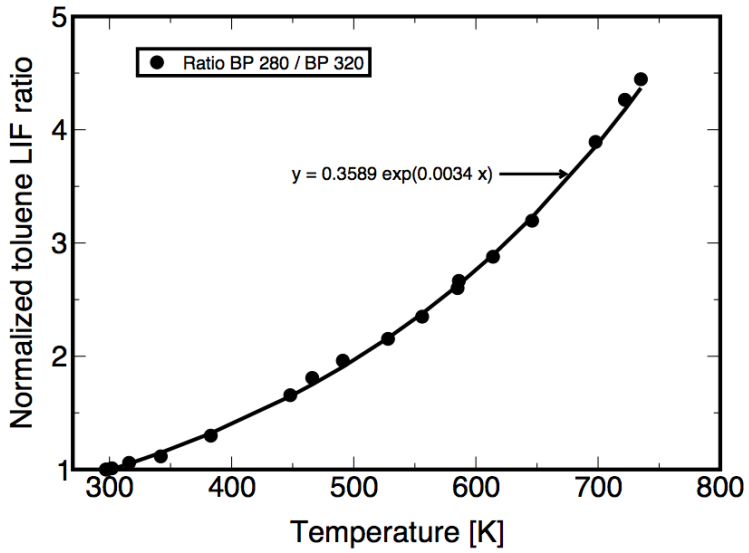

Figure 2.41: Normalized calibration curves of the Fluorescence signal ratio: BP 280 / BP 320

The corresponding calibration function is expressed as followed:

$$\left(\frac{S^{280}}{S^{320}}\right)_n = 0.359\ exp(0.0035\ T) \tag{2.13}$$

The equation was slightly modified in order to retrieve the ambient temperature of the experimental room which is approximately 293 K and not 300 K as it was the case during the calibration.

Temperature measurement procedure:

In order to obtain a reliable estimation of the temperature at the jet exit, we have decided to characterize the heating system of the experimental set-up. This can be simplified as shown in Fig. 2.42

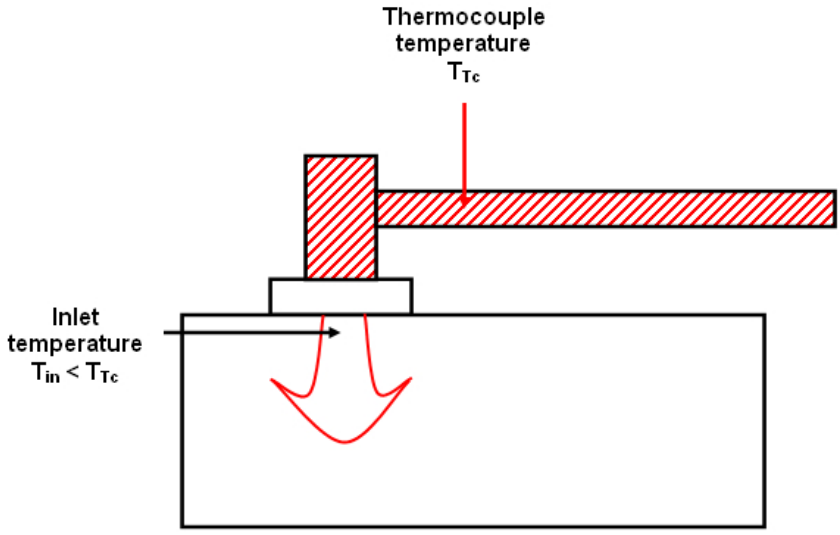

Figure 2.42: Simplified description of the heating system of the jet.

The objective is to characterize the correlation between the set temperature and the inlet temperature measured using the LIF-toluene technique. Four different temperatures measured with the thermocouple placed upstream of the injector were investigated. The corresponding fluorescence signal is always normalized by the fluorescence signal at ambient temperature T_a.

- Set-up: The experimental set-up is similar to the one used for the linearity study with an additional intensified CCD camera for performing the ratio of the fluorescence signals.

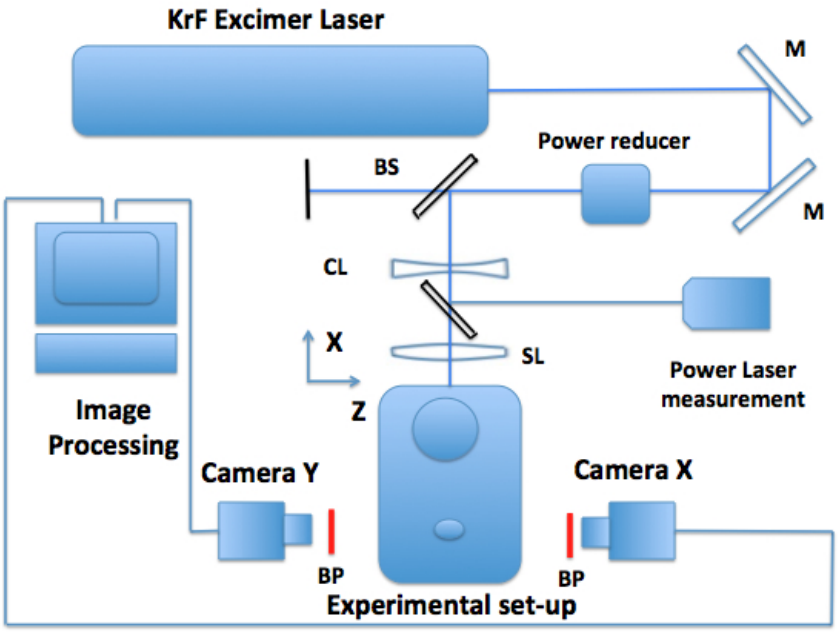

Figure 2.43: Schematic description of the LIF set-up for the inlet jet temperature measurement : M stands for mirror, SL the spherical lens, CL the cylindrical lens, BS the beam splitter and BP the band pass filter.

- Results:

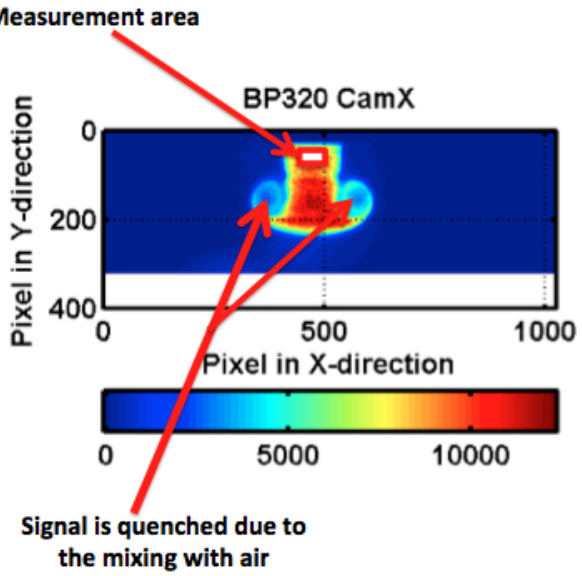

Figure 2.44: Single image of the jet showing the measurement area and the quenching effect on the fluorescent signal (strongly quenched in the vortices).

According to Eq. 2.13, the temperature is given by the following expression:

$$T = \frac{1}{0.0035} ln \left(\frac{1}{0.359} \left(\frac{S^{280}}{S^{320}} \right)_n \right) \tag{2.14}$$

Although Eq. 2.14 is quite simple, its application with the experimental data is complex and requires a well defined procedure. The ratio $\left(\frac{S^{280}}{S^{320}}\right)$ should be rewritten following:

$$\frac{S^{280}}{S^{320}} = \frac{S_X^{280}}{S_Y^{320}} \tag{2.15}$$

where X and Y stand respectively for camera X and Y. It means that a correction should be applied to account for the differences between the two cameras. Indeed, cameras are not perfectly identical and generally give different results with the same filters. A calibration is therefore required. It is then necessary to respect the following steps to take into account these requirements:

1. **Step 1**: Simultaneous acquisition: Camera X + PB 280 and Camera Y + PB 280

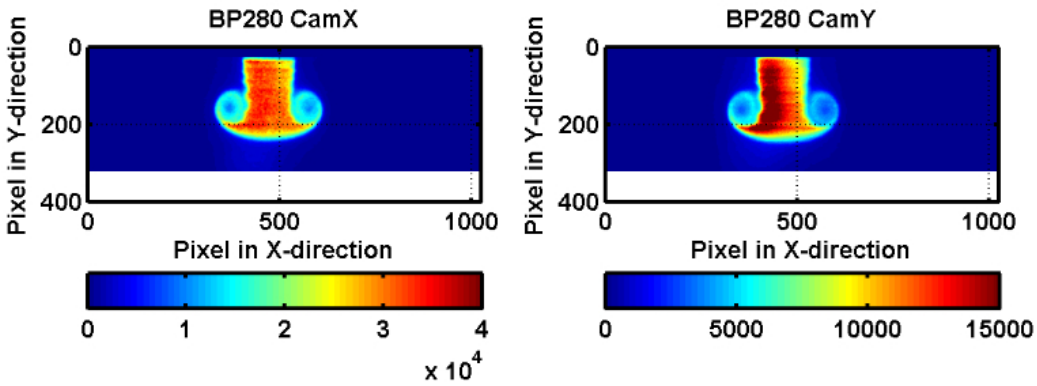

Figure 2.45: Comparison of the fluorescence signal obtained with camera X with the Band Pass filter 280 and camera Y with the Band Pass filter 280 at temperature 390 K.

This first step is important for quantifying the difference between the two cameras used. As it can be seen in Fig 2.45 the fluorescence signal obtained with the camera X is higher than the fluorescence signal obtained with camera Y although the same filters are used.

2. **Step 2**: Simultaneous acquisition: Camera X + PB 320 and Camera Y + PB 320

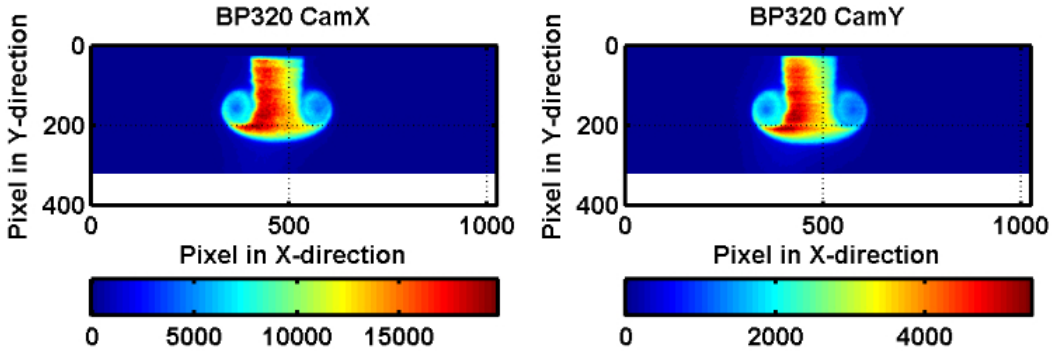

Figure 2.46: Comparison of the fluorescence signal obtained with camera X with an identical Band Pass filter 320 and camera Y with the Band Pass filter 320 at temperature 390 K.

The second step can be considered as a validation stage for the first step. Indeed, although the two cameras are not identical, one should make sure that this difference does not depend on the observation band (in a more rigorous analysis even the filter are not identical but the difference can be neglected). In other terms the ratio of the fluorescence signal of the two cameras obtained at the second step should be similar to the ratio obtained at the first step.

3. **Step 3**: Simultaneous acquisition: Camera X + PB 280 and Camera Y + PB 320

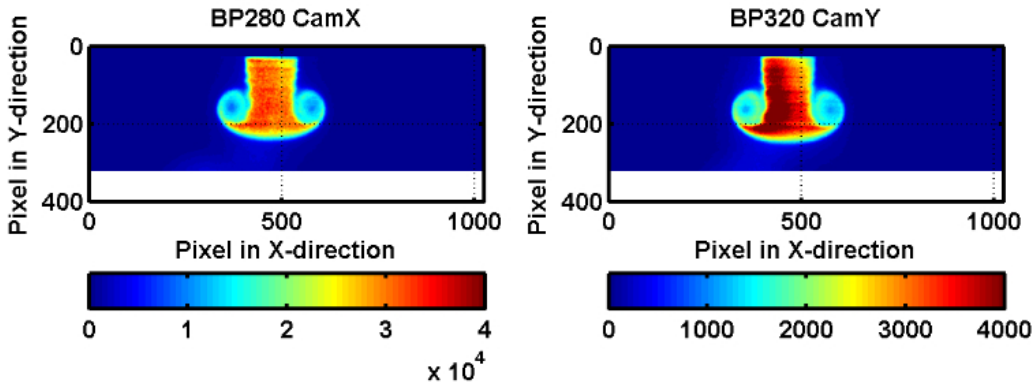

Figure 2.47: Comparison of the fluorescence signal obtained with camera X with the Band Pass filter 280 and camera Y with the Band Pass filter 320 at temperature 390 K.

If the two cameras were perfectly identical, it would have been possible to deduce at this single step the final temperature from the ratio of the two fluorescence signal. Obviously it is no the case and the ratio obtained here need to be corrected by the ratio obtained in the two previous steps.

4. **Step 4**: Simultaneous acquisition: Camera X + PB 320 and Camera Y + PB 280

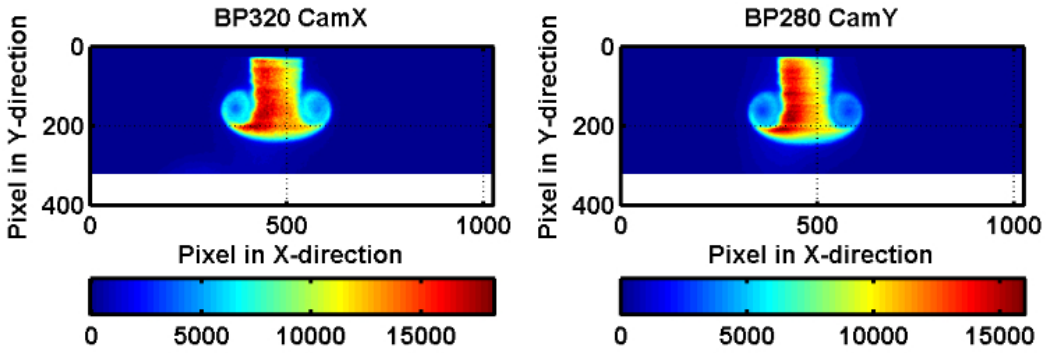

Figure 2.48: Comparison of the fluorescence signal obtained with camera X with the Band Pass filter 320 and camera Y with the Band Pass filter 280 at temperature 390 K.

Similarly to the second step, this stage helps to validate the corresponding temperature obtained at the third step. It will help to give a first estimation of the accuracy of the measurements.

Another important step during the post-processing, is the image registrations. It consists in making sure that the image recorded from one camera X corresponds spatially to the image of camera Y. It is based on error minimization. More details about the registration procedure can be found in [144]. We recall here that the LIF technique is applied only on a small surface close to the injector where quenching effects are avoided and not on the entire image (see Fig. 2.44).
Because of the heterogeneity of the fluorescence signal recorded from the two cameras as it can be seen in Fig. 2.45 to Fig. 2.48, one should wonder if the temperature is homogeneous at the jet exit. According to Eq. 2.11 the heterogeneity on a single image can be due to the tracer density heterogeneity. The advantage of using two cameras (and recording simultaneously two images) is that if the heterogeneity is due to tracer heterogeneity then this will be observed on the fluorescence profiles given by the two cameras identically (the density does not depends on the observed spectra bands). But if it is due to the temperature then the signal profile will be different from one camera to the other because it varies depending on the observation spectra bands.

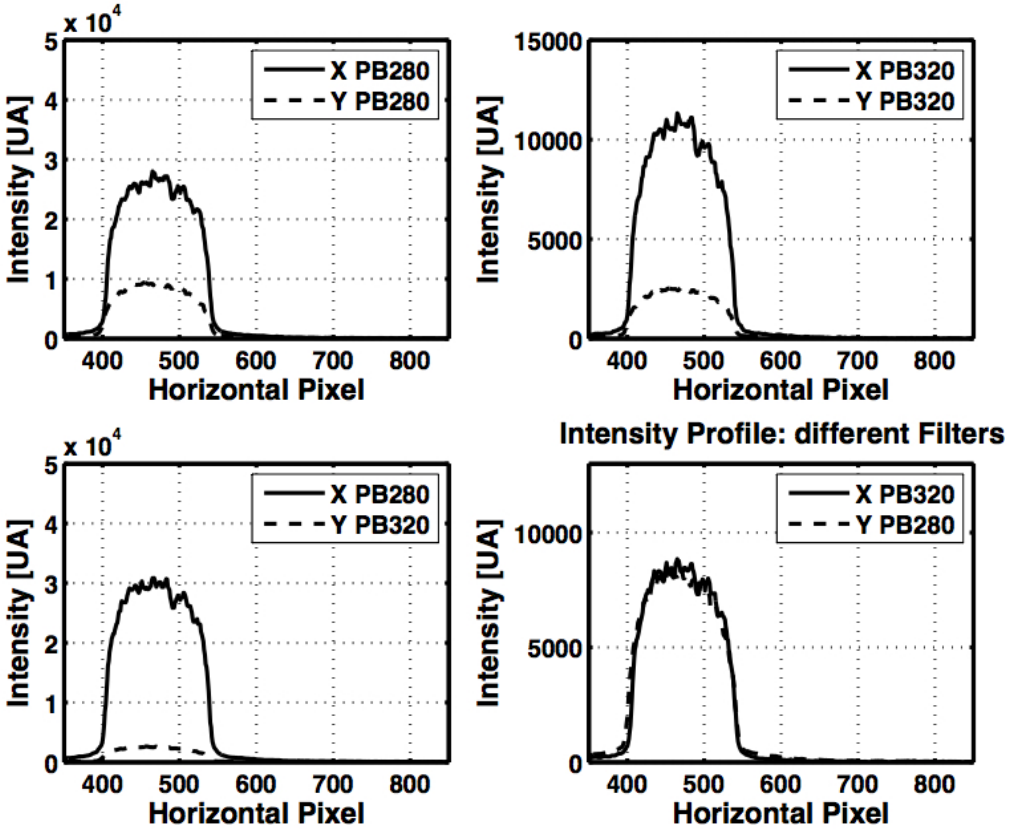

Figure 2.49: Fluorescence Profile recorded with the two cameras at Y= from the jet exit at the different steps (from step1 t o step 4) and at room temperature.

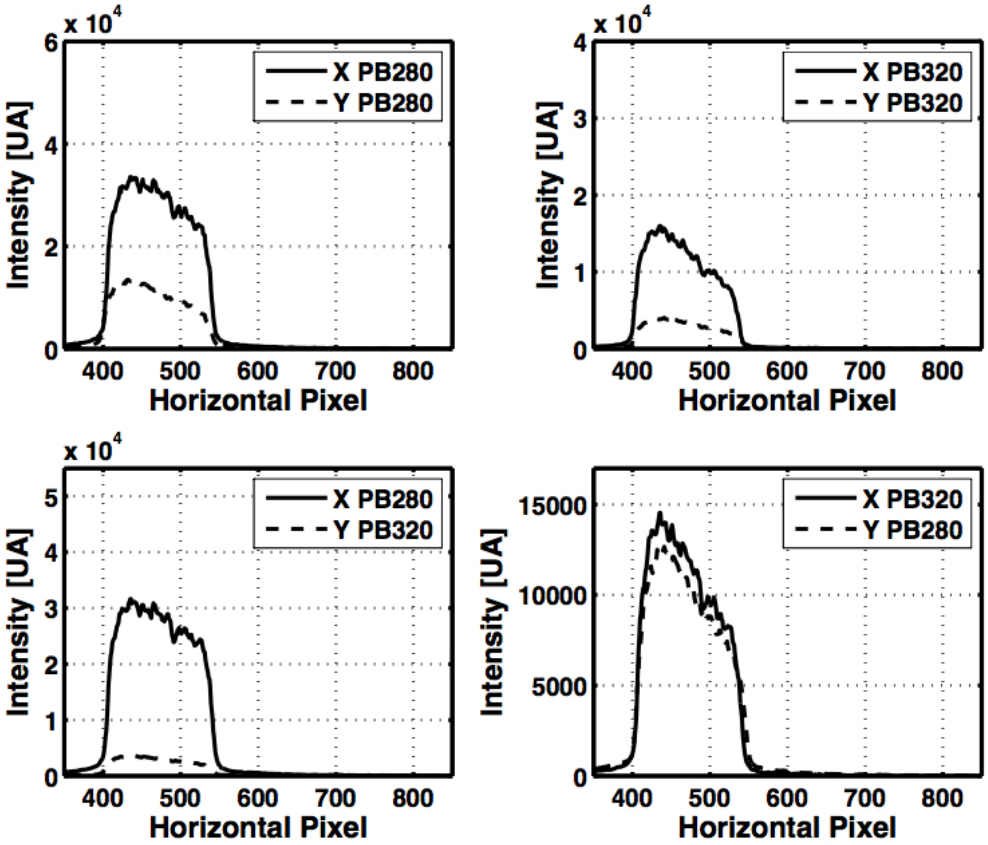

Figure 2.50: Fluorescence Profile recorded with the two cameras at Y= from the jet exit at the different steps (from step1 t o step 4) and at temperature $T = 390$ K.

We can see in Fig. 2.50 to 2.52 that the fluorescence profile follows exactly the same trends on the image recorded from the two cameras specially when different filters are used. This confirms the hypothesis that the temperature is homogeneous at the jet exit but the toluene seeding is not. The different figures also emphasized the intrinsic differences between the two camera and the necessity of step 1 and step 2.

Fig. confirms the homogeneity of the temperature on the surface considered. The ratio of the signals of the two camera on a profile inside the surface shows that the ratio is constant (constant for two similar band pass filter and also for two different band pass filter) on the jet exit. The corresponding temperature is $T = 445$ K.

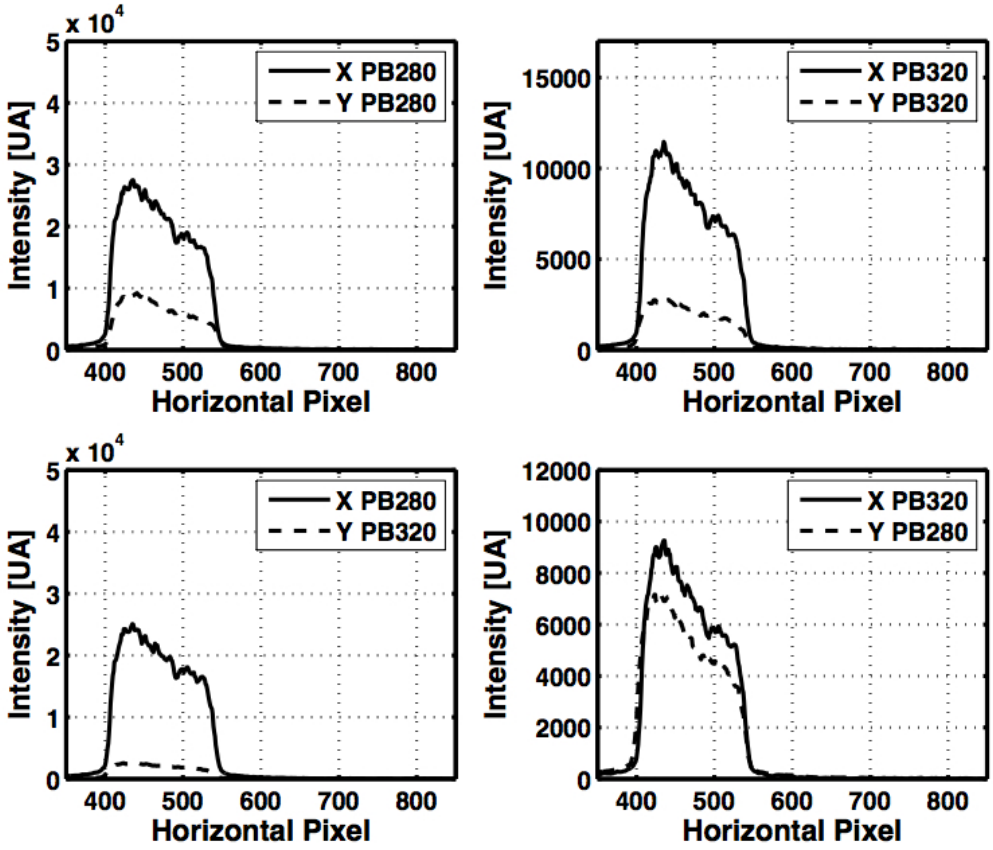

Figure 2.51: Fluorescence Profile recorded with the two cameras at Y= from the jet exit at the different steps (from step1 t o step 4) and at temperature $T = 445$ K.

The heterogeneity of the fluorescence signal in average (the profile presented are extracted from the average of 50 individuals snapshots) is less pronounced at ambient temperature as shown in Fig. 2.50. This result indicates that the density heterogeneity are very probably due to some condensation issue of the toluene inside the injector when the nitrogen is heated.

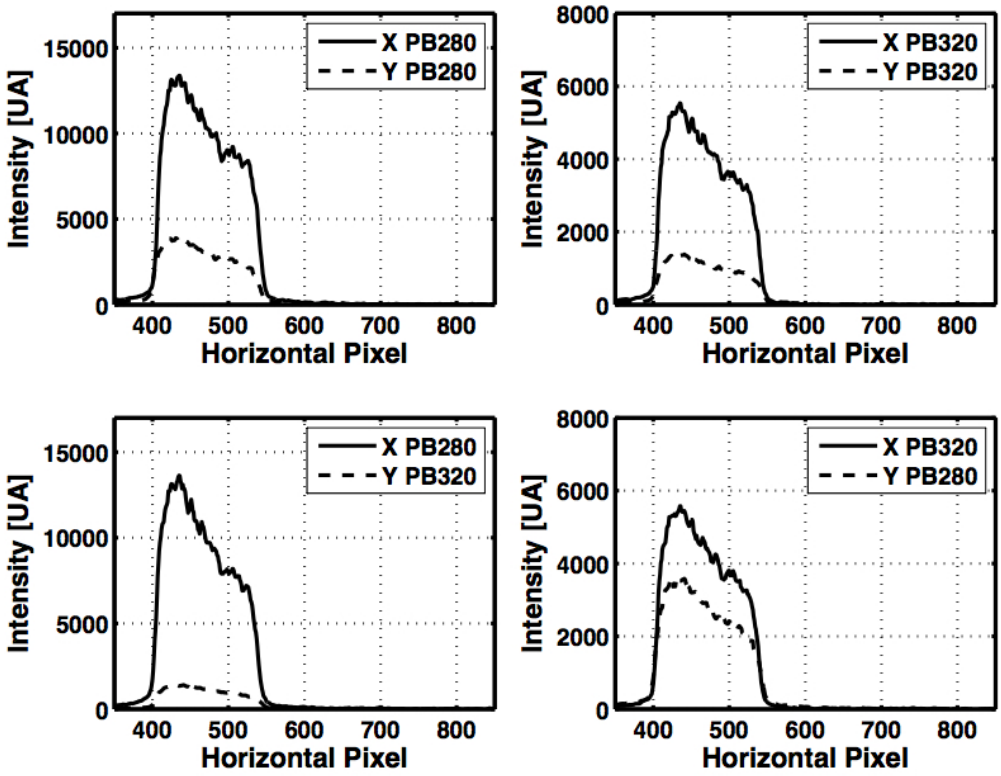

Figure 2.52: Fluorescence Profile recorded with the two cameras at Y= from the jet exit at the different steps (from step1 t o step 4) and at temperature $T = 585$ K.

Fig. 2.53 confirms the homogeneity of the temperature on the surface considered. The ratio of the signals of the two cameras on a profile inside the surface shows that the ratio is constant (constant for two similar band pass filters and also for two different band pass filters) on the jet exit from pixel position 425 to 525. The corresponding temperature is $T = 445$ K.

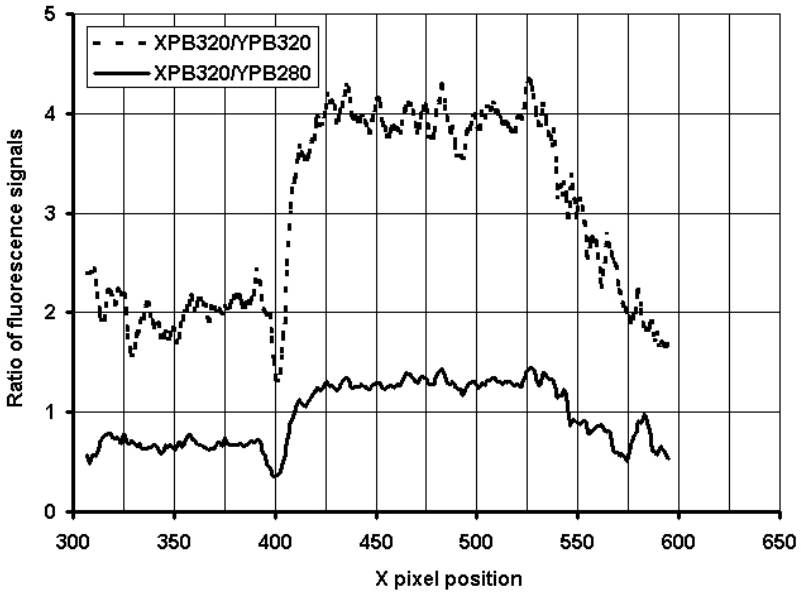

Figure 2.53: Ratio of the fluorescence signal on a profile inside the measurement surface for the step 2 and step 4 at temperature $T = 445$ K.

Finally two series (S1 and S2) of measurements were performed at four different temperatures 295 K, 390 K, 445 K and 585 K. For each measurement, the temperature was deduced using the two methods (M1 and M2) described above. As a result for each measurements, two ratios/temperatures S1M2 and S1M2 (or S2M1 and S2M2) are determined. Results of the ratios and the temperatures are respectively presented in Fig. 2.54 and Fig. 2.55.

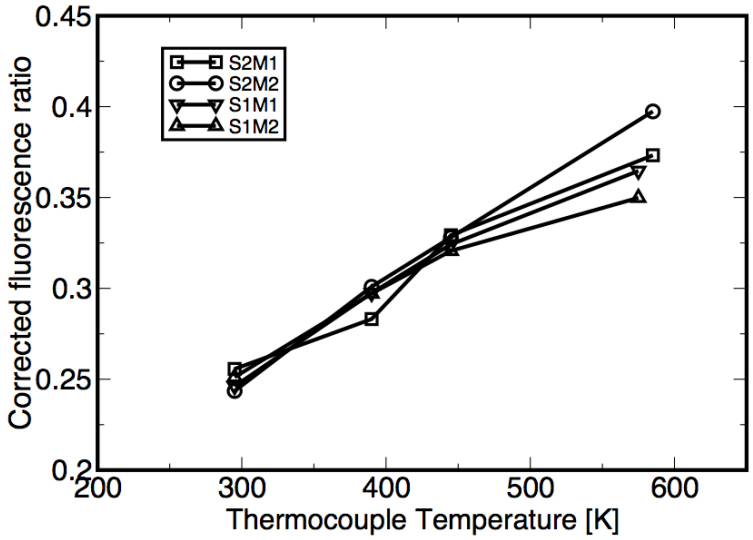

Figure 2.54: Corrected ratio for the two series of measurements obtained with LIF toluene at fours different temperatures.

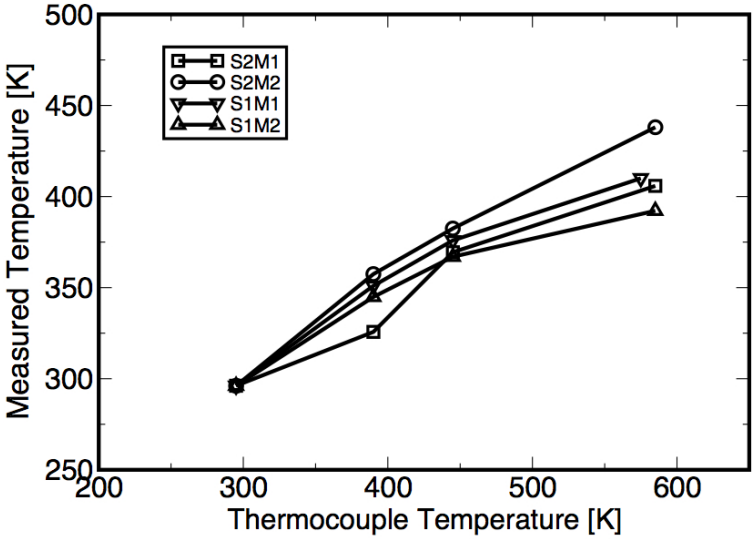

Figure 2.55: Measured temperature for the two series of measurements obtained with LIF toluene at fours different temperatures.

The two series show similar trend for both the ratio and the injector outlet-jet temperature. Concerning the jet temperature we can see that there is a difference between the measured temperature with the thermocouple and the temperature given by the LIF technique. It can be explained by the heat loss inside the system injector + convergent and also by the fact that the temperature given by the thermocouple is a global temperature influenced by the local Mach number (the section where the thermocouple is situated is very small compared with the outlet section). There are also some differences between the measured temperature due to the initial ratio which is not strictly the same for all the measurements and

also some measurements error due to the averaging and the background.
Finally, the two values that largely deviate from the rest of the data were not considered and a simple averaging of the data was done to obtain a law that expresses the inlet jet temperature T_{in} as a function of the thermocouple temperature T_{Tc} as follows :

$$T_{in} = -1.08\ 10^{-3} T_{Tc}^2\ + 1.32\ T_{Tc} \pm 5 \tag{2.16}$$

2.4.3 Mass fraction measurement: LIF Diacetyl

Knowing the inlet temperature of the nitrogen jet, the remaining unknown variable is the mass fraction. It will be obtained by fluorescence excitation of the diacetyl tracer. However, it was important to verify the hypothesis under which this tracer was used. This hypothesis already mentioned in the introduction is that the fluorescence intensity is not affected by temperature variations in the range investigated. Moreover, unlike the 2 line toluene LIF, LIF-measurements with diacetyl are proportional to laser intensity profile. Meaning that a knowledge of the laser profile is mandatory to perform laser corrections if necessary.

Temperature variations test:

This test consisted in changing the inlet temperature of the jet and in comparing the fluorescence signal at two different sections. Three imposed temperatures (temperature measured with the thermocouple: T_c) were investigated: 278 K, 369 K and 415 K. They corresponds respectively to an inlet temperature of the jet according to Eq. (2.16) of : 283.5 K, 340 K, 362 K.

Experimental set-up

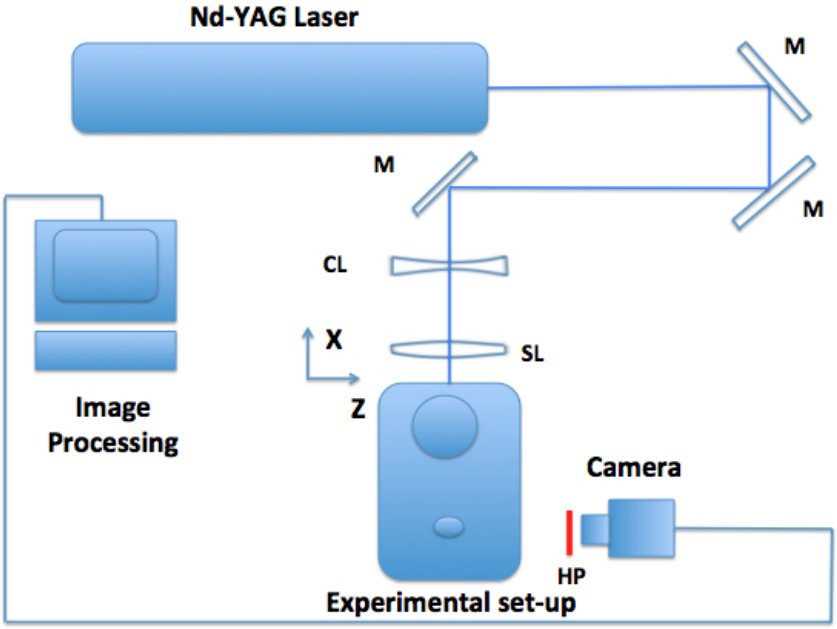

Figure 2.56: Schematic description of the LIF (with diacetyl) set-up for the linearity study: M stands for mirror, SL the spherical lens, CL the cylindrical lens and HP the High pass filter at 370 nm

Laser sheet: The laser sheet is generated by a NdYAG laser working at 355 nm. The laser plane was generated by a combination of a divergent cylindrical lens of 40 mm focal length and a convergent spherical

lens of 1000 mm focal length. Different mirrors reflecting at 355 nm were used to orientate the laser sheet. The width of the laser sheet was about 1.5 mm and the height 40 mm.

Seeding system and signal collection The flow was seeded with diacetyl by bubbling the nitrogen flow in a small tank containing a diacetyl solution. The signal was recorded with an intensified CCD camera. A High Pass filter centered at 370 nm was placed on the camera. Images were post-processed with an In-House software developed at IFPEN.

Measurements were performed without the impinging surface at the same injection time for the three temperatures. As it can be seen in Fig. 2.57 to Fig. 2.59 the fluorescence signal does not really vary significantly when varying the temperature. One can note that the penetration length of the jet slightly increases when the jet get hotter.

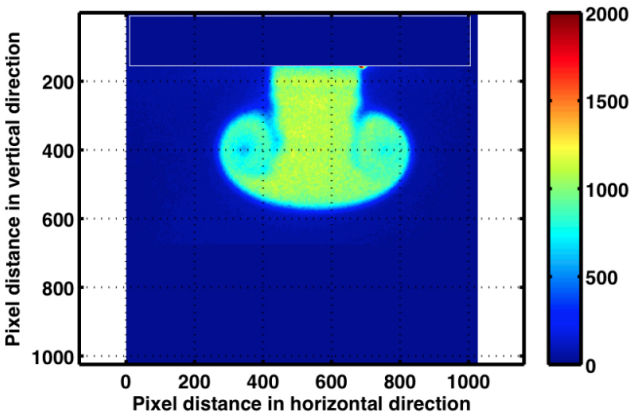

Figure 2.57: Fluorescence signal of diacetyl for the free jet at temperature $T = 298$ K

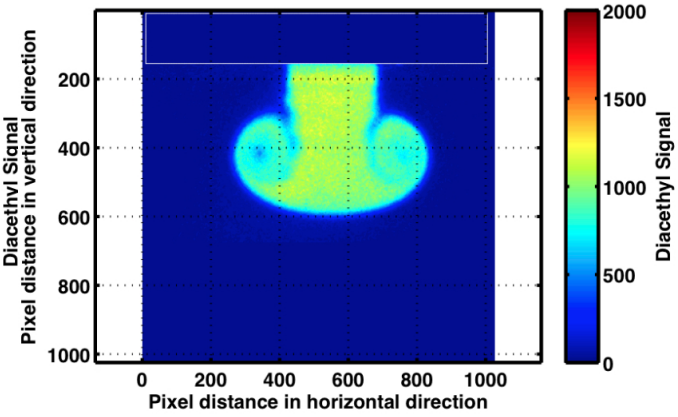

Figure 2.58: Fluorescence signal of diacetyl for the free jet at temperature $T = 369$ K

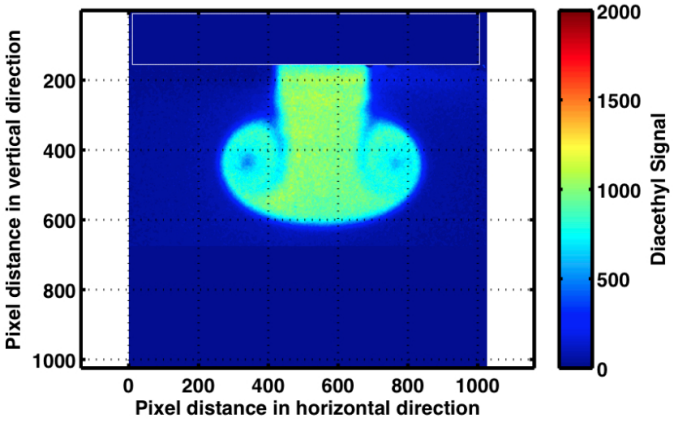

Figure 2.59: Fluorescence signal of diacetyl for the free jet at temperature $T = 415$ K

Fluorescence profiles on two different locations (vertical pixel location 200 and 400) show that the fluorescence signal is not sensitive to temperature variations (see Fig. 2.60 and Fig. 2.61). This result shows that diacetyl fluorescence can be used with temperature correction to measure the mass fraction of nitrogen. We can also note that the signal is relatively homogeneous for all temperature conditions showing that the diacetyl tracer is homogeneously distributed in the nitrogen flow and therefore diacetyl LIF can be used for nitrogen mass fraction measurements.

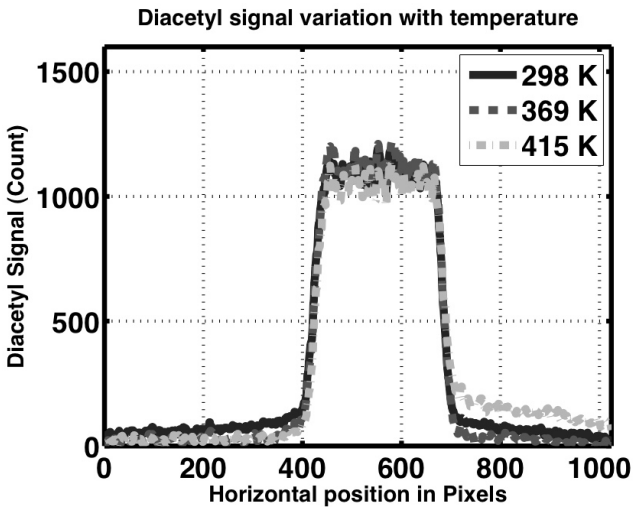

Figure 2.60: Comparison of diacetyl fluorescence signal for three different temperature at vertical location 200 pixels

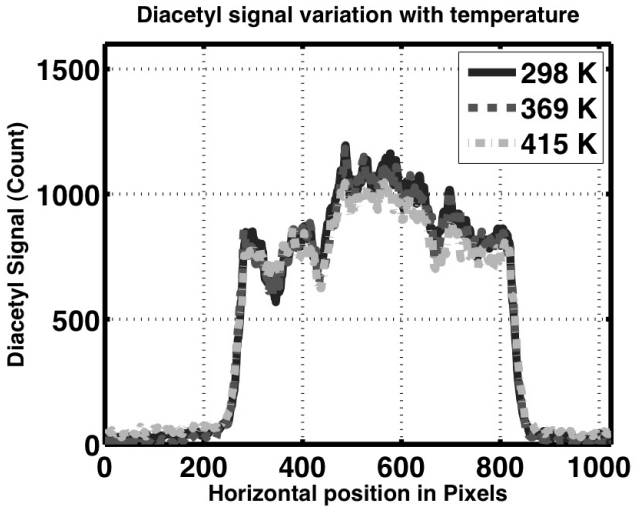

Figure 2.61: Comparison of diacetyl fluorescence signal for three different temperature at vertical location 400 pixels

Laser profile characterization:

The laser profile was characterize with a procedure that consists in injecting the nitrogen/diacetyl mixture with the injector inside a cylinder whose height corresponds to the height of the measurements section 20 mm. The signal was recorded after several injections considering that the mixing is homogeneous inside the cylinder. Fig. 2.62 shows the corresponding acquisition averaged over 50 individuals snapshots.

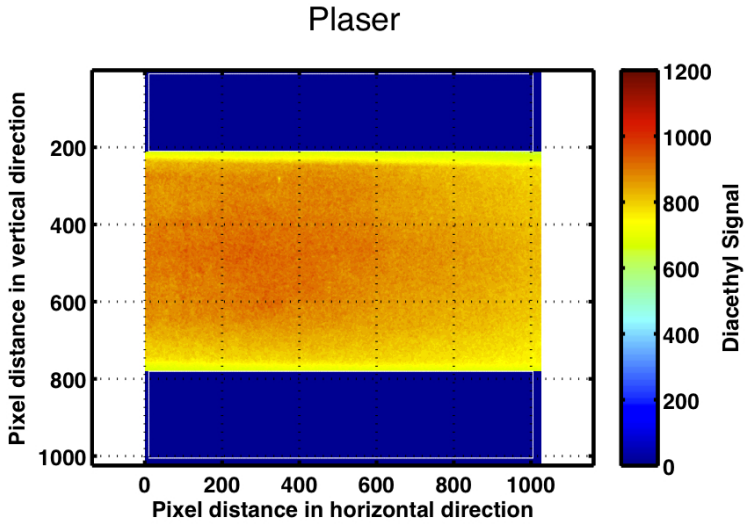

Figure 2.62: Laser plane for LIF diacetyl measurments.

The vertical profile of the laser is shown in Fig. 2.63. As it can be seen, variations in laser intensity are below 10%. No correction were therefore applied to the LIF signal since this value was considered to be below the measurement uncertainty.

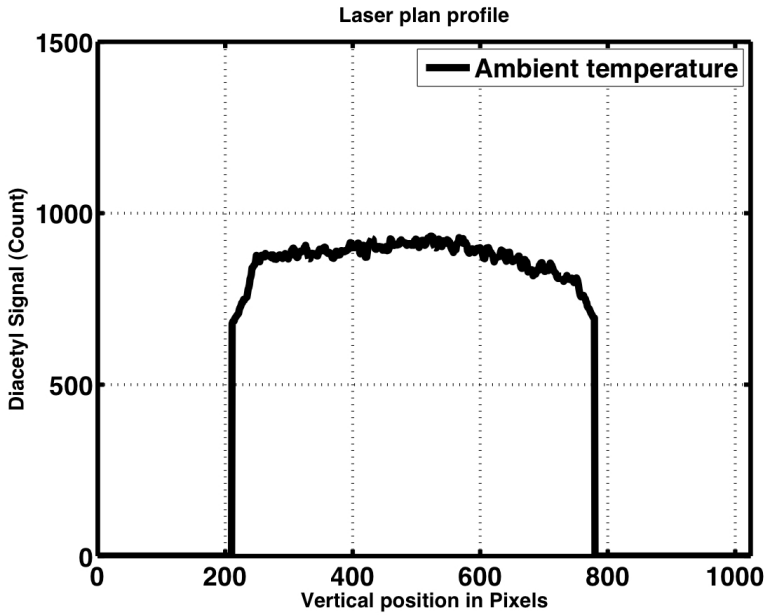

Figure 2.63: Profile of the laser plane at the horizontal location 400

Mass fraction measurements:

The experimental set-up is similar to the one used for the temperature variations tests. Measurements are performed with the cross flow and of course the impingement surface. The entire images are normalized by the diacetyl signal at the jet exit at early injection $t = 0.8$ ms in order to obtain the mass fraction Fig. 2.64 shows an example of a post-processed sample of images averaged over 50 snapshots at time $t = 1.2$ ms.

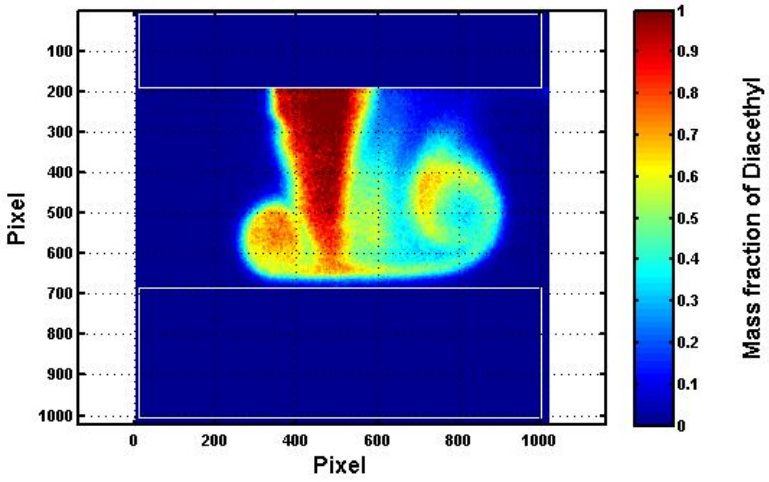

Figure 2.64: Mass fraction of diacetyl at time $t = 1.2$ ms.

We can see that, near the injector the mass fraction is approximately one and in the core of the vortices the mass fraction decreases because of the mixing with the cross flow. The latter should induce a decrease of the temperature of the jet. The final temperature field is obtained by using Eq. 2.10 knowing the inlet jet temperature. Results are compared in the chapter 4 with numerical results.

2.5 Wall temperature measurement: Laser Induced Phosphorescence Thermography:

The main issue for temperature measurement was to find a reliable technique that can be used for measuring a low temperature increase (around 4 K for a theoretical impinging temperature of 100 K) with a very fast response time (the interaction between the jet and the impinging surface lasts less than 10 ms) particularly on the specific material that the impinging surface is made of.
The first option was to used fast thermocouples such as those manufactured by nanmac (www.nanmac.com). They have the interesting property to give a very fast response time of the order of magnitude of the microsecond. But after several tests performed by the company, it was not possible to built sufficiently thin thermocouple probes that could be inserted in the impinging surface. This was mainly due to the friable structure of the selected material.
It was then decided, as second option, to use a recently developed technique that consists in depositing a small layer of phosphor on the measuring surface and in inducing a phosphorescence signal with a laser. The collected phosphorescence signal decay depends on the temperature of the surface. This technique is known in the literature as the LIPT which stands for Laser Induced Phosphorescence Thermography. Although the technique is intrusive because the temperature is measured not on the surface directly but on the phosphor layer, it has the advantage to have a very fast response time (the phosphorescence decay rate can be less than the microsecond). In order to avoid measurement bias due to the thickness of the phosphor layer, the application of the layer is well controlled so that the thickness is small as it can be seen in Fig. 2.65 and Fig. 2.66.

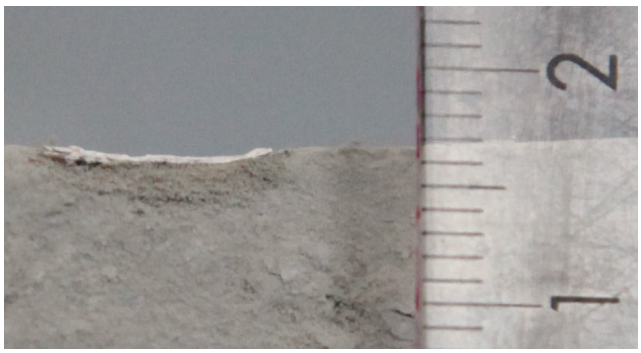

Figure 2.65: Thickness of the phosphor deposit

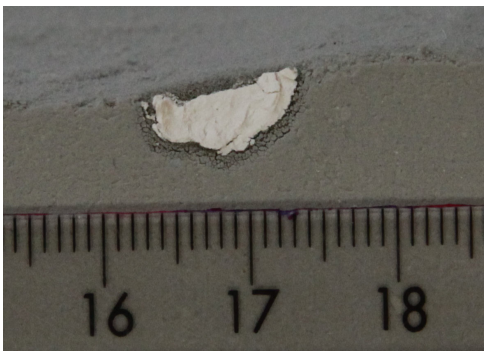

Figure 2.66: Top view of the phosphor deposit

2.5.1 Principle of the LIPT

LIP technique has became over the last past years a very reliable technique [3, 46, 66, 124, 145] since it allows a local and temporal tracking of surface temperature. It consists in inducing a phosphorescence signal after a laser excitation as shown in Fig 2.67.

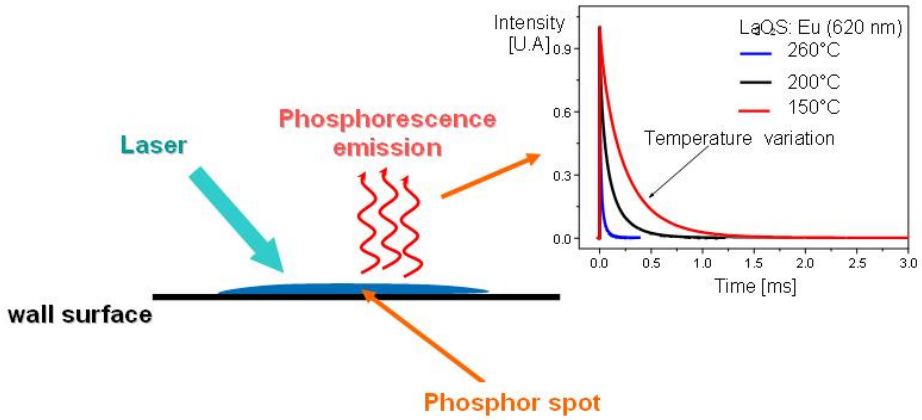

Figure 2.67: Principle of the LIP

The lifetime or the time duration of the phosphorescence intensity (when it decreases to $1/e$ of the initial intensity see Eq.2.17) depends on the temperature and hence with an appropriate calibration of the phosphor the temperature can be deduced.

$$I = I_0 exp\left(-\frac{t}{\tau}\right) + B \tag{2.17}$$

where I is the phosphorescence intensity at the initial time, B the baseline and τ the life time that depends on the temperature.

Another interesting advantage of the LIPT technique is that it covers a very wide range of temperature from very low temperature up to 2000 K or 3000 K. Fig 2.68 shows some calibration curves for different phosphors confirming the potential of this technique.

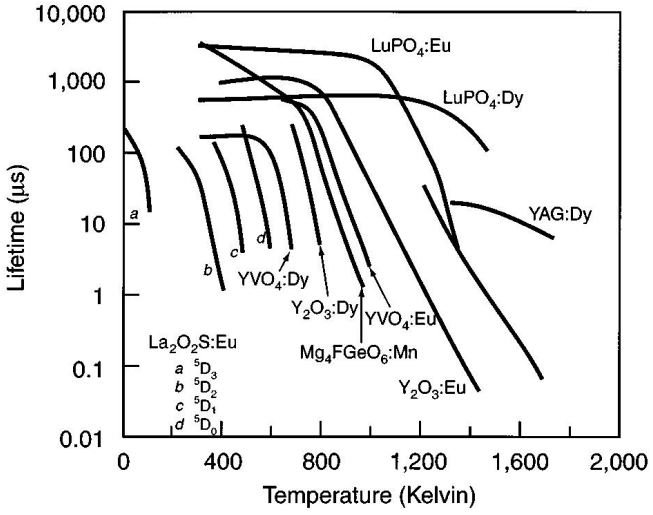

Figure 2.68: Calibration curves for different phosphor (Alison and Gillies [3])

It is worth nothing that the calibration function is strongly coupled with the collection filter band. Because of the large emission spectrum of a given phosphor different calibration curves can be obtained from the same excitation wavelength as shown in Fig. 2.69.

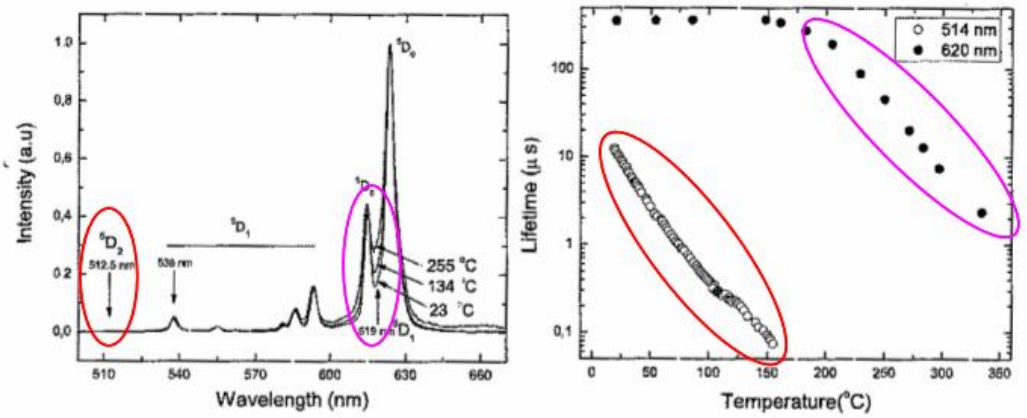

Figure 2.69: On the left hand side Emission spectrum for $La_2O_2 : Eu$ and on the right hand side two calibration curves corresponding to two different collections bands ([66]).

2.5.2 Experimental set-up:

The experimental set-up for the LIPT measurements is represented in Fig. 2.70.

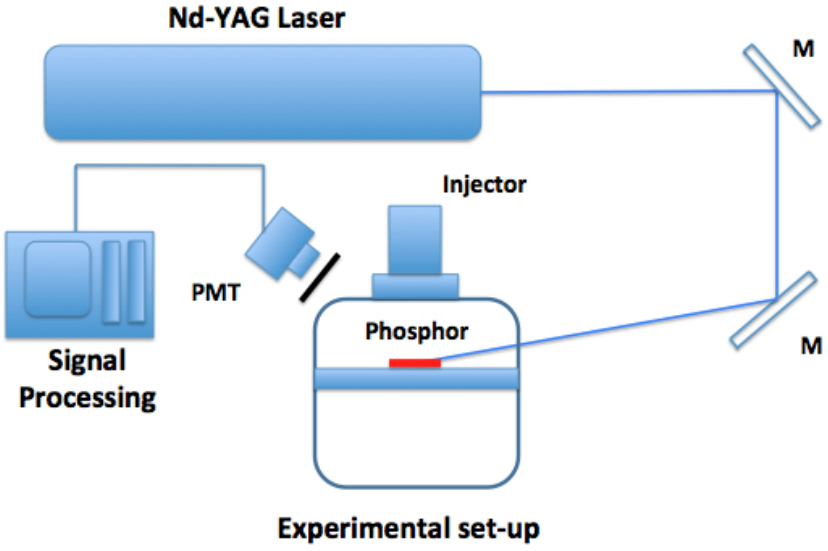

Figure 2.70: Experimental Set-up for the LIPT measurements

Laser beam: The laser signal was generated by a 1064 nm Nd:YAG-laser working at its third harmonic (355 nm). A combination of mirrors reflecting at the wavelength 355 nm were used to direct the beam to the phosphor layer.
Signal collection: La_2O_2Eu phosphor was chosen since it shows an interesting time decay dependency at low temperature. The temporal phosphorescence signal was recorded with Photo Multiplier Tubes (Hamamatsu type PMT, reference: H9306) along with a fast response oscilloscope (Textronix type oscilloscope). A pass-band filter centered at 532 nm was mounted on the PMT in order to restrict the collection to this spectral band.

2.5.3 Results and analysis:

The most critical step in LIPT technique measurement is the post-processing of the exponential curve (see Eq. 2.17) which leads to the determination of the lifetime. The principle consists in fitting the curve with an exponential fit with a minimization constraint (the best fit can correspond for example to the curve with the lowest error using a mean least square method). The problem that arises (according to the IFPEN experience) with this technique is that the exponential fit depends strongly of the initial intensity I_0 specially at low temperature. Indeed, a wrong estimation of the initial pic can lead to a bad prediction of the lifetime. Moreover the initial intensity can be affected by interferences that occur instant after laser excitation. In addition, large intensity variations occur in very short-time scales in these first instants and the PMT bandwidth might not be appropriate for such fast variations.
One of the method used at IFPEN to avoid this problem is to fit the curve with a bi-exponential fit instead of a single exponential. The phosphorescence signal is then expressed as follows:

$$I = I_1 exp\left(-\frac{t}{\tau_1}\right) + I_2 exp\left(-\frac{t}{\tau_2}\right) + B \tag{2.18}$$

where τ_1 is the shortest time that corresponds to the time duration close to the peak and τ_2 the longest time which is more reliable and more representative of the decay induced by the laser excitation. In what follows, the lifetime corresponds to τ_2 and each lifetime corresponds to an averaging over 100 single acquisitions.

Calibration:

The calibration of the phosphor was performed using a constant-temperature oil bath. A phosphor layer is deposited on a pastil which is then introduced inside the bath. The temperature of such a constant-temperature bath can be accurately controlled and allowed a fine calibration of the phosphor. The temperature is then increased by increments of 0.2 Kelvin and the associated lifetime is recorded.
Because the day to day variations of the ambient temperature in the cell, hence of the initial wall temperature at injection time, can be higher than the wall temperature variations during injection, it has been decided to analyze only the normalized calibration curve to limit the study to relative temperature variations. The calibration curves obtained are shown in Fig. 2.71 and 2.72.

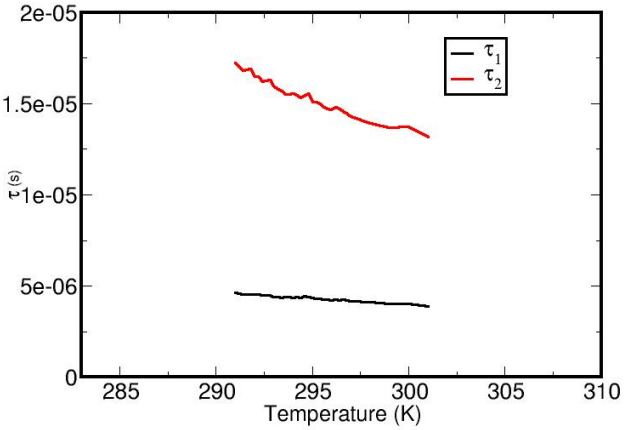

Figure 2.71: Calibration curves

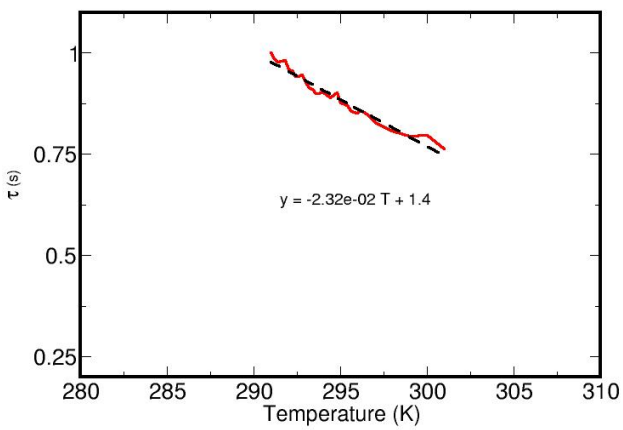

Figure 2.72: Normalized calibration curve

The calibration curve shows a linear dependency between the temperature (for the range investigated)

and the lifetime. The corresponding linear fit equation is expressed as:

$$\tau_{norm} = -2.32\ 10^{-2}\ T + 1.4 \tag{2.19}$$

Because we deal with a normalized curve, the most important parameter is the slope of this curve. Indeed knowing the slope, the room temperature and the normalized lifetime (with respect to the room temperature lifetime) can give the corresponding temperature increase.

Results:

The measurement point is situated just below the injector in order to optimize the temperature increase. If the center of the injector is considered as the origin, the measurement point is at the following coordinates: $X = 0$, $Y = -2D$ and $Z = 0$.
Two series of measurements were performed. The objective of the first one was to estimate the precision of the measurement technique in the presence of the turbulent non isothermal cross flow below the injector. Although the cross flow was initially isothermal just after the turbulent grid, it is heated by the hot wall on the top of the measurement section. The measurement of this preliminary tests consisted in determining the variations on the temperature (deduced from the decay time) induced by the turbulent cross flow without injection and at ambient temperature. Results showed a variation of the temperature of 0.2 K which can be considered as the precision of the technique in our configuration.

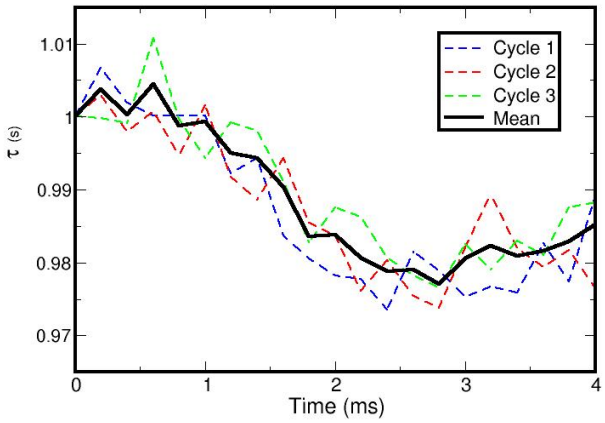

Figure 2.73: Normalized decay time

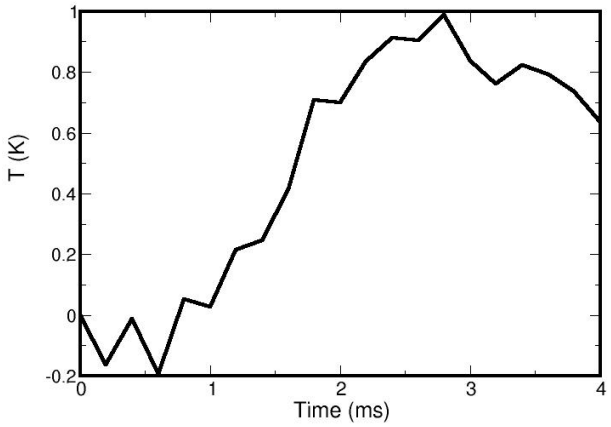

Figure 2.74: Mean temperature increasing

The second serie was the measurement of temperature increase during injection. The results are shown in Fig. 2.73 and Fig. 2.74. They show that the maximum temperature increase is around $1K$ which is lower than the theoretical expected increase. Several reasons can explain this difference. First the theoretical estimation is based on simplifying assumptions, and also the injected temperature is not 100 K as used in the theoretical analysis but 70 K (± 5 K) as shown during the determination of the inlet jet temperature with the LIF technique. As it will be seen in the analysis of the PIV results the increase occurs after the impingement and during the interaction between the jet and the solid boundary. After 2.5 ms the jet is deviated and the temperature progressively decrease to the ambient temperature. Since the magnitude of the temperature increase (1K) is not significant compared to the temperature gradient in the flow this result shows that the bottom wall temperature has no little influence on the flow motion.

Chapter 3

Numerical models development:

3.1 Academic tests cases

The main issue of SGS models for IC engines applications are their ability to predict free flows, wall-bounded flows and anisothermal flows at low Mach number. The first step in this thesis was to study separately those flows features in the following tests cases: Homogeneous Isotropic Turbulence and Turbulent Channels (isothermal or anisothermal).

3.1.1 Homogeneous Isotropic Turbulence (HIT)

The HIT is a very interesting and well used test case for assessing performances of models for various applications with turbulence interaction: Shock-turbulence interaction [38, 50, 83], Scalar mixing [44, 8], Combustion [14, 30], multiphase flows [79, 136, 152]. Concerning the development of SGS models, experimental HIT are standard cases for evaluating model's constants [6, 106, 109, 133]. There are two main experimental HIT databases: Comte-Bellot and Corsin (CBC) [31] experiment and Kang *et al.* [65] experiment. The later is an improvement of the CBC database with a larger inertial range. Before going further to the details of the two HIT characteristics, basic notions that can be found in the literature [7, 27, 127] are first recalled as well as the different steps for implementing and performing an HIT.

- **Characteristic lengths of an HIT** [1]

  The Homogeneous Isotropic Turbulence is at first sight the most simple configuration for studying turbulence phenomena because the statistics can be easily obtained. It can be re-defined as a flow in which the velocity gradient are only time dependent (homogeneity condition) and whose statistics are identical in all points and are invariant versus symmetry, translation and rotation (isotropy condition). An interesting function for describing the statistics in turbulence is the spatial correlation function:

$$R_{ij}(\mathbf{x},\mathbf{r},t) =< u_i^{'}(\mathbf{x},t)u_j^{'}(\mathbf{x}+\mathbf{r},t) >= R_{ij}(\mathbf{r},t) \tag{3.1}$$

  where the symbol <> represents the ensemble average. In the case of an homogeneous turbulence $R_{ij}(\mathbf{r},t) = R_{ji}(-\mathbf{r},t)$ and $R_{ii}(\mathbf{r},t) = R_{ii}(-\mathbf{r},t)$. The correlation function allows to define an important characteristic length of turbulence that is the integral length scale in the i^{th}-direction:

$$L_{nm}^{i} = \int_0^{\infty} R_{nm}(\mathbf{x})d\mathbf{x} \tag{3.2}$$

  One may distinguish the longitudinal integral length $L_1 = L_{11}^{(1)} = L_{22}^{(1)} = L_{33}^{(1)}$ and the transversal integral length $L_2 = L_{11}^{(2)}$. For an HIT, $L_1 = 2L_2$. The integral length can be directly associated to the length of the biggest eddies of the flows that carry the energy. Along with the integral length, another interesting length for describing the different scales of the turbulence is the Taylor's micro scale λ. It can be obtained by a Taylor expansion series of the cross correlation as follows:

$$R_{11}(r,0,0) = 1 - \frac{r^2}{\lambda_1^2} + \mathbf{O}(\mathbf{r^3}) \tag{3.3}$$

  where λ_1 is the Taylor micro-scale in the longitudinal direction. Indeed as for the integral length, there is the longitudinal and transversal Taylor micro-scale and in the case of an HIT $\lambda_1 = \sqrt{2}\lambda_2$. In contrary to the integral length, the Taylor micro-scale can not be directly linked to the size of eddies but it can be defined as the scale under which the viscous effect control the flow dynamic. The

[1] More details in this part can be found in [7, 127]

two experimental databases that are going to be used, based their Reynolds number on this scale because it is a good indicator of the size of the inertial range. The final length for fully describing an HIT is of course the Kolmogorov length scale η.

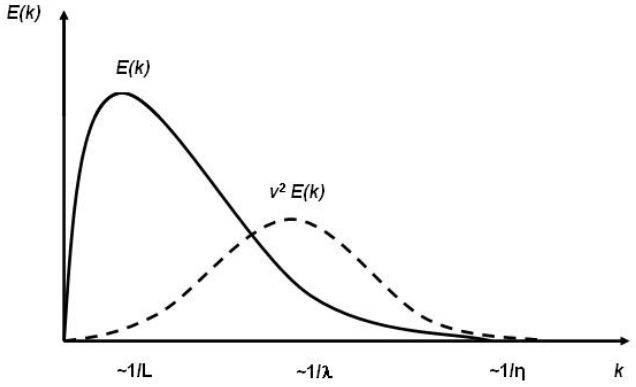

Figure 3.1: Schematic description of scales for an HIT.

The figure 3.1 summarizes the dynamic of an HIT. It represents both the kinetic energy spectrum and the viscous spectrum (normalized by the viscosity of the fluid) with respect to the wavenumber. The energy spectrum reaches its peak for eddies that roughly correspond to the integral length. As for the viscous spectrum the peak is obtained for eddies of size close to the Taylor micro-scale. Both spectra completely vanish at the Kolmogorov scale.

- **Numerical experiment of HIT**

The difficulty when dealing with HIT with a spacial solver is to generate a velocity field $\mathbf{u}$ in the physical base $(\mathbf{e_1}, \mathbf{e_2}, \mathbf{e_3})$ starting from a given energy spectrum $E(k)$ and the spectral base $(\mathbf{e_{k1}}, \mathbf{e_{k2}}, \mathbf{e_{k3}})$. The computation is usually initialized in a cubic box of size L_B.

The initialization starts first with the mass conservation equation rewritten in the spectral space as follows:

$$\mathbf{k}.\mathbf{u}(\mathbf{k}) = \mathbf{0} \tag{3.4}$$

(3.5)

The easiest way to satisfy this condition is to define an intermediate spectral base $(\mathbf{e^{int}_{k1}}, \mathbf{e^{int}_{k2}}, \mathbf{e^{int}_{k3}})$ so that :

$$\mathbf{e^{int}_{k3}} = \frac{\mathbf{k}}{k} \tag{3.6}$$

and the velocity vector can be rewritten with the intermediate coordinates as follows:

$$\mathbf{u} = \mathbf{a}(\mathbf{k})\mathbf{e^{int}_{k1}} + \mathbf{b}(\mathbf{k})\mathbf{e^{int}_{k2}} \tag{3.7}$$

with the additional condition for the kinetic energy:

$$\frac{1}{2}\int (\mathbf{a}.\mathbf{a}^* + \mathbf{b}.\mathbf{b}^*) d\mathbf{s}(\mathbf{k}) = E(k) \tag{3.8}$$

where $a(k)^*$ are $b(k)^*$ are respectively the conjugates of $a(k)$ and $b(k)$. Eq. (3.8) can be expressed as :

$$(\mathbf{a}.\mathbf{a}^* + \mathbf{b}.\mathbf{b}^*) = \frac{E(k)}{2\pi k^2} \tag{3.9}$$

the expression of the intermediate velocity in the $(\mathbf{e_{k1}^{int}}, \mathbf{e_{k2}^{int}}, \mathbf{e_{k3}^{int}})$ basis is then given by the following expression:

$$\mathbf{a(k)} = \sqrt{\frac{\mathbf{E(k)}}{\mathbf{2\pi k^2}}}\mathbf{cos}(\theta)\mathbf{exp(j}\theta_\mathbf{1}\mathbf{)} \tag{3.10}$$

$$\mathbf{b(k)} = \sqrt{\frac{\mathbf{E(k)}}{\mathbf{2\pi k^2}}}\mathbf{cos}(\theta)\mathbf{exp(j}\theta_\mathbf{2}\mathbf{)} \tag{3.11}$$

θ and θ_i are random number that define the phase of the vector $\mathbf{u}$. The last step consists in finding the corresponding velocity component in the physical space that corresponds to the intermediate calculated intermediate velocity component. This is achieved with a simple transformation that leads to the following coordinates u_i:

$$u_1 = \frac{a(k)k_2k + b(k)k_1k_3}{k\sqrt{(k_1^2 + k_2^2)}} \tag{3.12}$$

$$\tag{3.13}$$

$$u_2 = \frac{b(k)k_2k_3 - a(k)k_1k}{k\sqrt{(k_1^2 + k_2^2)}} \tag{3.14}$$

$$\tag{3.15}$$

$$u_3 = \frac{b(k)\sqrt{(k_1^2 + k_2^2)}}{k} \tag{3.16}$$

More about the initialization of an HIT can be found in work of Rogallo [122] and Boughanem and Trouve [16]. The figure 3.2 summarizes the initialization procedure of an HIT.

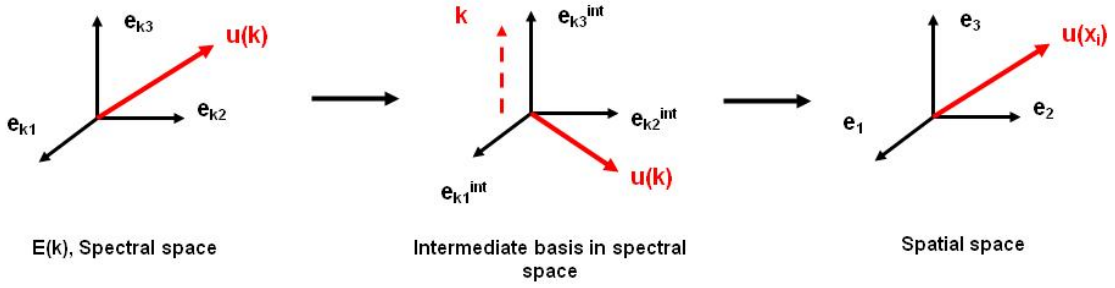

Figure 3.2: Numerical initialisation of an HIT.

- **The test case**

The two experiments of CBC and Kang *et al.* are quite similar. The main difference is in the method for generating the turbulence that leads to a higher Reynolds number in the case of the Kang *et al.* experiment. The latter was actually designed specially to improve the CBC database. In both cases, the HIT is generated via a continuous flow passing through grid of mesh size M and a convergent to ensure the isotropy. In a reference frame moving with the average flow velocity, the problem can

be defined as a freely decaying isotropic turbulence. It is modeled by considering the fluid inside a cubic box with periodic boundary conditions and size L_B^3. The computation is initialized with a synthetic turbulent field whose energy spectrum is the experimental one at the first time. Without SGS model, the effect of small scales is not modeled and the laminar viscosity of the fluid can not dissipate the energy provided by the bigger scales. The LES computation will then stop due to the accumulation of energy at high wavenumber. With the appropriate SGS model and the appropriate value of the constant, it should properly reproduce the experiment. The objective of the test case is then:

1. To compare the experimental spectra with the one obtained in LES

2. To compare the decay of the kinetic energy with respect to the time

3. In the case of dynamic models whose constants vary in the time, to compare the converged values of the dynamic constant of the model is compared to the "a priori" imposed value of the constant.

The simulation are performed with different mesh resolutions for testing the robustness of the models. Table 3.1 summarizes the characteristics of the two experiments.

Table 3.1: Characteristics of the HIT experimental database.

Parameter	Comte-Bellot and Corsin [31]	Kang *et al.* [65]
Mesh size $M(m)$	0.0508	0.152
Convective velocity $U_0(m/s)$	10	11.2
Taylor based Reynolds number	71.6	716
Non dimensional time $t^* = U_0 t/M$ spectra for which the spectra are available	42, 98, 171	20, 30, 40, 48

3.1.2 Turbulent channel:

The Turbulent Channel test case has became over the past years an absolute must and an interesting test case for assessing SGS models capability near solid boundaries. More generally, it is a simple but quite reliable test case used in CFD for multiple flow applications such as wall functions development [21, 49, 96], heat transfer studies [67, 153], passive scalar mixing [24, 70], flame quenching near walls [20, 82].

It consists in the simulation of a flow between two parallel walls with periodic boundary conditions in the streamwise and spanwise directions as shown in Fig 3.3. A source term is added to the Navier-Stokes equation in the streamwise direction to keep a permanent flow rate in the channel. In the case of the anisothermal channel, another source term is added in the energy equation. Throughout the thesis, the isothermal case corresponds to the configuration in which the temperature of the walls is at the same temperature as the flow inside the channel. In the anisothermal case, the wall temperature is lower than the temperature at the center of the channel.

The characteristic number of this configuration is the friction Reynolds Re_τ defined as follows:

$$Re_\tau = \frac{u_\tau h}{\nu_w} \tag{3.17}$$

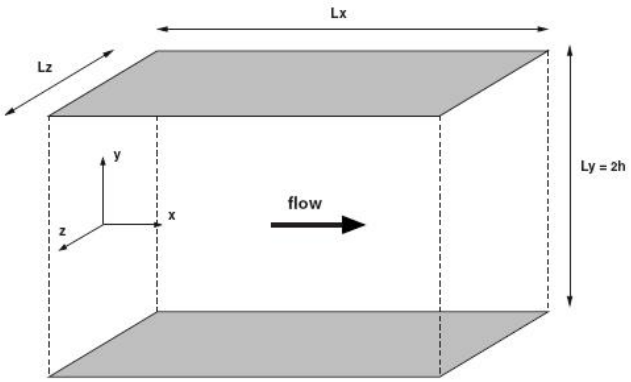

Figure 3.3: Periodic channel.

where h is the channel half height, ν_w is the kinematic viscosity of the fluid and $u_\tau = \sqrt{\frac{\tau_w}{\rho_w}}$ the friction velocity. The normalized wall distance parameter that defines the quality of the mesh resolution of the computation reads:

$$y^+ = \frac{y u_\tau}{\nu_w} \tag{3.18}$$

When dealing with non circular tube there is a parameter referred to the hydraulic diameter D_h that is somehow the corresponding diameter for a round tube. It is expressed as :

$$D_h = \frac{4\ Cross\ sectional\ area}{wetted\ perimeter} \tag{3.19}$$

It is usually associated to the bulk[2] Reynolds number:

$$Re_{b,D_h} = \frac{\rho_b u_b D_h}{\nu_b} \tag{3.20}$$

The database used for validation corresponds to the DNS of Moser *et al.* [99] that correspond to the friction Reynolds numbers $Re_\tau = 395$ and $Re_\tau = 590$.

The wall stress is linked with the center-line channel velocity by the Dean [34] expression modified in [71]:

$$\tau_w = 3.02 \times 10^{-3} \rho_w U_c^2 \tag{3.21}$$

This is an interesting relation that allows to impose the appropriate source term for the target friction Reynolds number. The source term in the i^{th}-direction is then expressed as :

[2]The corresponding "bulk" density, velocity and temperature respectively are expressed as follows:

$\rho_b = \frac{1}{h}\int_0^h \bar{\rho} dy$

$u_b = \frac{\int_0^h \bar{\rho}\bar{u} dy}{\int_0^h \bar{\rho} dy}$

and $T_b = \frac{\int_0^h \bar{\rho}\bar{u}\bar{T} dy}{\int_0^h \bar{\rho}\bar{u} dy}$

$$D_x = \frac{S_{target} - \frac{1}{V}\int\int\int_\Omega \rho u_x dv}{\tau_{relax}} \tag{3.22}$$

with $S_{target} = \rho U_c$ and $\tau_{relax} = \frac{1}{5}\frac{h}{u_\tau}$.

The corresponding friction coefficient reads:

$$C_f = \frac{\tau_w}{\frac{1}{2}\rho_{ref} U_{ref}^2} \tag{3.23}$$

"ref" stands for the chosen reference values that correspond to the channel center line values throughout this work.

In analogy to the friction velocity u_τ, a so-called friction temperature is introduced for anisothermal configuration:

$$T_\tau = \frac{q_w}{\rho c_p u_\tau} \tag{3.24}$$

this leads to the non-dimensional temperature:

$$T^+ = \frac{T_w - \bar{T}}{T_\tau} \tag{3.25}$$

The characteristics number for describing anisothermal flows is the Nusselt number expressed as :

$$Nu = \frac{q_w}{\lambda_{ref}\frac{T_w - T_{ref}}{h}} \tag{3.26}$$

It represents the ratio between the heat flux at the wall and the conduction heat flux evaluated with reference diffusion λ_{ref}.

A source term is also introduced in the energy equation to keep a continuous ratio between temperature in the center of the channel and temperature imposed at the walls during the computation. It is expressed as follows:

$$Q_x = \rho_b C_{v,mean} \frac{T_{target} - \frac{1}{V}\int\int\int_\Omega \rho_\omega T dv}{\tau_{relax}} \tag{3.27}$$

where $C_{v,mean}$ is the mean volume average of C_v in the channel.
Additional interesting correlations are available in the literature ([111, 129, 134, 143] for C_f and Nu depending on the flows conditions.

A particular attention was paid on the statistic convergence during the LES simulations of the turbulent channel case. The size of the channel for the entire simulation are chosen to meet the requirement of the minimum channel advised by Kim and Moin [71] and all the statistics are accumulated over at least 10 diffusion times after the convergence is established. The chosen dimensions proved to be sufficient to well recover first order statistics [22]. In addition, the total shear stress in the channel was evaluated to make sure that the balance among the resolved shear stress, the viscous shear stress, the SGS shear stress is respected. The similar analysis was also performed to the total heat flux.

3.2 Numerical implementation in AVBP:

This section is devoted to the description of the main solver used during this thesis: AVBP [1]. Particular emphasis is paid to the data structure, the implementation of the SGS models (time scale calculation and volume filter size definition) and the modification performed. The test filter useful for dynamic models implementation and the associated test volume filter are also presented. Additional solvers that were used to highlight the robustness of the models developed are also shortly described.

3.2.1 AVBP solver:

The AVBP solver is a property of CERFACS and IFPEn [1]. It was originally created by the Oxford University Computing Laboratory (OUCL) and CERFACS in 1993. The solver relies on the Cell-Vertex (CV) links with the Finite-Volume (FV) and Finite-Element (FE) methods. More details about those formulations can be found in works of [121, 123]. The two main characteristics and advantages of this software is the possibility to deal with non-structured/hybrid meshes and the possibility to run on heavy parallel platforms through the MPL library. This allows to study both academic configurations [146, 114] and industrial configurations with interesting results [101, 131, 139]. In what follows, some notions on the CV formulation (taken from the AVBP handbook [1]) are recalled: definitions of normal, calculations of residuals and gradients at nodes. They are indeed important for understanding the modification introduced concerning the implementation of SGS models in the solver and also for presenting the test filter used for the dynamic models.

Metrics, Principles of the Cell-Vertex formulation and gradients calculations

For sake of simplicity, the differential formulations of the Navier-Stokes equations can be written in the following compact form:

$$\frac{\partial \mathbf{w}}{\partial t} + \nabla \cdot \mathbf{F} = \mathbf{s}, \tag{3.28}$$

where $\mathbf{w} = (\rho, \rho v, \rho E)^T \in \mathbf{R}^m$ is the vector of conserved variables (m is the numbers of variables), $\mathbf{F} = (\mathbf{f}, \mathbf{g}, \mathbf{h})^T$ is the corresponding flux tensor and $s \in \mathbf{R}^m$ is the source term. The fluxes can be divided into an inviscid, convective part $\mathbf{F}^i$ and a viscous part $\mathbf{F}^v$ and expressed:

$$\mathbf{F} = \mathbf{F}^i(\mathbf{w}) + \mathbf{F}^v(\mathbf{w}, \nabla \mathbf{w}) \tag{3.29}$$

- **Normal definition**

  Because the data structure, metrics are cell-based, normals are defined at the cell vertices. To simplify coding and be able to write general formulation for divergence or gradient operators, whatever the considered element is, normals are built using the following way:

  1. Outward pointing face normals $\mathbf{n}_f$ are first calculated. They are weighted with the face area. One should note that generally, the four vertices of a quadrangular face do not belong to the same plane. The face is therefore divided into four triangles (along diagonals) and $\mathbf{n}_f$ is defined as the average of the four normals Fig 3.4.

     This way to calculate face normals enables to preserve a solution linearity (which is equivalent to a second-order accuracy for steady state on sufficiently smooth meshes).

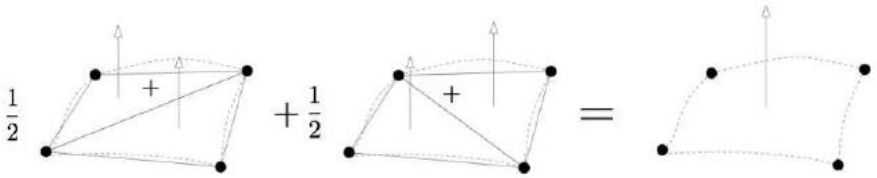

Figure 3.4: Face normal calculation for a quad, which vertices are not the same plane.

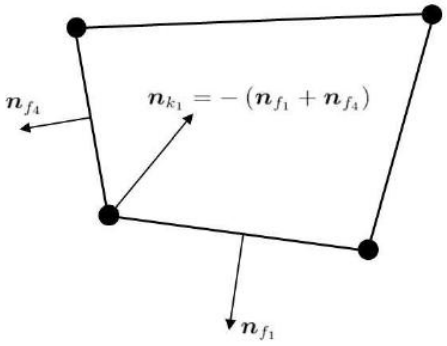

Figure 3.5: Node normal for a quad

2. Normal $\mathbf{n}_k$ associated with vertex k of a given cell C is a linear combination of face normals of the adjacent faces:

$$\mathbf{n}_k = \sum -\frac{d}{n_v^f}\mathbf{n}_f \tag{3.30}$$

d is the umber of dimensions. $\mathbf{n}_k$ is weighted by an area. Fig 3.5 gives an example for a non-regular quad.
Eventually, to ensure consistency the following relation must be verified:

$$\sum \mathbf{n}_k = 0 \tag{3.31}$$

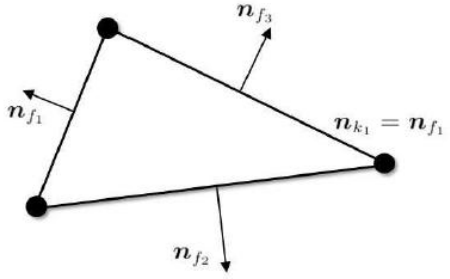

Figure 3.6: Node normal for a triangle

- **Cell-Vertex methods**

The CV method was first introduced by Ni [103] and later modified by Hall [57]. Different studies have been done to assess the precision of this methods in the past years [25, 98, 118, 123]. It has been developed by the OUCL team and shown to be an interesting alternative to the more classical

Cell-Centre (CC) FV method. On a FV point of view, the CV method consists in applying conservation relations to the grid cells, while solution is stored at the grid nodes.

The first step of the CV method is to "gather" the conservative variables to the cell using the CV connectivity and then calculate the cell residual, which corresponds to the flux divergence of Eq. 3.28 and is defined for cell C:

$$\mathbf{r}_C = \frac{1}{|C|} \int_C \nabla \cdot \mathbf{F}_h dv \tag{3.32}$$

where $|C|$ is the cell surface or volume depending of the dimension and $\mathbf{F}_h$ is the numerical approximation of the Fluxes $\mathbf{F}$. Using the Green-Gauss theorem it gives:

$$\mathbf{r}_C = \frac{1}{|C|} \oint_{\partial C} \mathbf{F}_h \cdot \mathbf{n} dv \tag{3.33}$$

The discretization of (3.33) uses trapezoidal rule to integrate the fluxes along the edges of C, which is equivalent to consider that the fluxes linearly vary along the edges. Thanks to node normal definition (3.30), whatever the consider is, we have:

$$\mathbf{r}_C = \frac{1}{d|C|} \sum_{k \in C} \mathbf{F}_k \cdot \mathbf{n}_k \tag{3.34}$$

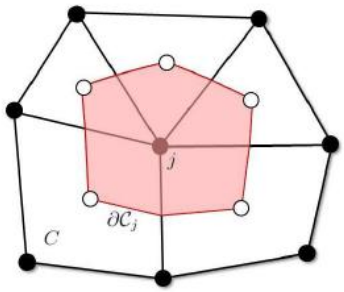

Figure 3.7: Control volume associated with j.

The linearity of the divergence operator is preserved if the volume $|C|$ is defined as followed:

$$|C| = -\frac{1}{d^2} \sum_{k \in C} \mathbf{x}_k \cdot \mathbf{n}_k \tag{3.35}$$

with $\nabla \cdot \mathbf{x} = d$.

Once the cell *residual is defined*, information has to be sent to the mesh nodes to obtain as many equations as there are degrees of freedom and update the solution vector. The *nodal residual* $\mathbf{r}_j$ is defined as a volume-weighted average of the *residuals* of the cells adjacent to *j*:

$$\mathbf{r}_j = \frac{1}{|C_j|} \sum_{C \in D_{j,C}} \mathbf{D}_{j,C} \mathbf{r}_C |C| \tag{3.36}$$

and

$$C_j = \sum_{C \in D_j} \frac{|C|}{n_v^C} \tag{3.37}$$

is the measure of the control volume C_j associated with j and merely corresponds to the median dual cell (see Fig 3.37). Conservation is ensured if :

$$\sum_{C \in D_j} \mathbf{D}_{k,C} = \mathbf{I} \tag{3.38}$$

$\mathbf{D}_{k,C}$ is the distribution matrix which allows to define the different schemes.
Finally, the semi-discrete approximation of the integral form of (3.28) is:

$$\frac{d\mathbf{u}_j}{dt} = -\mathbf{r}_j \tag{3.39}$$

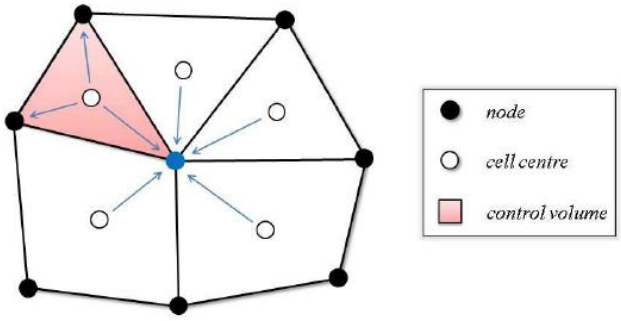

Figure 3.8: Hybrid mesh : (1) Element (coloured in pink) contribution to the vertices and (2) Cell contribution *scattering.*

Fig 3.8 well summarizes the cell-vertex procedure.

- **Gradient computations**

Since most of the SGS viscosity models's time scale are based on the gradient velocity tensor it is important to recall how it is evaluated on a CV solver. Similar to the residual computations procedure, the gradients $\vec{\nabla}\mathbf{w}$ are first calculated at cells and then distributed to the nodes. The cell-based gradient is defined so as to be transparent to linear solution variations:

$$(\frac{\partial \mathbf{w}}{\partial x})_C = \frac{1}{|C|} \int \int_C w \cdot \mathbf{n} dS \tag{3.40}$$

which leads to the approximation:

$$\nabla \mathbf{w}_C = \frac{1}{|C|} \sum_{k \in C} w_k \cdot \mathbf{n_k} \tag{3.41}$$

A nodal approximation of the gradient is then obtained using of a volume-weighted average of the cell-based gradients:

$$\nabla \mathbf{w}_j = \frac{1}{|C_j|} \sum_{C \in j} \nabla \mathbf{w}_C |C| \tag{3.42}$$

Numerical schemes

Different numerical schemes are available in AVBP but we will focus here on the description of the two numerical schemes that were used. More details about the other numerical schemes implemented in AVBP can be found in the Larmarque's thesis [80].

- **GRK**: It is a centered Galerkin finite element method which is 4^{th} order accurate in space with a 3^{rd} order Runge-Kutta temporal integration. It presents the advantage to have a very low numerical dissipation which is very important to assess the performances of SGS models. It was used to perform all the academics cases: HIT and Turbulent Channel.
- **Lax-Wendroff**: It is finite volume numerical scheme that is second order accurate in space with a single time step integration. It has the advantage to be less CPU demanding than the GRK scheme. It was used for running the more complex cases : Impinging Jet and some industrial applications.

3.2.2 Implementation of SGS models in AVBP:

The CV formulation presented in the previous section imposed some cautions when calculating/defining variables. A variable can either be calculated directly at the nodes or first at the cells and then "scatter" at the nodes. Two control volumes are also available: the cell control volume and the node control volume. Recalling the expression of the SGS viscosity $\nu_{sgs} = C_m^2 \Delta^2 D_m(\mathbf{u})$, the CV formulation rises some questions regarding the implementation of SGS viscosity models : choice of the filter width and calculation of the time scale. As for the dynamic models, the definition of the test filter width and the explicit filter is also important. A wrong definition of those parameters can lead to an over/under estimation of the SGS viscosity regardless of the accuracy of the model used.

Time scale calculation: $D_m(\mathbf{u})$

Let us consider for example the Smagorinsky time scale $D_m(\mathbf{u}) = \sqrt{2S_{ij}S_{ij}}$. With S_{ij} the strain rate of the velocity gradient tensor. We will simplified the problem to a 1D configuration with regular mesh of same size as shown in Fig 3.9 (not physically possible for the SGS viscosity of course).

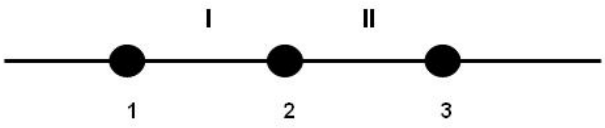

Figure 3.9: 1D Mesh.

The node 2 is shared by two cells I and II. According to relation 3.37 the volume of the cell is equal to the volume of the node.

The term $S_{ij}S_{ij_{node}}$ can be evaluated in two ways

1. At nodes knowing S_{ij} at nodes
   From relation 3.42

$$S_{ij_{node}} = \frac{|C|}{|C_{node}|} \left(S_{ij_I} + S_{ij_{II}}\right) \tag{3.43}$$

   then

$$(S_{ij}S_{ij})_{node} = \frac{|C|^2}{|C_{node}|^2} \left(S_{ij_I} + S_{ij_{II}}\right)^2 = \left(S_{ij_I} + S_{ij_{II}}\right)^2 \tag{3.44}$$

2. At cells and then scatter the results to nodes

$$(S_{ij}S_{ij})_{node} = \frac{|C|}{|C_{node}|}\left((S_{ij}S_{ij})_I + (S_{ij}S_{ij})_{II}\right) \;=\; \left((S_{ij}S_{ij})_I + (S_{ij}S_{ij})_{II}\right) \tag{3.45}$$

From Eq. 3.44 and 3.45, we can see that in the CV formulation the procedure to estimate the time scale of the SGS viscosity can lead to different results. In order to chose the most appropriate formulation, the HIT of CBC was selected as a test case. Simulations were performed with the Smagorinsky model ($C_s = 0.18$) on a 64^3 hexahedral type mesh.

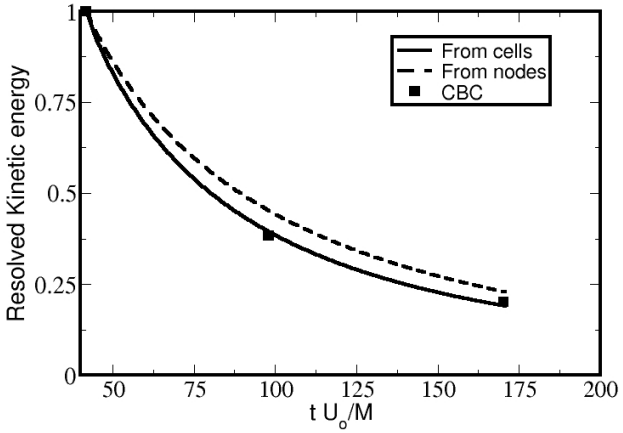

Figure 3.10: Resolved kinetic energy decay

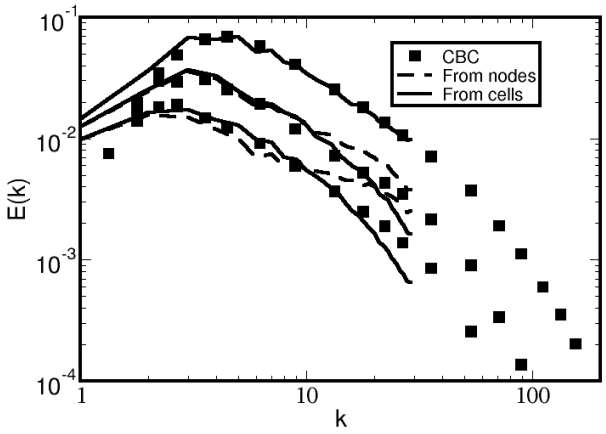

Figure 3.11: Time evolution of the energy spectra.

Fig. 3.10 shows that the best agreement with the experimental energy decay is obtained with the evaluation of the time scale at the cell level. The calculation at the node, leads to an underestimation of the resolved kinetic energy decay which is due to the accumulation of the energy at high wave number as shown in Fig. 3.11. The time evolution of the energy spectra is well predicted only when the time scale is evaluated at the cell level. It is worth noting that the accumulation of the energy leads after a longer time of simulation to the stop of the simulation. The effect of the unresolved small scales is not correctly reproduced and the viscosity of the fluid can not dissipate the energy accumulated at high wavenumbers. It emphasizes the importance of a correct implementation of the SGS viscosity in the particular case of solvers based on a CV formulation.

Choice of the length scale (initial filter width): Δ

At a first sight, the choice of the initial filter width can be considered as a simple task. Since the residuals and gradients are evaluated at the cell level, a natural choice would be to choose the cell volume as the initial filter width $\Delta = |C|^{1/3}$. However, this choice leads to a high dependency of the SGS viscosity to the type of the mesh (underestimation on tetrahedral meshes, large discontinuity of the SGS viscosity at interfaces on hybrid meshes ...).
One could consider that the SGS viscosity should depend on both the initial conditions and the mesh resolution but not on the cell/element types. When analyzing the expression of the SGS viscosity, the model time scale $D_m(\mathbf{u})$ is invariant by definition and the model constant as well. The problem observe when using the volume of the cell as length scale can be explained by considering two HIT simulations (the CBC HIT for example with the static Smagorinsky model. The time scale is of course calculated at the cell level) on a cube of Volume L^3 with N^3 nodes. The first simulation is performed on hexahedral

mesh (SH) and the second one with tetrahedral mesh (ST). Since the initial conditions and the mesh resolution are identical, results should be similar. But this is not the case because the SGS viscosity for the tetrahedral case is systematically lower than the one of the hexahedral mesh when the length scale is based on cells volume. Fig. 3.12 shows a comparison of the resolved kinetic energy decay for cases SH and ST with the length scale either based on the node volume or on the cell volume.

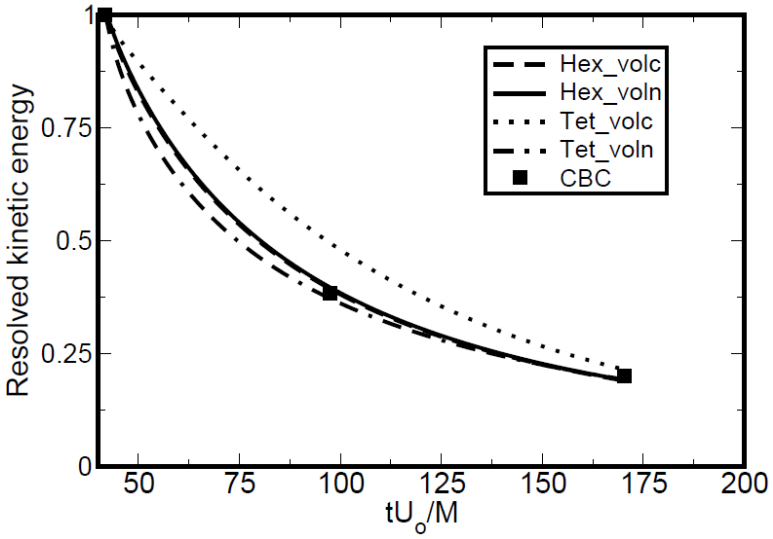

Figure 3.12: Resolved kinetic energy decay for different length scale and mesh type

We can see that the energy is overestimated in the case ST-cell because of the underestimation of the SGS viscosity. This is confirmed in Fig. 3.13 which shows that the SGS viscosity in the case ST-cell can be even 4 times smaller than the SGS viscosity when considering the node volume.

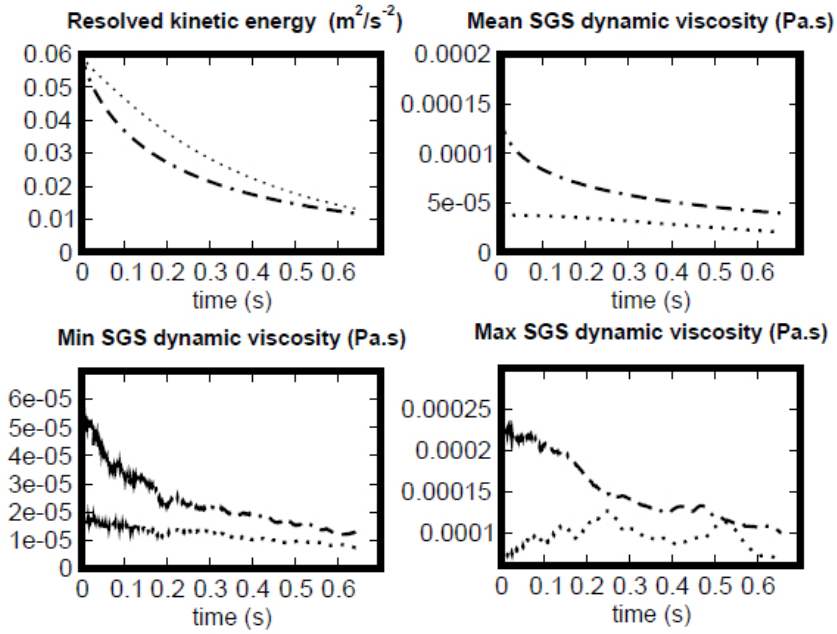

Figure 3.13: Comparison of the CBC simulations between ST with the length scale based on the node volume: dotted line and ST with the length scale based on the cell volume: dotted dashed line

This is not the case for the SH simulations. Indeed, according to Eq. 3.37, the node and the cell volume

are identical on a regular mesh and the simulations of the CBC as well (see Fig. 3.14). Results might be different for an irregular mesh configuration.

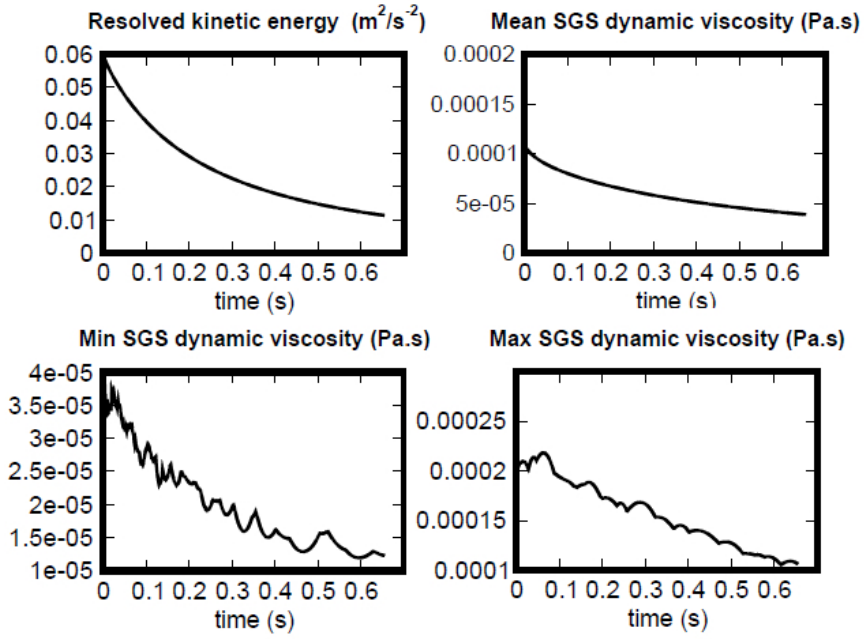

Figure 3.14: Comparison of the CBC simulations between SH with the length scale based on the node volume: thick line and ST with the length scale based on the cell volume: dashed line

A simple way to overcome the mesh type dependency is to define Δ so as to be invariant with respect to the cell/element type. The appropriate choice is the node volume. The latter is directly correlated with the number of nodes and the volume of the geometry and thus less dependent on the type of cells. For the two cases ST and SH the node volume is indeed the same. Fig. 3.12 shows that the SGS viscosity predicted in the cases ST-node and SH-node are quite similar. The resolved kinetic energy decay is also well retrieved with the two meshes. Some little differences appear because of the gradient calculation that is more accurate (also more CPU expensive) on tetrahedral compare to hexahedral.

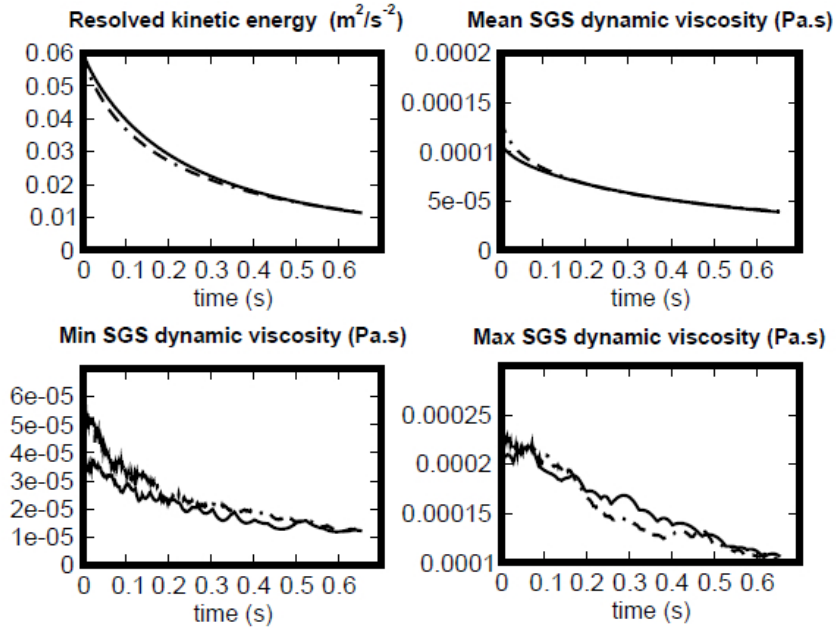

Figure 3.15: Comparison of the CBC simulations between ST with the length scale based on the node volume: dotted dashed line and SH with the length scale based on the node volume: thick line

Explicit filter and test filter width for dynamic models:

Dynamics model require the use of an additional filter known as the test filter. In contrary to the initial filter, the test filter need to be specified. In AVBP, the test filter is defined in two simple steps:

1. An averaging is performed at the cell :

$$\mathbf{w}_{\overline{C}} = \sum_{k \in C} \frac{1}{n_k} w_k \tag{3.46}$$

   where n_k is the number of vertices of the cell.

2. The final filtered quantity $\widehat{\mathbf{w}}_j$ is the volume weighted average of the cell that share the same node j:

$$\widehat{\mathbf{w}}_j = \frac{\sum_{C \in j} \mathbf{w}_{\overline{C}} |C|}{\sum_{C \in j} |C|} \tag{3.47}$$

   The corresponding test filter width at the node j is equal to the sum of the volume cells that share the node j.

$$\widehat{\Delta}_j = \left(\sum_{C \in j} |C| \right)^{1/3} \tag{3.48}$$

   This definition of the test filter and the test filter width allows to deal easily with hybrid meshes and complex geometries.

3.2.3 Others Solvers:

One of the difficulties when developing models is to assess if the model is solver independent. The influence of the numerics in LES is known to be sometimes predominant. As described in the previous section, the main solver AVBP (referred to as solver A) used during this thesis is a general purpose solver. This solver was then used for simulating academic test cases for which very specialized solvers exist. The different collaborations established during the thesis allowed us to test the performances of the developed models with other interesting solvers and to confirm the trends observe with AVBP. Here a short description of those solvers:

- **Solver B** :
  is a finite difference code dedicated to the computation of turbulent channels and developed at the Center for turbulence Research. It is based on a kinetic energy conserving, 4^{th} order scheme in space as proposed by Morinshi et al ref. A 3^{rd} order Runge-Kutta scheme is used for the time integration, except for the diffusion terms in the direction normal to the wall that are integrated thanks to an Cranck-Nickolson scheme. the divergence-free condition is met by a projection scheme. It was used specially to compute a periodic turbulent channel with the dynamic Smagorinsky model as reference model. Note that in contrary to the implementation used in solver A, the dynamic procedure is not applied locally in this case. Instead the Smagorinsky constant is averaged over plans parallel to the walls as followed:

  The presented results were performed by Sanjeeb Bose from Stanford University.

- **Solver C**:
  is a dealiased spectral code developed at Seoul National University. It is based on a 2^{nd} order semi-implicit scheme for time integration: diffusion terms are treated implicitly using the Crank-Nicolson method, and a 3^{rd} order Runge-Kutta scheme is applied to convection terms. The decaying isotropic turbulence from the Comte-Bellot & Corsin experiment ref and Kang et al was performed with this solver. The divergence-free initial field for each experiment was generated using an appropriate re-scaling method.

  The presented results were performed by Jungil Lee from Seoul National University.

- **Solver D**:
  is a pseudo-spectral code developed at the LEGI lab in Grenoble, France. With this tool, the viscous terms are treated exactly using a 2^{nd} order explicit Runge-Kutta time-advancement. A classical two-third rule is used for dealiasing the non-linear convection term. This tool was used to compute periodic plane jet. Several SGS formulations were considered, including the local dynamic Smagorinsky model with clipping and a planewise dynamic Smagorinsky model as it is done in solver B.

  The presented results were performed by Guillaume Balarac from LEGI laboratory in Grenoble.

3.3 An advanced static model: The Sigma model

The literature review performed early during this thesis has highlighted a certain numbers of drawbacks that most of the statics models (more specifically their time scale) share. During years, after the development of the Smagorinsky [135] model, the main issues to overcome was the over-dissipation of this model in shear regions. The Turbulent Channel was probably the best test case to show up this problem. Different methodologies already mentioned in the Introduction part such as damping function [35], dynamic procedure [52], Variational Multi Scale approaches were then developed to turn off the Smagorinsky time scale close to solid boundaries. It is only recently that new operators (referred to as advanced model throughout this thesis): WALE [106] and Vreman's [149] models were developed to naturally vanish in shear regions without any additional procedure. This breakthrough in SGS models was accomplished by using new tensors (different from the strain rate tensor used by Smagorinsky) and was a promising method to extend the use of SGS models to complex applications. However, because most of the efforts was devoted to vanish in shear region, little attention was paid to other canonical flows/simple laminar situations for which no SGS activity is expected neither. This was confirmed by works of Bricteux [18] on rotating flows (more precisely vortices) that showed that the WALE model does not vanish for pure rotating flows. This problem also hold for the Vreman model. The option chosen by Bricteux [18] was to develop a VMS WALE model that is a very interesting model that vanishes both for rotating flows with an appropriate behavior near solid boundaries. This works has also open a new question : Is it possible to develop a new time scale that vanishes for both shear and rotating flows ? More generally can one built a SGS time scale that vanishes for any 2D flows and other well known laminar situations such as pure dilatation and at stagnation point ? The latter question is the purpose of this chapter presented through an article published during the course of this study in the Physics of Fluids journal.

Using singular values to build a subgrid-scale model for Large Eddy Simulations

Franck Nicoud*

CNRS I3M 5149, University Montpellier 2.

Hubert Baya Toda

IFP Energies Nouvelles

Olivier Cabrit

CERFACS, Toulouse, France

Sanjeeb Bose

Center for Turbulence Research, Stanford, California

Jungil Lee

Seoul National University, Korea

(Dated: July 11, 2011)

Abstract

An eddy-viscosity based, subgrid-scale model for Large Eddy Simulations is derived from the analysis of the singular values of the resolved velocity gradient tensor. The proposed σ-model has by construction the property to automatically vanish as soon as the resolved field is either two-dimensional or two-component, including the pure shear and solid rotation cases. In addition, the model generates no subgrid-scale viscosity when the resolved scales are in pure axisymmetric or isotropic contraction/expansion. At last, it is shown analytically that it has the appropriate cubic behavior in the vicinity of solid boundaries without requiring any ad-hoc treatment. Results for two classical test cases (decaying isotropic turbulence and periodic channel flow) obtained from three different solvers with a variety of numerics (finite elements, finite differences or spectral methods) are presented to illustrate the potential of this model. The results obtained with the proposed model are systematically equivalent or slightly better than the results from the Dynamic Smagorinsky model. Still, the σ-model has a low computational cost, is easy to implement and does not require any homogeneous direction in space or time. It is thus anticipated that it has a high potential for the computation of non-homogeneous, wall-bounded flows.

PACS numbers: 47.10.ad, 47.27.ep, 47.27.em, 47.27.N-

* Corresponding author. Electronic address: franck.nicoud@univ-montp2.fr

I. INTRODUCTION

When dealing with Large Eddy Simulations (LES), the eddy-viscosity assumption is by far the most used because it reduces the modeling effort considerably. In this view, the subgrid-scale (SGS) tensor is written as (the implicit summation rule for repeated indices is used throughout this paper):

$$\tau_{ij}^{\mathrm{SGS}} - \frac{1}{3}\tau_{kk}^{\mathrm{SGS}}\delta_{ij} = 2\ \overline{\rho}\ \nu_{\mathrm{SGS}}\left(\widetilde{S}_{ij} - \frac{1}{3}\widetilde{S}_{kk}\delta_{ij}\right), \tag{1}$$

where $\widetilde{S}_{ij} = \frac{1}{2}\left(\widetilde{g}_{ij} + \widetilde{g}_{ji}\right)$ and $\widetilde{g}_{ij} = \partial\widetilde{u}_i/\partial x_j$ are respectively the strain and velocity gradient tensors of the resolved scales. Note that the low pass filter used to define the resolved scales from the total field, denoted by $\overline{f}$ and used to define the mass weighted filter $\widetilde{f} = \overline{\rho f}/\overline{\rho}$, will be omitted throughout this paper for simplicity. Equation 1 then reduces to:

$$\tau_{ij}^{\mathrm{SGS}} - \frac{1}{3}\tau_{kk}^{\mathrm{SGS}}\delta_{ij} = 2\ \rho\ \nu_{\mathrm{SGS}}\left(S_{ij} - \frac{1}{3}S_{kk}\delta_{ij}\right). \tag{2}$$

From a simple dimensional analysis, it is natural to model the subgrid-scale viscosity as

$$\nu_{\mathrm{SGS}} = \left(C_m\Delta\right)^2 \mathcal{D}_m(\mathbf{u}), \tag{3}$$

where C_m is the model constant, Δ is the subgrid characteristic length scale (in practice the size of the mesh), and $\mathcal{D}_m$ is a differential operator associated with the model, homogeneous to a frequency and acting on the resolved velocity field $\mathbf{u} = (u_i)$. The most classical operator is by far the strain rate; this leads to the Smagorinsky model [1] for which $\mathcal{D}_m = \mathcal{D}_s = \sqrt{2S_{ij}S_{ij}}$ and $C_m = C_s \approx 0.18$. This operator is known for not vanishing in near-wall regions. In the past, this major drawback motivated the use of damping functions [2], the development of the dynamic procedure [3] and other improvements such as the shear-improved Smagorinsky model [4] where the magnitude of the mean shear is assessed and removed from the local shear. It is actually possible to build invariants which do not have this drawback. Examples of such operators are used in the WALE (Wall Adapting Local Eddy viscosity) [5] and Vreman's models [6]. For these formulations, the differential operators read respectively:

$$\mathcal{D}_m = \mathcal{D}_w = \frac{\left(\mathcal{S}_{ij}^d\mathcal{S}_{ij}^d\right)^{3/2}}{\left(S_{ij}S_{ij}\right)^{5/2} + \left(\mathcal{S}_{ij}^d\mathcal{S}_{ij}^d\right)^{5/4}} \tag{4}$$

and

$$\mathcal{D}_m = \mathcal{D}_v = \sqrt{\frac{G_{11}G_{22} - G_{12}^2 + G_{11}G_{33} - G_{13}^2 + G_{22}G_{33} - G_{23}^2}{g_{ij}g_{ij}}}, \tag{5}$$

where $G_{ij} = g_{ki}g_{kj}$ and $\mathcal{S}^d_{ij}$ is the traceless symmetric part of the square of the velocity gradient tensor:

$$\mathcal{S}^d_{ij} = \frac{1}{2}\left(g^2_{ij} + g^2_{ji}\right) - \frac{1}{3}g^2_{kk}\delta_{ij}, \qquad \text{with} \qquad g^2_{ij} = g_{ik}g_{kj}.$$

Note that $\mathbf{g}$ is not symmetric so that $\mathbf{G}$ (of component $g_{ki}g_{kj}$) and $\mathbf{g}^2$ (of component $g_{ik}g_{kj}$) are two distinct tensors. The interesting common property shared by these two operators is that they generate zero SGS viscosity in the case of a pure shear. However, they both do not vanish in the particular case of a solid rotation (see discussion in section II D). The situation is the opposite for the Smagorinsky model which vanishes for pure rotation but not for pure shear. Thus, none of these models is satisfying since one could expect that a proper model generates zero SGS viscosity for both the pure shear and the solid rotation cases.

Independently on the properties of the underlying differential operator, all the models based on the eddy-viscosity assumption, Eq. (3), share the drawback that the model constant C_m must be adapted to the mesh refinement so that the proper amount of energy is drained from the resolved scales. This issue is well addressed by the introduction of the dynamic procedure [3] that can automatically adapt the model constant. Besides, because the existing static eddy-viscosity based models miss some desirable properties, many treatments (connected or not to the dynamic procedure) have been proposed over the years in order to improve their performances : one can cite among many others Porté-Agel *et al.* [7] who proposed a double filtering procedure for removing the scale-invariance assumption usually made for computing the model constant from the dynamic procedure; Hughes *et al.* [8] who proposed the Variational Multi-Scale (VMS) methodology where only the smallest resolved scales are directly affected by the SGS viscosity; Jeanmart and Winckelmans [9] who proposed a regularized version of the VMS approach for use in the physical space and Bricteux *et al.* [10] who subsequently used the WALE operator in order to obtain a Regularized Variational Multiscale model with the proper near-wall behavior (RVM-WALE model); Shi *et al.* [11] who added a constraint on the modeled SGS energy flux to better represent the overall dissipation; Lodato *et al.* [12] who developed a scale similarity [13] version of the WALE model, using ideas introduced originally to improve the Smagorisnky model [14].

Following the framework of Lilly [15], the model constant from the dynamic procedure is

computed resorting to a least squares approach as :

$$(C_m\Delta)^2 = -\frac{L_{ij}M_{ij}}{2M_{ij}M_{ij}}, \tag{6}$$

where $L_{ij} = \widehat{u_i\ u_j} - \widehat{u_i}\ \widehat{u_j}$ is the (modified) Leonard term based on the grid-based filter (which is omitted for clarity, $u_i = \widetilde{u_i}$) and test filter $\widehat{\cdot}$. In addition, M_{ij} is directly related to the differential operator of the underlying eddy-viscosity model and reads:

$$M_{ij} = \frac{\widehat{\Delta}^2}{\Delta^2}\widehat{\mathcal{D}_m}\widehat{S_{ij}}\ -\ \widehat{\mathcal{D}_m\ S_{ij}},$$

where $\widehat{\Delta}$ stands for the test filter width. Unfortunately, the original dynamic procedure most often requires some averaging in order to reduce the constant variability over space and time. Several improved versions of the dynamic Smagorinsky model were proposed in order to make it more robust and suitable for complex configurations where no homogeneous directions are present [16, 17]. Still, a common practice when dealing with complex geometries is to apply the least mean square formula over a small volume surrounding the current grid point and to clip the remaining negative values of the dynamically computed constant. This means replacing Eq. (6) by

$$(C_m\Delta)^2 = \max\left[-\frac{\langle L_{ij}M_{ij}\rangle_{\text{loc}}}{2\,\langle M_{ij}M_{ij}\rangle_{\text{loc}}}, 0\right], \tag{7}$$

where $\langle\cdot\rangle_{\text{loc}}$ stands for an integral taken over a small volume (typically a few grid cells) surrounding the current grid point. Note that the model constant then depends on both space and time.

The main motivation of the local dynamic procedure was to adapt the constant to compensate the non-vanishing behavior of the Smagorinsky model in near-wall regions. Recently, Ghorbaniasl & Lacor [18] proposed to extend the dynamic procedure to the WALE model. However, Baya Toda *et al.* [19] reported that the combination of the classical dynamic procedure with any SGS model that has the proper near-wall cubic behavior leads to a paradox: the underlying differential operator rapidly goes to zero near solid boundaries, which favors unstable computations. For the sake of robustness while keeping an adaptation of the model coefficient to the grid resolution and numerical errors, two concepts of global dynamic procedure emerged from the properties of the Vreman's model. The first one is based on the global equilibrium hypothesis [20] and was proposed by Park *et al.* [21] and later improved

by You & Moin [22]. The second one, based on the Germano identity, was also proposed in [21] and recently proved to be better suited for transient flows [23]. This global dynamic procedure amounts to change Eq. (6) to:

$$(C_m\Delta)^2 = -\frac{\langle L_{ij}M_{ij}\rangle_{\text{dom}}}{2\,\langle M_{ij}M_{ij}\rangle_{\text{dom}}}, \tag{8}$$

where $\langle\cdot\rangle_{\text{dom}}$ stands for an averaging over the whole computational domain; the model constant is then uniform over space by construction. It has the advantage of producing mostly positive values for the dynamic constant, thus avoiding the clipping issue. The price to pay is that the differential operator $\mathcal{D}_m$ must behave appropriately in basic flow configurations because no compensation from the dynamic procedure can be expected (the constant of the model is uniform over space). For example, such procedure is not expected to provide good results if applied to the Smagorinsky model since the eddy-viscosity would then not vanish near solid walls. The differential operators used in the WALE and Vreman models are not very appropriate either. For example, it can be shown analytically that the latter is linear with respect to the distance to solid boundaries instead of having a cubic behavior in near-wall regions. Also, they both produce non zero eddy-viscosity in simple flow configurations such as solid rotation.

From the previous discussion, Large Eddy Simulations of complex flows would benefit from the knowledge of a static SGS model with better intrinsic properties than existing formulations. Such model could be used either directly or as a first step for subsequent improvements based on the scale similarity concept, the Variational Multi-Scale framework or a (global) dynamic procedure. The objective of this paper is to propose such a static, eddy-viscosity model with improved properties. The differential operator which is used to define this model is described in section II where analytical developments are provided in order to establish the unique properties met by the proposed static SGS model. Numerical results for decaying isotropic turbulence and a periodic channel flow are shown in section III in order to illustrate the potential of the model.

II. A SINGULAR VALUES BASED MODEL

It would be a difficult task to establish a definite list of the desirable properties that an improved differential operator should meet. One can however draw up a set of properties

based on basic practical/physical considerations. Similar to the Smagorinsky, WALE and Vreman's models, the operator should be defined locally, involving only local gradients of the resolved velocity field. Such property is useful both in terms of implementation in general purpose LES solvers and in terms of physical interpretation of the results. Any non-local effect would most probably require the computation of two-point correlations which are not easy to compute in complex flows. Moreover, it is desirable that the differential operator generates only positive values. Although negative values can be justified from a physical point of view by referring to the backscatter phenomenon, positiveness is required in this study for stability reasons. This choice was made after the observation that the local dynamic procedure, which may lead to negative SGS viscosity, Eq. (6), suffers from stability issues in complex flow configurations where averaging over homogeneous directions is not an option. Besides, it is commonly accepted that the main objective of any (eddy-viscosity based) SGS model is to drain the proper overall amount of kinetic energy from the resolved velocity scales. To this end, a positive eddy-viscosity is most probably appropriate. In what follows, positiveness and locality will be collectively referred to as **Property P0**.

Similar to the WALE and Vreman's models, the differential operator should tend to zero in near-wall regions in order to mimic the turbulence damping due to the no-slip condition. It can be shown that the turbulent stress, thus the eddy-viscosity and the differential operator, should decay as the distance to the solid boundary to the third power [24] [**Property P1**]. At the same time, it should vanish in the case of a flow in solid rotation, like the Smagorinsky model, and in the case of a pure shear, like the WALE and Vreman models. More generally, the improved differential operator should be zero for any two-dimensional (2D) and/or two-component (2C) flows, where no subgrid scale activity is expected to occur [**Property P2**]. Indeed, although two-dimensional turbulence has been evidenced experimentally and numerically [25], it is a phenomenon of fundamental interest that "might [...] be viewed as just a toy model" [26]. Given that two- and three-dimensional turbulence are fundamentally different because of the absence of the vortex-stretching term in the former, it seems appropriate to make sure that any SGS model for three-dimensional turbulence switches off in the two-dimensional case. The alternative would be to switch to a SGS model appropriate for two-dimensional turbulence. Still, given the very little probability that a three-dimensional computation of a two-dimensional turbulent flow remains two-dimensional without any external action to maintain its two-dimensionality, this choice

Property name	Short Description
P0	a positive quantity which involves only locally defined velocity gradients
P1	cubic behavior near solid boundaries
P2	zero for any two-component or two-dimensional flows
P3	zero for axisymmetric or isotropic expansion/contraction

TABLE I. Desirable properties for an improved SGS viscosity model. In the case of a static model, these properties should be met by the differential operator ($\mathcal{D}_m$) the model is based on.

is not made in this paper. Another way to justify property **P2** is to argue that 2D or 2C resolved scales are not compatible with a subgrid-scale activity. Indeed, since the smallest resolved scales interact with subgrid scales which are presumably random-like and 3D/3C, they cannot remain 2D or 2C in the long run. The same reasoning leads to the conclusion that the SGS viscosity should be zero in the case where the resolved scales are either in pure axisymmetric or isotropic expansion (or contraction) [**Property P3**]. The former case corresponds to the situation of a laminar round jet impinging on a solid plate for which turbulent effect should indeed not be present. The latter is representative of the velocity field near an acoustic monopole or a spherical premixed flame, which again are not phenomena of turbulent nature. The desirable properties are recalled in Table I. Since they do not come from any mathematical theory of turbulence or fluid mechanics, we do not claim that they constitute a set of necessary and sufficient conditions that any SGS model should meet. Still, they seem *desirable* from a physical/numerical point of view as discussed above.

A. Meeting Properties P2-P3

Analyzing the spectral content of the velocity gradient tensor proves to be a proper framework to investigate how these properties can be met by a single differential operator. For example, the fact that one of the eigenvalues of $\mathbf{g}$ is zero would indicate that the flow is locally either 2D or 2C. Note, however, that the eigenvalues of $\mathbf{g}$ can be complex-valued in number of flow configurations (in the case of a solid rotation, for example). Using these quantities directly to build the differential operator $\mathcal{D}_m$ would thus not be very convenient. One way to avoid this difficulty is to consider the strain rate tensor instead of $\mathbf{g}$. In this

case, the three eigenvalues are real-valued, although their sign is not known a priori. This route was explored recently [27, 28]. In the present study, one relies on the singular values of $\mathbf{g}$ to build an improved differential operator for the SGS eddy viscosity. Specifically, let us introduce $\sigma_1 \geq \sigma_2 \geq \sigma_3 \geq 0$, the three singular values of $\mathbf{g} = (g_{ij})$. As discussed in the appendix, these quantities can be computed at moderate computational cost by different means. By definition, these values are always positive and equal the square root of the eigenvalues of the matrix $\mathbf{G} = \mathbf{g}^t\mathbf{g}$, where the superscript t denotes matrix transposition (these eigenvalues are always positive because $\mathbf{G}$ is symmetric semi-definite positive). The smallest singular value, σ_3, is null if and only if one row or column of $\mathbf{g}$ is zero up to a rotation of the coordinate system. In other words, $\sigma_3 = 0$ is a marker for two-dimensional and/or two-component flows, and any operator proportional to this singular value would meet property **P2**. Similarly, the knowledge of the singular values of $\mathbf{g}$ helps to detect the case where the resolved velocity field is in axisymmetric contraction or expansion. Indeed, an appropriate rotation of the coordinate system then makes the velocity gradient tensor diagonal:

$$\mathbf{g} = \mathrm{diag}\,(\beta, -\alpha, -\alpha), \tag{9}$$

where α is positive for a contraction and negative for an expansion. Depending on the relative values of the parameters α and β, the singular values of $\mathbf{g}$ read either $\sigma_1 = |\beta| > \sigma_2 = \sigma_3 = |\alpha|$ or $\sigma_3 = |\beta| < \sigma_1 = \sigma_2 = |\alpha|$. In other words, the marker for such flow situations is either $\sigma_2 = \sigma_3$ or $\sigma_1 = \sigma_2$. Thus, any differential operator proportional to $(\sigma_1 - \sigma_2)(\sigma_2 - \sigma_3)$ would be zero as soon as the resolved velocity field is in axisymmetric contraction/expansion. The same operator would also be zero for any isotropic configuration since this situation corresponds to $\sigma_1 = \sigma_2 = \sigma_3$. At the end, such operator would meet property **P3**. Note that the divergence-free assumption was not made to obtain the above results (β not necessarily equal to 2α).

B. Near wall behavior

From the above analysis, a differential operator proportional to $\sigma_3(\sigma_1-\sigma_2)(\sigma_2-\sigma_3)$ would meet both properties **P2** and **P3**. It is now time to investigate whether property **P1** is also met. This requires analyzing the asymptotic behavior of the singular values in the vicinity of a solid boundary. Without loss of generality, one may decide that this boundary is located

within the (x_1, x_3)=(x, z) plane; the normal direction to this boundary then coincides with the $x_2 = y$ direction. Using Taylor expansions of the resolved velocity components (recall u_i must be understood as $\widetilde{u}_i$):

$$\begin{aligned} u_1 &= ay + O(y^2), \\ u_2 &= by^2 + O(y^3), \\ u_3 &= cy + O(y^2) \end{aligned} \tag{10}$$

leads to the following expression for the velocity gradient tensor:

$$\mathbf{g} = \begin{bmatrix} a_x y + O(y^2) & a + O(y) & a_z y + O(y^2) \\ b_x y^2 + O(y^3) & 2by + O(y^2) & b_z y^2 + O(y^3) \\ c_x y + O(y^2) & c + O(y) & c_z y + O(y^2) \end{bmatrix} \tag{11}$$

In these expressions, $O(y^p)$ denotes a term of order p which behaves like y^p when the distance to the solid boundary vanishes, $y \longrightarrow 0$. Moreover, subscripts denote partial derivatives (e.g.: $a_x = \partial a/\partial x$). For sake of simplicity, the first order term in the expansion of the wall normal velocity component has been zeroed. From the continuity equation, the coefficient of the neglected linear term equals

$$\left.\frac{1}{\rho}\frac{\partial \rho}{\partial t}\right|_{y=0}$$

since the no-slip condition imposes $\partial u_1/\partial x = \partial u_3/\partial z = 0$ at $y = 0$. This writing is thus strictly valid in the incompressible case and most probably well justified for flows bounded by walls submitted to stationary isothermal conditions and/or for compressible flows in the low subsonic regime.

By definition, the singular values of $\mathbf{g}$ are the square roots of the eigenvalues of $\mathbf{G} = \mathbf{g}^t\mathbf{g}$. Denoting by $\lambda_1 \geq \lambda_2 \geq \lambda_3 \geq 0$ these eigenvalues, they are the roots of the characteristic polynomial of $\mathbf{G}$:

$$P(\lambda) = -\lambda^3 + \mathcal{I}_1\lambda^2 - \mathcal{I}_2\lambda + \mathcal{I}_3, \tag{12}$$

where the coefficients read:

$$\begin{aligned} \mathcal{I}_1 &= \mathrm{tr}(\mathbf{G}), \\ \mathcal{I}_2 &= \frac{1}{2}\left(\mathrm{tr}(\mathbf{G})^2 - \mathrm{tr}(\mathbf{G}^2)\right), \\ \mathcal{I}_3 &= \det(\mathbf{G}), \end{aligned} \tag{13}$$

with tr() and det() denoting the trace and the determinant of a tensor. A classical result of linear algebra is that the coefficients of Eq. (12) are tensorial invariants (they keep the same values in every coordinate system). In particular, they can be assessed either in the (x, y, z) coordinate system where $\mathbf{G}$ reads:

$$\mathbf{G} = \begin{bmatrix} (a_x^2 + c_x^2)y^2 + O(y^3) & (aa_x + cc_x)y + O(y^2) & (a_x a_z + c_x c_z)y^2 + O(y^3) \\ (aa_x + cc_x)y + O(y^2) & (a^2 + c^2) + O(y) & (aa_z + cc_z)y + O(y^2) \\ (a_x a_z + c_x c_z)y^2 + O(y^3) & (aa_z + cc_z)y + O(y^2) & (a_z^2 + c_z^2)y^2 + O(y^3) \end{bmatrix} \tag{14}$$

or in the principal axis where $\mathbf{G}$ is simply:.

$$\mathbf{G} = \begin{bmatrix} \lambda_1 & & \\ & \lambda_2 & \\ & & \lambda_3 \end{bmatrix} \tag{15}$$

In this latter case, the invariants are given by:

$$\begin{aligned} \mathcal{I}_1 &= \lambda_1 + \lambda_2 + \lambda_3, \\ \mathcal{I}_2 &= \lambda_1\lambda_2 + \lambda_1\lambda_3 + \lambda_2\lambda_3, \\ \mathcal{I}_3 &= \lambda_1\lambda_2\lambda_3. \end{aligned} \tag{16}$$

Then, using Eq. (13) to calculate the same invariants from Eq. (14) allows obtaining the following estimates:

$$\begin{aligned} \lambda_1 + \lambda_2 + \lambda_3 &= O(y^0), \\ \lambda_1\lambda_2 + \lambda_1\lambda_3 + \lambda_2\lambda_3 &= O(y^2), \\ \lambda_1\lambda_2\lambda_3 &= O(y^6). \end{aligned} \tag{17}$$

A rapid examination of Eq. (14) may lead to the erroneous conclusion that the determinant of $\mathbf{G}$ should be of order y^4 instead of y^6 as reported in Eq. (17). Actually, it can readily be shown that the y^4 and y^5 terms in the Taylor expansion of $\det(\mathbf{G})$ are exactly zero. Since $\mathbf{G} = \mathbf{g}^t\mathbf{g}$ and $\det(\mathbf{G}) = \det(\mathbf{g}) \times \det(\mathbf{g})$, the 6^{th} order behavior reported in Eq. (17) is also consistent with the estimate $\det(\mathbf{g}) = O(y^3)$ which comes directly from Eq. (11). With the convention $\lambda_1 \geq \lambda_2 \geq \lambda_3$, the first equality in Eq. (17) imposes that $\lambda_1 = O(y^0)$ and the second and third rows imply:

$$\begin{aligned} \lambda_2 + \lambda_3 + \lambda_2\lambda_3 &= O(y^2), \\ \lambda_2\lambda_3 &= O(y^6). \end{aligned} \tag{18}$$

Injecting the second row of Eq. (18) into the first implies $\lambda_2 + \lambda_3 = O(y^2)$ which imposes $\lambda_2 = O(y^2)$ since $\lambda_2 \geq \lambda_3$ by convention. At last, the second row of Eq. (18) then leads to $\lambda_3 = O(y^4)$. Eventually, since the singular values of $\mathbf{g}$ are the square roots of the λ's, one obtains the following estimates in the near wall region:

$$\begin{aligned} \sigma_1 &= O(y^0), \\ \sigma_2 &= O(y^1), \\ \sigma_3 &= O(y^2) \end{aligned} \tag{19}$$

C. The σ-model

Eqs. 19 indicate that the product $\sigma_3(\sigma_1 - \sigma_2)(\sigma_2 - \sigma_3)$ selected to meet properties **P2** and **P3** is of order $O(y^3)$ near solid boundaries and thus meets property **P1**. The derivation of the differential operator is finished by choosing a scaling factor so that a frequency scale is obtained. A natural choice is the use of the largest singular value σ_1, which is nothing but the norm of $\mathbf{g}$, and which would not change the asymptotic behavior of the ratio since of order y^0. Finally, the proposed differential operator and related SGS model read

$$\begin{aligned} \mathcal{D}_\sigma &= \frac{\sigma_3(\sigma_1 - \sigma_2)(\sigma_2 - \sigma_3)}{\sigma_1^2}, \\ \nu_{\text{SGS}} &= (C_\sigma \Delta)^2 \, \mathcal{D}_\sigma \end{aligned} \tag{20}$$

Since the three singular values are ordered such that $\sigma_1 \geq \sigma_2 \geq \sigma_3 \geq 0$, this model is positive by construction. Besides, it involves only combinations of the locally defined velocity gradient tensor and thus meets property **P0**. It will be referred to as the *σ-model* in the remaining of this paper.

D. Discussion

Table II summarizes the properties of different differential operators and associated models. From Eqs. 5 and 13, one may note that the Vreman's model is proportional to $\sqrt{\mathcal{I}_2}$. Recalling that $\mathcal{I}_2$, the second invariant of $\mathbf{G}$, is quadratic in y (see Eq. 17), the asymptotic behavior of the Vreman's model is linear in y instead of being cubic. Thus, only the WALE and σ models comply with property **P1** (as well as any model based on the corresponding

differential operator, e.g. the RVM-WALE model of [10]). Note however that the first order behavior of the Vreman's model is enough to make it more suitable for wall-bounded flows than the Smagorinsky model for which the eddy-viscosity does not tend to zero because $\mathcal{D}_s = O(y^0)$. Table II also shows that the σ-model meets properties **P2**-**P3**, contrary to the other formulations which all fail at some point. It also shares with the three other models the property to involve only locally defined velocity gradients and is thus easy to implement in any general purpose LES solver. For the Smagorinsky model, it is possible to obtain an asymptotic value of the C_s constant by assuming an isotropic homogeneous turbulence at infinite Reynolds number and a grid-cutoff lying into the inertial range. Lilly [29] then found $C_s = (2/3C_K)^{3/4}/\pi$ which leads to $C_s \approx 0.165$ if assuming the $C_K \approx 1.6$ for the Kolmogorov constant. Unfortunately, such theoretical analysis cannot be conducted for the other SGS models and the model constants are usually obtained from numerical experiments. The value reported for the model constant, $C_\sigma \approx 1.35$, is a rough assessment generated by equating the averaged SGS dissipation obtained by feeding the Smagorinsky model and Eq. (20) with a large sample of random velocity gradient tensors. Interestingly, this crude random procedure used to provide a first assessment of C_σ leads to fair estimates of the WALE and Vreman's constants [$C_w \approx 0.57$ and $C_v \approx 0.26$, to be compared with the values recommended by Nicoud and Ducros [5] and Vreman [6] and reported in Table II]. Besides, computations of decaying isotropic turbulence confirm this value, as discussed in section III.

III. NUMERICAL EXPERIMENTS

Two academic configurations were considered in order to test the capability of the proposed SGS model, namely the decaying isotropic turbulence case and the periodic channel flow. In each case, LES results are compared to either experimental or Direct Numerical Simulation (DNS) data. For the channel flow case, the σ-model was also benchmarked against the dynamic Smagorinsky model. At last, in order to make sure that the conclusions drawn in terms of SGS model potential do not depend on a specific numerical method, different solvers were used during the course of this study. The three solvers considered are the following:

Model	Smagorinsky [1]	WALE [5]	Vreman [6]	σ-model Present
Operator	$\sqrt{2S_{ij}S_{ij}}$	Eq. (4)	Eq. (5)	Eq. (20)
Model constant	$C_s \approx 0.165$	$C_w \approx 0.50$	$C_v \approx 0.28$	$C_\sigma \approx 1.35$
P0	YES	YES	YES	YES
Asymptotic	$O(y^0)$	$O(y^3)$	$O(y)$	$O(y^3)$
P1	NO	YES	NO	YES
Solid rotation	0	≈ 0.90	≈ 0.71	0
Pure shear	1	0	0	0
P2	NO	NO	NO	YES
Axisymmetric	≈ 3.46	≈ 0.15	≈ 1.22	0
Isotropic	≈ 2.45	0	1	0
P3	NO	NO	NO	YES

TABLE II. Properties of the SGS models considered. Labels Axisymmetric and Isotropic refer to axisymmetric and isotropic contraction/expansion respectively. The numerical entries in the **P2** and **P3** blocks are the values taken by the differential operators when all the velocity derivatives are zero except: Solid rotation: $du_1/dx_2 = -1$ and $du_2/dx_1 = 1$; Pure shear: $du_1/dx_2 = 1$; Axisymmetric: $du_1/dx_1 = \pm 2$, $du_2/dx_2 = \mp 1$, $du_3/dx_3 = \mp 1$; Isotropic: $du_1/dx_1 = \pm 1$, $du_2/dx_2 = \pm 1$, $du_3/dx_3 = \pm 1$

- **Solver A**: The general purpose AVBP code developed at CERFACS and IFP Energies Nouvelles solves the compressible Navier-Stokes equations. It is based on a cell-vertex formulation and embeds a set of finite element/ finite volume schemes for unstructured meshes [30, 31]; its efficiency and accuracy have been widely demonstrated for flow configurations with [32] or without [33] chemical reaction. In the present study a centered Galerkin finite element method (4^{th} order in space) with a 3^{rd} order Runge-Kutta temporal integration is retained for the investigation of two configurations: the decaying isotropic turbulence from the Comte-Bellot & Corrsin[34] (CBC) experiment and a periodic turbulent channel flow at low subsonic Mach number. These flows were computed with the Dynamic Smagorinsky model and the present static σ-model.

The dynamic procedure was applied locally, without averaging over homogeneous directions. Negative values of the dynamically tuned constant were clipped to ensure stability (see Eq. 7).

- **Solver B**: a finite difference code dedicated to the computation of turbulent channels and developed at the Center for Turbulence Research. It is based on a kinetic energy conserving, 4^{th} order scheme in space as proposed by Morinishi *et al.* (1998)[35]. A 3^{rd} order Runge-Kutta scheme is used for the time integration, except for the diffusion terms in the direction normal to the wall that are integrated thanks to an Crank-Nicholson scheme. The divergence-free condition is met by a projection scheme. It was used to compute a periodic turbulent channel flow case with both the dynamic Smagorinsky model and the present static σ-model. Note that contrary to the implementation used in the general purpose AVBP solver, the dynamic procedure is not applied locally in this case. Instead, the Smagorinsky constant is computed as

$$(C_s\Delta)^2 = -\frac{\langle L_{ij}M_{ij}\rangle_{\text{plane}}}{2\langle M_{ij}M_{ij}\rangle_{\text{plane}}}, \tag{21}$$

  where $\langle\cdot\rangle_{\text{plane}}$ stands for an integral taken over homogeneous planes parallel to the walls of the channel. This avoids clipping while keeping the favorable dependence of the model constant on the distance to the solid boundaries.

- **Solver C**: a dealiased spectral code developed at Seoul National University [23]. It is based on a 2^{nd} order semi-implicit scheme for time integration: diffusion terms are treated implicitly using the Crank-Nicolson method, and a 3^{rd} order Runge-Kutta scheme is applied to convection terms. The decaying isotropic turbulence from the Comte-Bellot & Corrsin [34] and the Kang *et al.*[36] experiments were computed with a dynamic version of the σ-model. The Germano-based global dynamic procedure [21, 23] was used (see Eq. 8), meaning that a single-model constant was computed for the whole domain at each time step. The divergence-free initial field was generated using an appropriate re-scaling method [36].

Note that the σ-model was implemented in other solvers [37], including another general purpose LES solver developed at the CORIA lab (Rouen, France) and a pseudo-spectral solver developed at the LEGI lab (Grenoble, France). Only results from the three solvers

	Solver A	**Solver B**	**Solver C**
Key reference	[30, 31]	[35]	[23]
Spatial scheme	- Fourth-order Galerkin - finite element/finite volume	- Fourth-order - kinetic energy conserving - finite differences	- Dealiased spectral
Time integration	- RK	- RK - CN for diffusion (wall normal)	- RK - CN for diffusion
Dynamic procedure	- local averaging - clipping required - Eq. (7)	- plane averaging - clipping optional - Eq. (21)	- global averaging - no clipping - Eq. (8)

TABLE III. Properties of the solvers A, B and C used to compute the academic cases considered. RK: Third-order Runge-Kutta. CN: Second-order Crank-Nicolson

A-C described above are shown in this paper for sake of simplicity and because the same trends were observed independently on the numerical tools. The main characteristics of the solvers used in the following are gathered in Table III.

A. Isotropic decaying turbulence

We first validate the behavior of the σ-model for the simple case of a freely decaying isotropic homogeneous turbulence. The experiment by Comte-Bellot & Corrsin [34] on decaying turbulence behind a grid is simulated first, where the mesh size of the grid turbulence is $M = 5.08 \times 10^{-2}$ m and the free-stream velocity is $U_0 = 10$ m/s. The Taylor micro-scale Reynolds number is $R_\lambda = u_{rms}\lambda/\nu = 71.6$ at time $tU_0/M = 42$ and decreases to 60.6 at $tU_0/M = 171$. In a reference frame moving with the average flow velocity the

problem can be thought of as freely decaying isotropic turbulence. We model this by considering the fluid to be inside a cube-shaped box with periodic boundary conditions and size $(11M)^3$. The flow was first computed with the general purpose code AVBP (Solver A), where the static σ-model was implemented. Several values of the model constant were tested, $C_\sigma = 1.3; 1.4; 1.5; 1.6; 1.7$, for two grid resolutions, namely 48^3 and 64^3. The corresponding computational mesh size-to-Kolmogorov length scale ratio Δ/η are 40 and 30 respectively. The computations are initialized with a synthetic turbulent field whose energy spectrum is the experimental one at reduced time $tU_0/M = 42$. The time evolutions of the resolved kinetic energy obtained from the 10 simulations (two grid resolutions and 5 constant values) are shown in Figure 1. For the 64^3 grid resolution, the best agreement with experimental data at times $tU_0/M = 98$ and $tU_0/M = 171$ is obtained for $C_\sigma \approx 1.5$ whereas a larger value, in the range $1.6-1.7$ seems more adequate for the 48^3 case. Note that the dependency of the model constant on the grid resolution is a common drawback of all static SGS models (and to a less extend of dynamic models when using very coarse grids) and is not specific to the σ-model (see Cocle *et al.* [38] for a detailed discussion on the dependence of several model constants on Δ/η). Note also that the increase of the model constant with the increase of the Δ/η ratio is coherent with previous studies [38, 39]. Figure 2 (top plot) shows that the computed spectra obtained for $C_\sigma = 1.5$ and the 64^3 grid resolution are in fair agreement with the experimental data. The biggest differences are obtained for the smallest scales; they are most probably due the large numerical errors that characterize finite volume/finite element methods for large wave numbers. To confirm this statement, an additional computation was performed with the spectral Solver C. As shown in Figure 2 (bottom plot), the agreement with the experimental spectra is now very good even for the smallest resolved scales, although the grid resolution was even coarser (32^3, $\Delta/\eta \approx 60$). Note that the global dynamic σ-model was used in this case, as another mean to establish the appropriate C_σ value. More precisely, the global dynamic procedure based on the Germano identity and proposed by Park *et al.*[21] and Lee *et al.*[23] was used in order to compute the constant value (homogeneous in space) at each time step. The time evolution of the dynamically tuned constant is displayed in Figure 3. Because an appropriate re-scaling method [36] was used to generate the initial velocity field at time $tU_0/M = 42$, there is no strong variations of the computed constant during the first instants of the simulation. Moreover, the range of variation of the constant throughout the computation is roughly 1.4-1.7, consistently with

the value suggested by the computations performed with Solver A (fig. 1). To further support this result and make sure that the σ-model can handle demanding LES (with larger Δ/η ratio and Reynolds number), the isotropic decaying turbulence of Kang *et al.*[36] was also simulated. In this case, the mesh size of the experimental grid turbulence is $M = 0.152$ m and the free-stream velocity is $U_0 = 11.2$ m/s. The Taylor micro-scale Reynolds number is $R_\lambda = 716$ at location $x/M = 20$ (or time $tU_0/M = 20$) and decreases to 626 at $x/M = 48$ (or $tU_0/M = 48$). Solver C was used to solve the flow equations in a computational domain of size $(33.7M)^3$ at grid resolution 128^3; this corresponds to a $\Delta/\eta \approx 360$. This computation is thus substantially more challenging than the 32^3 Comte-Bellot & Corrsin case in terms of SGS modeling, with a Reynolds number and Δ/η ratio 10 and 6 times larger respectively. The corresponding time evolution of the dynamically tuned constant is also displayed in Figure 3; it is found to be smaller in this case, close to 1.35. Given the large values of the Reynolds number and Δ/η ratio, it is fair to consider this later value as close to the asymptotic [38] C_σ value to be used for demanding LES ($\Delta/\eta > 100$) of fully turbulent flows; as a matter of fact, $C_\sigma \approx 1.35$ is also the value obtained from the random procedure used in section II D (see Table II).

Despite a larger Δ/η ratio, this value is smaller than the range of values obtained from the Comte-Bellot & Corrsin case at 32^3 grid resolution ($1.4-1.7$). Contrary to what may be erroneously concluded, this behavior is not contradictory with the expected increase [38, 39] of the model constant for increasing Δ/η. Instead, the observed decrease is most probably due to small values taken by the L/Δ ratio, where $L = k^{3/2}/\epsilon$ is the integral length scale based on the total turbulent kinetic energy k and its dissipation ϵ. Recall that the constant of the Smagorinsky model increases strongly with L/Δ when the latter is in the low range, $L/\Delta < 10$ say [40, 41]; the same trend is expected to hold for any eddy-viscosity based subgrid-scale model, although the critical value of L/Δ above which the model constant becomes independent on this ratio may change from one model to the other. Now, given that L/Δ is only 2.6 for the 32^3 Comte-Bellot & Corrsin case while it reaches 13.4 for the case of Kang *et al.* with 128^3 grid resolution, it is expected that the model constant significantly varies due to L/Δ when going from the Comte-Bellot & Corrsin to the Kang's case. In other words, the observed decrease of C_σ most probably results from the Δ/η effect being offset by the L/Δ influence.

The computed spectra at time $tU_0/M = 30$, 40 and 48 are shown in figure 4 together

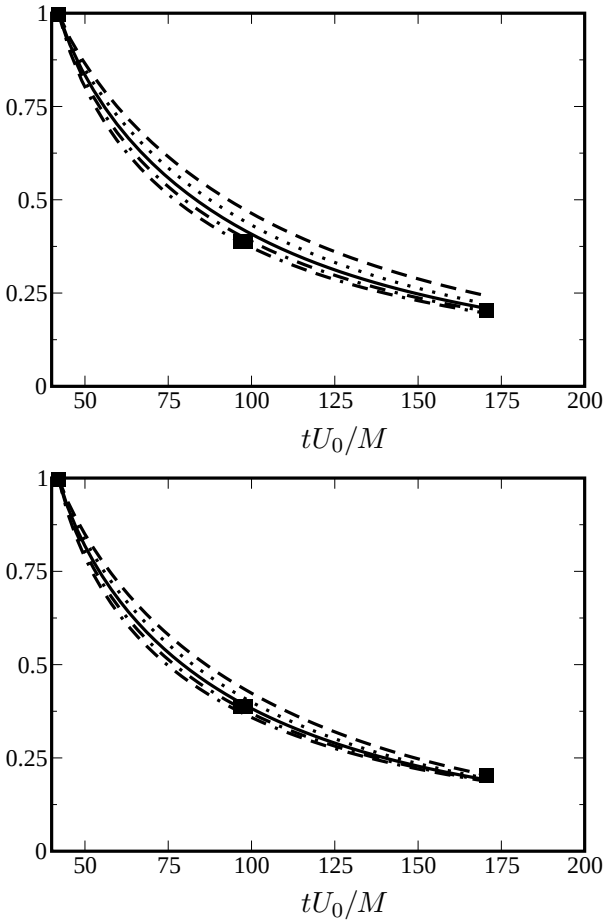

FIG. 1. Time evolutions of the scaled kinetic energy for the freely decaying isotropic turbulence corresponding to the Comte-Bellot & Corrsin [34] experiment. All computations performed with the general purpose solver AVBP (Solver A) and the σ-model with $C_\sigma = 1.3$ (- - -); $C_\sigma = 1.4$ (·····); $C_\sigma = 1.5$ (——); $C_\sigma = 1.6$ (—·—); $C_\sigma = 1.7$ (——·);. Symbols are experimental measurements corresponding to the three-dimensionless times $tU_0/M = 42$, 98 and 171. Top: 48^3 grid resolution. Bottom: 64^3 grid resolution.

with the experimental data [36]. The overall agreement is again quite good for most of the wavenumbers. The energy rise near the largest wavenumber is a well-known behavior for approaches where the same eddy-viscosity is applied to the whole range of scales and has motivated the development of spectral eddy viscosity [42] and multiscale [8, 9] models. From all the results presented in this section, it is fair to propose $1.3 - 1.5$ as a reasonable range of values for the C_σ constant of the σ-model (Eq. 20).

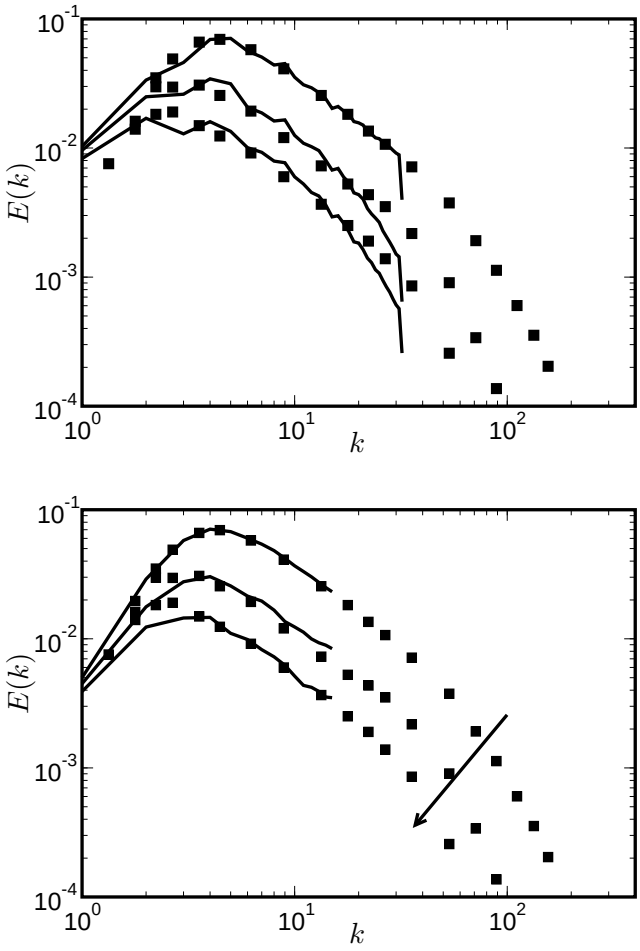

FIG. 2. Time evolutions of energy spectra for the freely decaying isotropic turbulence corresponding to the Comte-Bellot & Corrsin [34] experiment. Symbols are experimental measurements corresponding to the three-dimensionless times $tU_0/M = 42$, 98 and 171. Top: Results from the general purpose solver AVBP (Solver A) with grid resolution 64^3 and $C_\sigma = 1.5$. Bottom: Results from a spectral method (Solver C) with grid resolution 32^3 and a global dynamic procedure applied to the σ-model.

B. Turbulent Channel flow

The performance of the static σ-model for wall-bounded flows was investigated by computing LES of turbulent channel flows at friction Reynolds number $R_\tau = 395$ and 590. As usual, $R_\tau = u_\tau h/\nu$ with u_τ being the friction velocity, h the channel half-height and ν the molecular kinematic viscosity. Two different solvers were used for studying the channel flow configuration, namely solvers A and B (see Table III). For sake of simplicity, only results

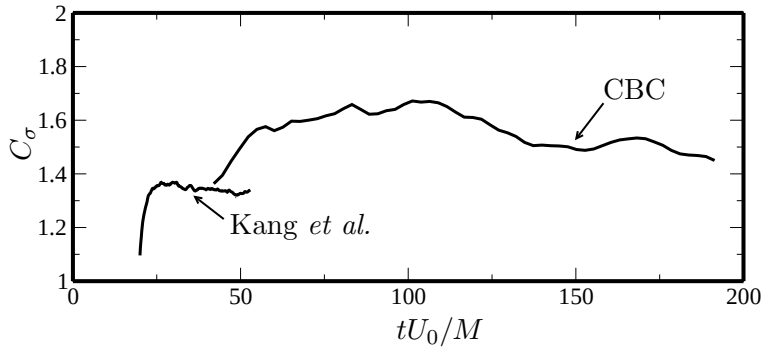

FIG. 3. Time evolution of model constant for the freely decaying isotropic turbulence corresponding to the Comte-Bellot & Corrsin (CBC) [34] and Kang *et al.*[36] experiments. The computation is based on a spectral method (Solver C) and a global dynamic version of the σ-model. Grid resolution is 32^3 and 128^3 respectively.

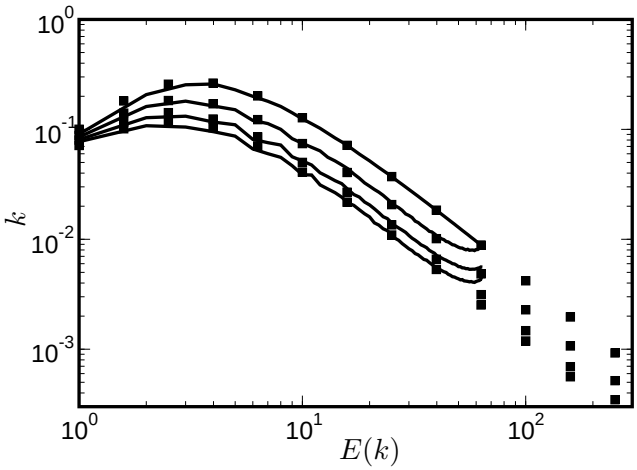

FIG. 4. Time evolutions of energy spectra for the freely decaying isotropic turbulence corresponding to the Kang *et al.*[36] experiment. Symbols are experimental measurements corresponding to the three-dimensionless times $tU_0/M = 20$, 30, 40 and 48. Results are from the spectral Solver C with grid resolution 128^3 and a global dynamic procedure applied to the σ-model.

from Solver A at $R_\tau = 395$ and from Solver B at $R_\tau = 590$ are discussed in the following. Classical values for the size of the computational domain and the grid resolution have been used, as reported in Table IV. Note however that the grid resolution is only marginal for the 590 case, especially in the spanwise direction: $\Delta z^+ \approx 30$ while 20 wall units would be more appropriate for a fair representation of the near-wall elongated structures with a

R_τ	Solver	L_x	L_y	L_z	N_x	N_y	N_z	Δx^+	Δy^+	Δz^+
395	A	3.5	2	1.3	30	138	50	48	$1-17$	10
590	B	6.3	2	3.1	64	64	64	58	$0.7-50$	29

TABLE IV. Properties of the channel flow cases. L_x, L_y and L_z stand for the size of the computational domain in the streamwise, normalwise and spanwise directions and are scaled by the channel half-height h; N_x, N_y and N_z are the corresponding number of grid cells. Grid spacings are given in classical wall units; the mesh is stretched in the y-direction to increase resolution in the near wall regions. R_τ stands for the friction Reynolds number based on the friction velocity and channel half-height.

fourth-order scheme as in Solver B. Additional computations with twice finer spanwise resolution ($\Delta z^+ \approx 15$) with or without refinement in the streamwise direction were performed. The corresponding results (not shown) confirm the good behavior of the σ-model which will be illustrated in the remaining of this section. Besides, in order to properly represent the steep gradients in the viscous and buffer layers, the mesh is stretched in the wall normal direction by using either a geometric progression with common ratio close to 1.04 (Solver A) or an hyperbolic tangent law with stretching parameter close to 2.9 (Solver B). At last, the Δ^2 term in the eddy-viscosity, Eq. (3), was computed as the 2/3-power of the local cell volume. In all cases, statistics were accumulated over more than 10 diffusion times h/u_τ and their convergence was checked by looking at the symmetry of the profiles over the channel height. In each case, the results from the σ-model with $C_\sigma = 1.5$ were compared with the (filtered) DNS data from Moser *et al.*[43]. They were also compared to the results from an implementation of the dynamic Smagorinsky model, as available in each solver (see Table III).

All the LES mean velocity profiles are in good agreement with the reference data from the available DNS, as displayed in Fig. 5. The largest difference is obtained for the $R_\tau = 395$ case computed with solver A and the dynamic Smagorinsky model. This is most probably due to the fact that the Germano identity is applied locally in this general purpose solver (see Table III). To ensure numerical stability, it is then necessary to clip the negative values obtained for the SGS viscosity, using Eq. (7). A closer look at this computation shows that the clipping process is activated for approximately one-third of the constant computations.

It is then not surprising that the overall quality of the results degrades, as observed in Figure 5. On the other hand, when the dynamic procedure is applied planewise, accounting for the homogeneous directions in the channel flow configuration, the clipping operation is virtually never activated. Consistently, the results from the dynamic Smagorinsky model as implemented in the dedicated solver B ($R_\tau = 590$ case) are in very good agreement with the filtered DNS data. Because the σ-model is positive and has the proper near wall behavior, it requires no clipping and the corresponding results are good in both cases. This point is confirmed by Figure 6 which displays the velocity fluctuations. Surprisingly, the situation is opposite to Figure 5, with the overall agreement being better for the $R_\tau = 395$ case. Some kind of modeling/numerical error compensation might be the reason why the dynamic Smagorinsky implementation of solver A gives better results in terms of rms than mean velocity. Interactions between different sources of errors are expected to occur in LES but are out of the scope of this paper. On the other hand, results from the σ-model ($R_\tau = 395$) are just as good as for the mean velocity profile. As far as the $R_\tau = 590$ case is concerned, discrepancies with the filtered DNS data are larger, especially for the rms velocity in the streamwise direction for which the two models considered give equivalent results. Note however that the σ-model leads to some improvement in the profiles of the spanwise and wall normal velocity fluctuations. As expected, a clear improvement was also observed when using a finer mesh in the spanwise direction ($\Delta z^+ \approx 15$ instead of 29 in Fig. 6). The maximum of streamwise rms velocity in then approx. 2.8 wall units, in better agreement with the DNS data (the maximum is approx. 3.1 for $\Delta z^+ = 29$ against 2.7 for the filtered DNS, see Fig. 6).

It is often accepted that the asymptotic behavior of the SGS viscosity in near wall regions is an important factor when dealing with wall resolved LES. Thus, the different computations were post-processed and the resulting behaviors plotted in Fig. 7. The theoretical behavior of the σ-model near solid boundaries ($\nu_{\text{SGS}} = O(y^3)$) is well retrieved numerically. Note that the amount of SGS eddy-viscosity is not negligible in front of the molecular viscosity, at least in the core region. This reflects the fact that the grid resolution is far from what is required to perform DNSs of the same flows (see Table IV). This is illustrated by the no-model calculation performed in the $R_\tau = 590$ case (see figure 5) which shows measurable (although not huge) error compared to the σ-model result (the no-model velocity profile being roughly 5 % smaller than the filtered DNS profile over most of the channel height).

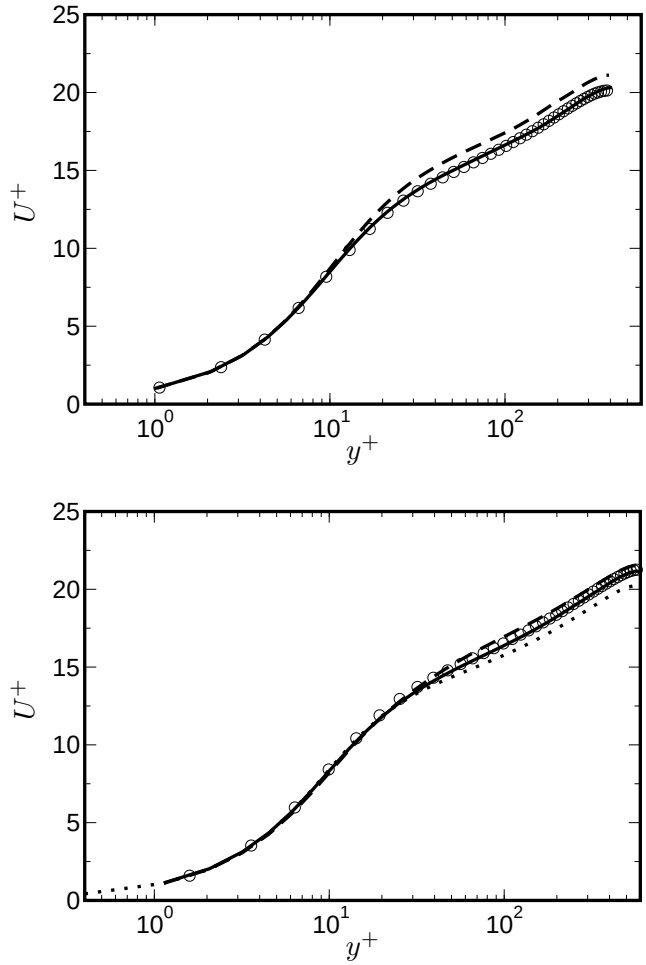

FIG. 5. Mean velocity profile from the static σ-model (——) and the dynamic Smagorinsky model (- - -). Symbols correspond to the filtered DNS data [43]. Top: Results from the general purpose solver AVBP (Solver A) at $R_\tau = 395$. Bottom: Results from the channel code (Solver B) at $R_\tau = 590$. A no-model simulation (·····) is also shown in this latter case.

Another indication of the effectiveness of the SGS contribution is that the no-model computation proved unstable with Solver A which is not kinetic energy conserving, contrary to Solver B. Figure 7 also illustrates that the proper asymptotic behavior is obtained with the dynamic Smagorinsky model only when the plane-wise procedure (Eq. 21) is applied, as for the case $R_\tau = 590$ and Solver B. Recall that this procedure can be used only for simple cases with homogeneous directions. Conversely, the asymptotic behavior is built in the σ-model's differential operator itself and no specific dynamic procedure/homogeneous directions is required.

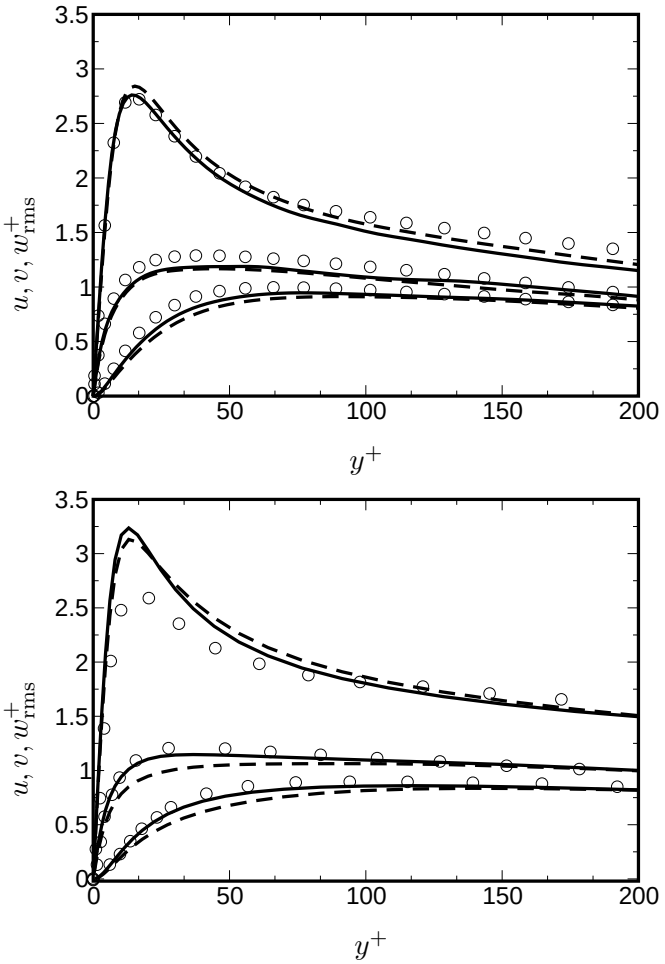

FIG. 6. Velocity fluctuations (rms) from the static σ-model (——) and the dynamic Smagorinsky model (---). Symbols correspond to the filtered DNS data [43]. Top: Results from the general purpose solver AVBP (Solver A) at $R_\tau = 395$. Bottom: Results from the channel code (Solver B) at $R_\tau = 590$.

IV. CONCLUSIONS

A differential operator based on the singular values of the velocity gradient tensor is proposed as a basis for an improved SGS eddy-viscosity model. It is shown that the proposed static σ-model generates zero eddy-viscosity for any two-dimensional or two-component flows, as well as for axisymmetric and isotropic compressions/expansions. It also has the proper cubic behavior in near-wall regions. Implemented in three LES solvers with different numerics, the model gave promising results for two academic configurations. Owing to its unique properties, ease of implementation and low computational cost, it is anticipated that

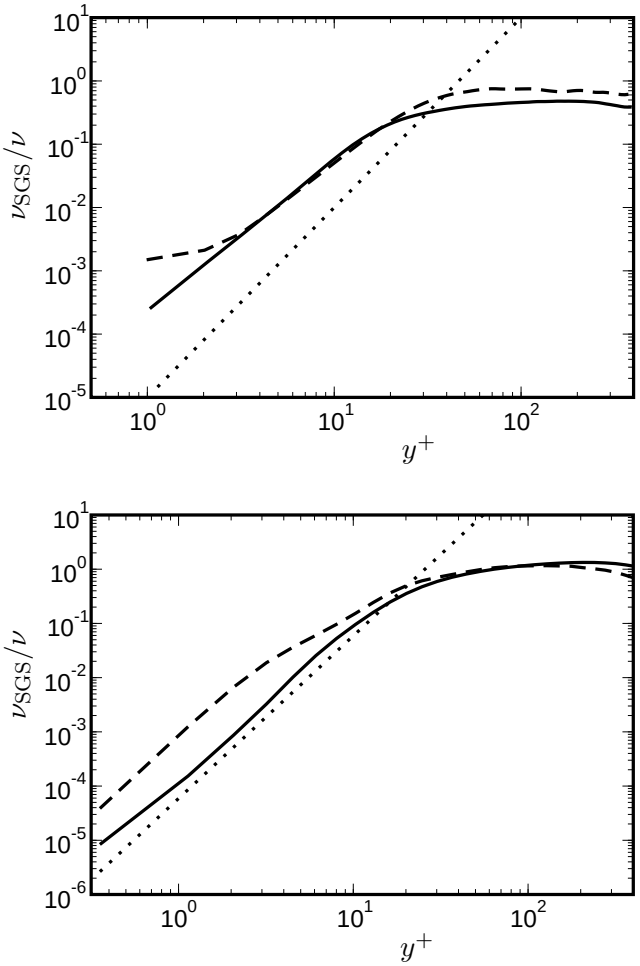

FIG. 7. Scaled SGS eddy-viscosity from the static σ-model (——) and the dynamic Smagorinsky model (---). The dotted lines correspond to the proper y^3 asymptotic behavior. Top: Results from general purpose solver AVBP (Solver A) at $R_\tau = 395$. Bottom: Results from the channel code (Solver B) at $R_\tau = 590$.

the σ-model could be useful in the current effort to make LES even more suitable for complex flow configurations. Notably, it is well suited for any global dynamic procedure which adapts the overall model constant to the grid resolution and numerical errors.

ACKNOWLEDGMENTS

Hubert Baya Toda gratefully acknowledges support from IFP Energies Nouvelles. The authors acknowledge the MRI-R2 award for providing computing resources that have con-

tributed to the research results reported within this paper. This award (Acquisition of a Hybrid CPU/GPU and Visualization Cluster for Multidisciplinary Studies in Transport Physics with Uncertainty Quantification) is funded under the American Recovery and Reinvestment Act of 2009 (Public Law 111-5). The authors also acknowledge CINES and IDRIS of GENCI for giving access to supercomputing facilities. Professors P. Moin and H. Choi are warmly acknowledged for fruitful discussions during the course of the 2010 Summer Program of the Center for Turbulence Research. Dr G. Lodato is thank for his comments on a preliminary version of this paper. At last, the authors are grateful to the anonymous reviewers for their constructive comments regarding the discussion of section III A.

Appendix: Computation of the singular values of g

For each SGS viscosity assessment, the σ-model requires the computation of the three singular values of the local velocity gradient tensor. It is important that this computation is performed both efficiently and accurately. The two following methods were used with success during the course of this study:

- **Method A:** The first idea is to rely on optimized routines of linear algebra as available in scientific libraries as LAPACK. The computation of the σ's is then done in three steps:

  1. build the matrix $\mathbf{G} = \mathbf{g}^t\mathbf{g}$ from the resolved velocity gradient. This 3×3 matrix is symmetric semi-definite positive and its eigenvalues are thus always positive,
  2. compute the eigenvalues of $\mathbf{G}$, for example by using the `SSYEV/DSYEV` routines from LAPACK, and order them so that $\lambda_1 \geq \lambda_2 \geq \lambda_3 \geq 0$,
  3. compute the singular values of $\mathbf{g}$ from $\sigma_1 = \sqrt{\lambda_1}$, $\sigma_2 = \sqrt{\lambda_2}$ and $\sigma_3 = \sqrt{\lambda_3}$.

- **Method B:** This method [44] is self-contained and does not require the use of an external scientific library. It consists in the following steps:

  1. build the matrix $\mathbf{G} = \mathbf{g}^t\mathbf{g}$ from the resolved velocity gradient,

2. compute its invariants as in Eq. (13), namely:

$$\begin{aligned}\mathcal{I}_1 &= \mathrm{tr}(\mathbf{G}),\\ \mathcal{I}_2 &= \frac{1}{2}\left(\mathrm{tr}(\mathbf{G})^2 - \mathrm{tr}(\mathbf{G}^2)\right),\\ \mathcal{I}_3 &= \det(\mathbf{G}),\end{aligned}$$

where the square of $\mathbf{G}$ is $\mathbf{G}^2_{ij} = \mathbf{G}_{ik}\mathbf{G}_{kj}$,

3. compute the following angles from the above invariants:

$$\begin{aligned}\alpha_1 &= \frac{\mathcal{I}_1^2}{9} - \frac{\mathcal{I}_2}{3},\\ \alpha_2 &= \frac{\mathcal{I}_1^3}{27} - \frac{\mathcal{I}_1\mathcal{I}_2}{6} + \frac{\mathcal{I}_3}{2},\\ \alpha_3 &= \frac{1}{3}\arccos\frac{\alpha_2}{\alpha_1^{3/2}},\end{aligned}$$

4. compute the singular values as:

$$\begin{aligned}\sigma_1 &= \left(\frac{\mathcal{I}_1}{3} + 2\sqrt{\alpha_1}\cos\alpha_3\right)^{1/2},\\ \sigma_2 &= \left(\frac{\mathcal{I}_1}{3} - 2\sqrt{\alpha_1}\cos\left(\frac{\pi}{3} + \alpha_3\right)\right)^{1/2},\\ \sigma_3 &= \left(\frac{\mathcal{I}_1}{3} - 2\sqrt{\alpha_1}\cos\left(\frac{\pi}{3} - \alpha_3\right)\right)^{1/2}\end{aligned}$$

From the experience gained during this study, the two above methods give virtually identical results. It is also interested to assess the computational cost related to these computations. Since the σ-model is proposed as an alternative to perform LES in complex geometries, Solver A (the general purpose solver, see Table III) was used for this purpose. Using Method A, the overall computation time required for a 64^3 decaying turbulence case with the σ-model was approximately 10 % larger than what is required with the static Smagorinsky model. Of course, this assessment may depend on the efficiency of the scientific library available on the target computer. Still, given the number of properties met by the σ-model compared to the Smagorinsky one, this extra cost is certainly worth being paid. More interestingly, the extra CPU cost becomes hardly measurable (less than 1 %) when Method B is used to compute the singular values. This method being moreover self-contained (no need for specific scientific libraries), it is certainly the best option to compute the required

singular values.

---

[1] J. Smagorinsky. General circulation experiments with the primitive equations: 1. the basic experiment. *Mon. Weather Rev.* , 91:99–164, 1963.

[2] P. Moin and J. Kim. Numerical investigation of turbulent channel flow. *J. Fluid Mech.* , 118:341–377, 1982.

[3] M. Germano, U. Piomelli, P. Moin, and W. Cabot. A dynamic subgrid-scale eddy viscosity model. *Phys. Fluids* , 3(7):1760–1765, 1991.

[4] E. Lévêque, F. Toschi, L. Shao, and J-P. Bertoglio. Shear-improved Smagorinsky model for large-eddy simulation of wall-bounded turbulent flows. *J. Fluid Mech.* , 570:491–502, 2007.

[5] F. Nicoud and F. Ducros. Subgrid-scale stress modelling based on the square of the velocity gradient. *Flow, Turb. and Combustion* , 62(3):183–200, 1999.

[6] A. Vreman. An eddy-viscosity subgrid-scale model for turbulent shear flow: Algebraic theory and applications. *Phys. Fluids* , 16(10):3670, 2004.

[7] F. Porté-Agel, C. Meneveau, and M. Parlange. A scale-dependent dynamic model for large-eddy simulation: application to a neutral atmospheric boundary layer. *J. Fluid Mech.* , 415:261–284, 2000.

[8] T. J. R. Hughes, L. Mazzei, A. A. Oberai, and A. A. Wray. The multiscale formulation of large eddy simulation: Decay of homogeneous isotropic turbulence. *Phys. Fluids* , 13(2):505–512, 2001.

[9] H. Jeanmart and G. Winckelmans. Investigation of eddy-viscosity models modified using discrete filters: A simplified regularized variational multiscale model and an enhanced field model'. *Phys. Fluids* , 19(055110):1–12, 2007.

[10] L. Bricteux, M. Duponcheel, and G. Winckelmans. A multiscale subgrid model for both free vortex flows and wall-bounded flows. *Phys. Fluids* , 21:105102/1–12, 2009.

[11] Y. Shi, Z. Xiao, and S. Chen. Constrained subgrid-scale stress model for large eddy simulation. *Phys. Fluids* , 20(011701):1:4, 2008.

[12] G. Lodato, L. Vervisch, and P. Domingo. A compressible wall-adapting similarity mixed model for large-eddy simulation of the impinging round jet. *Phys. Fluids* , 21(3):035102, 2009.

[13] J. Bardina, J. H. Ferziger, and W. C. Reynolds. Improved subgrid scale models for large-eddy simulations. *Am. Inst. Aeronaut. Astronaut. J.* , 34:1111–1119, 1980.

[14] Y. Zang, R. L. Street, and J. R. Koseff. A dynamic mixed subgrid-scale model and its application to turbulent recirculating flows. *Phys. Fluids* , 5(12):3186–3196, 1993.

[15] D. K. Lilly. A proposed modification of the germano sub-grid closure method. *Phys. Fluids* , 4(3):633–635, 1992.

[16] S. Ghosal, T. Lund, P. Moin, and K. Akselvoll. A dynamic localization model for large-eddy simulation of turbulent flows. *J. Fluid Mech.* , 286:229–255, 1995.

[17] C. Meneveau, T. Lund, and W. Cabot. A lagrangian dynamic subgrid-scale model of turbulence. *J. Fluid Mech.* , 319:353–385, 1996.

[18] G. Ghorbaniasl and C. Lacor. Sensitivity of SGS models and of quality of LES to grid irregularity. In *J. Meyers et al. (Eds), Quality and Reliability of Large-Eddy Simulations.* Springer Science + Business Media B.V., 2008.

[19] H. Baya Toda, K. Truffin, and F. Nicoud. Is the dynamic procedure appropriate for all SGS models ? In J. C. F. Pereira and A. Sequeira, editors, *V European Conference on Computational Fluid Dynamics, ECCOMAS*, Lisbon, Portugal, 14-17 June 2010.

[20] C. B. Da Silva and O. Metais. On the influence of coherent structures upon interscale interaction in turbulent plane jets. *J. Fluid Mech.* , 473:103–145, 2002.

[21] N. Park, S. Lee, J. Lee, and H. Choi. A dynamic subgrid-scale eddy viscosity model with a global model coefficient. *Phys. Fluids* , 18:125109, 2006.

[22] D. You and P. Moin. A dynamic global-coefficient subgrid-scale eddy-viscosity model for large-eddy simulation in complex geometries. *Phys. Fluids* , 19:065110/1–8, 2007.

[23] J. Lee, H. Choi, and N. Park. Dynamic global model for large eddy simulation of transient flow. *Phys. Fluids* , 22:075106, 2010.

[24] D. Chapman and G. Kuhn. The limiting behavior of turbulence near a wall. *J. Fluid Mech.* , 170:265–292, 1986.

[25] M. Lesieur. *Turbulence in Fluids.* Springer Verlag - 4th edition, 2008.

[26] U. Frisch. *Turbulence: The Legacy of A.N. Kolmogorov.* Cambridge University Press, 1995.

[27] R. Verstappen. When does eddy viscosity restrict the dynamics to large eddies ? In J. C. F. Pereira and A. Sequeira, editors, *V European Conference on Computational Fluid Dynamics, ECCOMAS*, Lisbon, Portugal, 14-17 June 2010.

[28] R. Verstappen, S. Bose, J. Lee H. Choi, and P. Moin. A dynamic eddy-viscosity model based on the invariants of the rate-of-strain. In *Proc. of the Summer Program* , pages 183–192. Center for Turbulence Research, NASA Ames/Stanford Univ., 2010.

[29] D. K. Lilly. The representation of small-scale turbulence in numerical simulation experiments. In *Proceedings of the IBM Scientific Computing Symposium on Environmental Sciences*, Yorktown Heights, USA, 1967.

[30] O. Colin and M. Rudgyard. Development of high-order taylor-galerkin schemes for unsteady calculations. *J. Comput. Phys.* , 162(2):338–371, 2000.

[31] V. Moureau, G. Lartigue, Y. Sommerer, C. Angelberger, O. Colin, and T. Poinsot. Numerical methods for unsteady compressible multi-component reacting flows on fixed and moving grids. *J. Comput. Phys.* , 202(2):710–736, 2005.

[32] O. Cabrit and F. Nicoud. Direct simulations for wall modeling of multicomponent reacting compressible turbulent flows. *Phys. Fluids* , 21(5):055108, May 2009.

[33] S. Mendez and F. Nicoud. Large-eddy simulation of a bi-periodic turbulent flow with effusion. *J. Fluid Mech.* , 598:27–65, 2008.

[34] G. Comte-Bellot and S. Corrsin. Simple eulerian time correlation of full- and narrow-band velocity signals in grid generated, 'isotropic' turbulence. *J. Fluid Mech.* , 48:273–337, 1971.

[35] Y. Morinishi, T. Lund, O. Vasilyev, and P. Moin. Fully conservative higher order finite difference schemes for incompressible flow. *J. Comput. Phys.* , 143(1):90–124, 1998.

[36] H. S. Kang, S. Chester, and C. Meneveau. Decaying turbulence in an active-grid-generated flow and comparisons with large-eddy simulation. *J. Fluid Mech.* , 480, 2003.

[37] H. Baya Toda, O. Cabrit, G. Balarac, S. Bose, J. Lee, H. Choi, and F. Nicoud. A subgrid-scale model based on singular values for les in complex geometries. In *Proc. of the Summer Program* , pages 193–202. Center for Turbulence Research, NASA Ames/Stanford Univ., 2010.

[38] R. Cocle, L. Bricteux, and G. Winckelmans. Scale dependence and asymptotic very high reynolds number spectral behavior of multiscale subgrid models. *Phys. Fluids* , 21:085101/1–12, 2009.

[39] C. Meneveau and T. Lund. The dynamic smagorinsky model and scale-dependent coefficients in the viscous range of turbulence. *Phys. Fluids* , 9(12):3932–3934, 1997.

[40] J. Meyers and P. Sagaut. On the model coefficients for the standard and the variational multi-scale smagorinsky model. *J. Fluid Mech.* , 569:287319, 2006.

[41] J. Meyers, C. Meneveau, and B. Geurts. Error-landscape-based multiobjective calibration of the smagorinsky eddy-viscosity using high-reynolds-number decaying turbulence data. *Phys. Fluids* , 22(12):125106, 2010.

[42] M. Lesieur and O. Metais. New trends in large-eddy simulations of turbulence. *Ann. Rev. Fluid Mech.* , 28:45 – 82, 1996.

[43] R.D. Moser, J Kim, and N.N. Mansour. Direct numerical simulation of turbulent channel flow up to $\mathrm{R}e_\tau = 590$. *Phys. Fluids* , 11(4):943–945, 1999.

[44] K. Hasan, P. Basser, D. Parker, and A. Alexander. Analytical computation of the eigenvalues and eigenvectors in dt-mri. *J. of Magnetic Resonance*, 152:41–47, 2001.

3.4 The global dynamic Sigma model

The development of the sigma time scale was the first step for investigating a model that could be used in IC engines. The road investigated by Germano consisted to start from a crude time scale and then built a dynamic model to meet the local and global requirements of a good SGS model. But the dynamic Smagorinsky model suffers from the need of homogeneous directions that can not be easily identified in complex configurations. In this section another option is presented. It consists in using the Sigma time scale to meet the local properties and then estimate the global dissipation with the constant that is homogeneous in space but can vary in time. This is done as recommended by Lee et al. [81] using the Germano-identity. An important modification is introduced to account for the solid boundaries. One could wonder why the Sigma time scale is not directly combined with the Germano-identity to built a local dynamic σ-model. It will be showed that the combination of an advanced time scale and the local dynamic procedure leads to a model that is not an improvement of the static model thus reinforcing the idea that a global dynamic method should be used for the constant.

3.4.1 Paradox of the local dynamic procedure and advanced time scales:

It might be thought that using time scales that have intrinsic better properties than the Smagorinsky model (such as the WALE, Vreman and the Sigma time scales) for building a dynamic model would necessarily lead to a better model than the dynamic Smagorinsky one. But this is not true specially for wall-bounded flows. Indeed, when looking carefully at Eq.1.84 recalled here:

$$C^2 = -\frac{1}{2}\frac{L_{ij}M_{ij}}{M_{ij}M_{ij}} \tag{3.49}$$

one can observe that the drawback of the Smagorinsky time scale (M_{ij} for the Smagorinsky model's time scale is constant and non zero near solid boundaries but L_{ij} tends to zero) that is not to vanish in the shear region is a real advantage for determining its coefficient. In the contrary, a model that has the skill to vanish near solid boundaries (M_{ij} for advanced model's time scales tend to zero near solid boundaries and L_{ij} as well) is now disadvantaged because its coefficient computation is ill-posed. A simple way to understand this paradox is to consider the following asymptotic behavior for the filtered velocity field u_i using Taylor expansions (assuming that the solid boundary is located within (x,z) where y is the direction perpendicular to the wall):

$$u_1 = ay + O(y^2) \tag{3.50}$$

$$u_2 = by^2 + O(y^3) \tag{3.51}$$

$$u_3 = cy + O(y^2) \tag{3.52}$$

where a, b, c depend on x, z and time. Only the most important components when getting close to solid boundaries are considered. It means M_{ij} and L_{ij} are simplified to M_{12} and L_{12} and are expressed as followed:

$$M_{12} = \tilde{\Delta}^2|\widetilde{D(\tilde{u})}|\tilde{S}_{12} - \Delta^2|\widetilde{D(u)}|S_{12} \tag{3.53}$$

$$L_{12} = \widetilde{u_1 u_2} - \tilde{u}_1 \tilde{u}_2 \tag{3.54}$$

From the expression 3.50, 3.51, 3.52, we have:

$$S_{12} = a + O(y) \tag{3.55}$$

$$u_1 u_2 = acy^3 + O(y^4) \tag{3.56}$$

The expression of the time scale depends on the model used. For the smagorinsky time scale:

$$D^{smag} = \sqrt{2}a + O(y) \tag{3.57}$$

and for the σ-model:

$$D^{\sigma} = fy^3 + O(y^4) \tag{3.58}$$

With the relation Eq. 3.57, Eq. 3.58, Eq. 3.55 and Eq. 3.56 the terms L_{ij}, M_{12}^{smag} and M_{12}^{σ} have the following behavior:

$$M_{12}^{smag} = \tilde{\Delta}^2 \sqrt{2} a^2 - \widetilde{\Delta^2 \sqrt{2} a^2} + O(y) \tag{3.59}$$

$$M_{12}^{\sigma} = \tilde{\Delta}^2 f a y^3 - \widetilde{\Delta^2 f a y^3} + O(y^4) \tag{3.60}$$

$$L_{12} = (\widetilde{ac} - \tilde{a}\tilde{c}) y^3 + O(y^4) \tag{3.61}$$

Then near the wall, the dynamic constant converges to the following expression for the Smagorinsky model:

$$C^{smag} = \frac{(\widetilde{ac} - \tilde{a}\tilde{c}) y^3}{\tilde{\Delta}^2 \sqrt{2} a^2 - \widetilde{\Delta^2 \sqrt{2} a^2}} + O(y^4) \tag{3.62}$$

and for the σ-model:

$$C^{\sigma} = \frac{(\widetilde{ac} - \tilde{a}\tilde{c}) y^3}{\tilde{\Delta}^2 f a y^3 - \widetilde{\Delta^2 f a y^3}} + O(y) \tag{3.63}$$

The latter relation shows that the dynamic constant formally behaves like y^0 near the wall. However, the leading order term in Eq. 3.63 is the ratio of two very small quantities (behaving like y^3) whose numerical

assessment strongly depends on the details of the test filter application and stabilization procedure. This situation is obviously ill-posed numerically and can lead to very large value of the dynamic constant. Fig. 3.16 shows the time evolution of the mean values of the constant and we can see that it converges to a value that is almost twice larger than the expected constant for this test case. Moreover the maximum of the constant can reach very large values as shown on Fig. 3.17.

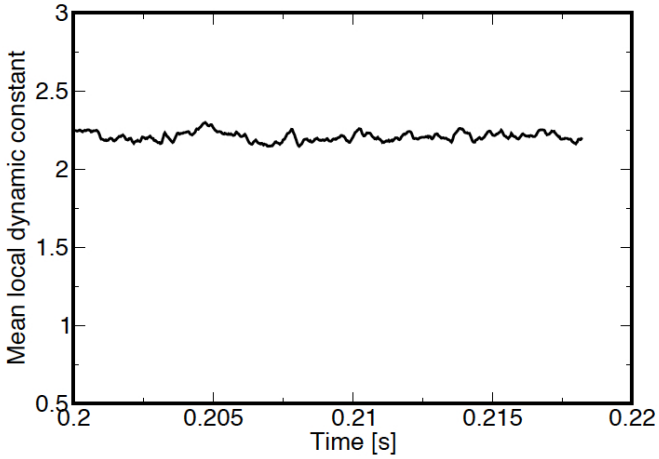

Figure 3.16: Mean value of the local dynamic σ-constant for the channel test case at $Re_\tau = 395$

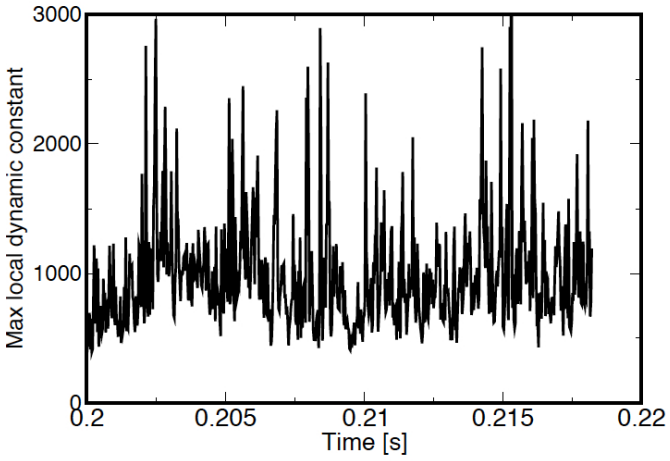

Figure 3.17: Maximum value of the local dynamic Sigma constant for the channel test case at $Re_\tau = 395$

Note that the situation is drastically different when the dynamic procedure is applied to the Smagorinsky model. In this case, the time scale spatial operator behaves like y^0 and the denominator also (see Eq. 3.62). A model with a proper asymptotic behavior seems to be more sensitive to the choice of the filters and the stabilization, specially near the wall. Results obtained showed that in the case of the WALE and the σ-model (see Fig. 3.18), predictions of their local dynamic extension are worst than the simple static model. This issue is discussed in an article (see APPENDIX C) available in the V European Conference on Computational Fluid Dynamics proceeding.

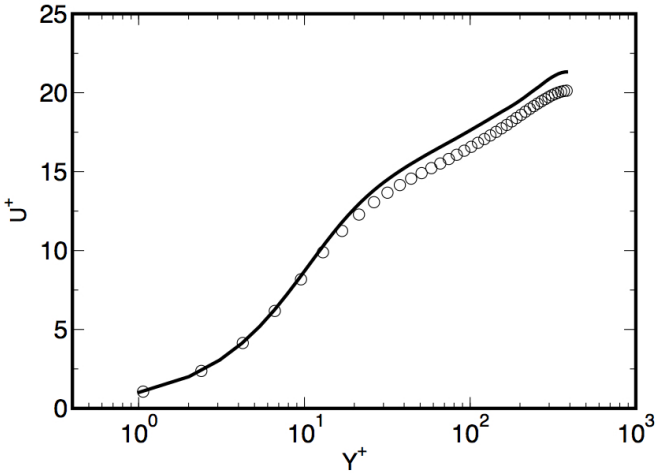

Figure 3.18: Mean velocity obtained with the local dynamic σ-model for the channel test case at $Re_\tau = 395$: (thick line) local dynamic σ-model, (symbols) DNS of Moser *et al.* [99]

3.4.2 The Global dynamic Sigma model:

- **Classic Global dynamic procedure**
  The development of advanced time scales (Vreman and WALE) already mentioned above gives now the possibility to evaluate globally rather than locally the coefficient. Indeed, because they meet several local properties, it remains only necessary to evaluate the proper global dissipation. Two global dynamic [108, 157] procedures are now available and the most efficient according to the study of Lee et al. [81] and easy to implement consists in performing a volume weighted averaging of local values that are obtained through the Germano identity. The resulting coefficient homogeneous in space is then expressed as:

$$C_G^2 = -\frac{1}{2}\frac{< L_{ij} M_{ij}^\sigma >}{< M_{ij}^\sigma M_{ij}^\sigma >} \tag{3.64}$$

  The superscript $()^\sigma$ is for emphasizing that the σ-model's time scale is used in this case. The signs $< >$ stand for the volume weighted averaging. The Global dynamic procedure was already introduced during the development of the static σ-model. Results are very interesting in the case of unbounded flows such as the CBC, the Kang *et al* HIT and the periodic jet perfomed by G. Balarac during the CTR summer Program. Surprisingly, when the global dynamic σ-model is applied for modeling wall-bounded flows such as the turbulent channel, results are not as good as expected. Fig 3.19 and Fig. 3.20 shows respectively the mean velocity and rms velocity predicted.

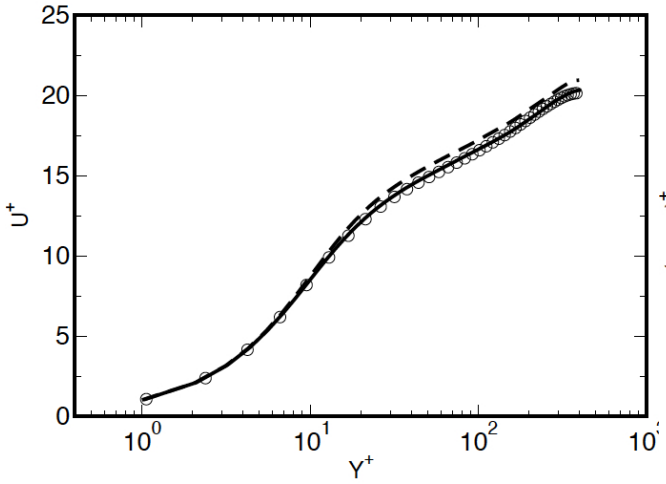

Figure 3.19: Mean Velocity for the channel test case $Re_\tau = 395$: (dashed line) Global σ-model. (thick line) σ-model, (symbols) DNS of Moser *et al.* [99]

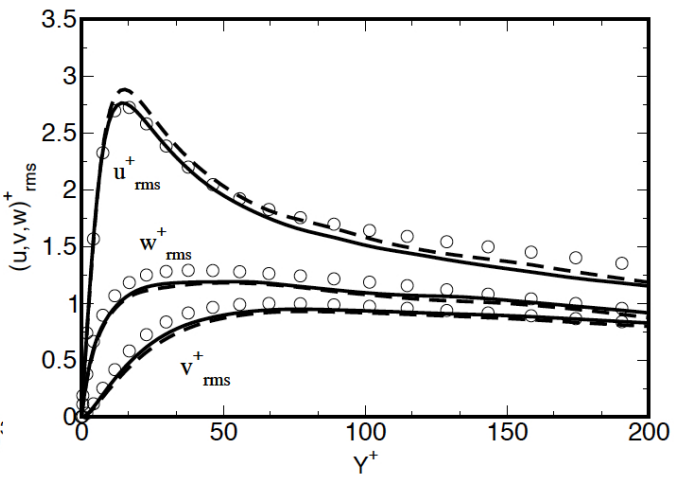

Figure 3.20: rms Velocity for the channel test case $Re_\tau = 395$: (dashed line) Global σ-model, (thick line) σ-model, (symbols) DNS of Moser *et al.* [99]

There is an overestimation of the mean velocity that can be explained by the large value to which the global constant converged. Fig. 3.21 shows the time evolution of the constant that is greater than the asymptotic value 1.35.

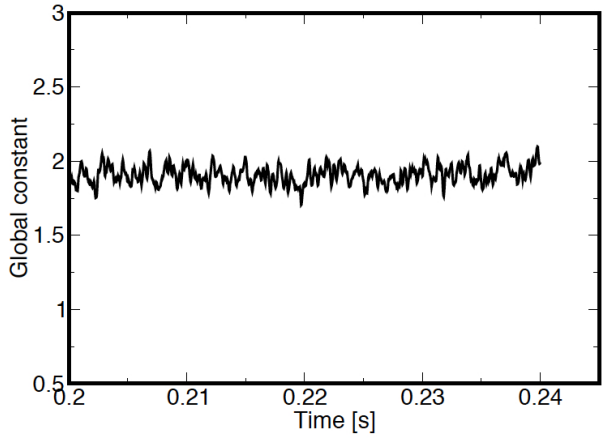

Figure 3.21: Time evolution of the dynamic global constant for the turbulent channel $Re_\tau = 395$

This leads to a higher level of the SGS velocity compared to the static model as showed on Fig. 3.22.

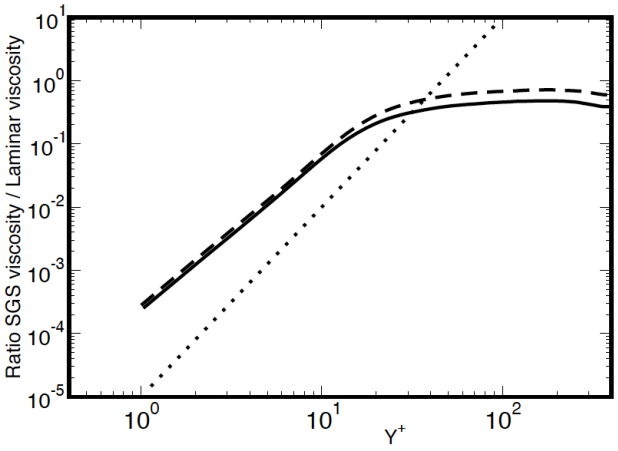

Figure 3.22: Comparison of the ratio ν^{sgs}/ν for the turbulent channel $Re_\tau = 395$: (dashed line) Global σ-model. (thick line) σ-model.

- **Modified Global dynamic procedure**
  The problem that appears when using the classic Global dynamic procedure can be explained by representing the two terms $L_{ij}M_{ij}$ and $M_{ij}M_{ij}$ in the channel. Fig. 3.23 shows the profile of those two terms in the channel for a $Re_\tau = 395$. It is interesting to note that the two terms reach a pic where their values is higher than the value in the center of the channel increase strongly when approaching the wall.

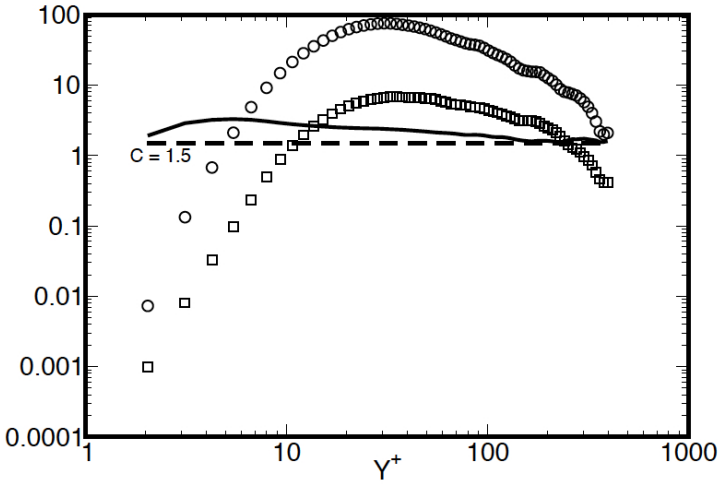

Figure 3.23: Profile of $L_{ij}M_{ij}$ (circles), $M_{ij}M_{ij}$ (squares) and $C = \sqrt{\frac{<L_{ij}M_{ij}>_{plane}}{M_{ij}M_{ij}>_{plane}}}$ (thick line) in the turbulent channel case at $Re_\tau = 395$.

As expected the values of $L_{ij}M_{ij}$ and $M_{ij}M_{ij}$ near the wall (where viscous effects dominates) are much smaller than their values in the center of the channel (where the flow is effectively turbulent). It turns out that the ratio of these two very small numbers generates a large dynamic constant in the wall region. As a direct consequence, the volume weighted averaging is biased because of the large values near the solid boundaries. In this region the flow is dominated by viscous effects and it is not representative of the turbulent in the channel. We can also see that when one evaluate "a posteriori" the constant in the channel using the corresponding $L_{ij}M_{ij}$ and $M_{ij}M_{ij}$ (with an averaging over plans parallel to the walls), the values obtained in the center of the channel are more closed to the expected value 1.5 for the σ-model.

Proposal of solution

A simple way to overcome the problem mentioned is to damp values close to the wall. In other terms, restrict the volume average to values that are effectively relevant and representative of the turbulent intensity. This can be achieved with a sensor that vanishes near walls and that is almost constant far from the wall. The choice of such a sensor is certainly not unique but in any case the sensor should be applicable also in all types of configurations from simple channel to very complex geometries.

Damping sensor
Recalling the asymptotic behavior of the singular values of the velocity gradient tensor: g_{ij}: $\sigma_1 = O(y^0)$, $\sigma_2 = O(y^1)$, $\sigma_3 = O(y^2)$ two damping sensors were tested:

$$s_1 = \frac{\sigma_2}{\sigma_1} \tag{3.65}$$

$$s_2 = \left(\frac{\sigma_2}{\sigma_1})^3\right) \tag{3.66}$$

s_1 and s_2 have respectively the asymptotic behavior $O(y^1)$ and $O(y^3)$.

Results for the channel flow at: $Re_\tau = 395$
The modified global constant C_G^* is now expressed as:

$$C_G^{*2} = -\frac{1}{2}\frac{< L_{ij}M_{ij}^\sigma >_s}{< M_{ij}^\sigma M_{ij}^\sigma >_s} \tag{3.67}$$

where $<>_s$ stands for an ensemble averaging procedure [3] weighted by the sensor s_1 or s_2.

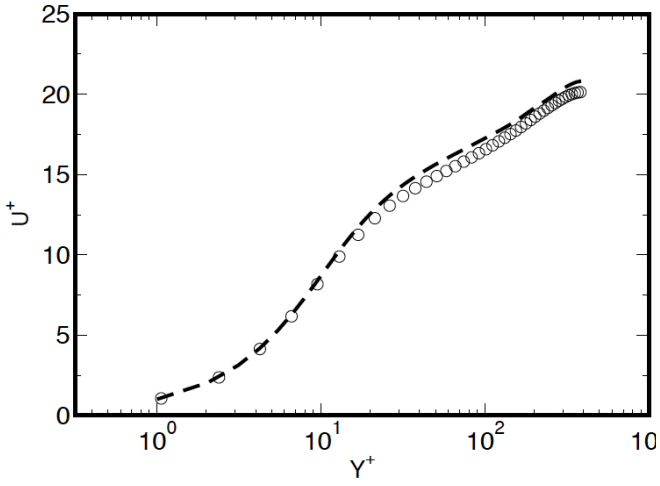

Figure 3.24: Mean Velocity for the channel test case $Re_\tau = 395$: (dashed line) Global σ-model with sensor s_1, (symbols) DNS of Moser *et al.* [99]

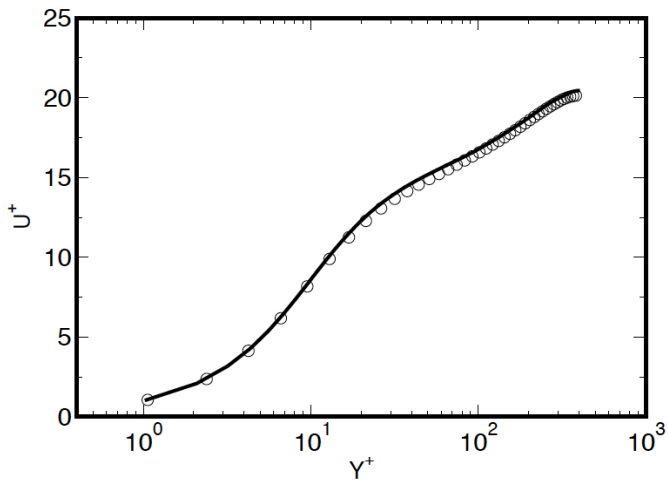

Figure 3.25: Mean Velocity for the channel test case $Re_\tau = 395$: (thick line) Global σ-model with sensor s_2, (symbols) DNS of Moser *et al.* [99]

Fig. 3.24 and Fig. 3.25 show the mean velocity predicted respectively with the sensor s_1 and s_2. Results are presented separately for sake of clarity. There is still a slight overprediction of the mean

[3] For a scalar ϕ, we have:

$$< \phi >_s = \frac{\int \phi \; s \; dv}{\int \; s \; dv} \tag{3.68}$$

velocity when using the s_1 sensor. In contrary, results are in better agreement with the DNS when using s_2. Obviously s_1 does not damp enough the values close to the wall. Fig. 3.26 shows the evolution of the two sensors in the channel. The asymptotic behavior of each sensor is correctly retrieved. But the damping induced by the first sensor is lower than for the second sensor s_2. This is confirmed by the temporal evolution of the constant on Fig. 3.27.

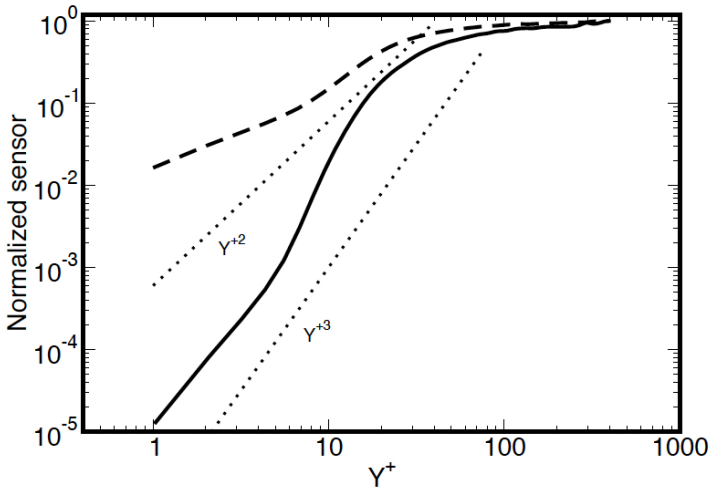

Figure 3.26: Profile of the sensor s1 and s2 in the channel.

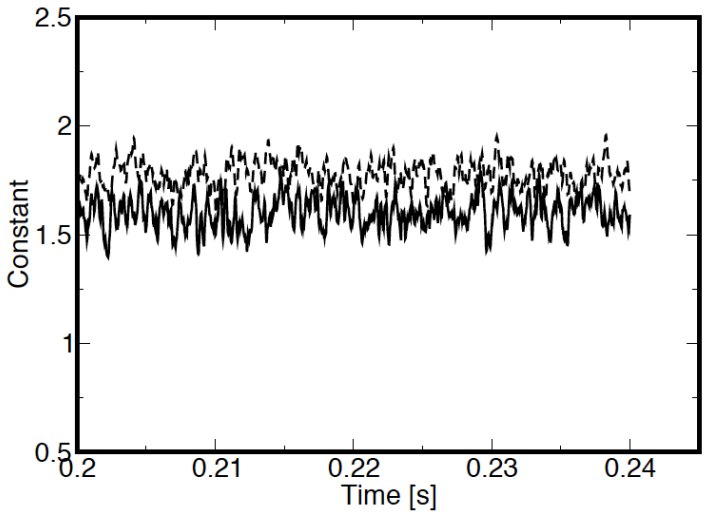

Figure 3.27: Time evolution of the global constant predicted with the sensors s_1 and s_2.

Prediction of the rms velocity shown on Fig. 3.28 are also in good agreement with sensor s_2.

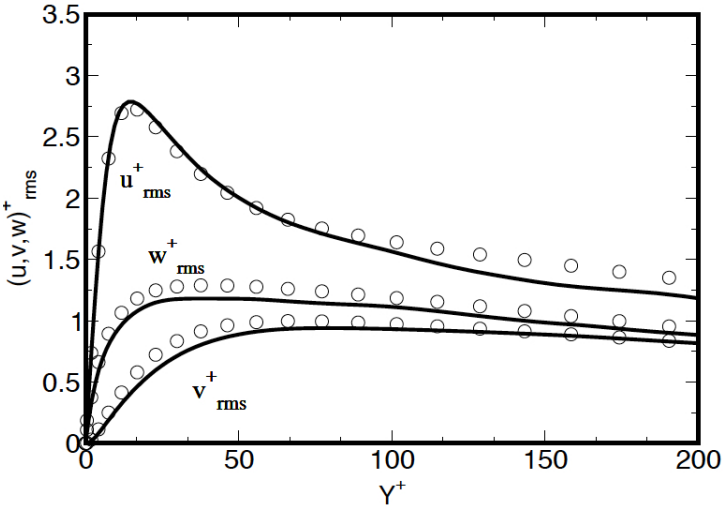

Figure 3.28: rms Velocity for the channel test case $Re_\tau = 395$: (thick line) global σ-model with sensor s_2, (symbols) DNS of Moser *et al.* [99]

Finally, the use of dimensionless damping sensors to improve predictions of the global dynamic procedure seems to be a promising solution for extending the global dynamic σ-model to wall bounded flows. Indeed, for non-wall bounded flows the models performed very well on various cases: such as HIT and also periodic Jet (see APPENDIX B for results concerning the results in the periodic Jet). However the presence of solid boundaries seems to alter the prediction and it is then necessary to use one of the method (sensor s_2) aforementioned. Still, more test cases need to be performed at different Reynolds numbers and with other solvers as it was done with the σ-model in order to definitely validate the proposed solution.

3.5 Extension to the SGS conductivity

The difficulty with the validation of the dynamic SGS conductivity model is the lack of DNS database on anisothermal (with high temperature ratio between the channel temperature center and the wall temperature) flows at low Mach number. The objective of the simulations which will be presented is to make sure that the model has been properly implemented in AVBP before using the model for the simulation of the experimental set-up. After comparing the non dimensional mean velocity and temperature, the behavior of the dynamic Prandlt number in the channel is analyzed. The reference data for this part is the wall-resolved LES of Cabrit and Nicoud (see Case C in [22]) for which the channel center is 3 times hotter than the wall. Characteristics of the mesh used in simulations and during this work are presented in table. 3.2:

Table 3.2: Characteristics of the LES simulations for the anisothermal case.

Case	L_x/h	L_z/h	N_x	N_y	N_z	Δ_x^+	Δ_y^+	Δ_z^+	Re_τ
Present LES simulations	3.5	1.3	44	99	44	82	1-80	30	1000
Cabrit and Nicoud LES simulations	3.5	1.3	44	159	44	82	1-30	30	1000

The "reference" wall resolved LES of Cabrit and Nicoud were performed with the WALE model and the SGS turbulent Prandtl number was set to 0.5. In our case the SGS Prandtl number for the constant case is equal to 0.7. It is important to emphasize that the objective is not to quantitatively validate the SGS conductivity based with a dynamic constant. Studies [19, 63] have already shown that in a Turbulent channel this formulation shows only little differences compared to the constant SGS Prandtl number method. Rather the goal is to establish the proper implementation of the dynmic conductivity in the AVBP solver [1]. In what follows, comparisons are performed regarding the mean non dimensional temperature and velocity when changing only the SGS conductivity. All the simulations are performed with the same initial conditions and are averaged over 12 diffusion times.

Dynamic Smagorinsky model and dynamic SGS conductivity

Two LES simulations were performed both with the dynamic Smagorinsky model concerning the SGS viscosity and with a constant SGS Prandtl number and a dynamic conductivity SGS model.

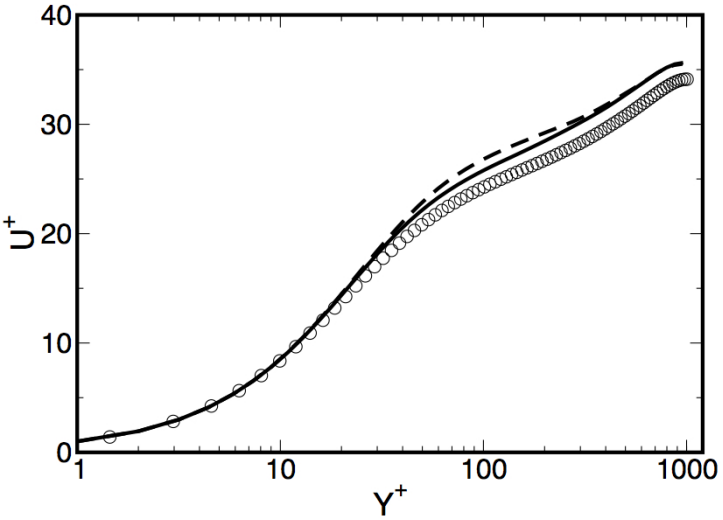

Figure 3.29: Mean velocity profile in the anisothermal turbulent channel case: (dash line) dynamic Smagorinsky model with constant SGS Prandtl, (thick line) dynamic Smagorinsky model with dynamic SGS Prandtl, (symbols) Cabrit and Nicoud [22] LES.

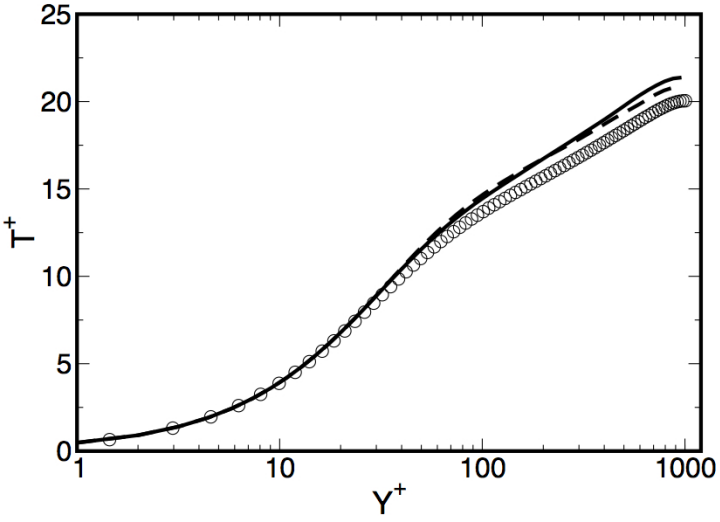

Figure 3.30: Mean temperature profile in the anisothermal turbulent channel case: (dash line) dynamic Smagorinsky model with constant SGS Prandtl, (thick line) dynamic Smagorinsky model with dynamic SGS Prandtl, (symbols) Cabrit and Nicoud [22] LES

Results of the mean non dimensional velocity in Fig. 3.29 shows little differences between the two formulations of the SGS conductivity specially in the region around $y^+ = 100$. In the two cases predictions are higher than LES simulations of Cabrit and Nicoud but of the same order of magnitude. Concerning the temperature profiles shown in Fig. 3.30, results are similar except in the channel center where the formulation with the dynamic Prandtl is slightly higher than the prediction of the constant Prandtl number.

Global SIGMA model and dynamic SGS conductivity

Similar to the simulations performed in the precedent section, two simulations were performed with the Global dynamic σ-model with the two formulations of the SGS conductivity.

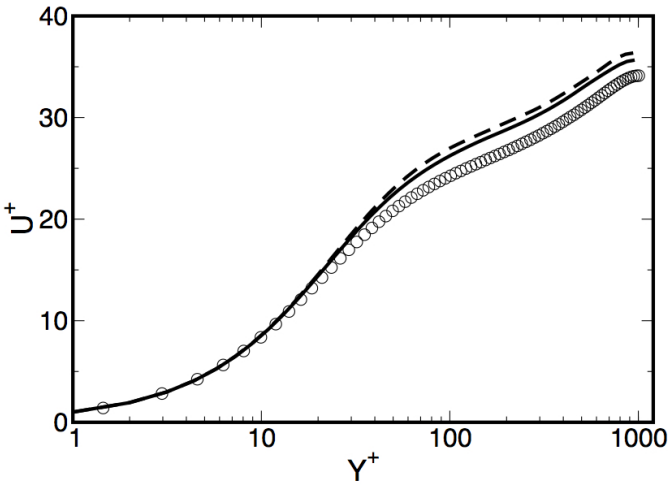

Figure 3.31: Mean velocity profile in the anisothermal turbulent channel case: (dash line) Global σ-model with constant SGS Prandtl, (thick line) Global σ-model with dynamic SGS Prandtl, (symbols) Cabrit and Nicoud [22] LES

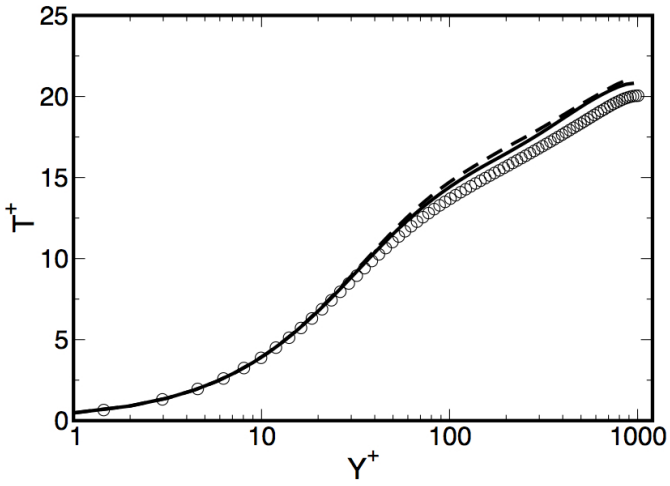

Figure 3.32: Mean temperature profile in the anisothermal turbulent channel case: (dash line) Global σ-model with constant SGS Prandtl, (thick line) Global σ-model with dynamic SGS Prandtl, (symbols) Cabrit and Nicoud [22] LES

Results of the mean non dimensional velocity and temperature profile in Fig. 3.31 and Fig. 3.32 are similar as in the case of the dynamic Smagorinsky model. The differences between the two formulations are not high and predictions of the LES simulations are also in same order of magnitude as LES simulation of Cabrit and Nicoud [22].

SGS viscosity and SGS Prandtl number

Comparisons in Fig. 3.33 show that the choice of the formulation of the conductivity has almost no influence on the SGS viscosity. In Fig. 3.34 the SGS Prandtl number evaluated a posteriori is shown. Indeed, because it is the SGS conductivity which is explicitly calculated as explained in the literature review section, the SGS Prandtl number is evaluated a posteriori over planes parallel to the top and bottom walls of the channel. Results show an expected behavior of the SGS Prandtl number: close to the wall, viscous effect dominates and the heat transfer is mostly due to the laminar conductivity. In the channel center where the flow is turbulent, the SGS Prandtl number decreases thus enhancing the SGS heat flux. The two terms are indeed inversely proportional.

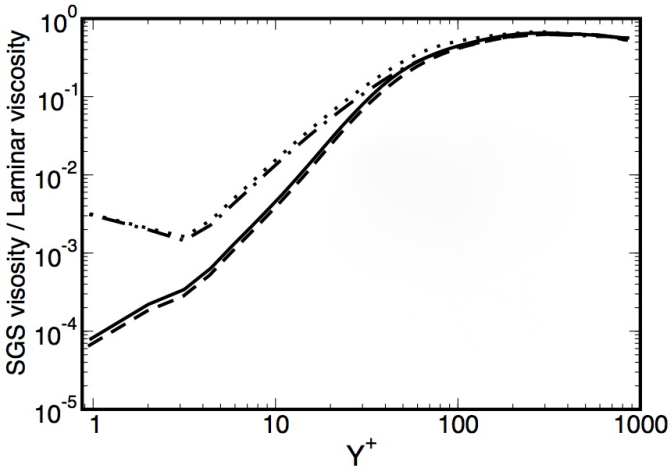

Figure 3.33: Comparison of the predictions of the SGS viscosity in the anisothermal turbulent channel case: (dot line) dynamic Smagorinsky model with dynamic SGS Prandtl, (dot dash line) dynamic Smagorinsky model with constant SGS Prandtl, (dash line) Global σ-model with constant SGS Prandtl, (thick line) Global σ-model with dynamic SGS Prandtl

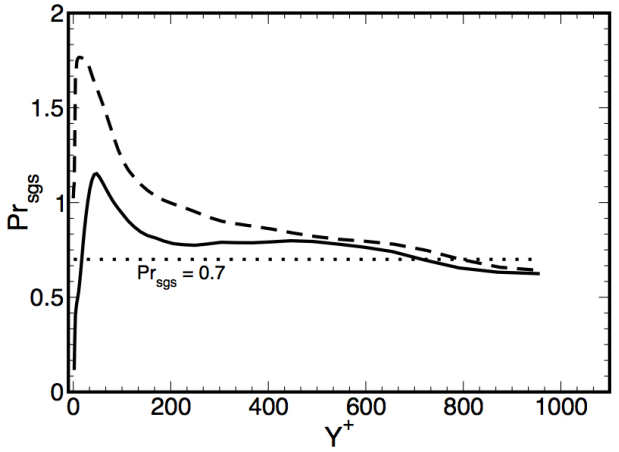

Figure 3.34: Comparison of the predictions of the dynamic SGS Prandtl number in the anisothermal turbulent channel case: (dash line) SGS Prandtl number evaluated from the dynamic Smagorinsky model, (thick line) SGS Prandtl number evaluated from the Global σ-model

3.6 An alternative to the clipping of the dynamic Smagorinsky constant:

We have seen on academic cases specially wall-bounded cases that the use of the local version of the dynamic Smagorinsky model (with clipping) can lead to an overestimation of the dissipation. However, this is probably the easiest way to use this model in complex geometries. In what follows, a simple alternative to the local clipping is presented which is based on a concept of the redistribution of the global constant of the dynamic Smagorinsky model. The suggested alternative was tested on the turbulent periodic jet by G. Balarac with solver D and on the Turbulent channel with solver A. In both cases, it shows better or equivalent results than the local dynamic Smagorinsky model.

Error on the global dissipation

The use of the Germano-identity with Lilly correction [84] aims at minimizing the quantity $\epsilon_{ij}\epsilon_{ij}$, where ϵ_{ij} is expressed as followed:

$$\epsilon_{ij} = T_{ij}^{sgs} - \widetilde{\tau_{ij}}^{sgs} - L_{ij} \tag{3.69}$$

and represents the Germano-identity error which should be zero in the perfect case.
The problem that arises when the minimization is applied locally is that the values of the coefficient can be negative and they are clipped to avoid any unstable computations. The overall dissipation of the SGS model $< \tau_{ij}^{sgs}\widetilde{S_{ij}}^{sgs} >$ can be split into two terms :

$$< \tau_{ij}^{sgs}\widetilde{S_{ij}}^{sgs} > = < \tau_{ij}^{sgs}\widetilde{S_{ij}}^{sgs} >^{+} + < \tau_{ij}^{sgs}\widetilde{S_{ij}}^{sgs} >^{-} \tag{3.70}$$

where superscripts $()^+$ and $()^-$ stand respectively for a quantity evaluated with positive and negative values of the dynamic constant.
The term $< \tau_{ij}^{sgs}\widetilde{S_{ij}}^{sgs} >^{+}$ is of course positive and $< \tau_{ij}^{sgs}\widetilde{S_{ij}}^{sgs} >^{-}$ is negative. When the model is applied locally and applied locally, the last term is set to zero and the overdissipation induced by the SGS model is equal to that term.
It is worth noting that the problem is different when the coefficient is averaged over the homogeneous directions meaning that the dissipation is also averaged over those directions.

$$< \tau_{ij}^{sgs}\widetilde{S_{ij}}^{sgs} > = \sum_h < \tau_{ij}^{sgs}\widetilde{S_{ij}}^{sgs} >_h = \sum_h \left(< \tau_{ij}^{sgs}\widetilde{S_{ij}}^{sgs} >_h^{+} + < \tau_{ij}^{sgs}\widetilde{S_{ij}}^{sgs} >_h^{-} \right) \tag{3.71}$$

where the underscript h stands for a homogeneous direction and $< \tau_{ij}^{sgs}\widetilde{S_{ij}}^{sgs} >_h$ the SGS dissipation on h which is expressed as follows:

$$< \tau_{ij}^{sgs}\widetilde{S_{ij}}^{sgs} >_h = C_h^2 \left(< 2\rho\Delta^2 D_s^{+}(\mathbf{u})\widetilde{S_{ij}}^{sgs}\widetilde{S_{ij}}^{sgs} >_h^{+} + < 2\rho\Delta^2 D_s^{-}(\mathbf{u})\widetilde{S_{ij}}^{sgs}\widetilde{S_{ij}}^{sgs} >_h^{-} \right) \tag{3.72}$$

where C_h^2 is the constant obtained with the dynamic procedure, D_s^+ and D_s^- respectively the Smagorinsky time scale for positive and negative values of the constant. Because C_h^2 is rarely negative on an entire plane (thus no use of clipping) there is almost no over dissipation induced when averaging over homogeneous directions is used. In addition to the fact that this procedure preserves the correct near wall behavior of the SGS viscosity, averaging over homogeneous directions do not lead to any increase of the overall

dissipation.
When using the Smagorinsky time scale, there is no other choices than a local dynamic procedure to overcome the drawback of the time scale itself. But this should be achieved so as to preserve the overall dissipation. The alternative suggested here consists in two steps : first calculate globally the model constant and then redistribute the global constant.

Global dissipation:

The global constant is obtained by assuming that there is a constant C_G that should lead to the same overall SGS dissipation of the Smagorinsky model than the dissipation induced by the local constant C_i:

$$< \tau_{ij}^{sgsG} \widetilde{S_{ij}}^{sgs} >=< \tau_{ij}^{sgs} \widetilde{S_{ij}}^{sgs} > \tag{3.73}$$

which leads to the following relationship between C_G and C_i:

$$C_G^2 < 2\rho\Delta^2 D_s(\mathbf{u}) \widetilde{S_{ij}}^{sgs} \widetilde{S_{ij}}^{sgs} >=< 2\rho C_i^2 \Delta^2 D_s(\mathbf{u}) \widetilde{S_{ij}}^{sgs} \widetilde{S_{ij}}^{sgs} > \tag{3.74}$$

Eq.(3.74) can be simplified to:

$$C_G^2 \approx < C_i^2 > \tag{3.75}$$

Since the Smagorinsky time scale $D_s(\mathbf{u})$ does not meet several properties like vanishing in near wall region, it is not possible to use the global constant C_G uniformely over the flow domain. The latter should be redistributed to overcome the drawback of the time scale.

Redistribution procedure:

The redistribution should be performed so as to preserve the overall SGS dissipation. Meaning that if we assume C^{Gi} the redistributed local constant the following relation should be satisfied:

$$< \tau_{ij}^{sgsGi} \widetilde{S_{ij}}^{sgs} >=< \tau_{ij}^{sgsG} \widetilde{S_{ij}}^{sgs} > \tag{3.76}$$

Let us note Θ_i the redistribution function:

$$C^{Gi} = \Theta_i C^G \tag{3.77}$$

Injecting Eq. (3.77) in Eq. (3.76) leads to the following constraint on the redistribution function:

$$< \Theta_i >= 1 \tag{3.78}$$

additionally Θ_i should be positive to ensure positive eddy-viscosity everywhere (assuming $C_G > 0$). The following expression was chosen:

$$\Theta_i = \frac{|C_i| + C_i}{2} \frac{V_T}{V_n} \tag{3.79}$$

where V_T is the total volume and V_n is the volume.

The final expression of the viscosity is then:

$$\nu_{sgs} = (C_G \Theta_i)^2 \Delta^2 D_s(\mathbf{u}) \tag{3.80}$$

Results

Results of the alternative formulation (referred to as RGS which stands for Redistributed Global Smagorinsky) are compared with results of the local dynamic Smagorinsky model with clipping on different academic test cases:

- **Turbulent periodic Jet**
  The potential of the suggested alternative for non wall-bounded flow was investigated in the spectral solver D by Guillaume Balarac. Results are compared with the dynamic Smagorinsky model with a constant averaged over homogeneous directions (DSMh). The results from 64^3 LES are compared to 256^3 DNS data obtained by running the same spectral code.The configuration is close to the one studied in Da Silva & Pereira [32] except for the jet width-to-initial momentum thickness, which is 20 instead of 35. The computational domain is periodic in the three spatial directions and its size is four times the initial jet width. The DNS initial field is generated by super-imposing divergence-free random fluctuations to the mean velocity profile. The LES initial condition is obtained from the DNS data by spectral interpolation. Because periodic conditions are imposed in both the streamwise and spanwise directions, the flow is not statistically steady and the jet keeps growing thicker and thicker as time increases.

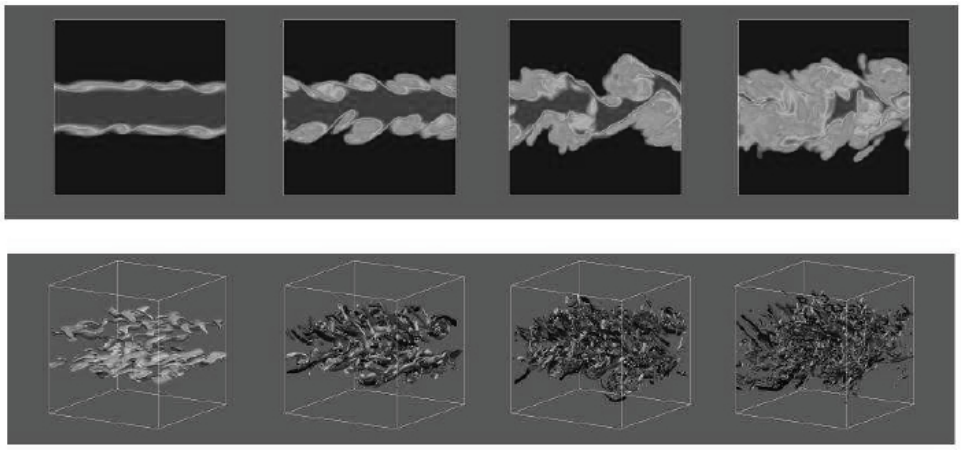

Figure 3.35: From left to the right jet at different times: t1 = 5h/U, t2 = 10h/U, t2 = 15h/U and t2 = 20h/U. Top: Passive scalar in the jet. Bottom : Q criterium colored by the axial vorticity.

A passive scalar was introduced into the jet in order to represent the mixing with the environment. Comparison between the DNS and LES simulations are done at 4 different times: $t_1 = 5h/U$, $t_2 = 10h/U$, $t_2 = 15h/U$ and $t_2 = 20h/U$ where h is the jet half thickness and U is the maximum mean velocity. Fig. 3.35 shows on the top the evolution of the passive scalar and on the bottom the Q criterion color by the axial vorticity. The later gives an idea of the turbulent activity. As it can be seen the four chosen times are well representative of flow states that can be met in a non

wall-bounded flow. The comparisons are focused on the prediction of the turbulent kinetic energy predicted by the different SGS models in comparison to the filtered DNS. Only results of the three last times are presented.

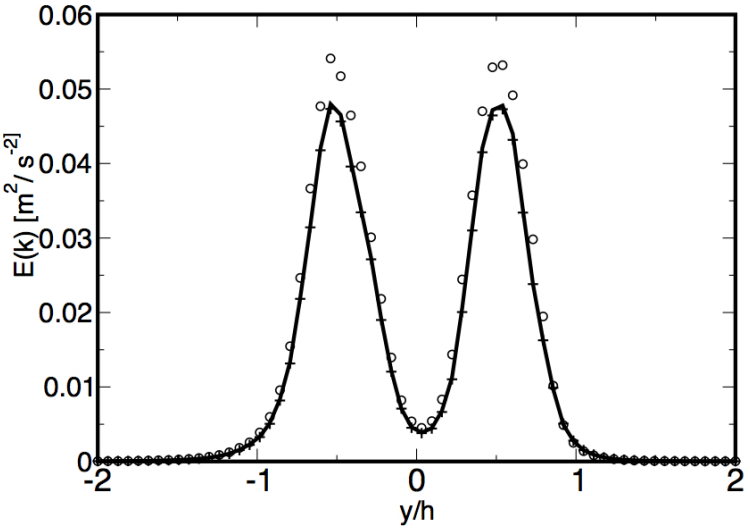

Figure 3.36: Turbulent planar jet test case at time 10h/U. Resolved turbulent kinetic energy. Circles represent the filtered DNS. Thick line: RGS and plus symbols DSMh.

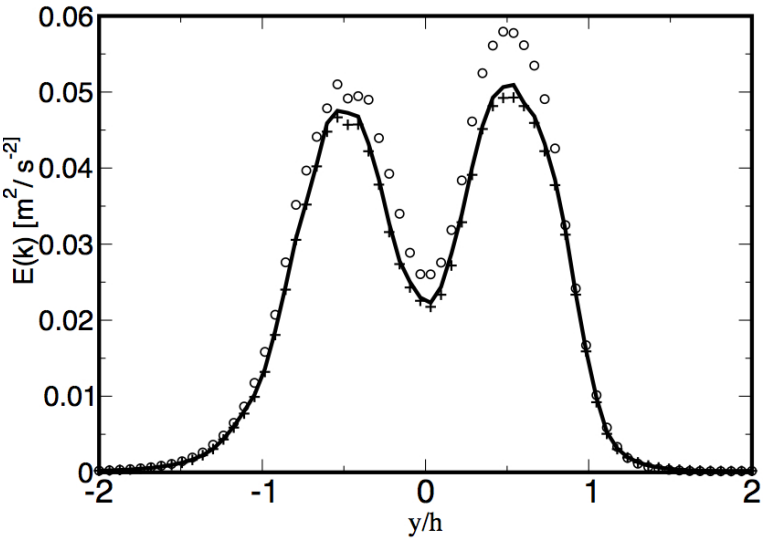

Figure 3.37: Turbulent planar jet test case at time 15h/U. Resolved turbulent kinetic energy. Circles represent the filtered DNS. Thick line: RGS and plus symbols DSMh.

Fig. 3.36 to Fig. 3.38 show that the redistribution of the global constant of the Smgorinsky model leads to equivalent results than the recommended dynamic Smagorinsky model with homogeneous directions for unbounded flows.

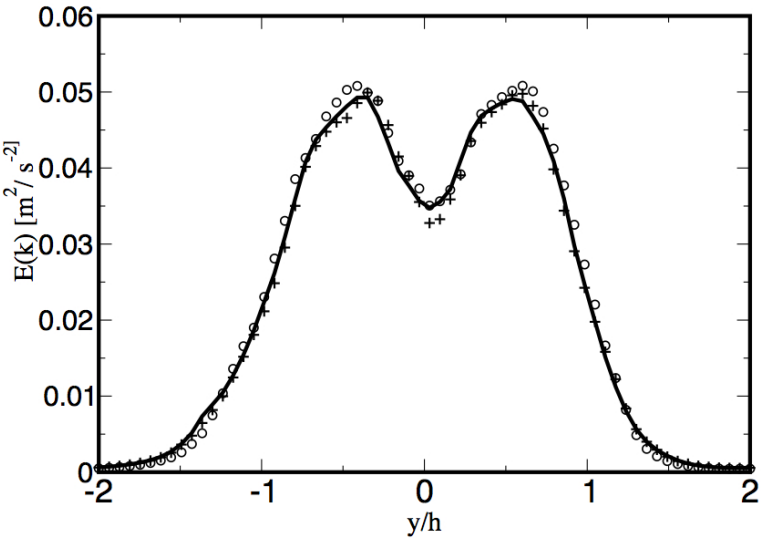

Figure 3.38: Turbulent planar jet test case at time 20h/U. Resolved turbulent kinetic energy. Circles represent the filtered DNS. Thick line: RGS and plus symbols DSMh.

- **Turbulent channel**
  Simulations of the case $Re_\tau = 395$ with the modified dynamic Smagorinsky model were performed and compared with the local dynamic Smagorinsky model with clipping. Fig. 3.39 and Fig. 3.40 show the mean dynamic constant and the viscosity in the channel. The constant of the two models decreases in the near wall region in oder to damp the Smagorinsky's time scale but the constant (and thus the SGS viscosity) of the modified dynamic Smagorinsky model is lower than the constant of the local dynamic Smagorinsky model.

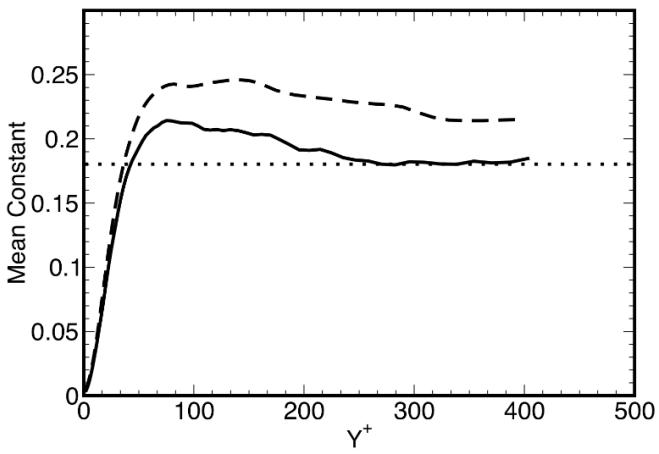

Figure 3.39: Dynamic constant of the models the channel test case $Re_\tau = 395$: dashed local dynamic Smagorinsky model. Thick line RGS Symbols DNS of Moser *et al.* [99]

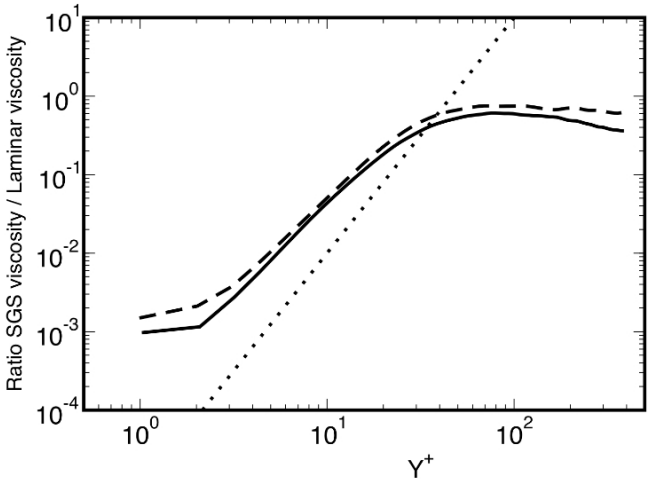

Figure 3.40: Ratio ν_{sgs}/ν_{lam} in the channel test case $Re_\tau = 395$: dashed local dynamic Smagorinsky model. Thick line RGS. Symbols DNS of Moser *et al.* [99]

Results of the mean and rms velocity in Fig. 3.41 and Fig. 3.42 show that the suggested modification leads to better results than the local dynamic Smagorinsky model.

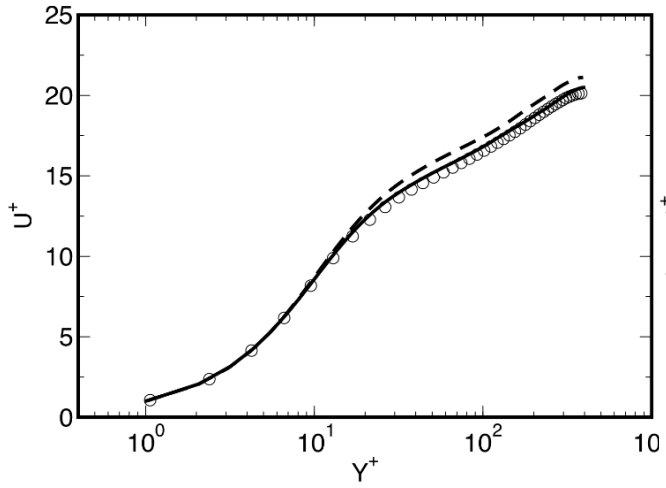

Figure 3.41: Mean Velocity for the channel test case $Re_\tau = 395$: dashed local dynamic Smagorinsky model. thick line modified dynamic Smagorinsky model. Symbols DNS of Moser *et al.* [99]

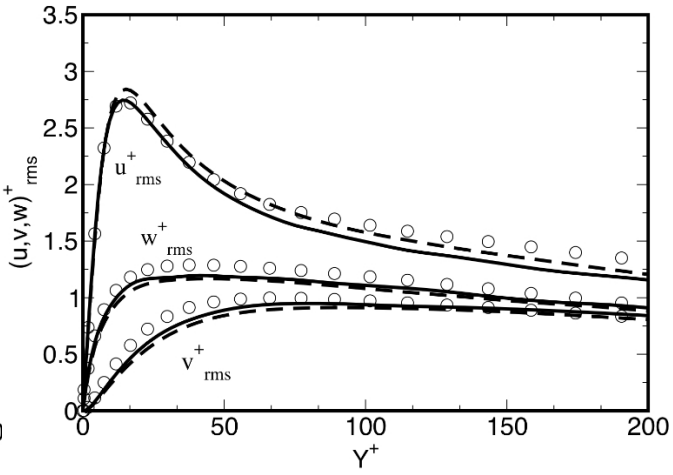

Figure 3.42: rms Velocity for the channel test case $Re_\tau = 395$: dashed local dynamic Smagorinsky model. Thick line RGS. Symbols DNS of Moser *et al.* [99]

The results presented concerning the proposed RGS formulation shows that it can be considered as an alternative to the local dynamic Smagorinsky model with clipping specially for unbounded flows. More tests should be performed in complex configurations. However, this formulation does not overcome the issues of the use of the Germano-identity for coarser resolution at the wall. Simulations of the turbulent channel case were performed with a good resolution and a smooth stretching of the mesh in the wall normal directions. Meaning that the hypothesis of a small variation of the constant which can then be taken out of the test filter is still valid. For very coarse meshes this hypothesis is not valid specially near the wall where the constant should vanish.

Chapter 4

Experimental and Numerical results:

Once the model developed, the SGS dynamic conductivity implemented in AVBP, the next step was to assess performances of those models compared with the (local) dynamic Smagorinsky model in a more realistic configuration. In this chapter, the complete numerical procedure for computing the experiment test case is presented: geometry, boundary conditions and initial conditions. Preliminary simulations are performed to assess the impact of the numerical scheme and number of solutions used for the averaging before comparing predictions from the aforementioned models.

4.1 Numerical set-up of the JICF:

4.1.1 Geometry and mesh:

The geometry and the mesh were realized by Olivier Cabrit[1] who is also acknowledged for his advices and recommendations during the simulations of the experiments.

Geometry and measurements planes

The experimental set-up was design for LES simulation purposes. The whole experimental set-up was simulated with three modifications: the injection system is not taken into consideration because the geometry of the injector was unknown. The geometry starts from the top of the convergent as shown in Fig. 4.1 and Fig. 4.2.

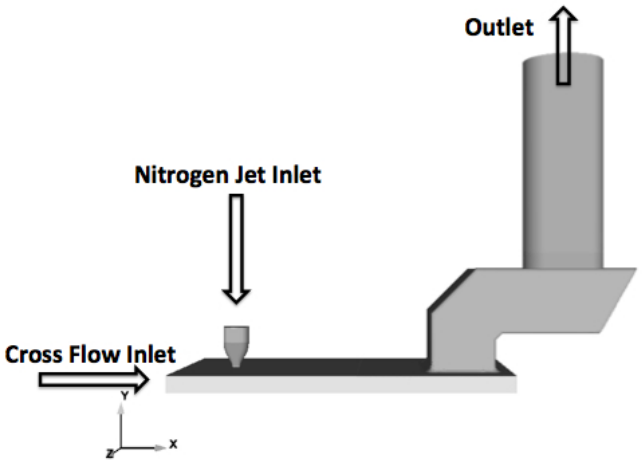

Figure 4.1: Lateral view of the geometry used for the simulation of the experimental set-up

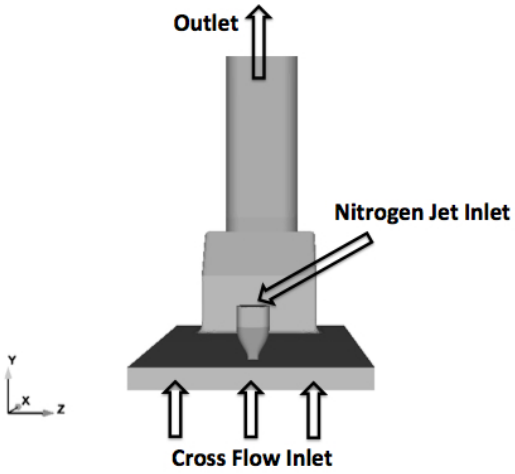

Figure 4.2: Front view of the geometry used for the simulation of the experimental set-up

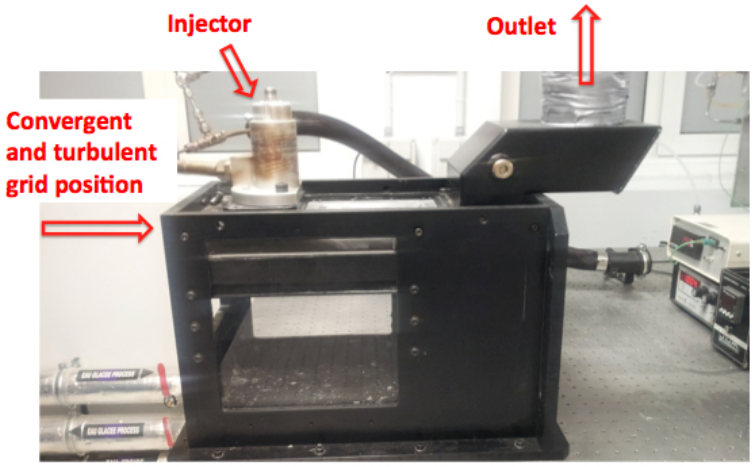

Figure 4.3: View of the experimental set-up without convergent

[1] o.cabrit@unimelb.edu.au

The length of the pipe of the extraction part is limited because the real dimension are too large to be taken into account. Still, the length in the simulation is long enough to avoid any effects of the boundary condition on the flow.

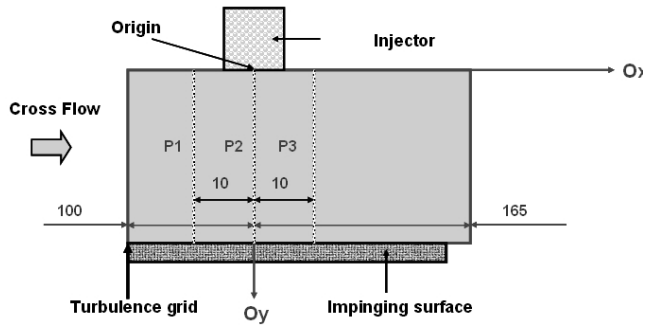

Figure 4.4: Lateral view of the PIV planes

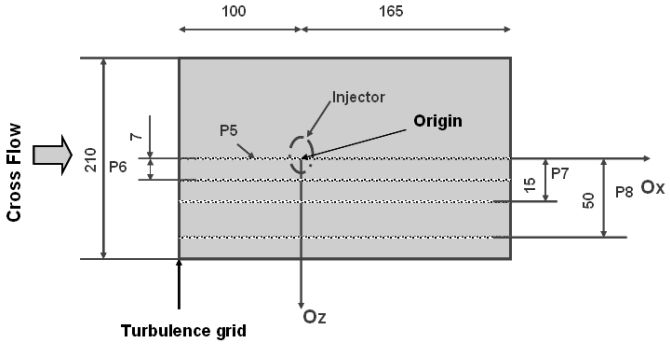

Figure 4.5: Top view of PIV planes

A simplified view of the measurement section is shown in Fig. 4.4 and 4.5 (there is no scaling on the figures. They are schematic representations of the position of the PIV planes). One can see the origin of the set-up situated at the center of the convergent exit. The orientation of the different axis is also presented. Positions of the different measurements planes for PIV are also shown in Fig. 4.4 and Fig. 4.5. They are 7 planes: 3 in the X-direction (streamwise direction) at location $X = -1D$ (P1), $X = 0D$ (P2), $X = 1D$ (P3) and 4 in the Z^+-direction (spanwise direction) at the location $Z = 0D$ (P5), $Z = 0.7D$ (P6), $Z = 1.5D$ (P7) and $Z = 5D$ (P8). The acquisitions were performed at the following time : 0.6 ms, 0.8 ms, 1.0 ms, 1.2 ms, 1.4 ms, 1.6 ms, 1.8 ms, 2.0 ms, 3.0 ms, 4.0 ms, 5.0 ms, 6.0 ms, 7.0 ms. Only the most relevant planes will be presented in the manuscript. The measurements planes for the LIF correspond to the 3 first planes in the spanwise direction: P5, P7 and P8.

Mesh parameters

As in most CFD simulations, the resolution of the mesh plays an important role in the results quality, specially in LES simulations for which the size of the node volumes defines the cutoff length. A particular attention was paid on the mesh resolution near the wall in order to accurately track near wall effects and also in the convergent in order to have sufficient nodes resolution over the diameter to well reproduce the velocity profile at the convergent exit.

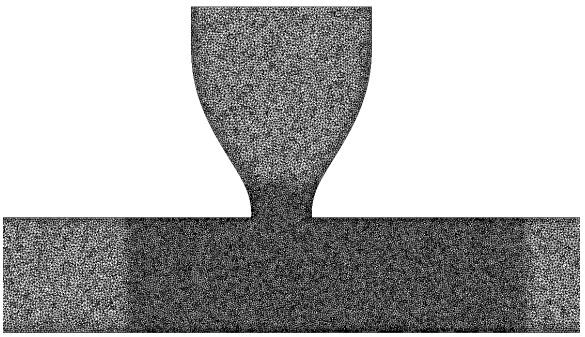

Figure 4.6: Mesh refinement of the measurement section

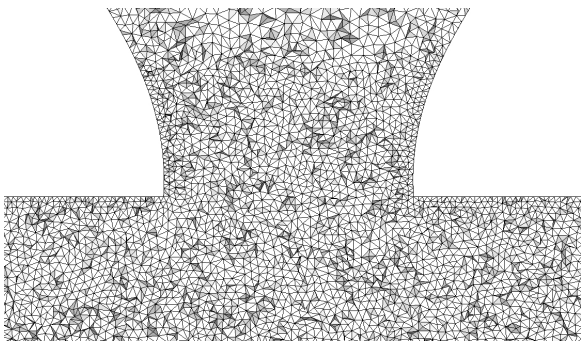

Figure 4.7: Mesh refinement of the convergent

The mesh size was based on the correlation in turbulent channel based on the maximum cross flow velocity

around 12 m/s. The cells size under the injector exit was chosen in oder to have a $y^+ \approx 4$ regarding the cross flow velocity. It also allows to have at least 30 nodes on the exit diameter of the convergent in order to well reproduce the velocity profile (see Fig. 4.6 Fig. 4.7). The mesh is uniform around the injector diameter, in the streamwise direction from $X = -2.5D$ to $X = 4.5D$ and in the spanwise direction from $Z = -2D$ to $Z = 2D$. In the rest of the geometry, the cell size is progressively increased as shown in Fig. 4.8 and Fig. 4.9.

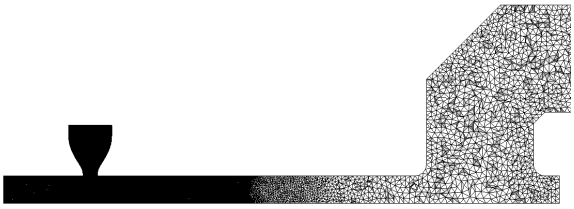

Figure 4.8: Progressive increase of the mesh size

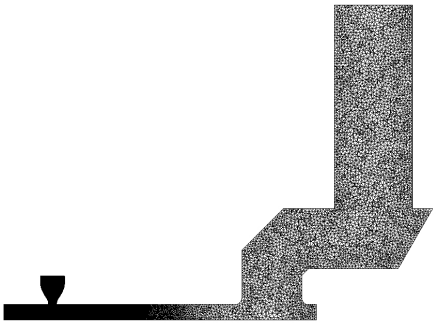

Figure 4.9: Lateral view of the mesh used for the simulation of the experimental set-up

Boundary conditions

Table 4.1: List of the boundary conditions

Patch	Boundary conditions
1	INLET RELAX UVW T Y TURB
2	INLET RELAX RHO UVW T Y
3	OUTLET RELAX P 3D
4	WALL LAW COUPLED ADIAB
5	WALL NOSLIP ADIAB
6	WALL NOSLIP ADIAB
7	WALL NOSLIP ADIAB
8	WALL LAW COUPLED ADIAB
9	WALL NOSLIP ADIAB
10	WALL LAW COUPLED ADIAB
11	WALL LAW COUPLED ADIAB
12	WALL NOSLIP ADIAB
13	WALL SLIP RELAX T
14	WALL SLIP RELAX
15	WALL LAW COUPLED ADIAB
16	WALL NOSLIP ISOT

Table 4.1 summarizes the different boundary conditions imposed in the simulation. These conditions were considered as the most appropriated to fully represent the different physical effects at the boundary[2].

[2]More precisions on the parameters and the boundary patches are given in appendix C

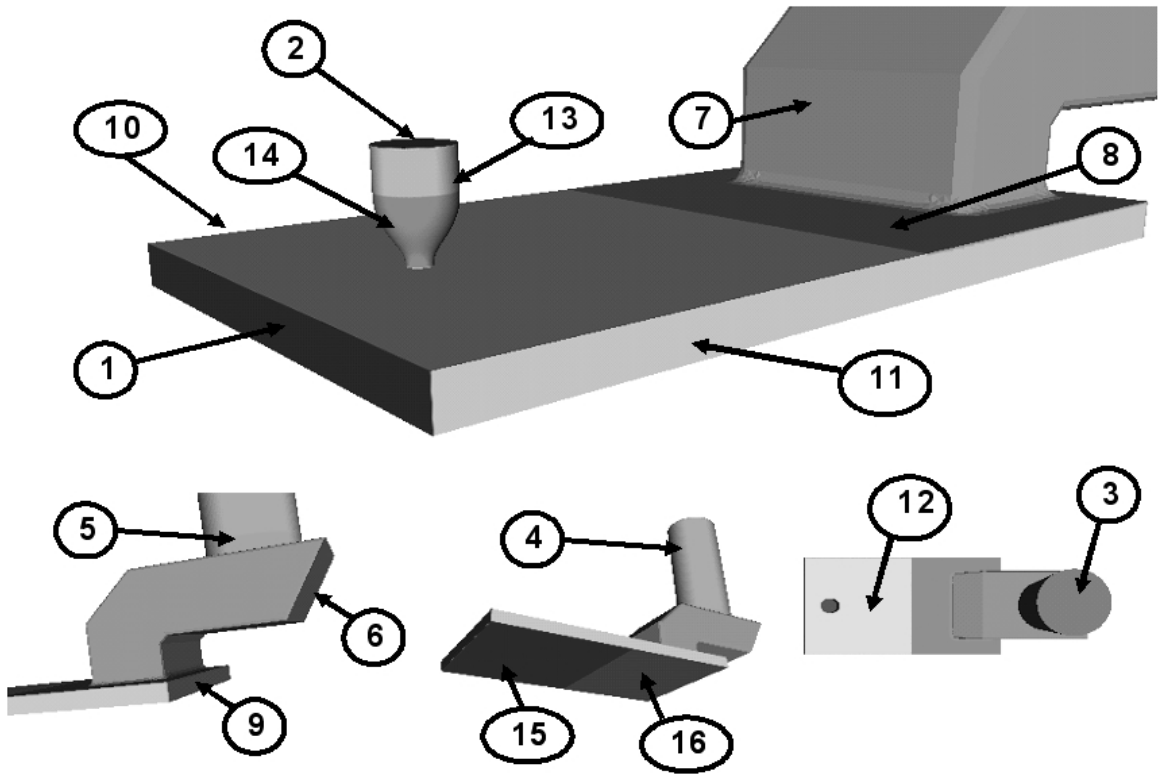

Figure 4.10: Different patches for the LES simulation of the experimental set-up

Fig. 4.10 shows the surfaces to which the different patches refer to.

4.1.2 The flow rate of the injector:

Helmholtz Resonator

It was found during the characterization of the injector, using PIV measurement that the flow rate of the injector can be defined in two parts: an unsteady and a steady phase. The steady phase is characterized by low velocities and is controlled by a frequency $f_h \approx 1000$ Hz (see Fig. 2.22) induced by the convergent at injector exit which acts as an Helmholtz resonator. The objective of this section is to make sure that the frequency observed experimentally is also obtained in the simulations.
The test focuses only on the frequency induced by the shape of the convergent when a continuous signal is imposed. It consists in imposing at the convergent inlet (top of the convergent) a continuous rectangular flow rate signal of 1.6 g/s and to measure the signal obtained at the injector exit.

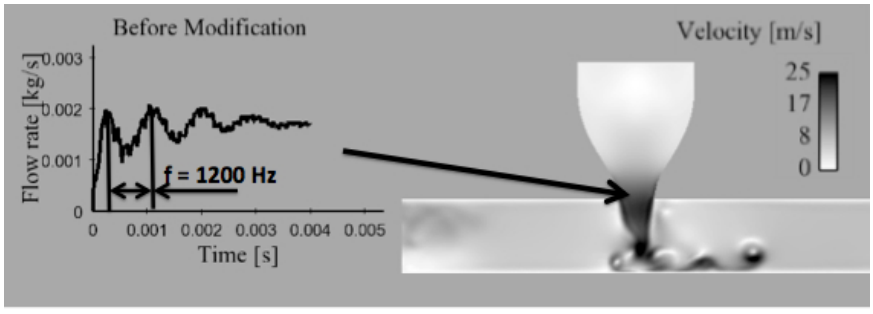

Figure 4.11: Frequency induced by the convergent shape before modification

It can be seen in Fig. 4.11 that the convergent acts as a Helmholtz resonator also in the LES simulation. But the frequency 1200 Hz is different from the observed frequency in the experiment 1000 Hz. This is probably due to the fact the entire injection part is not taken into account in the simulation. In order, to obtain the same frequency as the one of the experiment, a modification was performed on the convergent height thanks to Eq. 2.8. The new convergent was then 13.2 mm longer than the one of the experiment. Fig. 4.12 shows the result of the same rectangular signal test performed with the new convergent. It can be seen that the experimental frequency is well reproduced with the new convergent. The modification of the convergent volume ensure to have the same frequency that controls the jet during the steady phase also in the LES simulations.

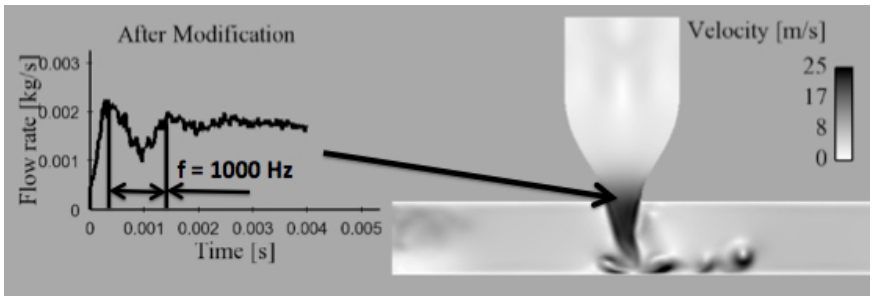

Figure 4.12: Frequency induced by the convergent shape after modification

The inlet flow rate

It was decided to reproduce the inlet flow rate by imposing a source term in a small volume inside the convergent. The inlet flow rate/velocity profile was then modified in order to fit the inlet flow rate of the experiment. Indeed, the velocity profile shown in Fig. 2.23 was done for understanding the behavior of the injector but the PIV measurements were performed without the impingement surface and also without the cross flow.

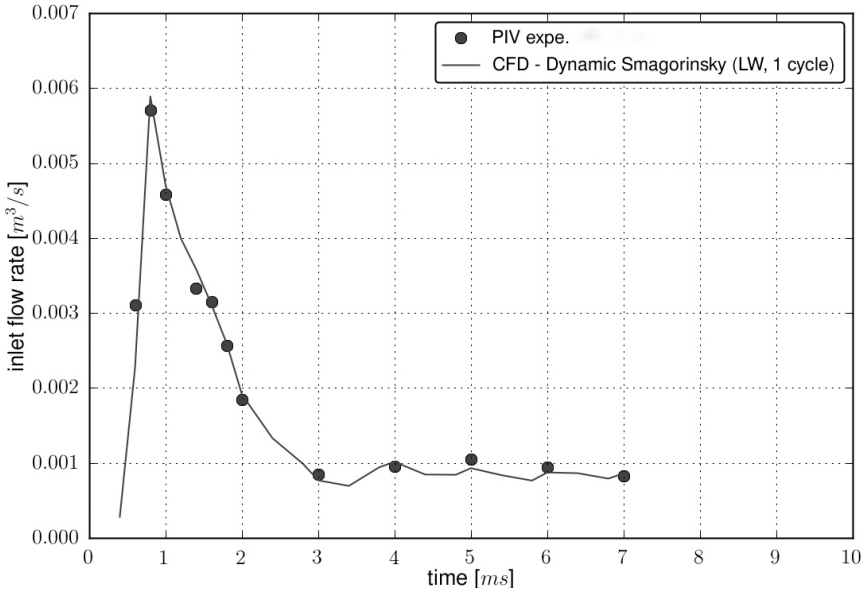

Figure 4.13: Comparisons of the flow rate obtained from the experiment with cross flow and the LES simulation performed with the dynamic Smagorinsky model

We can see in Fig.4.13 that the experimental flow rate is well reproduced and that the flow rate obtained in the simulation (result of the flow rate is similar with the σ-model) is in good agreement with the

experiments. This is confirmed by the comparison of the velocity profile at different times at the location $Y = -1.5$ mm (not shown here).
It is important to emphasize that as the flow rate profile imposed through the source term was defined in order to have a velocity profile close as possible to the experimental velocity profile specially at the convergent exit. One can consider that at this location SGS models have almost no impact and a little error on the flow rate at a section so close to the injector will corrupt the further comparisons between the experiments and the simulations at others sections far from the injector.

4.1.3 The cross flow

Along with the injection flow rate, the velocity profile of the cross flow is also an important initial condition that had to be well defined. The main issue for completely reproducing the experimental set-up was the injection frequency: 1Hz. Indeed, regarding the order of magnitude of the time step in LES simulations ($\approx 10^{-6}$ s), it would have been difficult to respect this time duration between two consecutive injections.

The cross flow initial conditions were obtained as follows:

- PIV measurements were performed on the 4 planes: P5, P6, P7 and P8. The streamwise velocity profile imposed in the simulation at the grid location ($X = -10D$) corresponds to the mean velocity profile obtained on the 4 enumerated planes at the section $X = -4D$ (See Fig. 4.14). Fig. 4.15 shows the imposed mean wall normal velocity which corresponds to the mean wall normal velocity on the plane P5 at the section $X = -4D$. The latter strategy was also used for the root mean square (rms) streamwise and wall normal velocity as shown respectively in Fig. 4.16 and Fig. 4.17. The synthetic turbulence field was imposed following the procedure available in AVBP [1]. More about the procedure for imposing a synthetic turbulent flows can be found in [72, 73].

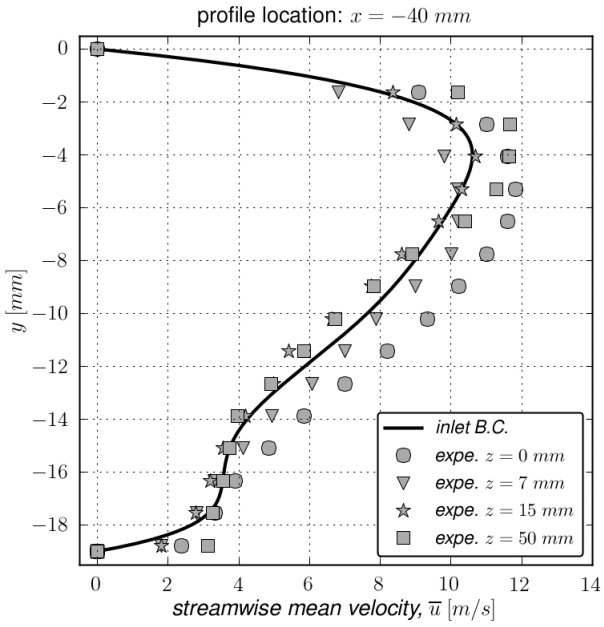

Figure 4.14: Mean streamwise cross flow velocity imposed in the simulations

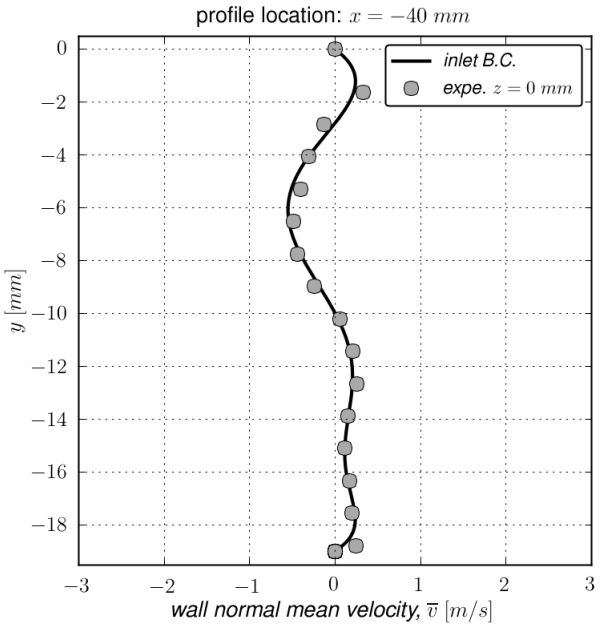

Figure 4.15: Mean wall normal cross flow velocity imposed in the simulations

Although the grid is homogeneous in the spanwise direction, there are some differences on the velocity profile on the 4 planes which are not perfectly similar. Note however that the slight differences observed are still in the measurements uncertainty of the PIV. We can also see that the intensity of

the mean velocity decreases from the top wall to the bottom.The low level of velocity near the wall will reduce the impact of the initial conditions on the vortices propagation and will help to assess performances of the different SGS models in case of wall vortex interaction. Such an assessment has not been done to our knowledge so far.

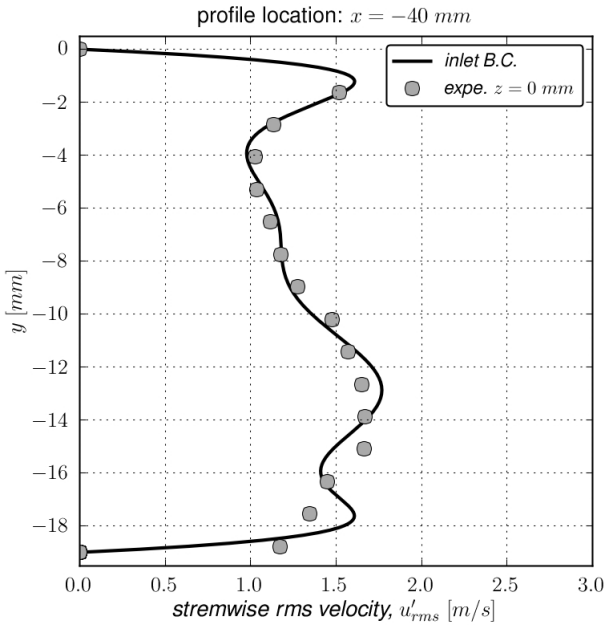

Figure 4.16: rms streamwise cross flow velocity imposed in the simulations

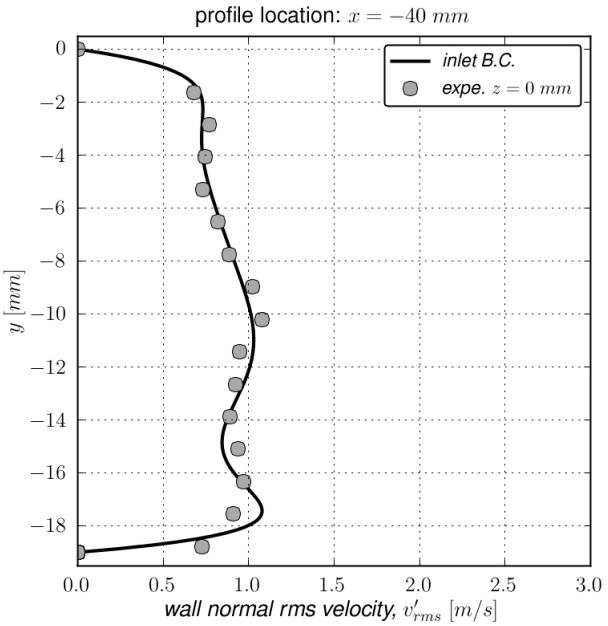

Figure 4.17: rms wall normal cross flow velocity imposed in the simulations

- Once the velocity profile is imposed, simulations are performed without injection in order to have a fully developed turbulence in the channel. The duration of this phase is approximately 50 ms which leads to a statistically converged flow under the injector as shown in Fig. 4.18. The difficulty for simulating the experimental set-up was in reproducing the unsteadiness. It was decided to perform ensemble average starting with equivalent but uncorrelated cross flow initial conditions. Indeed, after the first 50 ms, depending of the number of cycles that will be simulated, solutions are stored every 10 ms. Each of these solutions were the initial conditions for the corresponding injection and cycle. Fig. 4.19 shows a schematic representation of the procedure used for the LES simulations of the experimental set-up.

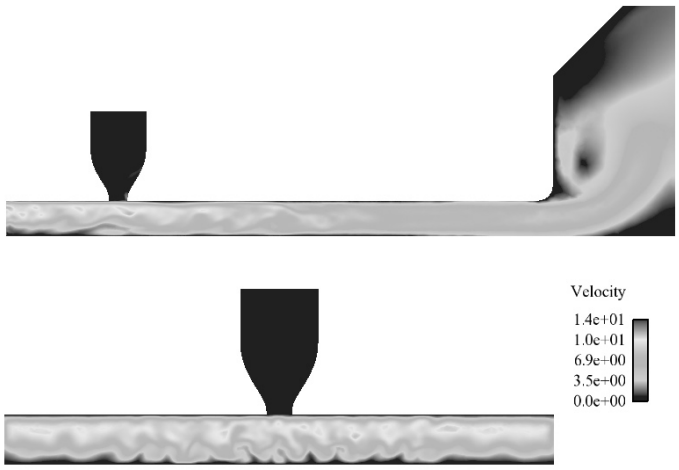

Figure 4.18: Lateral view (top image) and front view (bottom image) of the cross flow field for the first cycle.

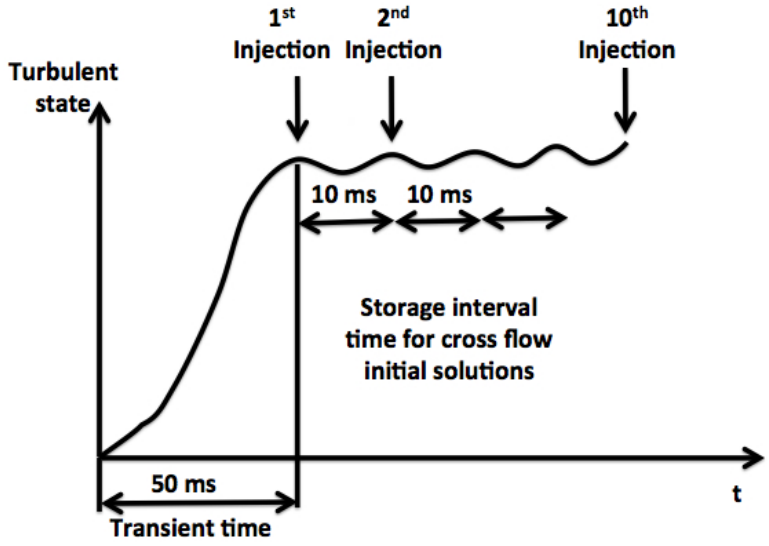

Figure 4.19: Schematic representation of the numerical procedure for the LES simulation of the experiment

4.2 Velocity comparisons

Before comparing the predictions of the different models, it was decided to perform some preliminary tests:

- Statistical convergence of the PIV data: the objective is to make sure that the number of snapshots is enough to reach statistical convergence.
- Influence of natural convection: this can be due to the gradient density inside the measurement section. A source term $\rho\mathbf{g}$ (where $\mathbf{g}$ is the gravitational vector and ρ the fluid density) was introduced in the Navier-Stokes equation but no impact was observed on the results.
- Numerical Scheme: the academic cases were performed with a low dissipative scheme quite accurate in time which is generally not used for industrial applications. The objective is to evaluate the influence of using a more simple numerical scheme on the simulations results.
- Number of solutions used for the averaging in LES simulations: due to the computational time costs, comparisons between the models is performed with an ensemble averaging over 10 solutions referred to as cycles. The objective was to evaluate how the number of cycles influences the quality of the results.

For sake of simplicity only results over the median plane P5 are presented when dealing with preliminary tests. Results from the other planes are of course available and are presented for comparing predictions of the σ-model and the dynamic Smagorinsky model. Finally, the influence of the dynamic SGS conductivity is presented.

4.2.1 Statistical convergence of the PIV data

The analysis was performed on a single time at $t = 1.4$ ms which is one the most challenging instant because of the impingement of the ring vortex with the bottom wall as shown in Fig. 4.20.

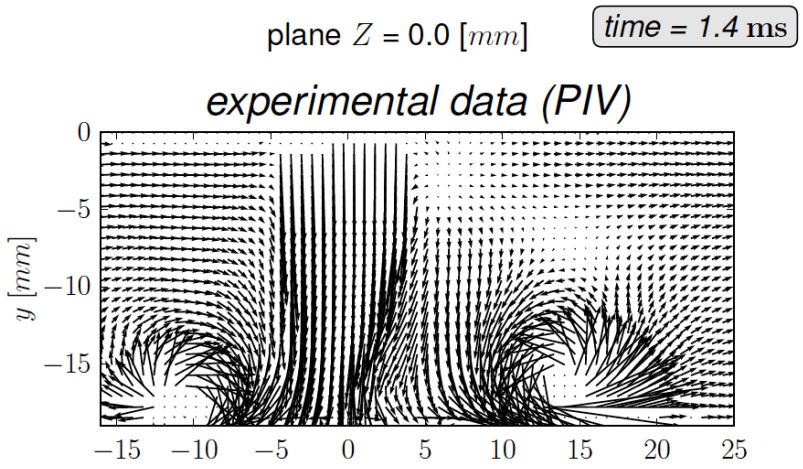

Figure 4.20: PIV results averaged over 400 snapshots at time $t = 1.4$ ms

Different series of averaging were performed respectively over 100, 200, 300, 400 snapshots. The mean velocity and the root mean square (rms) velocity were compared at different sections corresponding roughly (the desired position can not be exactly obtained as in simulation, one has to find the closest pixel line) to $Y = -0.5D$, $Y = -D$, $Y = -1.5D$ and $Y = -1.75D$.

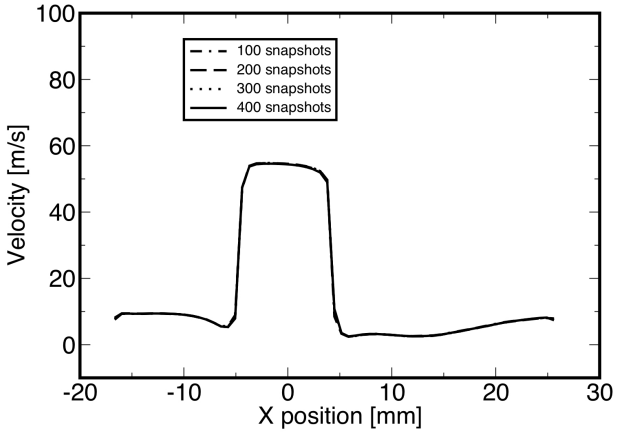

Figure 4.21: Mean velocity at position $Y = -0.5D$ at time $t = 1.6$ ms on the plane P5

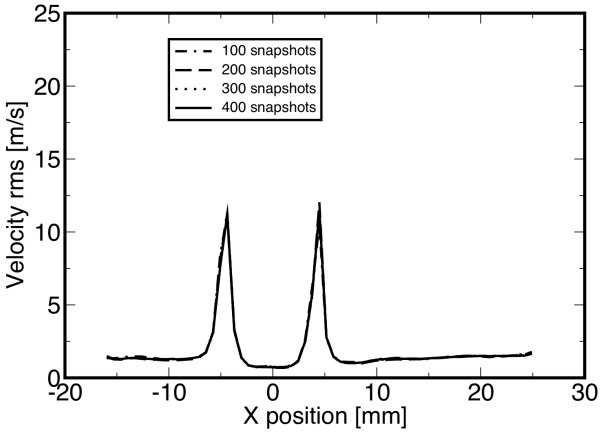

Figure 4.22: rms velocity at position $Y = -0.5D$ at time $t = 1.6$ ms on the plane P5

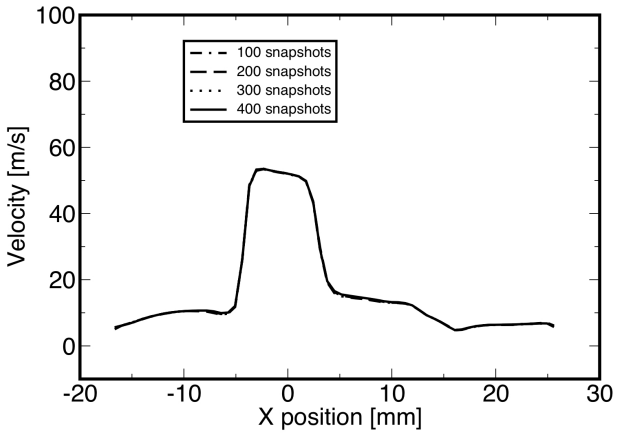

Figure 4.23: Mean velocity at position $Y = -D$ at time $t = 1.6$ ms on the plane P5

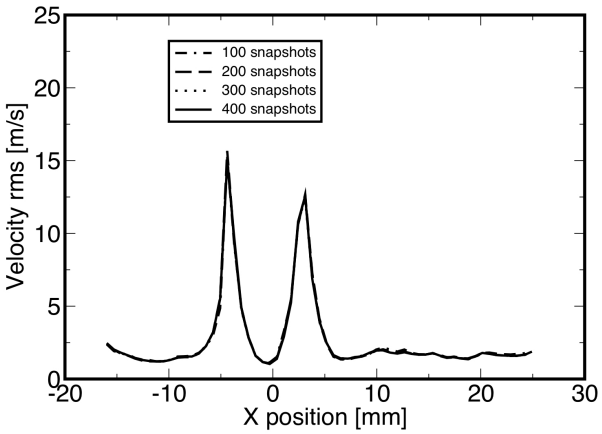

Figure 4.24: rms velocity at position $Y = -D$ at time $t = 1.6$ ms on the plan $Z = 0D$

We can see in Fig. 4.21 to Fig. 4.24 that close to the convergent region the statistics are steady even for the rms velocity. We can also see that in this region the flow is mostly controlled by the inlet condition. The influence of the cross flow starts at $Y = -D$ as shown in Fig. 4.23 and 4.24 for which the velocity is no longer symmetric.

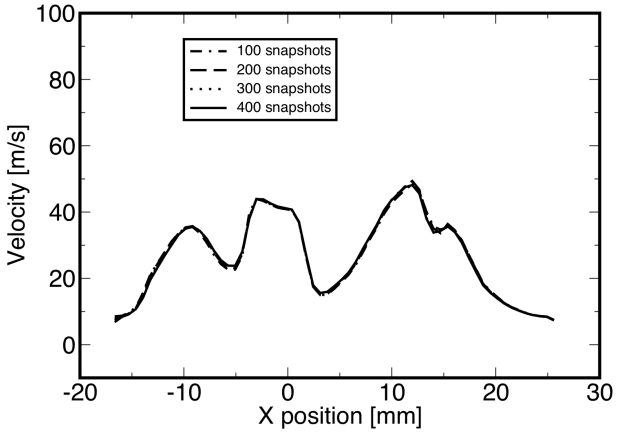

Figure 4.25: Mean velocity at position $Y = -1.5D$ at time $t = 1.6$ ms on the plane P5

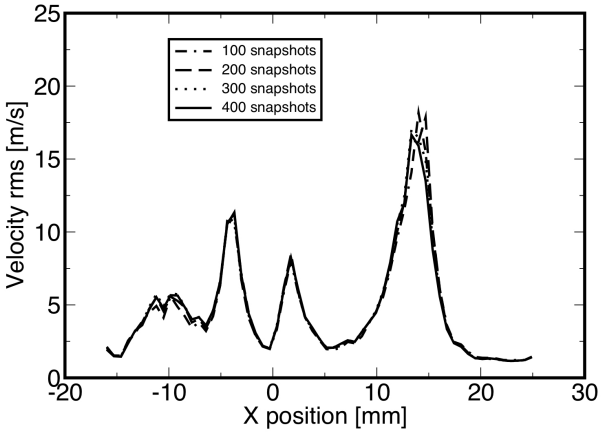

Figure 4.26: rms velocity at position $Y = -1.5D$ at time $t = 1.6$ ms on the plane P5

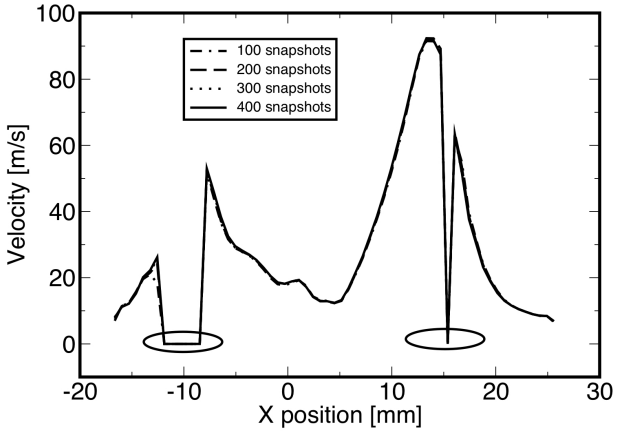

Figure 4.27: Mean velocity at position $Y = -1.75D$ at time $t = 1.6$ ms on the plane P5

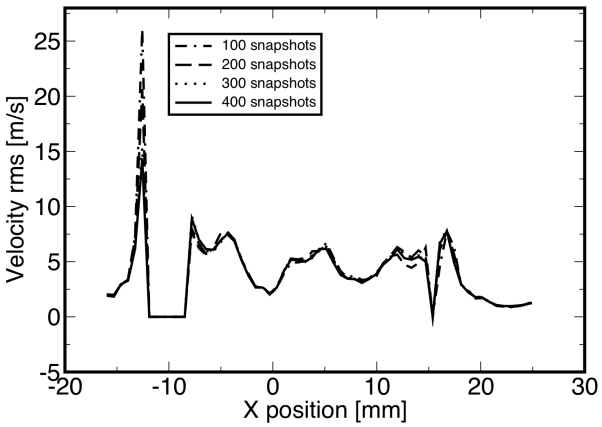

Figure 4.28: rms velocity at position $Y = -1.75D$ at time $t = 1.6$ ms on the plane P5

The same trend as in the convergent is observed in the region close to the wall. Statistic convergence is reached allowing a reliable comparison with the simulation even very close to the wall. However, in the core of the vortex during the impingement specially at $Y = -1.75D$ the post-processing did not provide any valid vectors which leads to a null velocity as shown in Fig. 4.27. Those points will not be considered during the rest of the comparisons.
Finally, an estimation of the error on the PIV measurements was done as proposed in [58] where half of the pixel size is used to estimate the velocity measurement uncertainty:

$$\Delta PIV = \frac{0.5 Pixel}{\Delta t} \tag{4.1}$$

where $\Delta t = 2\mu$s is the time delay between the two laser pulses. For the entire comparison of velocity profiles on the median plane done in what follows $Pixel = 1.07\ 10^{-5}$ m, and then $\Delta PIV \approx 5$ m/s.

This analysis shows that the number of sample collected for performing the PIV measurements are large enough to allow quite reliable comparisons except in the center of the vortices (in the very near wall region) center where unsufficient number of valid vectors were obtained.

4.2.2 Impact of the numerical scheme

As mentioned in the literature review, numerical schemes in LES can have a major impact on the final solution because of the dissipation they may introduce. It was then decided to perform the academic test cases : HIT, turbulent channel and periodic jet with very low dissipative schemes. The two first test cases were performed with AVBP with a Galerkin type scheme (GRK) which is 4^{th} order accurate in space with 3 Runke-Kutta steps integration. As for the periodic jet, a spectral code was used.
However, in industrial applications, the used of those numerical is most ofen not possible. The Lax-Wendroff scheme was then used because it is commonly used at IFPEN for complex geometries. It was then necessary to assess the performances of SGS models in the same framework.

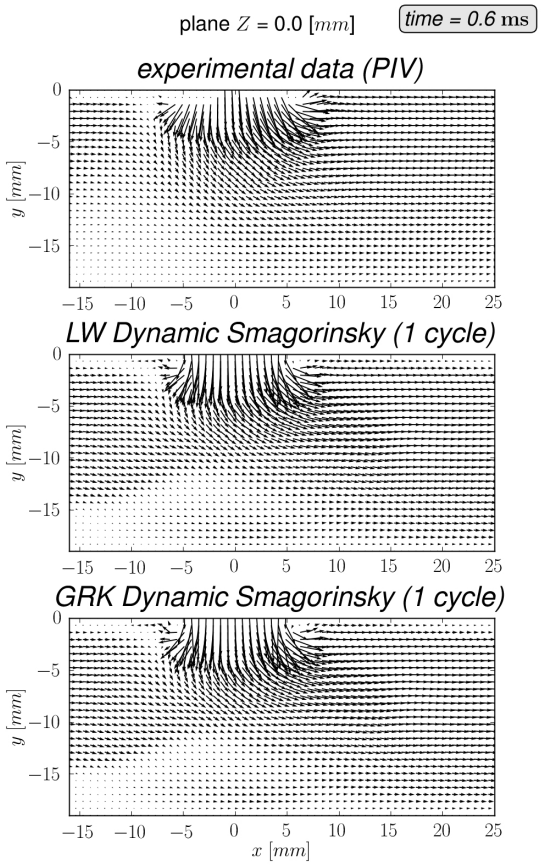

Figure 4.29: Velocity vectors comparison: Influence of the numerical scheme at time $t = 0.6$ ms

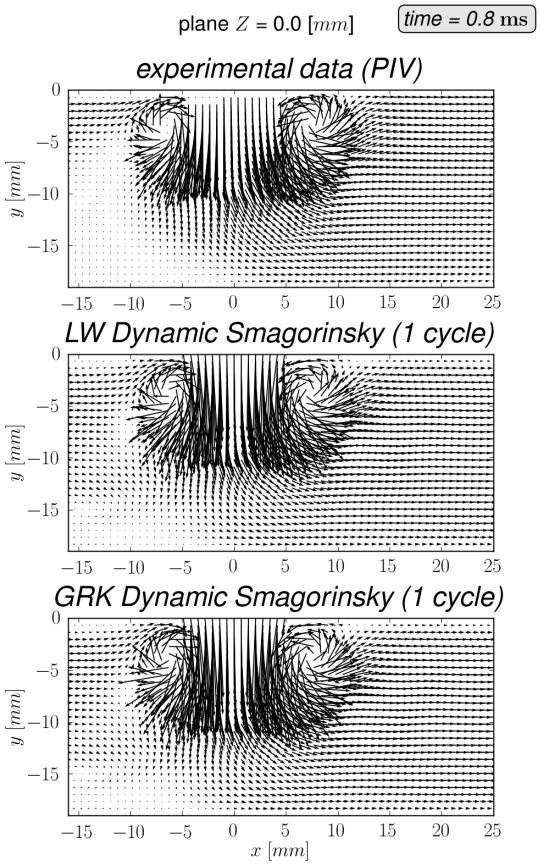

Figure 4.30: Velocity vectors comparison: Influence of the numerical scheme at time $t = 0.8$ ms

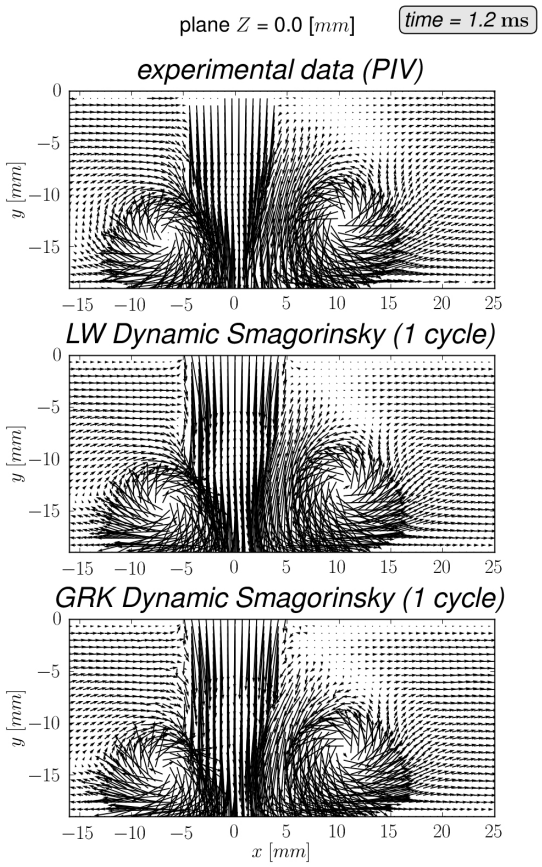

Figure 4.31: Velocity vectors comparison: Influence of the numerical scheme at time $t = 1.2$ ms

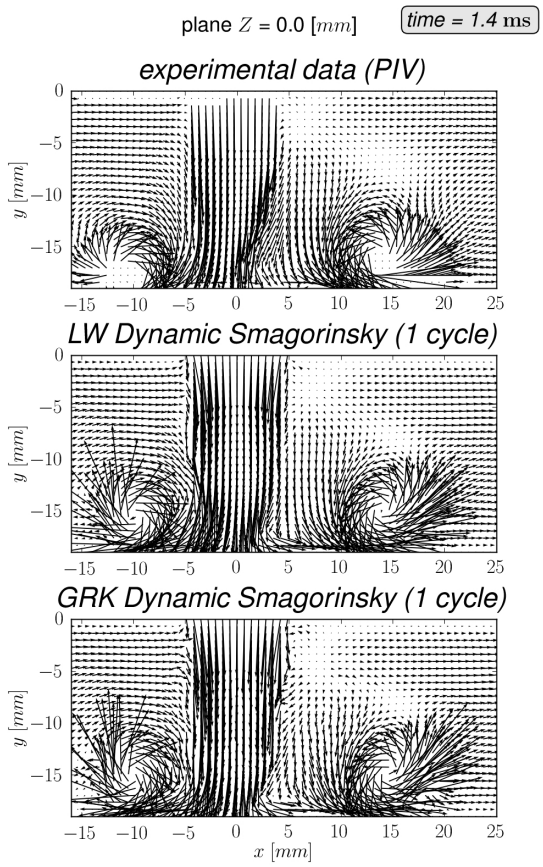

Figure 4.32: Velocity vectors comparison: Influence of the numerical scheme at time $t = 1.4$ ms

Fig 4.29 to Fig 4.38 show comparison between PIV measurements and LES simulations performed with the two numerical schemes from time 0.6 ms to 7 ms. We can see that both numerical schemes lead qualitatively to the same predictions. Before the impingement with the bottom wall, the vortex ring is well predicted. After the impact (at time $t = 1.6$ ms), the propagation of the vortex on the solid surface in both cases is not well predicted. Indeed, the propagation velocity is clearly under-predicted even with the GRK scheme. However, after the complete dissipation of the energy of the vortex, the deviation of the jet by the cross flow is well predicted. The over-estimation of the velocity on the vortices is slightly less pronounced with the GRK after the impingement.

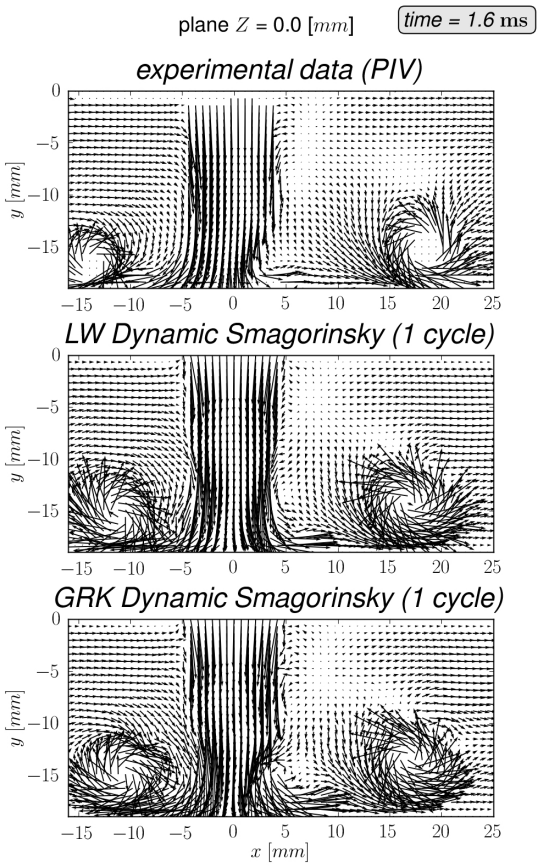

Figure 4.33: Velocity vectors comparison: Influence of the numerical scheme at time $t = 1.6$ ms

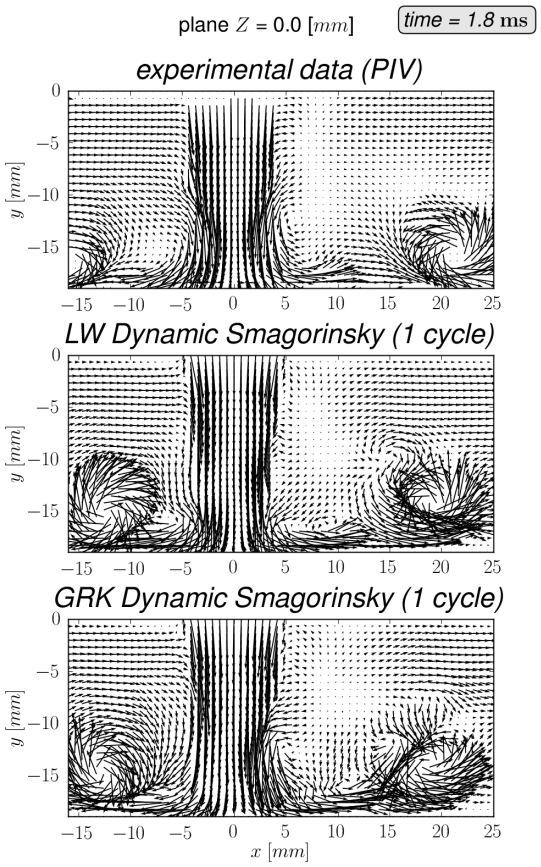

Figure 4.34: Velocity vectors comparison: Influence of the numerical scheme at time $t = 1.8$ ms

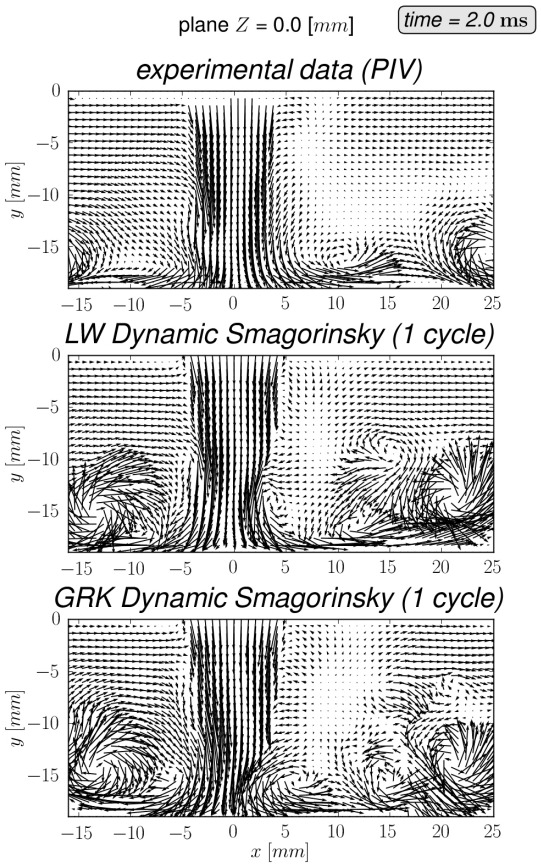

Figure 4.35: Velocity vectors comparison: Influence of the numerical scheme at time $t = 2.0$ ms

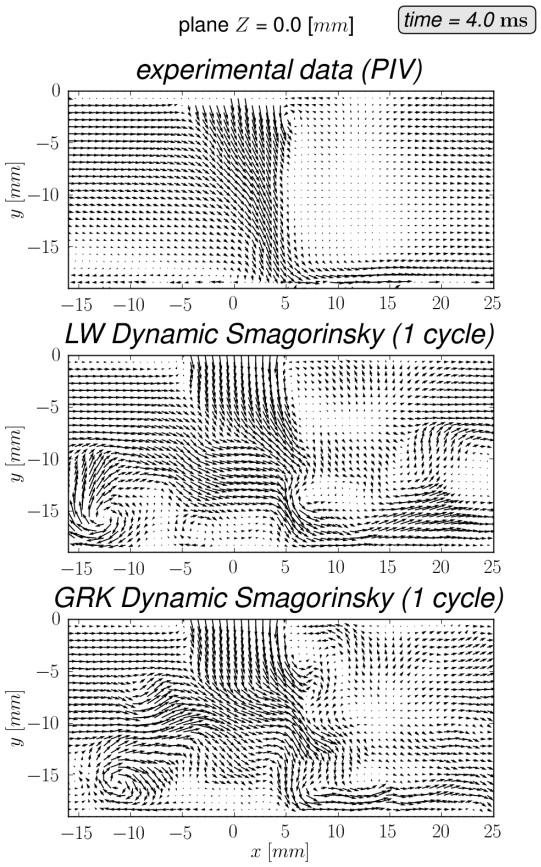

Figure 4.36: Velocity vectors comparison: Influence of the numerical scheme at time $t = 4.0$ ms

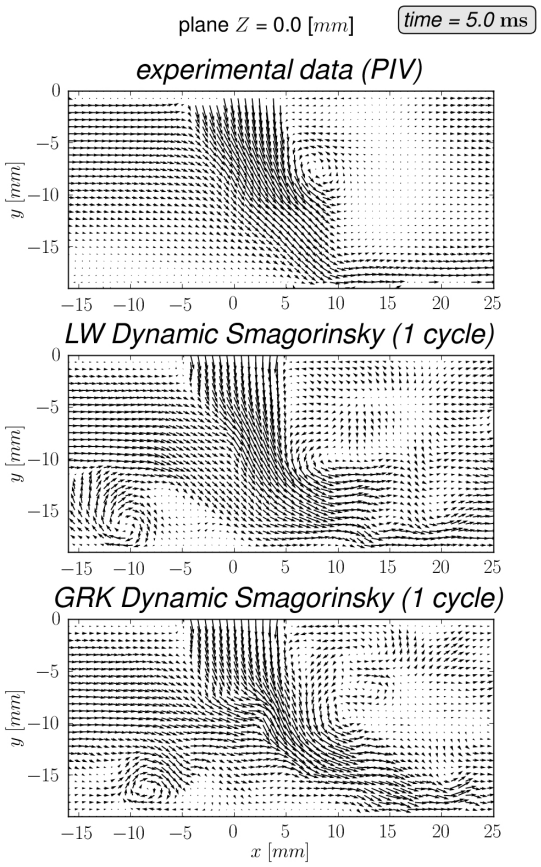

Figure 4.37: Velocity vectors comparison: Influence of the numerical scheme at time $t = 5.0$ ms

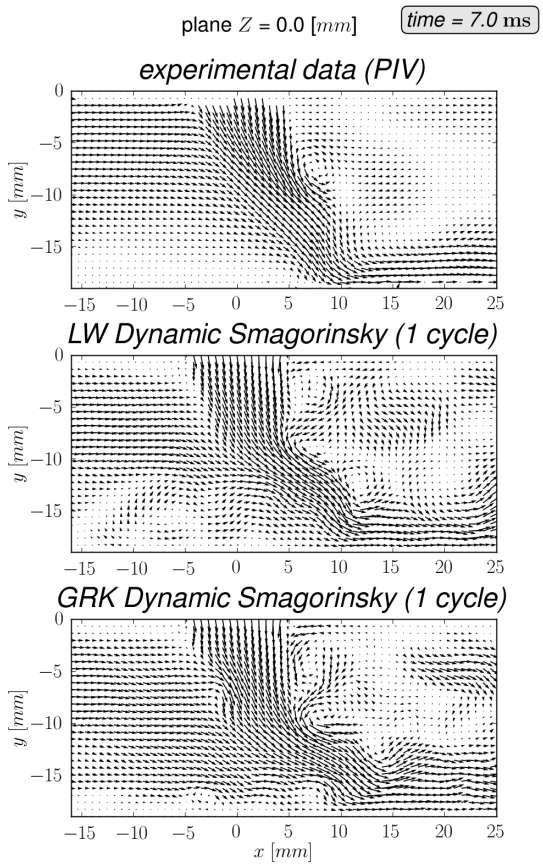

Figure 4.38: Velocity vectors comparison: Influence of the numerical scheme at time $t = 5.0$ ms

Fig. 4.39 to Fig 4.50 show a more precise comparison between the two numerical schemes at different locations $Y = -D$ and $Y = -1.5D$. It confirms the good predictions of the two numerical schemes far from the impingement surface specially at early injection times. Even during the impingement (see Fig. 4.40 and Fig. 4.41), the simulations are in good agreement with the experiment and no noticeable influence of the numerical scheme is observed. The dynamic of the flow is controlled by the inlet flow rate conditions in the near convergent region at the early time. Concerning the late injection times (see Fig. 4.43 and Fig. 4.44), the lack of accumulation over cycles (the numerical results displayed here correspond to one single injection) can explain the difference between simulations and experiments in the near convergent region.

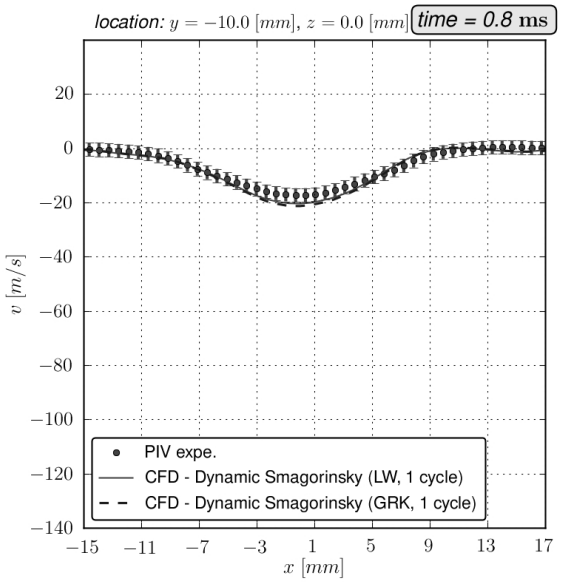

Figure 4.39: Velocity profile comparison: Influence of the numerical scheme at time $t = 0.8$ ms

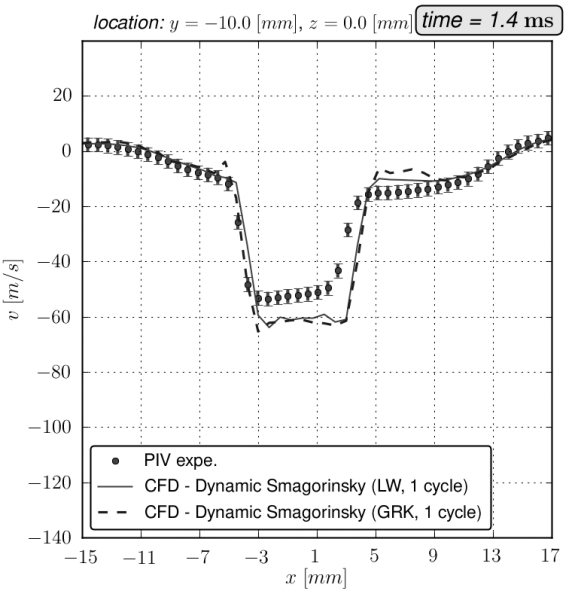

Figure 4.40: Velocity profile comparison: Influence of the numerical scheme at time $t = 1.4$ ms

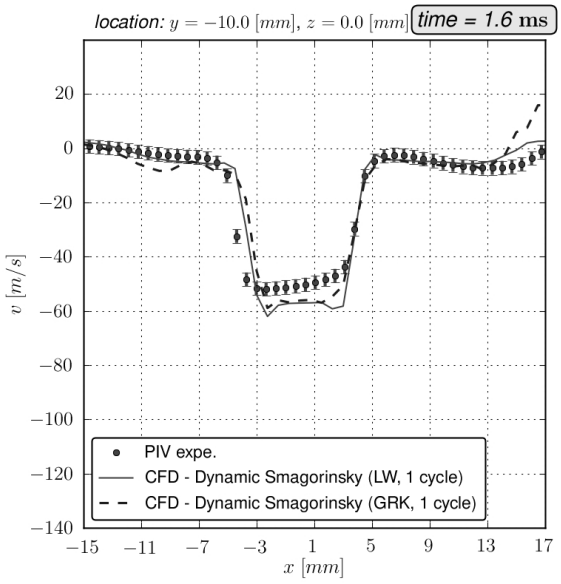

Figure 4.41: Velocity profile comparison: Influence of the numerical scheme at time $t = 1.6$ ms

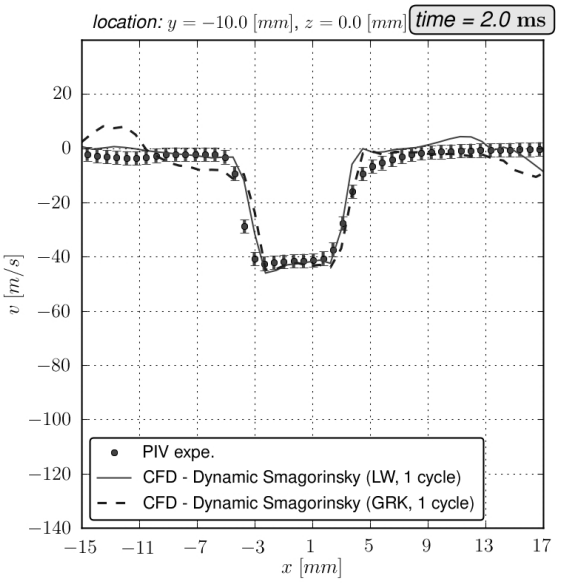

Figure 4.42: Velocity profile comparison: Influence of the numerical scheme at time $t = 2.0$ ms

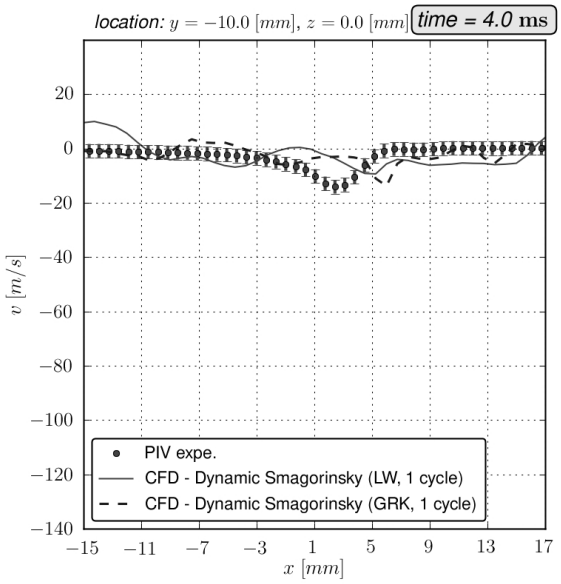

Figure 4.43: Velocity profile comparison: Influence of the numerical scheme at time $t = 4.0$ ms

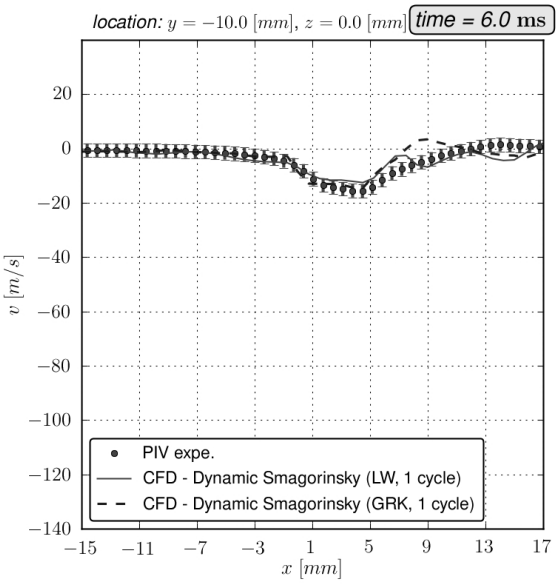

Figure 4.44: Velocity profile comparison: Influence of the numerical scheme at time $t = 6.0$ ms

Concerning the near wall regions at $Y = -1.5D$, during the impingement the bad predictions of the two numerical schemes are due to the convection velocity of the vortex ring which is not correctly retrieved in the simulations. The LW scheme seems to slightly over predict the velocity more than the GRK scheme. Fig. 4.49 and Fig. 4.50 suggest that at late injection times close to the wall a higher number of cycles would be necessary to accurately match the experiment results.

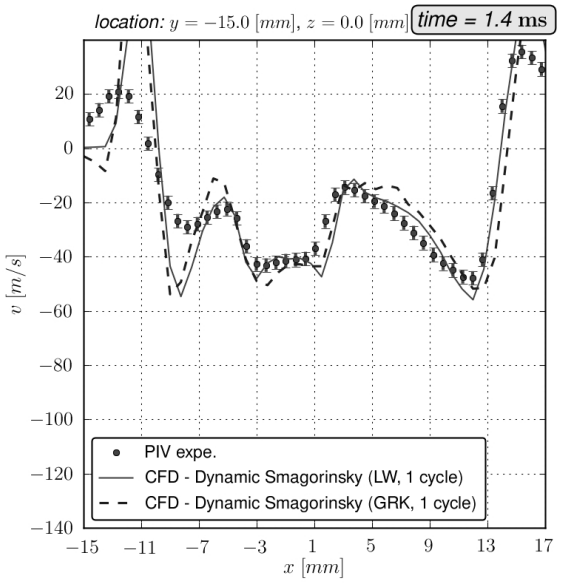

Figure 4.45: Velocity profile comparison: Influence of the numerical scheme at time $t = 1.4$ ms

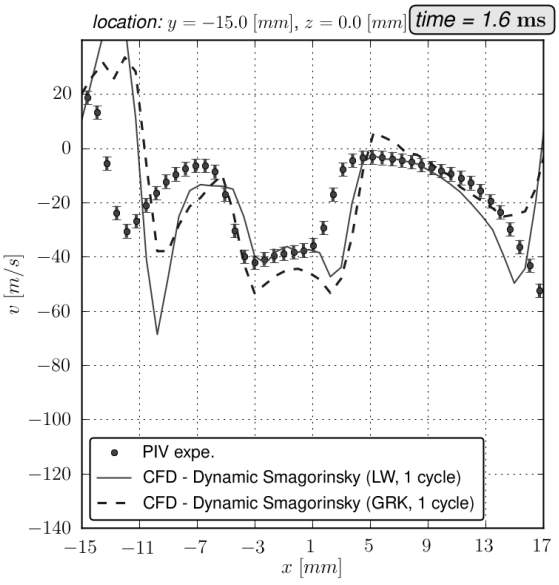

Figure 4.46: Velocity profile comparison: Influence of the numerical scheme at time $t = 1.6$ ms

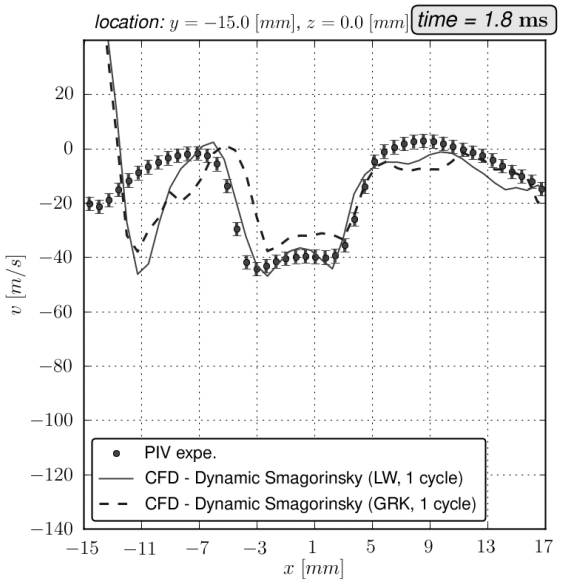

Figure 4.47: Velocity profile comparison: Influence of the numerical scheme at time $t = 1.8$ ms

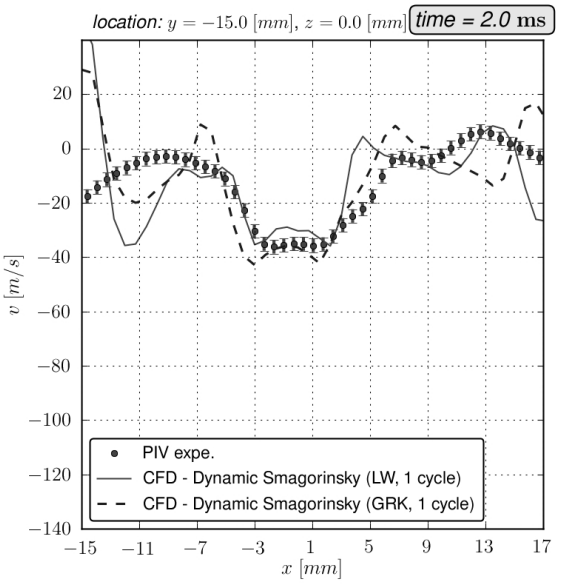

Figure 4.48: Velocity profile comparison: Influence of the numerical scheme at time $t = 2.0$ ms

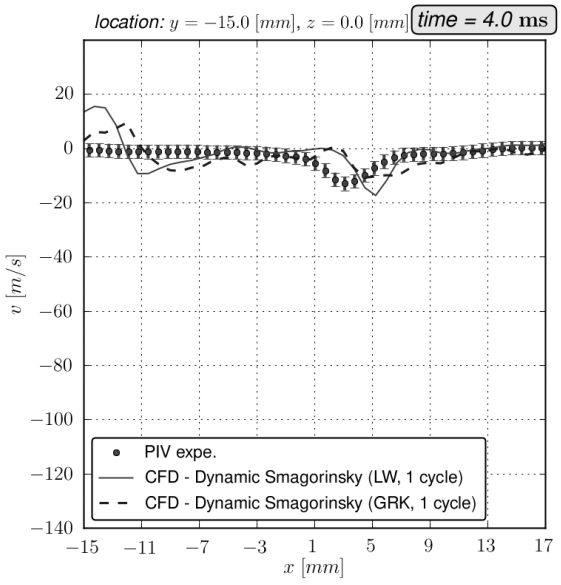

Figure 4.49: Velocity profile comparison: Influence of the numerical scheme at time $t = 4.0$ ms

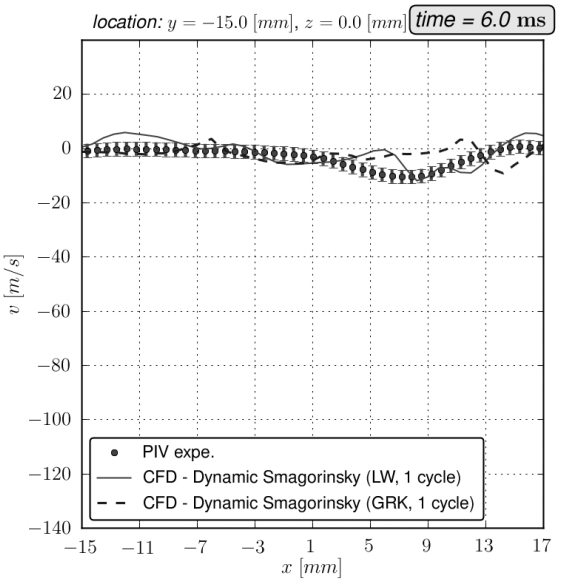

Figure 4.50: Velocity profile comparison: Influence of the numerical scheme at time $t = 6.0$ ms

In conclusion, we note that the influence of the numerical scheme is not that important and simple scheme can be used. Note that this conclusion is not general but holds only for the particular case considered. Moreover, it should be stressed that the two schemes considered are rather "LES compatible" since the corresponding numerical dissipation is quite small (much smaller than the upwind schemes for example). In what follows, simulations are performed with the Lax-Wendroff scheme which is almost 2.5 times faster than the Galerkin scheme. The influence of the number of cycles is potentially more preponderant than the numerical scheme in our configuration. The latter is studied in the next section.

4.2.3 Impact of the number of cycles used for the averaging

Because turbulent flows are very chaotic in nature, a reliable comparison between LES results and PIV measurements can theoretically be done only between statistically converged quantity. Unfortunately, the CPU time required for LES is still an issue and LES results can not be averaged over a large number of solutions as in the experiments for which 400 individuals snapshots were used. It was then decided to perform an ensemble average over 10 solutions (10 cycles) and to compare the results with a single solution (1 cycle) in order to assess the influence of the averaging. Simulations are of course performed with the same model: the dynamic Smagorinsky model. Comparisons are done on the median plane P5.

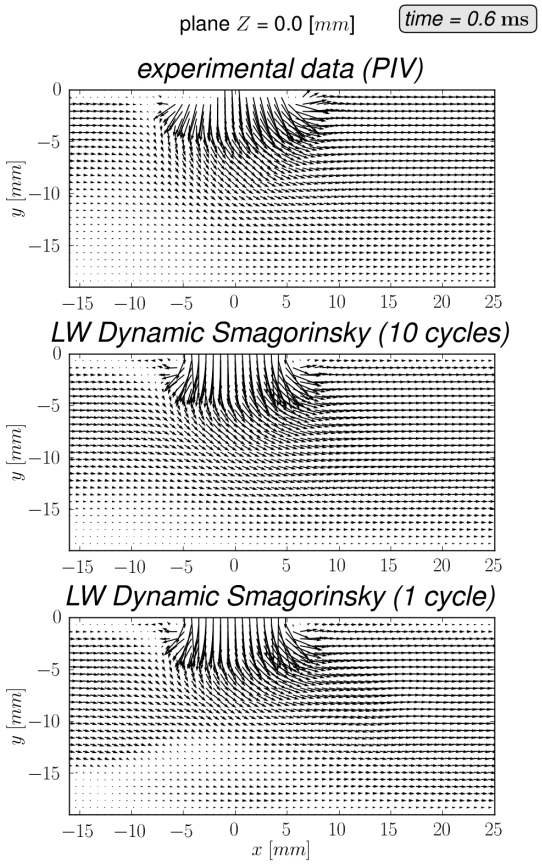

Figure 4.51: Velocity vectors comparison: Influence of the number of solutions for the averaging at time $t = 0.6$ ms

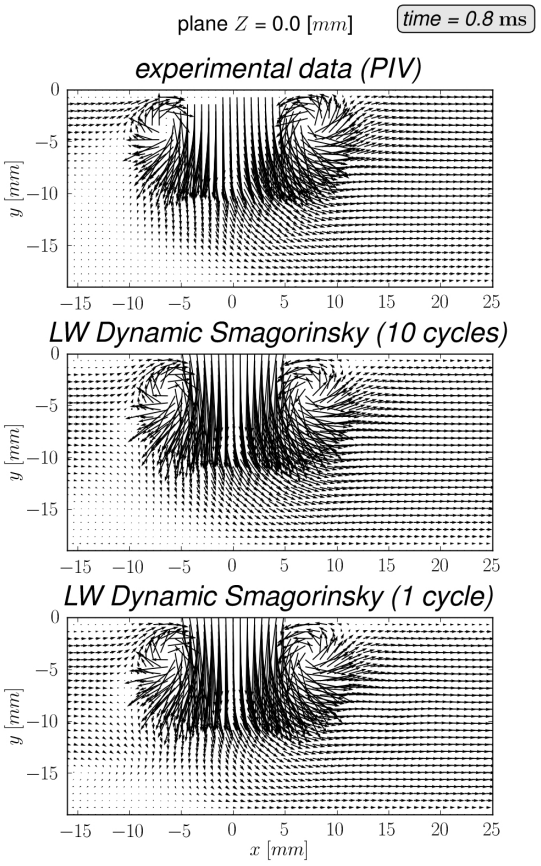

Figure 4.52: Velocity vectors comparison: Influence of the number of solutions for the averaging at time $t = 0.8$ ms

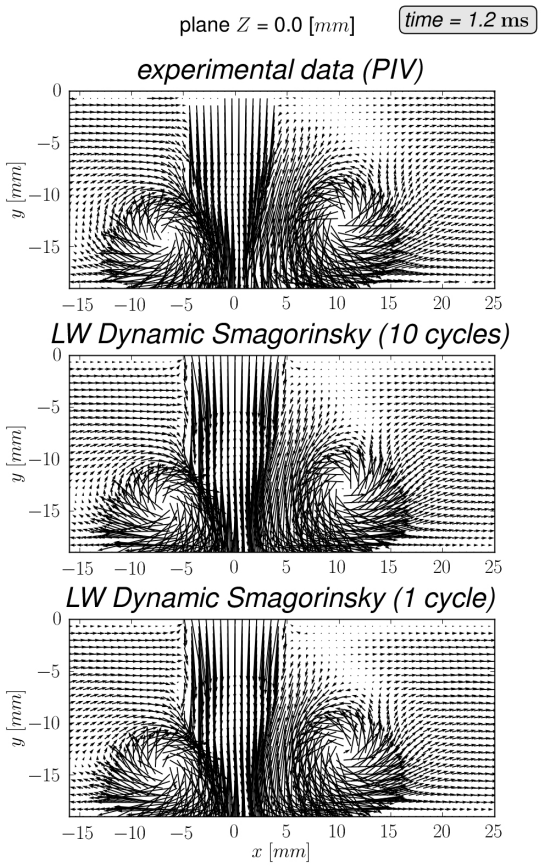

Figure 4.53: Velocity vectors comparison: Influence of the number of solutions for the averaging at time $t = 1.2$ ms

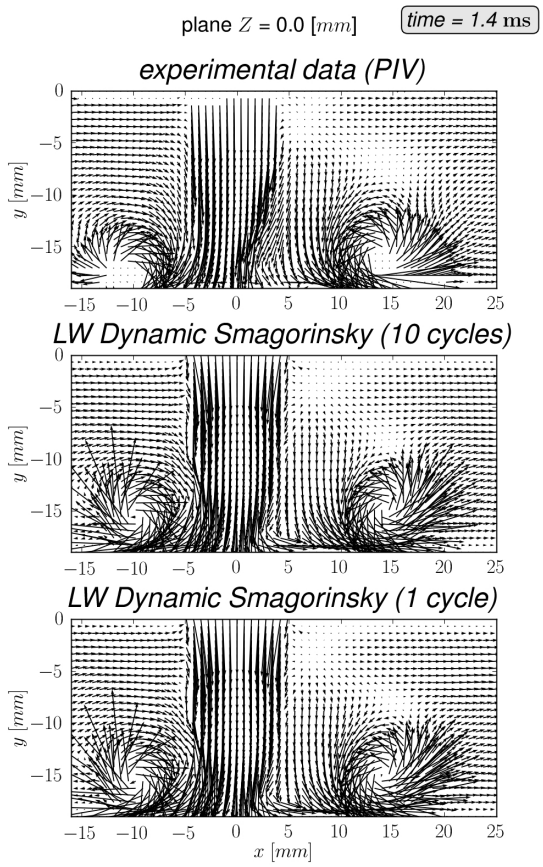

Figure 4.54: Velocity vectors comparison: Influence of the number of solutions for the averaging at time $t = 1.4$ ms

Qualitatively, when looking at the velocity vectors we can see that results for one cycle are quite similar to the results from 10 cycles. There are little differences because: fluctuations are small as the flow is characterized by a controlled pulse jet and large scales vortices (see Fig. 4.51 and Fig. 4.54). This trend is confirmed when examining the velocity profiles (Fig. 4.55 to Fig. 4.58). Indeed, in the region near the convergent both results are similar specially in the core of the jet where the flow is mostly laminar whereas differences become larger in the near wall region where the turbulent activity is stronger.

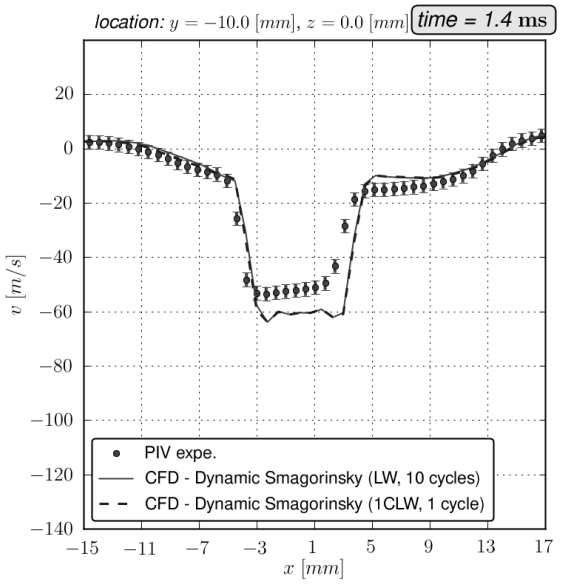

Figure 4.55: Velocity profile comparison: Influence of the number of cycles for the averaging at time $t = 1.4$ ms

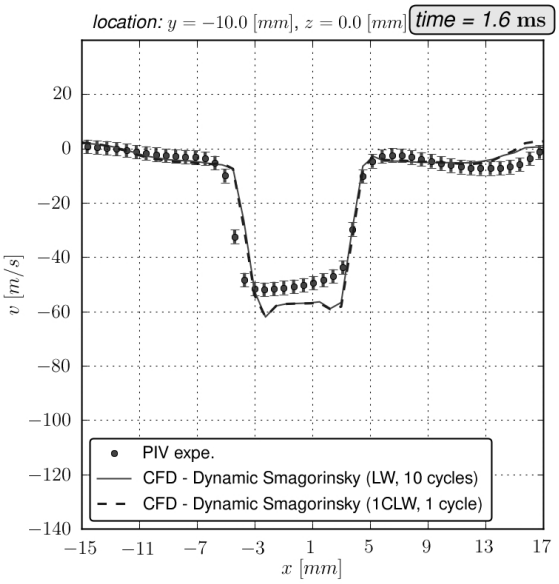

Figure 4.56: Velocity profile comparison: Influence of the number of cycles for the averaging at time $t = 1.6$ ms

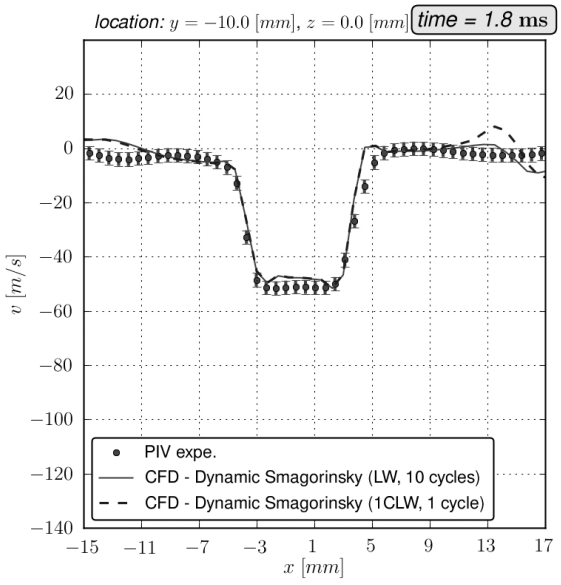

Figure 4.57: Velocity profile comparison: Influence of the number of cycles for the averaging at time $t = 1.8$ ms

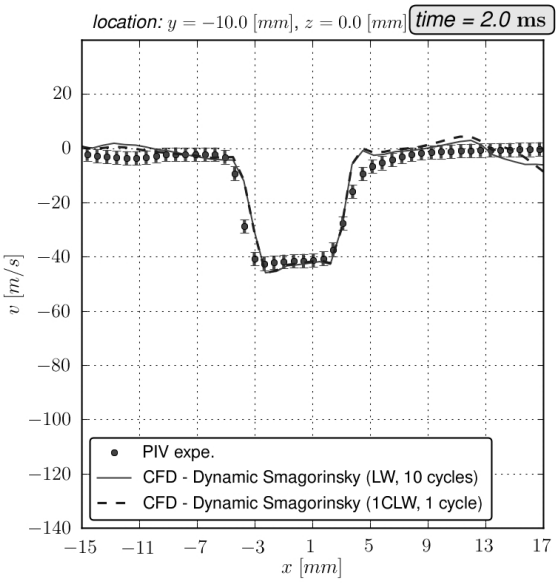

Figure 4.58: Velocity profile comparison: Influence of the number of cycles for the averaging at time $t = 2.0$ ms

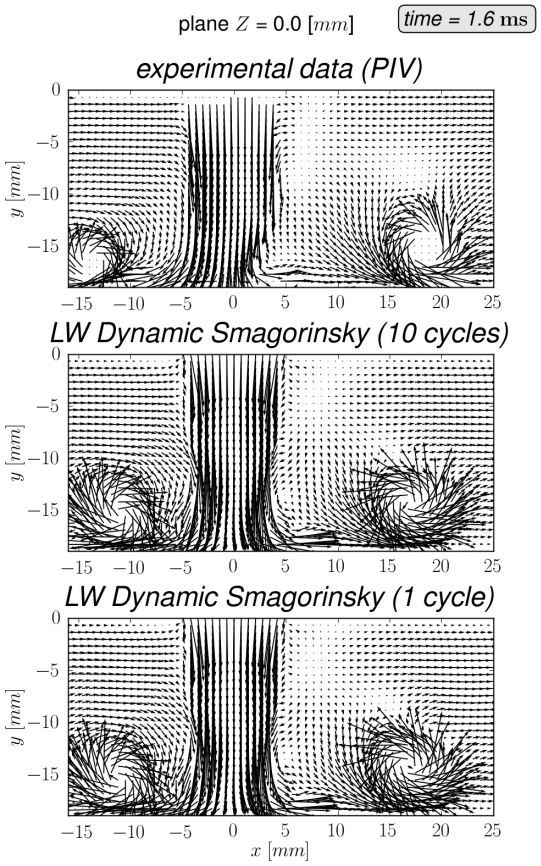

Figure 4.59: Velocity vectors comparison: Influence of the number of solutions for the averaging at time $t = 1.6$ ms

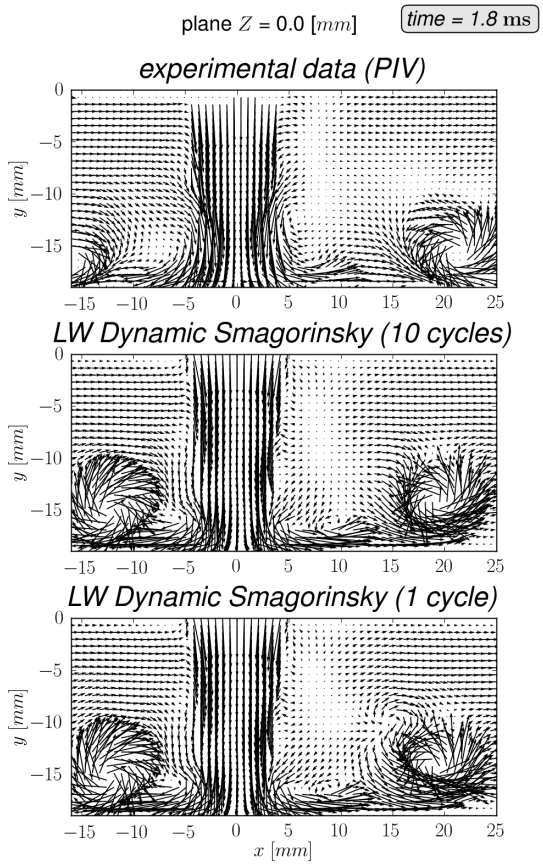

Figure 4.60: Velocity vectors comparison: Influence of the number of solutions for the averaging at time $t = 1.8$ ms

In areas of weak velocities out of the core jet, the averaging over 10 cycles and even more is necessary because the fluctuations level is high compared to the mean velocity value. An averaging over more than 10 cycles would have been necessary to have a better match between the experiments and the simulations specially at the late injection times as shown in Fig. 4.61 and Fig. 4.62.

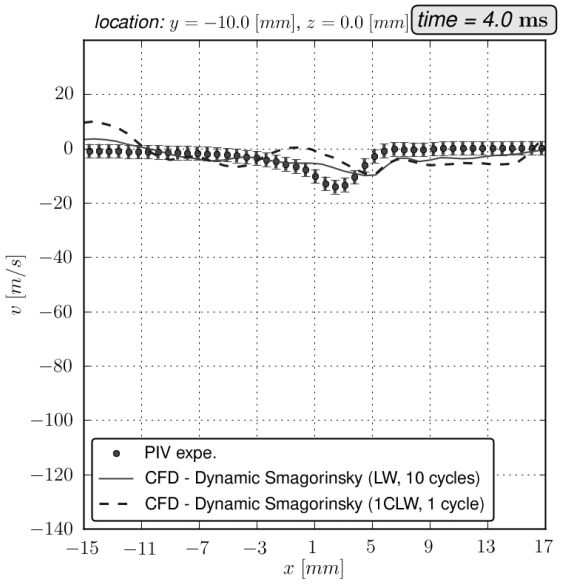

Figure 4.61: Velocity profile comparison: Influence of the number of cycles for the averaging at time $t = 4.0$ ms

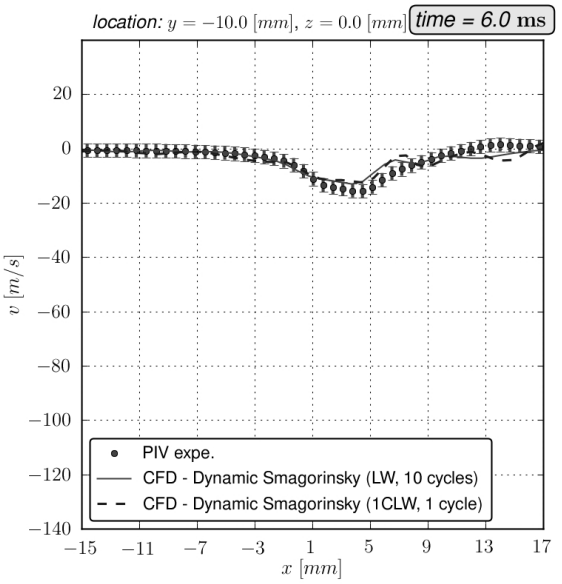

Figure 4.62: Velocity profile comparison: Influence of the number of cycles for the averaging at time $t = 6.0$ ms

Concerning the region close to the wall where the flow is influenced by the presence of the solid boundary, the large difference between LES simulations and the experiment are mostly due to the bad prediction of the convection of the vortex ring. This issue is not related to the averaging issue. There are some improvements with 10 cycles at late injection times but overall, it seems that some errors could not be decreased by increasing the number of averaging (see Fig. 4.67 and Fig. 4.68).

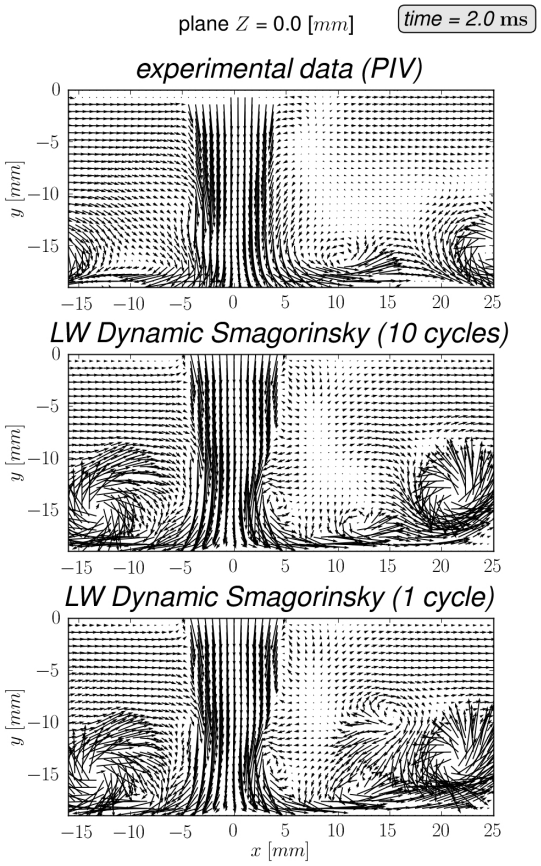

Figure 4.63: Velocity vectors comparison: Influence of the number of solutions for the averaging at time $t = 2.0$ ms

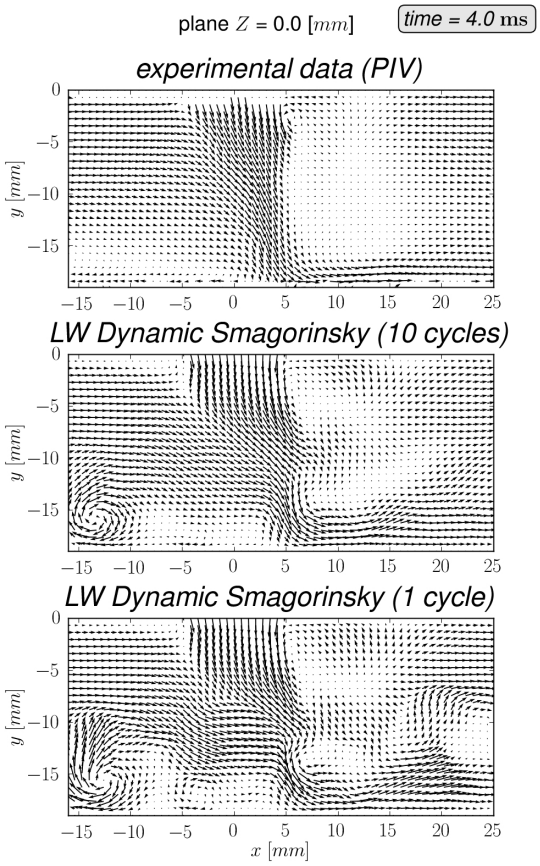

Figure 4.64: Velocity vectors comparison: Influence of the number of solutions for the averaging at time $t = 4.0$ ms

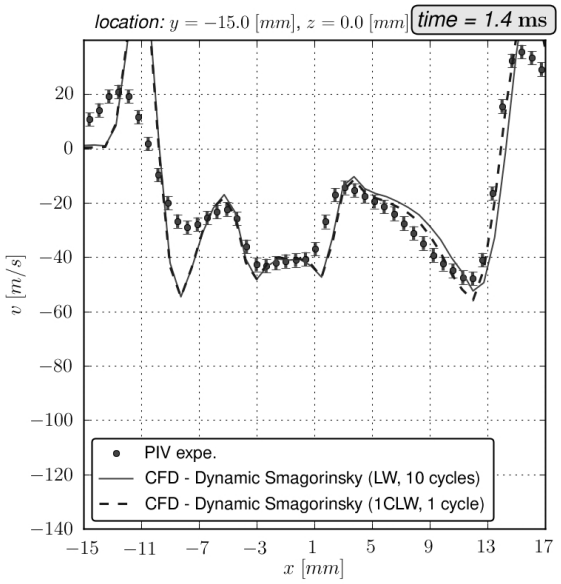

Figure 4.65: Velocity profile comparisons: Influence of the number of cycle for the averaging at time $t =$ 1.4 ms

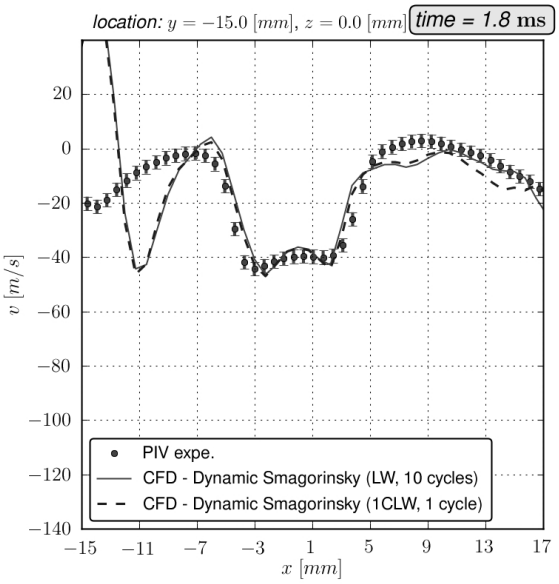

Figure 4.66: Velocity profile comparisons: Influence of the number of cycle for the averaging at time $t =$ 1.8 ms

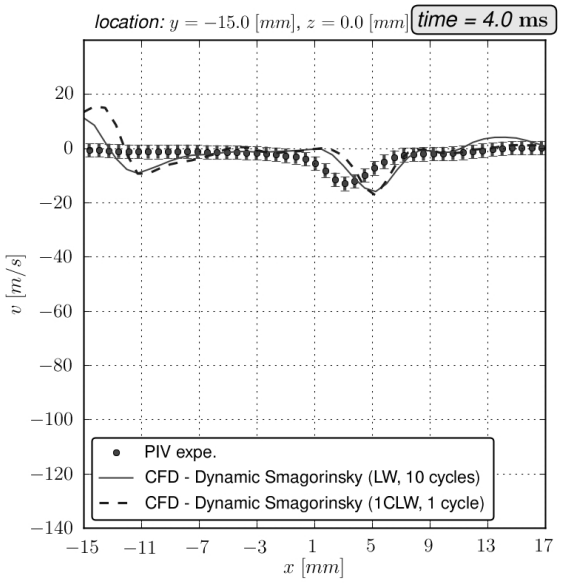

Figure 4.67: Velocity profile comparisons: Influence of the number of cycle for the averaging at time $t =$ 4.0 ms

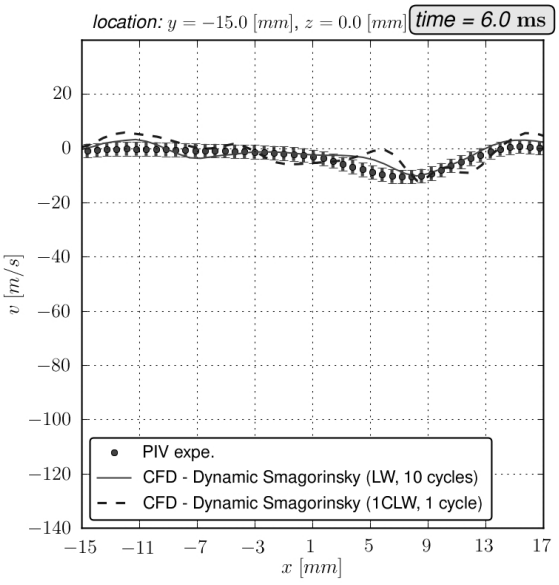

Figure 4.68: Velocity profile comparisons: Influence of the number of cycle for the averaging at time $t =$ 6.0 ms

4.2.4 Impact of the SGS viscosity models

The precedent tests allowed to evaluate how the numerical scheme and the numbers of cycles computed could impact the quality of the LES simulations. No influence of the buoyancy forces were observed neither (not shown here). In what follows, the influence of the SGS viscosity model is investigated by comparing results from the σ-model and the dynamic Smagorinsky model. In both cases, results are averaged over

10 cycles and performed and with the Lax-Wendroff scheme. The region of interest is divided into two parts: the near convergent region (NC region) which starts from the convergent exit $Y = 0D$ to $Y = 1D$ and the near wall region (NW region) starting from $Y = 1D$ to the impingement surface $Y = 2D$.

Qualitative analysis: Velocity vectors fields

It can be seen in Fig. 4.69 to Fig. 4.71 that in the early injection time predictions from the two models are quite similar. This is not surprising because in this phase the dynamic of the flow is mostly controlled by the large dominant structures induced by the inlet flow rate conditions.

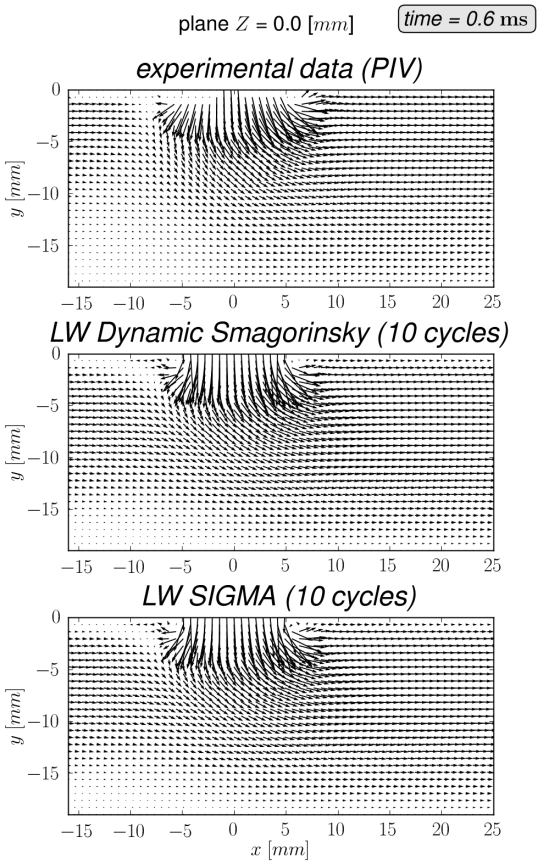

Figure 4.69: Velocity vectors comparison: Influence of the SGS model at time $t = 0.6$ ms on the plane P5

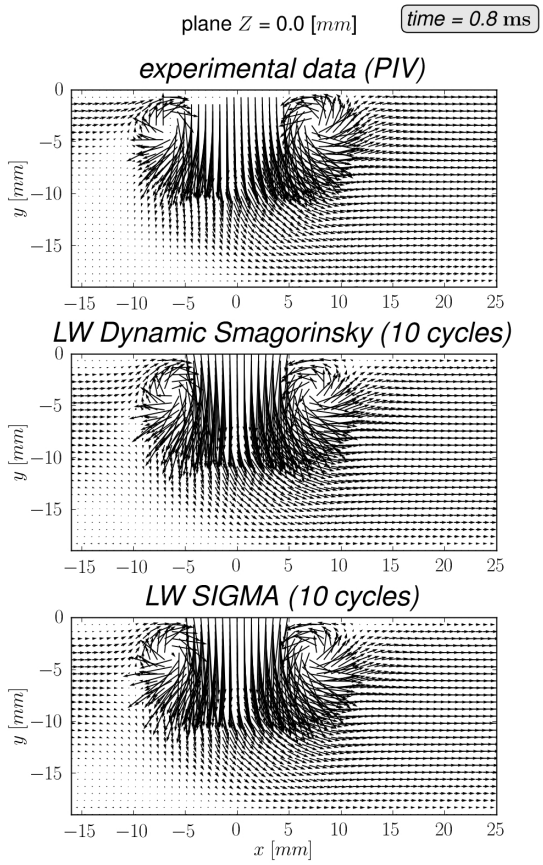

Figure 4.70: Velocity vectors comparison: Influence of the SGS model at time $t = 0.8$ ms on the plane P5

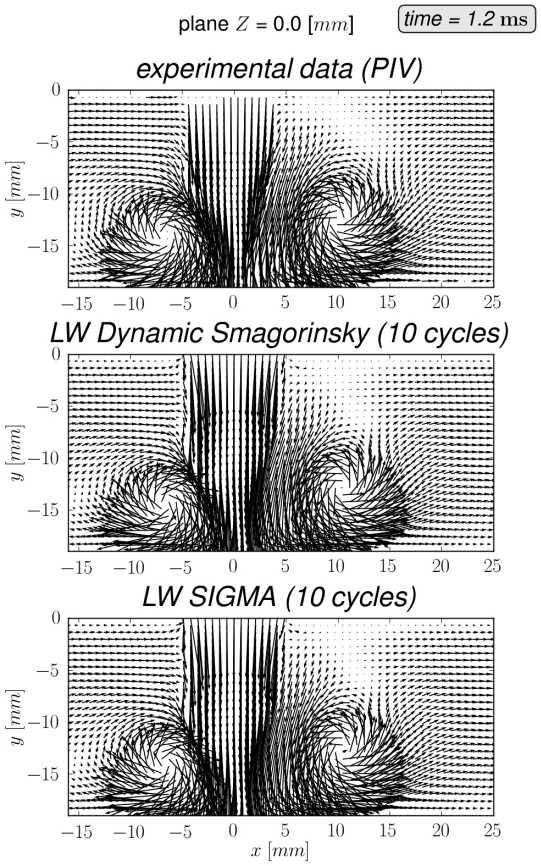

Figure 4.71: Velocity vectors comparison: Influence of the number of the SGS model at time $t = 1.2$ ms on the plane P5

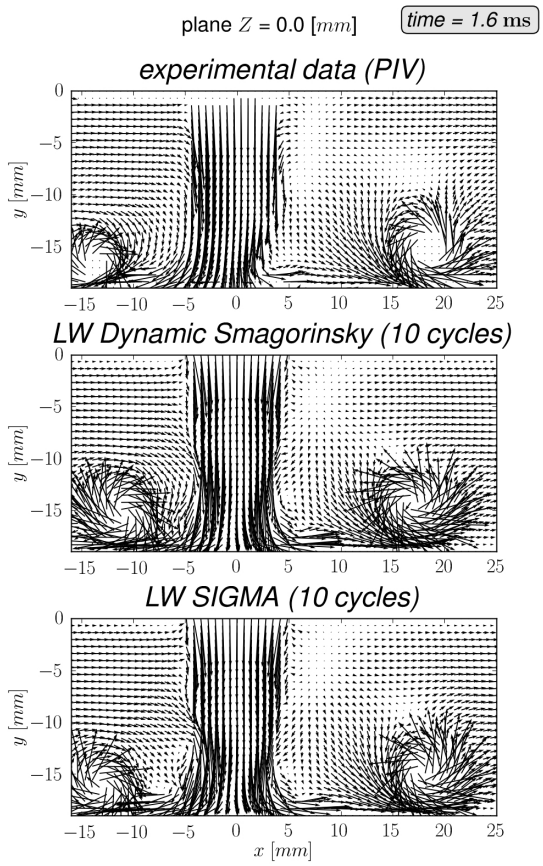

Figure 4.72: Velocity vectors comparison: Influence of the SGS model at time $t = 1.6$ ms on the plane P5

In the second phase (Fig. 4.72 to Fig. 4.75), during the interaction between the vortex ring and the wall, we can see the first differences between the two SGS models. The convection velocity of the vortex ring is well predicted by the σ-model but not as well by the dynamic Smagorinsky model. This is especially true on the upstream side of the impingement point ($X < 0$).

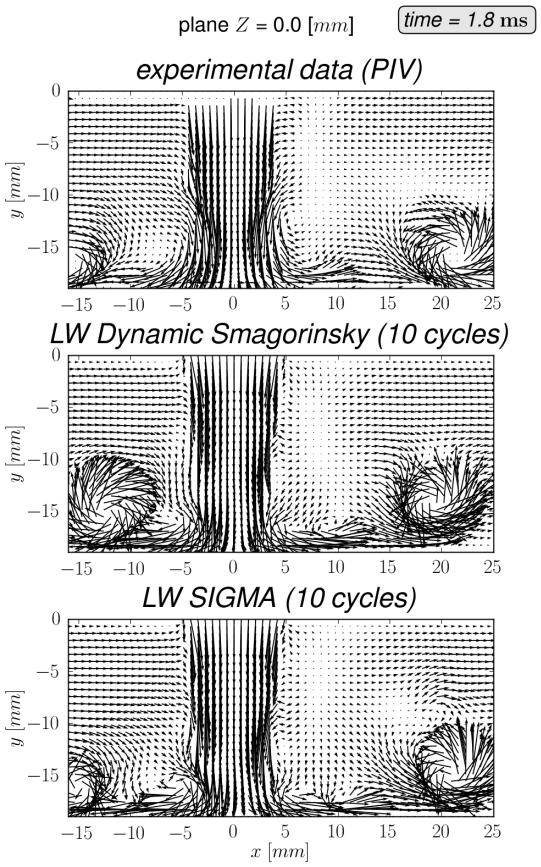

Figure 4.73: Velocity vectors comparison: Influence of the SGS model at time $t = 1.8$ ms on the plane P5

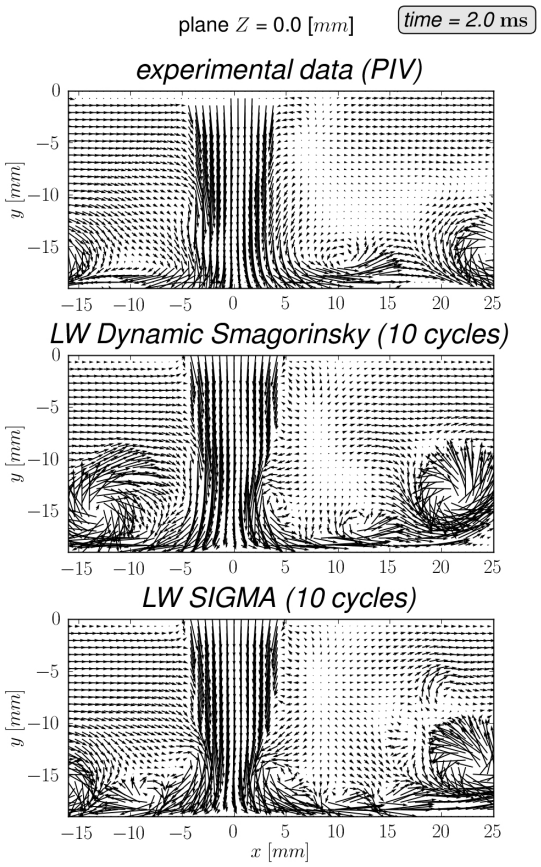

Figure 4.74: Velocity vectors comparison: Influence of the SGS model at time $t = 4.0$ ms on the plane P5

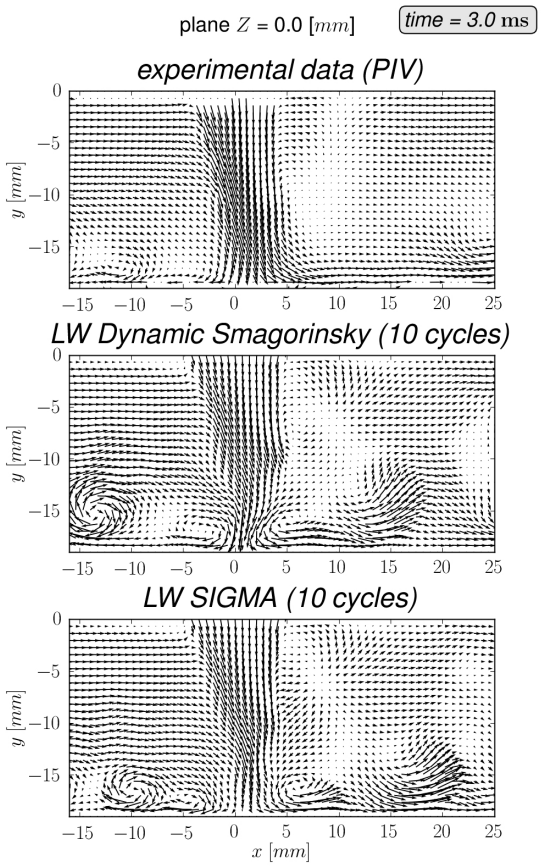

Figure 4.75: Velocity vectors comparison: Influence of the SGS model at time $t = 3.0$ ms on the plane P5

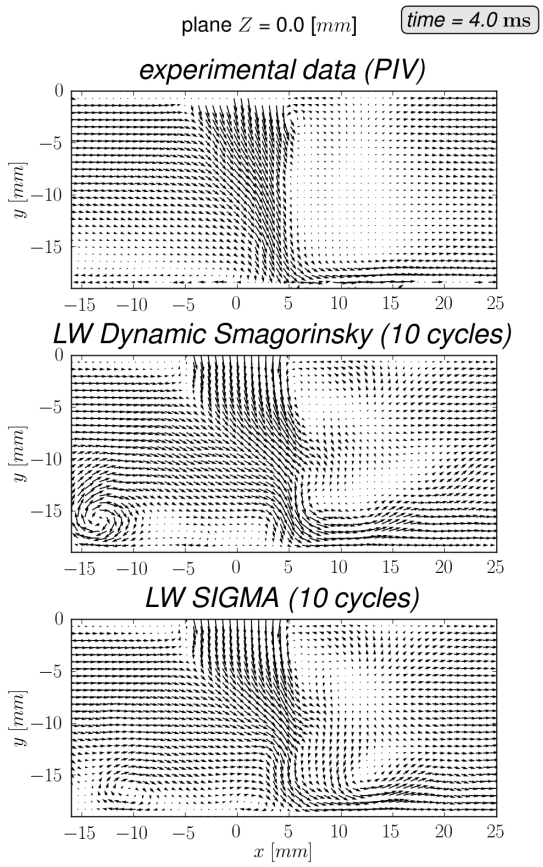

Figure 4.76: Velocity vectors comparison: Influence of the SGS model at time $t = 4.0$ ms on the plane P5

For the late injection times, predictions of the σ-model and the experiment are also in good agreement. In both cases, the vortices are already out of the visualization section and the deviation of the jet is well predicted. Concerning the dynamic Smagorinsky model, the vortex on the left hand side is still inside the visualization section as it can be seen in Fig.4.75 and Fig.4.76.

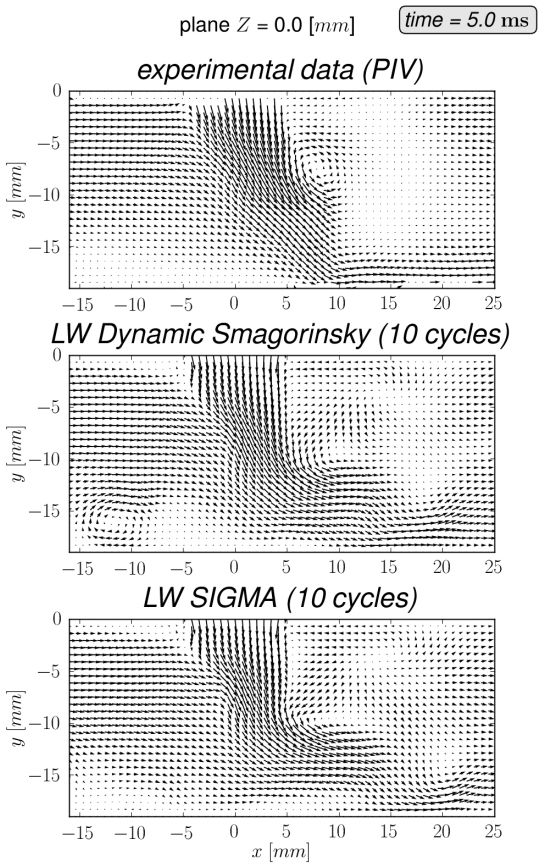

Figure 4.77: Velocity vectors comparison: Influence of the SGS model at time $t = 4.0$ ms on the plane P5

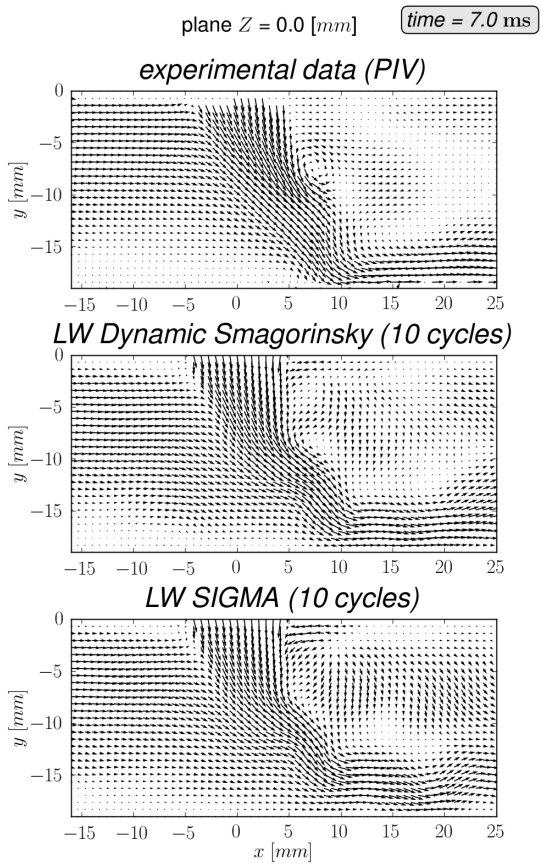

Figure 4.78: Velocity vectors comparison: Influence of the SGS model at time $t = 7.0$ ms on the plane P5

The trend observed on the median plane $Z = 0$ mm is confirmed on the other planes. On the plane $X = 0$ mm (see Fig. 4.79 to Fig. 4.82) the convection velocity of the vortex ring on the wall is under estimated by the dynamic Smagorinsky model. In contrary, the σ-model leads to results in good agreement in the spanwise direction.

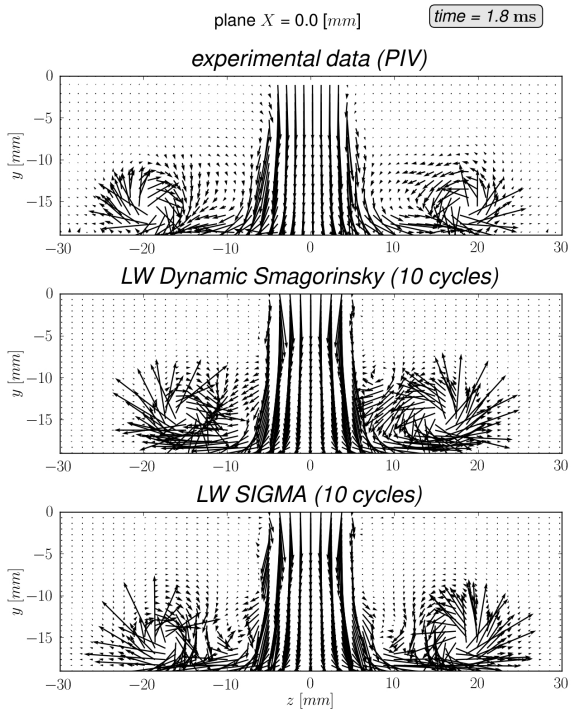

Figure 4.79: Velocity vectors comparison: Influence of the SGS model at time $t = 1.8$ ms on the plane P1

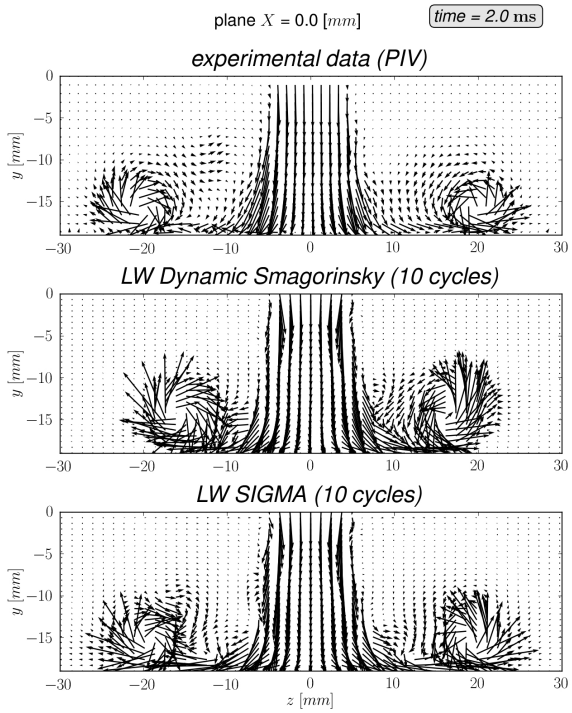

Figure 4.80: Velocity vectors comparison: Influence of the SGS model at time $t = 2.0$ ms on the plane P1

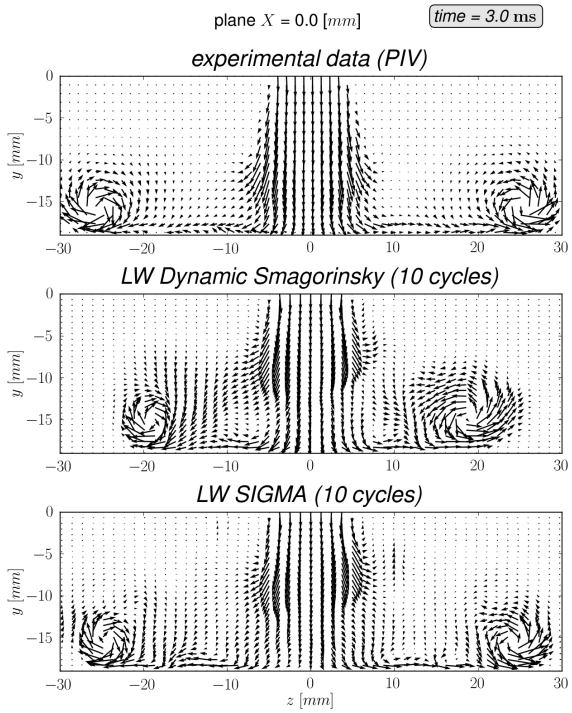

Figure 4.81: Velocity vectors comparison: Influence of the SGS model at time $t = 3.0$ ms on the plane P1

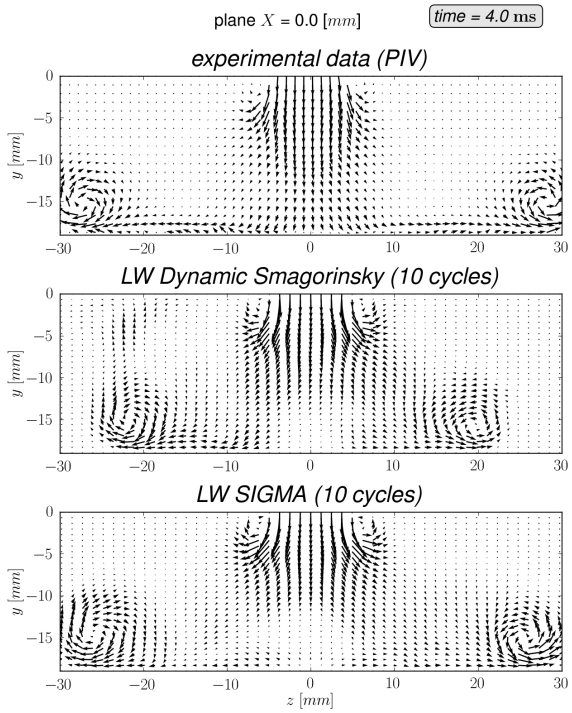

Figure 4.82: Velocity vectors comparison: Influence of the SGS model at time $t = 4.0$ ms on the plane P1

In order to better understand the difference between the predictions of the two SGS models, the SGS viscosity field on the plane just above the impingement plate was analyzed. The vertical median plane is colored by the velocity vector and the horizontal (situated on the first off grid point) plane by the SGS viscosity. We can see that because the SGS viscosity of the dynamic Smagorinsky model relies explicitly on the mesh resolution (through the Leonard term and the use of the test filter) its prediction at early times without the jet gives an estimation of the mesh quality: refined in the measurement section and coarse far from this section (see Fig. 4.83). Although the two models depend on the initial filter size Δ, mesh variations affect the dynamic Smagorinsky model more than the σ-model. This is probably because when the initial filter mesh Δ is coarse the test filter $\hat{\Delta}$ is even coarser. The evaluation of the useful terms (L_{ij} and M_{ij} terms) is not accurate specially near the walls where the hypothesis of low variations of the dynamic constant that can be taken out of the test filter is not true.

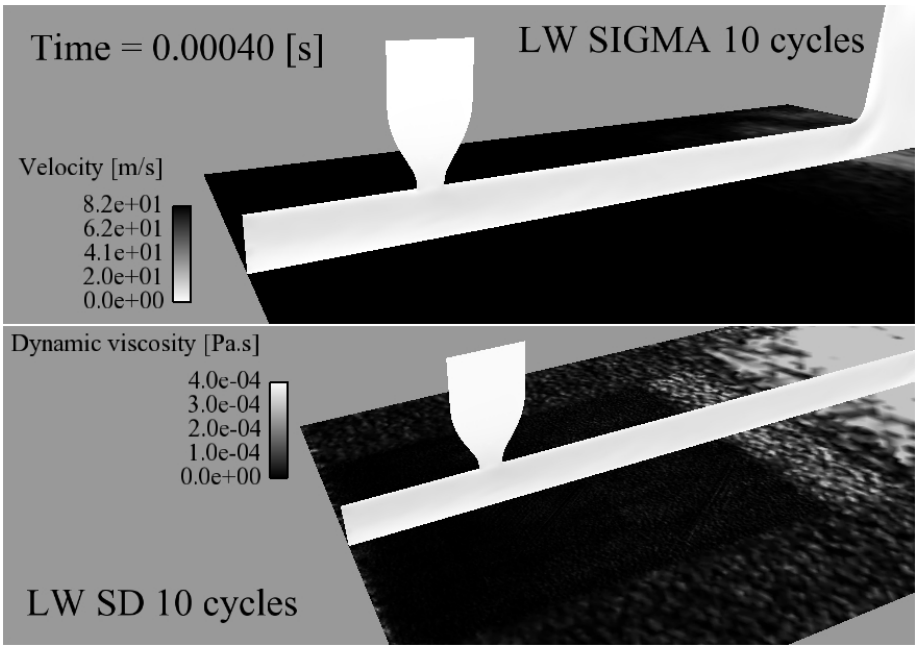

Figure 4.83: SGS viscosity comparison at time $t = 0.4$ ms

We can see that during the impingement the SGS viscosity of the Smagorinsky model (see Fig. 4.84 to Fig. 4.85) increases which leads to a rapid dissipation of the strength of the vortex ring and to a bad convection of the vortex ring along the wall. Concerning the σ-model the level of SGS viscosity does not increase during the impingement of the vortex because the model automatically vanishes in the near wall region and at stagnation point; the strength of the vortex ring is thus not dissipated which leads to a better convection.

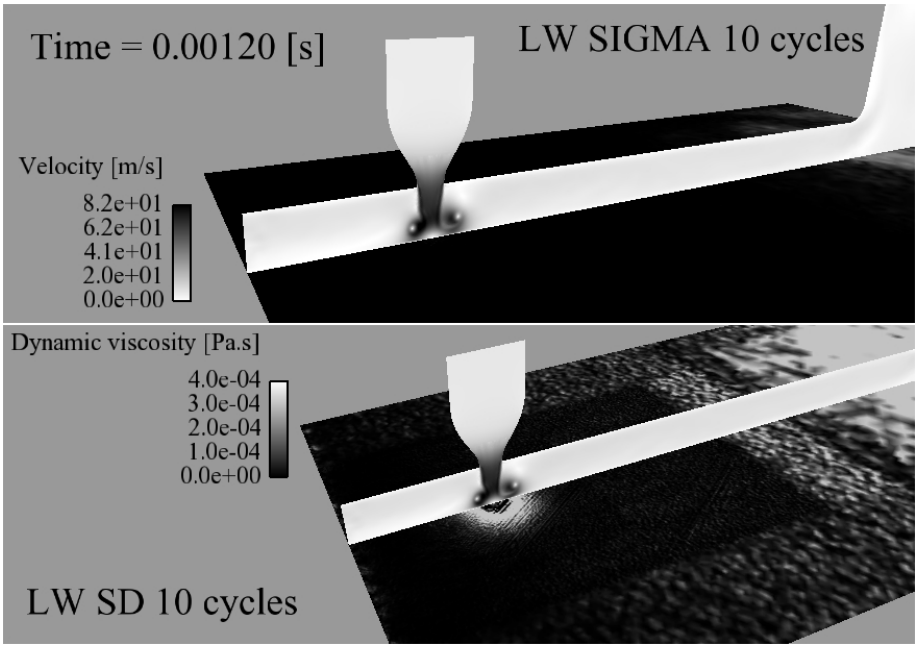

Figure 4.84: SGS viscosity comparison at time $t = 1.2$ ms

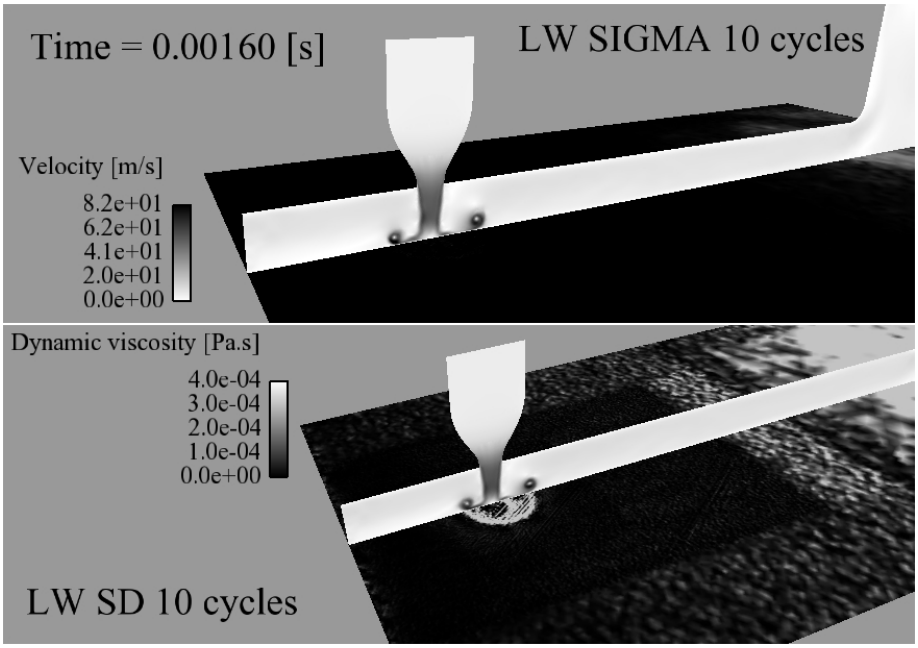

Figure 4.85: SGS viscosity comparison at time $t = 1.6$ ms

At later time $t = 6.0$ ms as shown in Fig. 4.86, the interaction between the jet and the solid boundary is less important and the deviation of the jet is well predicted also by the dynamic Smagorinsky model.

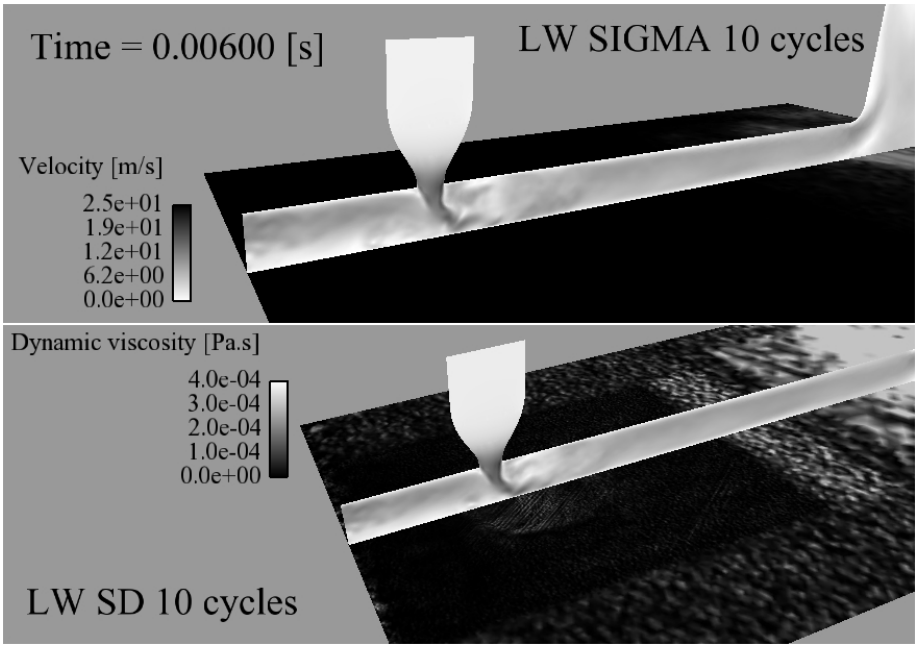

Figure 4.86: SGS viscosity comparison at time $t = 6.0$ ms

The observation from the velocity field are also confirmed by a comparison of the SGS viscosity field on plane P5.

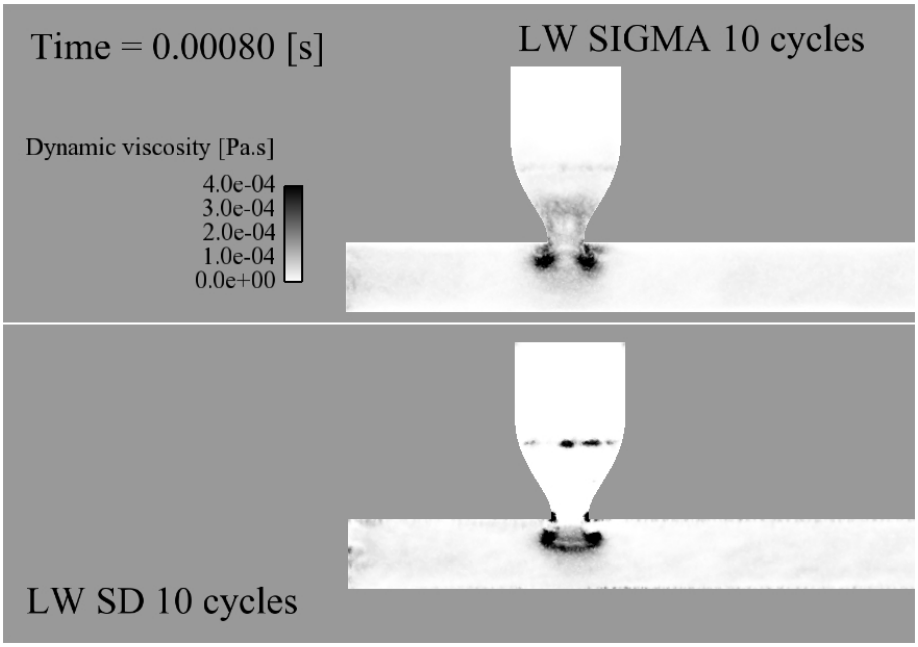

Figure 4.87: SGS viscosity field on plane P5 at time $t = 0.8$ ms

At early time ($t = 0.8$ ms), predictions of the two models are of the same order of magnitude as shown in Fig. 4.87. SGS viscosity predictions are mostly in the vortices region and at the shear regions between the injected nitrogen and the air cross flow.

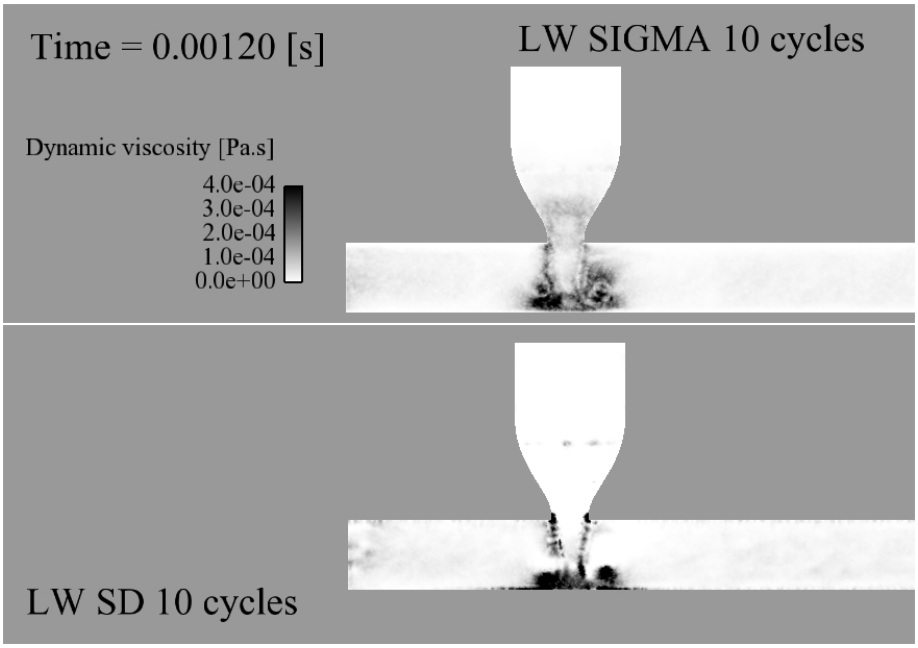

Figure 4.88: SGS viscosity field on plane P5 at time $t = 1.2$ ms

During the impingement, differences appear in the region close to the bottom wall where the SGS viscosity of the dynamic Smagorinsky model strongly increases. This increase leads as already mentioned to a bad prediction of the propagation velocity of the vortices by the dynamic Smagorinsky model (see Fig. 4.88 and Fig. 4.89). At later injection times, when the influence of the bottom wall on the flow is negligible, predictions of the two models are again of the same order of magnitude which confirms the similar results obtained for the velocity field (see Fig. 4.90).

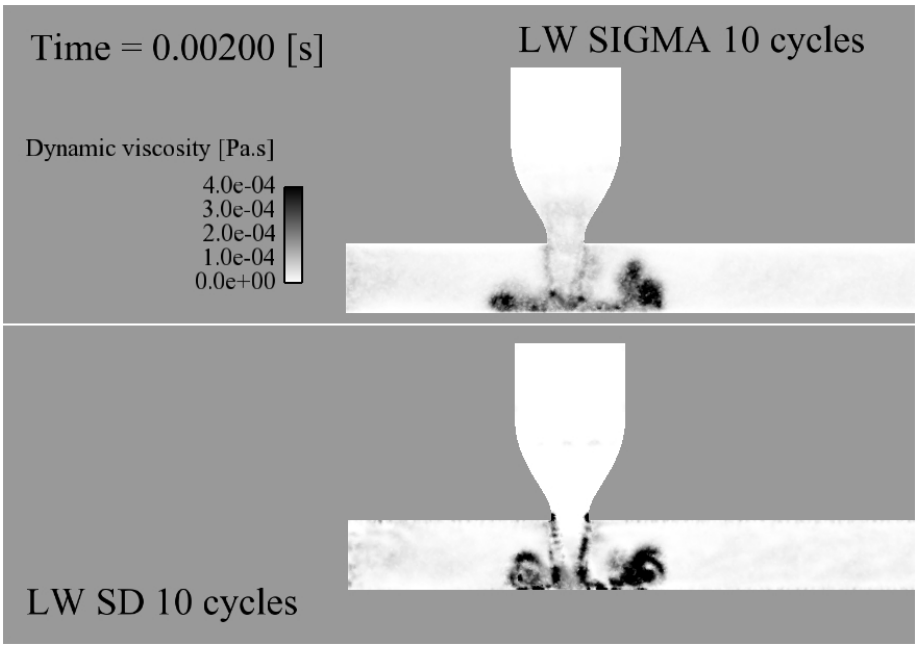

Figure 4.89: SGS viscosity field on plane P5 at time $t = 2.0$ ms

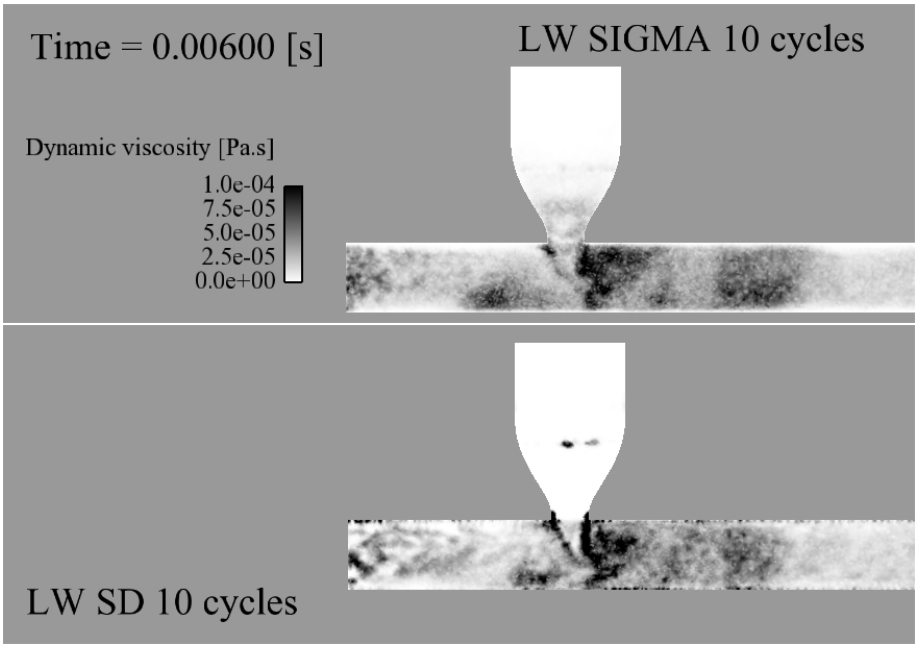

Figure 4.90: SGS viscosity field on plane P5 at time $t = 6.0$ ms

Different reasons can explain the increase of the SGS viscosity predicted by the dynamic Smagorinsky model in a region where the flow should be dominated by viscous effects:

- The mesh type and the cell-vertex connectivity used in AVBP does not allow to identify homogeneous directions. Indeed, there is no possible homogeneous directions since the information on a single node depends on the values of the cells that share this node. Except in the case of an HIT it would be a difficult task to identify homogeneous directions.
- The formulation of the dynamic Smagorinsky model is done locally; this leads to a systematic clipping of the negative values and to an overestimation of the overall viscosity. Those negative values would have damped the effect of the SGS viscosity. An interesting exercise would have been to evaluate in a volume close to jet and cross flow interaction part, the percentage of clipping and compared with the percentage observed in the turbulent channel case which can reach 35%.
- As we have seen in Fig. 4.83 even when there is no jet, the prediction of the SGS dynamic model is bad in the region where the mesh is coarse meaning that the results quality of this model depends strongly on the mesh resolution. It would have been necessary to increase the mesh resolution in the wall interaction region to have a better prediction of the dynamic Smagorinsky model; of course this would have dramatically increased the computational time cost of the simulation.

Quantitative analysis: Velocity profiles on the plane P5

In the near convergent region at $Y = -1D$, predictions of the two models are similar as expected. In the NC region as it was seen in the previous analysis, the inlet flow rate controls the flow dynamics specially during the early injection times. At later injection times, results of the two models are also similar and differences are probably due to the number of cycles used.

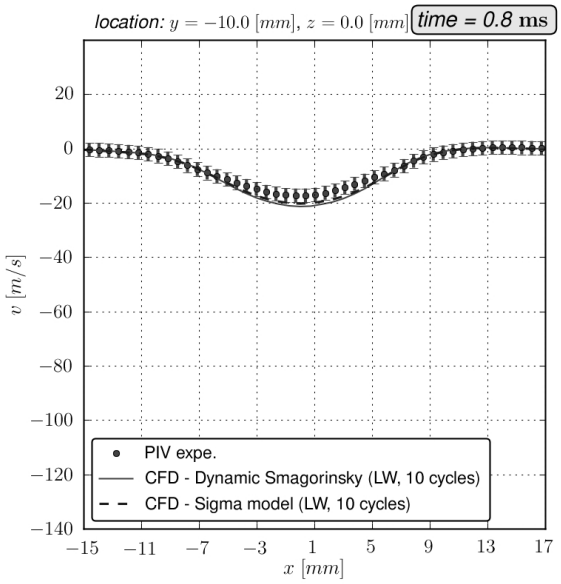

Figure 4.91: Velocity profile comparison: Influence of the SGS viscosity model at time $t = 0.8$ ms

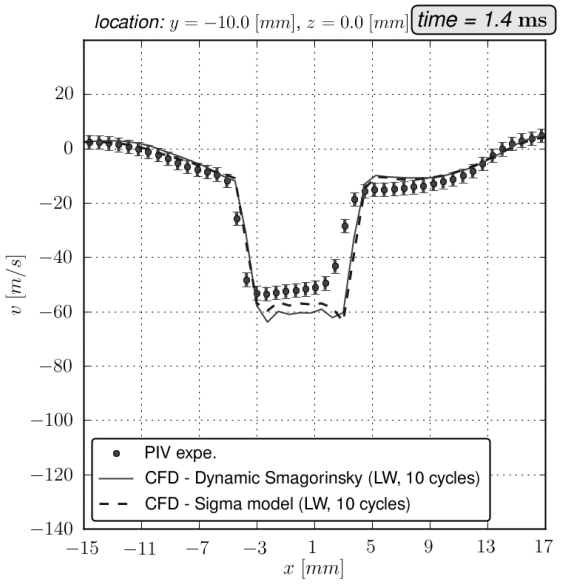

Figure 4.92: Velocity profile comparison: Influence of the SGS viscosity model at time $t = 1.4$ ms

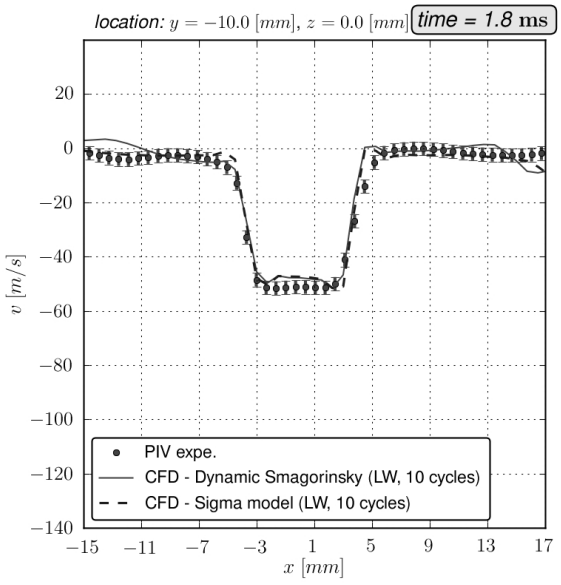

Figure 4.93: Velocity profile comparison: Influence of the SGS viscosity model at time $t = 1.8$ ms

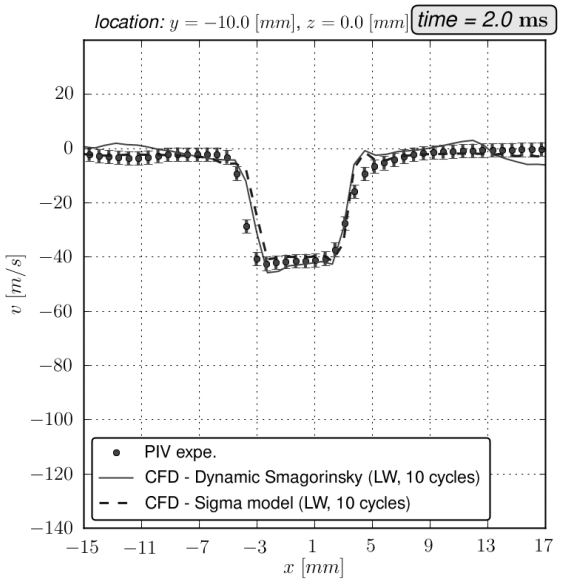

Figure 4.94: Velocity profile comparison: Influence of the SGS viscosity model at time $t = 2.0$ ms

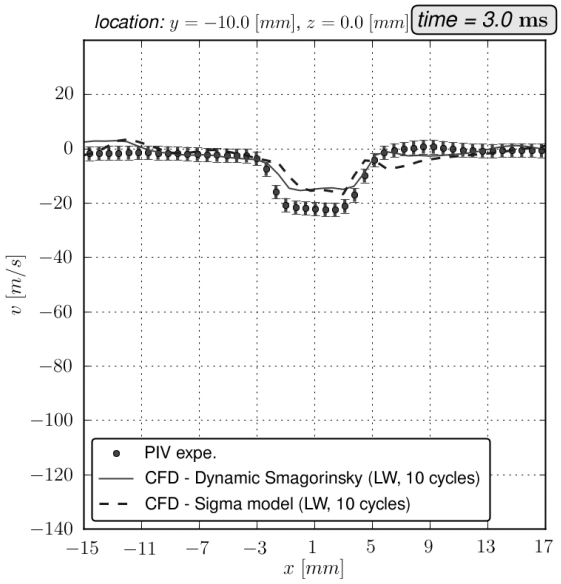

Figure 4.95: Velocity profile comparison: Influence of the SGS viscosity model at time $t = 3.0$ ms

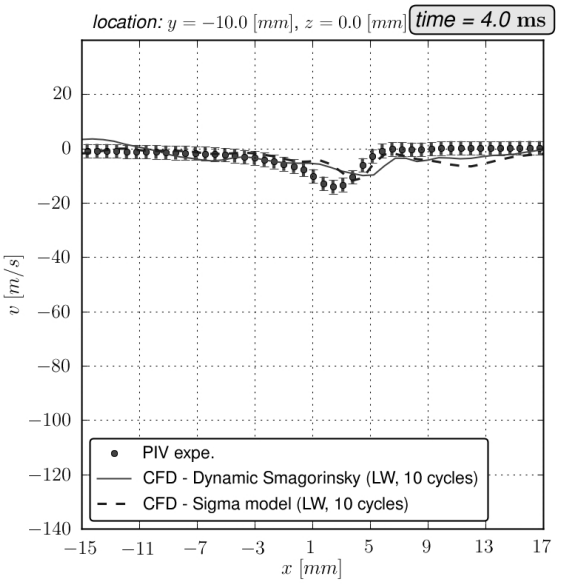

Figure 4.96: Velocity profile comparison: Influence of the SGS viscosity model at time $t = 4.0$ ms

In the near wall region after the impingement of the vortex ring, results from the σ-model are in good agreement with the experiment as shown in Fig.4.97 to Fig. 4.100. The trend observed on the velocity field is confirmed on the velocity profiles.

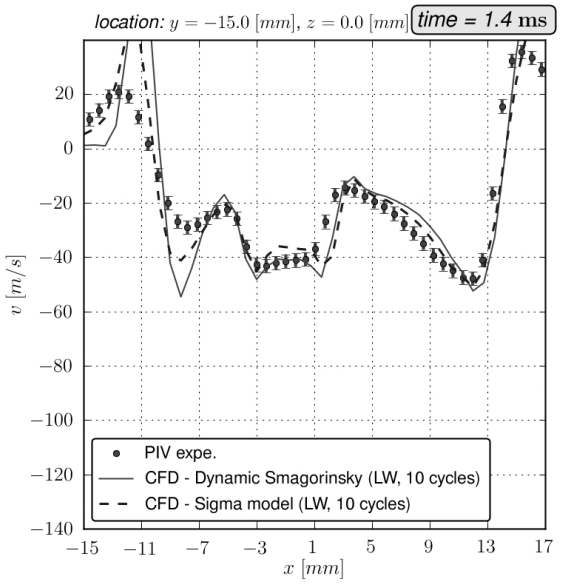

Figure 4.97: Velocity profile comparison: Influence of the SGS viscosity model at time $t = 1.4$ ms

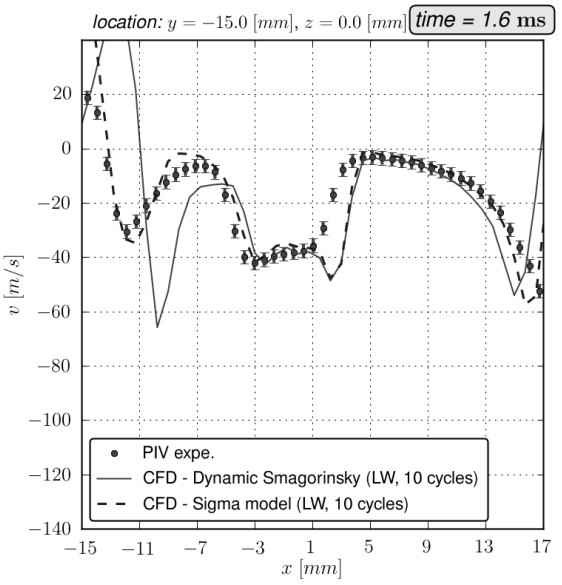

Figure 4.98: Velocity profile comparison: Influence of the SGS viscosity model at time $t = 1.6$ ms

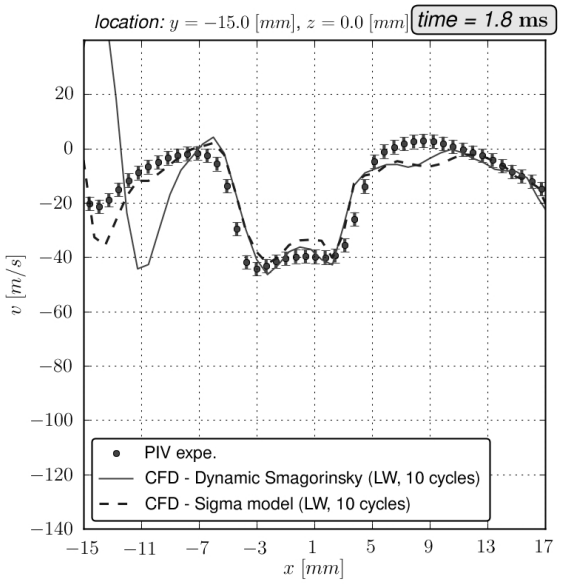

Figure 4.99: Velocity profile comparison: Influence of the SGS viscosity model at time $t = 1.8$ ms

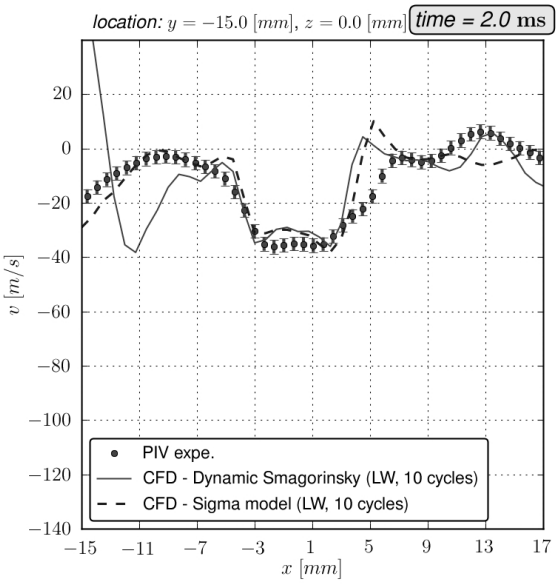

Figure 4.100: Velocity profile comparison: Influence of the SGS viscosity model at time $t = 2.0$ ms

During the late injection times, after the deviation of the jet, predictions of the two models are similar as seen in Fig.4.101 and Fig.4.102.

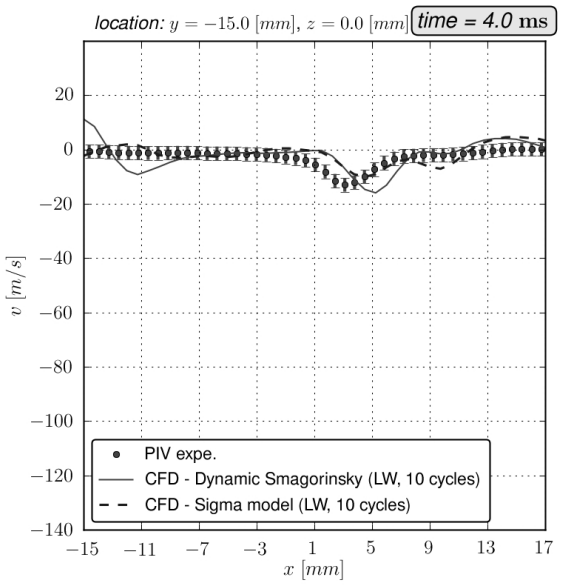

Figure 4.101: Velocity profile comparison: Influence of the SGS viscosity model at time $t = 4.0$ ms

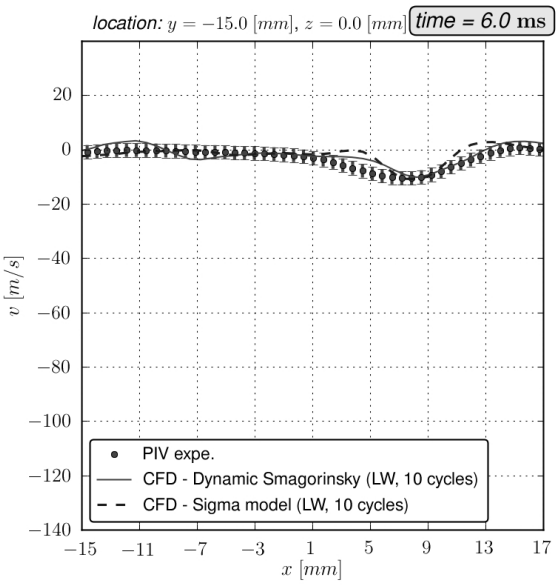

Figure 4.102: Velocity profile comparison: Influence of the SGS viscosity model at time $t = 6.0$ ms

It comes from this analysis that the dynamic Smagorinsky model underpredicts the radial expansion of the vortex ring on the impingement surface. This is mostly due to the over-prediction of the SGS viscosity which leads to a rapid dissipation of the strength of the vortex ring. When the vortex impinges with the bottom wall, there is no increase of the SGS viscosity because it automatically vanishes near solid boundary and the strength of the vortex ring is preserved so that they can be convected along the wall. Since the vortex ring is most probably key ingredient in the heat transfer towards the wall,

the under-prediction of the vortex span would lead to a bad estimation of the heat transfer at the wall no matter which heat transfer model is used. At the same time, results with the σ-model are in good agreement with the experiment.

4.2.5 Impact of the dynamic SGS conductivity

In the precedent simulations with the σ-model, the SGS Prandtl number was constant and the SGS conductivity was given by Eq. (1.97). Additional simulations were performed to analyze the impact of the SGS conductivity based on the Germano-identity as described in the Chapter I and used in [19, 37, 97]. The differences between the two cases regarding the SGS viscosity/conductivity are summarized in table 4.2:

Table 4.2: Characteristics of the simulations for the study of the impact of the SGS conductivity.

Case	SGS viscosity	SGS conductivity
σ-model constant SGS Prandtl 10 cycles	$(C_\sigma\Delta)^2 D_\sigma(\tilde{\mathbf{u}})$	$\frac{\bar{\rho}C_p}{Pr^{sgs}}(C_\sigma\Delta)^2 D_\sigma(\tilde{\mathbf{u}})$
σ-model dynamic SGS Prandtl 10 cycles	$(C_\sigma\Delta)^2 D_\sigma(\tilde{\mathbf{u}})$	$\bar{\rho}C_p\ (C_\lambda\Delta)^2 D_s(\tilde{\mathbf{u}})$

where $D_\sigma(\tilde{\mathbf{u}})$ is the σ-model time scale, $D_s(\tilde{\mathbf{u}})$ the Smagorinsky model time scale and C_λ the constant of the SGS conductivity which is evaluated dynamically with the Germano-identity. For sake of simplicity, the second case is referred to as the dynamic SGS Prandtl/conductivity case.

The comparison of the SGS conductivity fields on plane P5 shows noticeable differences on the predictions of the two methods. Indeed, for the constant SGS Prandtl number the SGS conductivity is predicted systematically in turbulent regions no matter the temperature gradient (see Fig. 4.103 to 4.105). As for the dynamic case the SGS conductivity is predicted only in regions where there might be temperature fluctuations. The magnitude of the turbulence is more important than the magnitude of temperature fluctuations and it leads to a prediction of the SGS conductivity higher in the case of the constant SGS Prandtl than in the case of the dynamic SGS Prandtl. But in the two cases, the resulting SGS heat flux should be negligible in regions where the temperature gradient is low (the SGS heat flux is directly proportional to the temperature gradient).

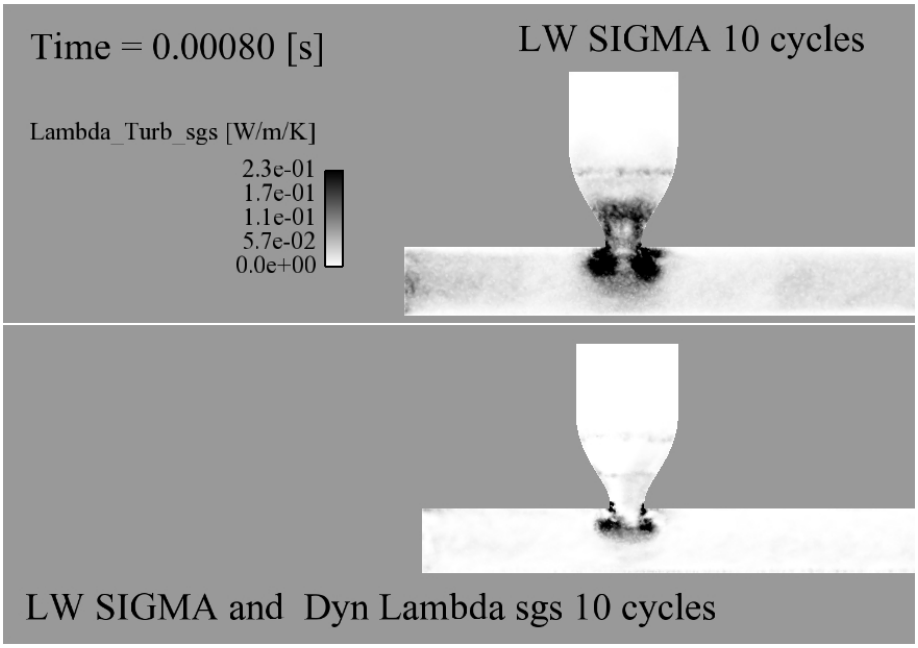

Figure 4.103: SGS conductivity field on plane P5 at time $t = 0.8$ ms

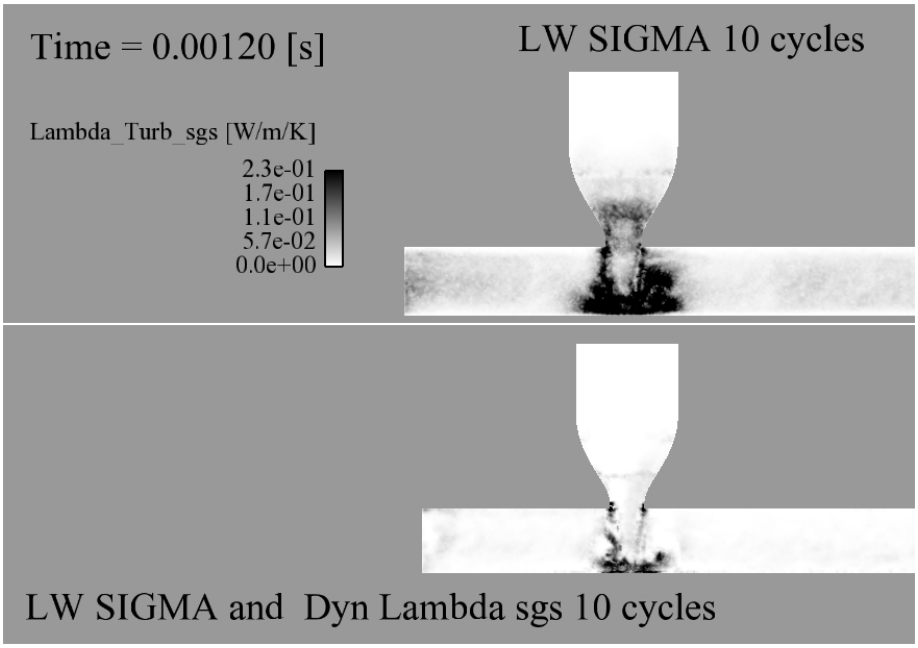

Figure 4.104: SGS conductivity field on plane P5 at time $t = 1.2$ ms

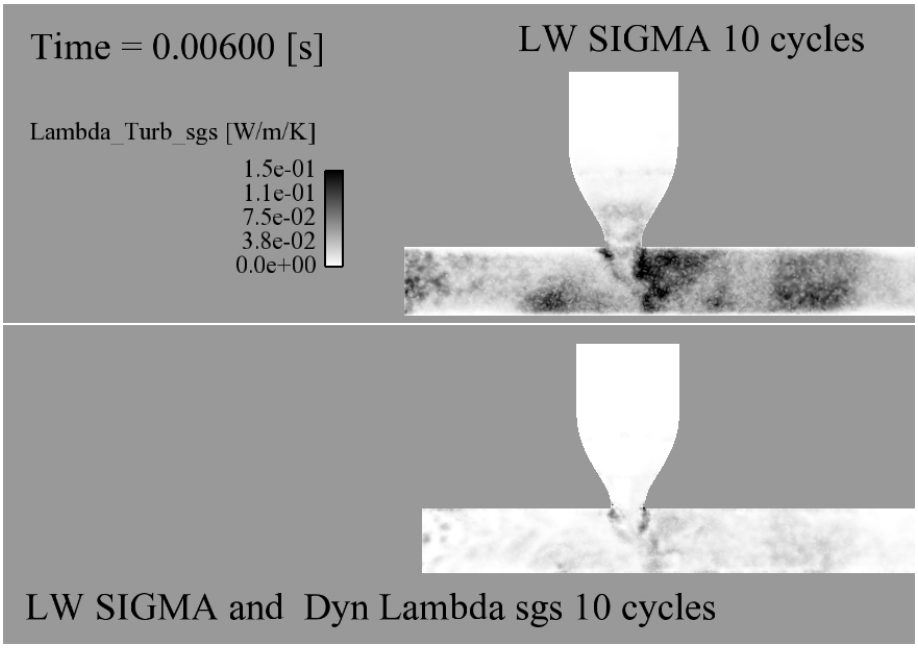

Figure 4.105: SGS conductivity field on plane P5 at time $t = 6.0$ ms

Another interesting comparison is the prediction of the SGS conductivity model near the wall. Because the dynamic SGS conductivity case is evaluated in a similar way as the dynamic Smagorinsky model, its prediction suffers from the same issues.

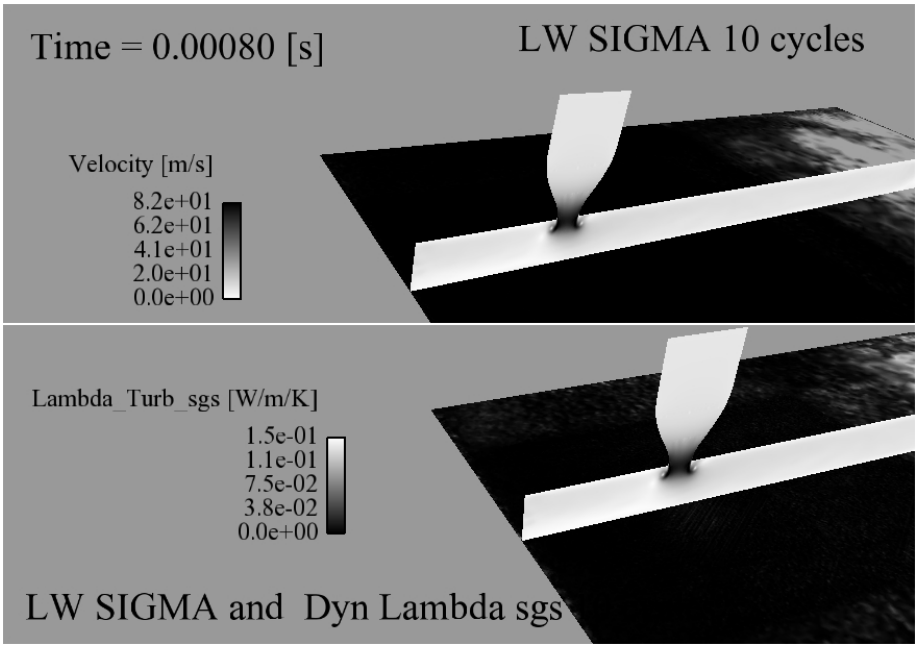

Figure 4.106: SGS conductivity comparison at time $t = 0.8$ ms. Vertical plane Velocity field and horizontal plane SGS conductivity

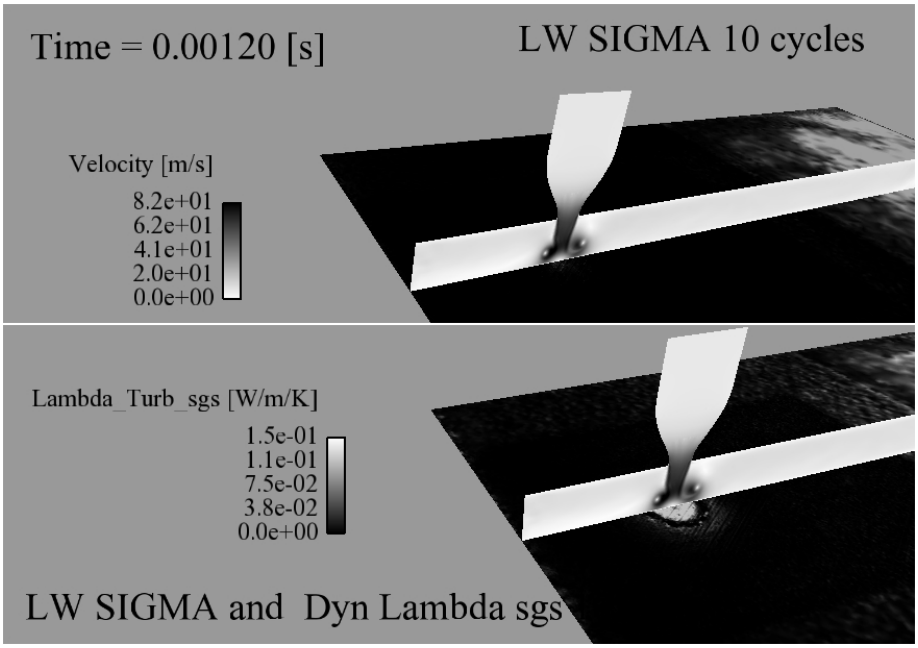

Figure 4.107: SGS conductivity comparison at time $t = 1.2$ ms. Vertical plane Velocity field and horizontal plane SGS conductivity

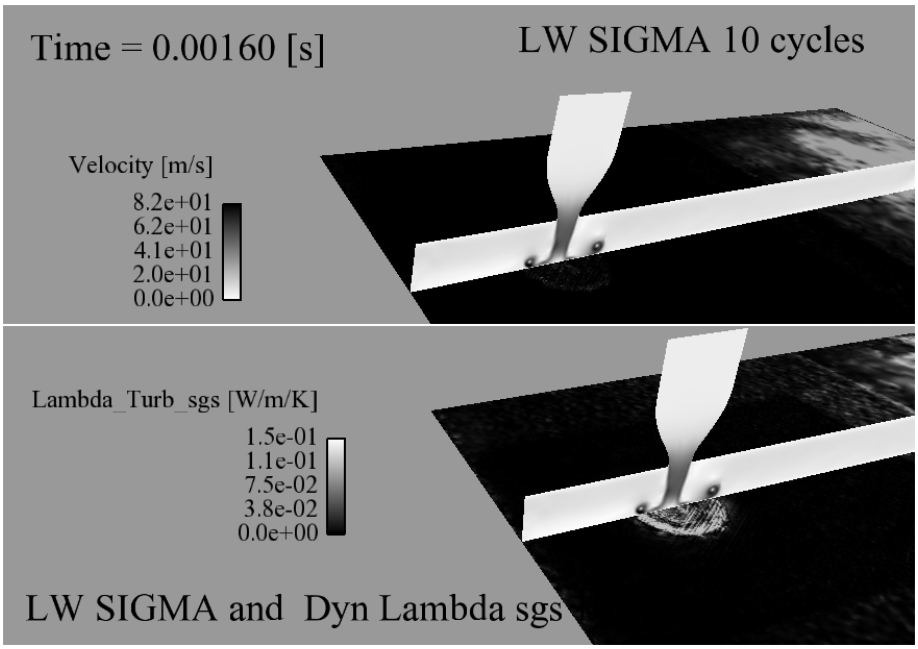

Figure 4.108: SGS conductivity comparison at time $t = 1.6$ ms. Vertical plane Velocity field and horizontal plane SGS conductivity

During the impingement, the dynamic SGS conductivity increases at the wall (see Fig. 4.106 to Fig. 4.108). Concerning the constant SGS conductivity there is no increase because it is based on the σ-model time scale. However, comparisons of the velocity field do not exhibit any significant differences between the two cases as shown in Fig. 4.109 to Fig. 4.112. The over-prediction of the SGS conductivity does not influence the propagation of the vortices as it was the case for the SGS viscosity.

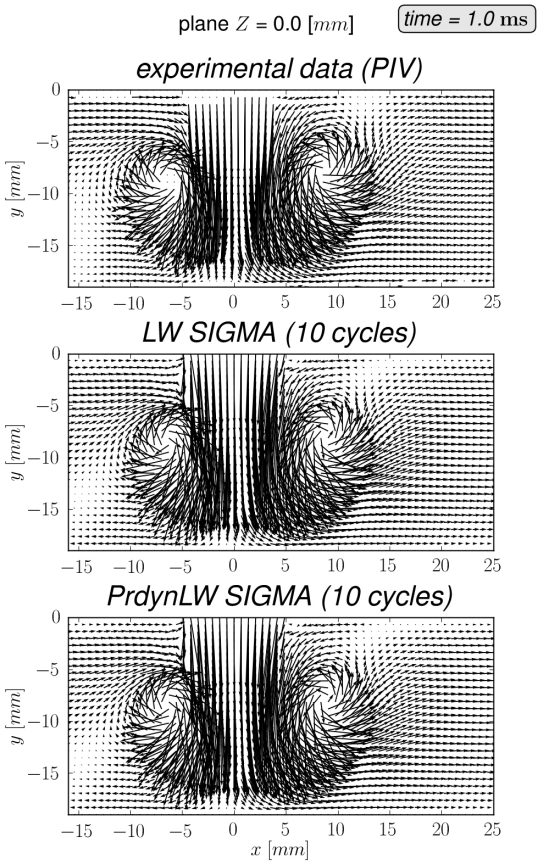

Figure 4.109: Velocity vectors comparison: Influence of the SGS conductivity at time $t = 1.0$ ms

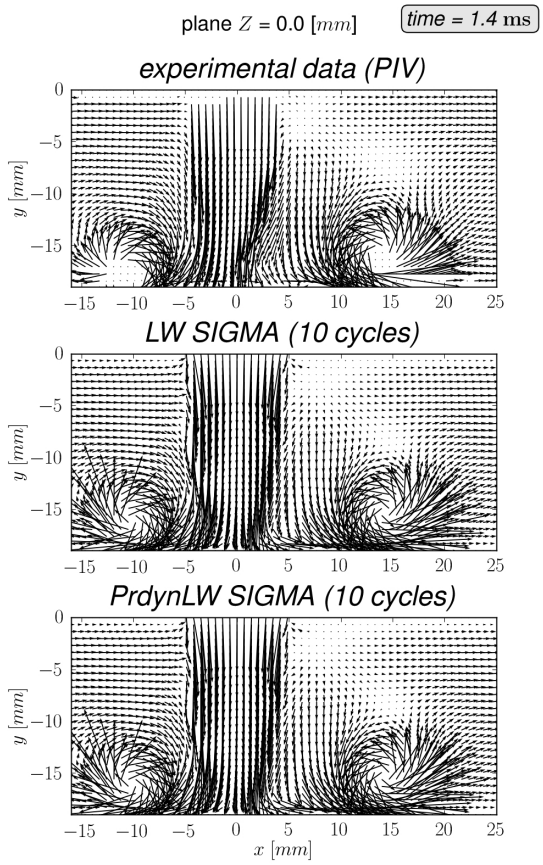

Figure 4.110: Velocity vectors comparison: Influence of the SGS conductivity at time $t = 1.4$ ms

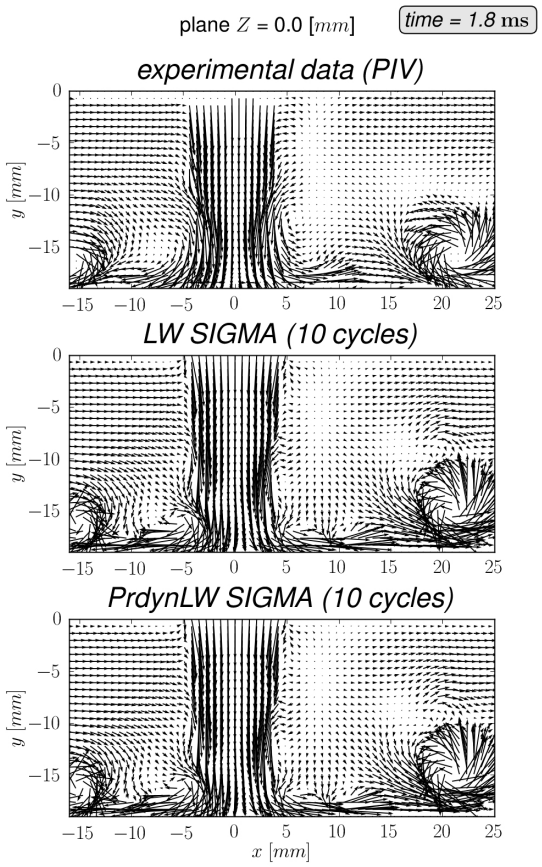

Figure 4.111: Velocity vectors comparison: Influence of the SGS conductivity at time $t = 1.8$ ms

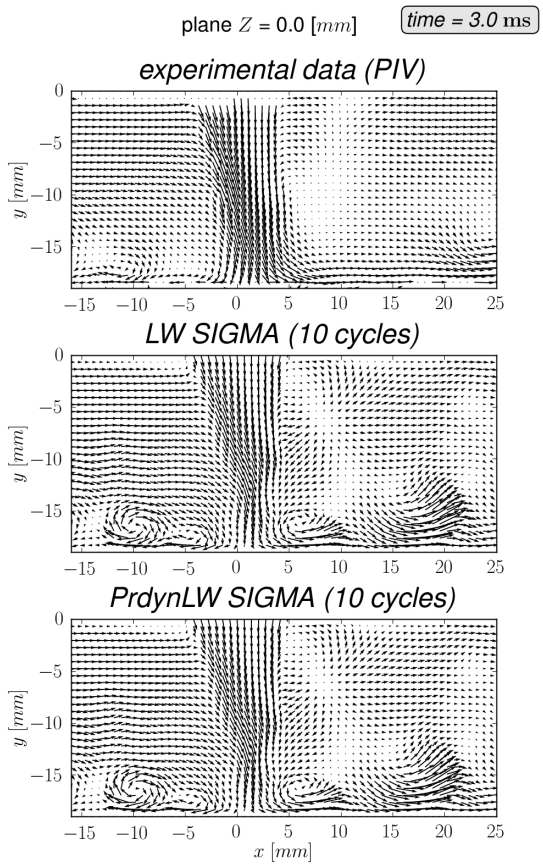

Figure 4.112: Velocity vectors comparison: Influence of the SGS conductivity at time $t = 3.0$ ms

Predictions of the vortex ring is well reproduced during the impingement, as expected and the deviation as well. The influence of the temperature on the velocity field is negligible in this case. This is confirmed by the velocity profiles (not shown here) at different sections on the median plane which are very similar.

4.3 Temperature comparison:

Diacetyl LIF experiments were performed to access the temperature field during injection and jet interaction with the wall. The temperature was determined from the application of the adiabatic mixing model (AMM) on the nitrogen mass fraction information obtained by diactetyl LIF (the complete method is described in 2.4), taking into account the ambient temperature and the jet temperature at the injector exit (determined by 2 line toluene LIF) for the boundary conditions of the model.
Before presenting the results, it is necessary to point out particularities of the experimental set-up since as it will be shown these particularities will have consequences on the analysis of the results. They concern the cross flow generation and control. The cross flow was generated by a fan mounted downstream of the visualization section. Two different setups were used during the experiments because the experiment had to be moved from one test bench to another during the campaign due to a renovation of the building where the test bench were located. The main difference concern the control of the cross flow:

- In the initial test bench that was used for the PIV measurements, the cross flow was controlled by the fan speed. The rotation velocity of the fan was varied automatically. Fig. 4.113 shows a illustration of the set up and of the expected shape of the flow generated in such a configuration. A relatively flat mean velocity profile was expected, so that in this set up the control of the cross flow magnitude is not expected to be sensitive to the position of the hot wire.

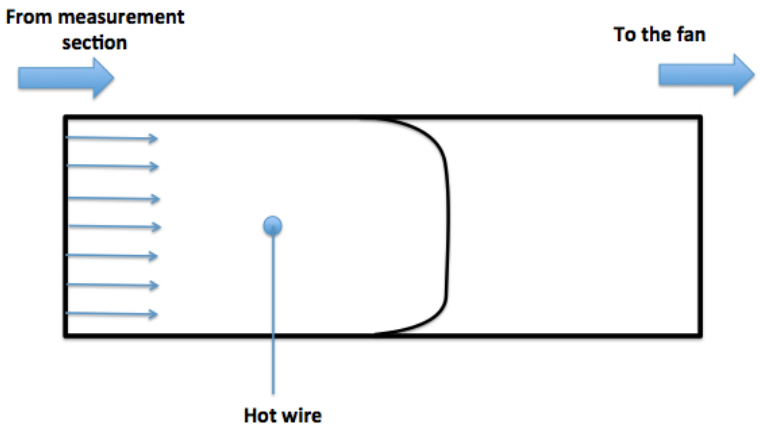

Figure 4.113: Schematic representation of the position of the hot wire during PIV measurements

- In the second test bench that was used for the toluene and diacetyl LIF experiments, the rotation velocity of the fan was fixed. The intensity of the cross flow rate was adjusted with an obstruction placed downstream of the hot wire and upstream of the fan. In this configuration the velocity profile in the duct is not expected to be uniform as illustrated in Fig. 4.114. As a result the control of the cross flow magnitude was expected to be more sensitive to the position of the hot wire. For this reason a great care was taken during the experiment to keep a fixed position of the hot wire in the duct.

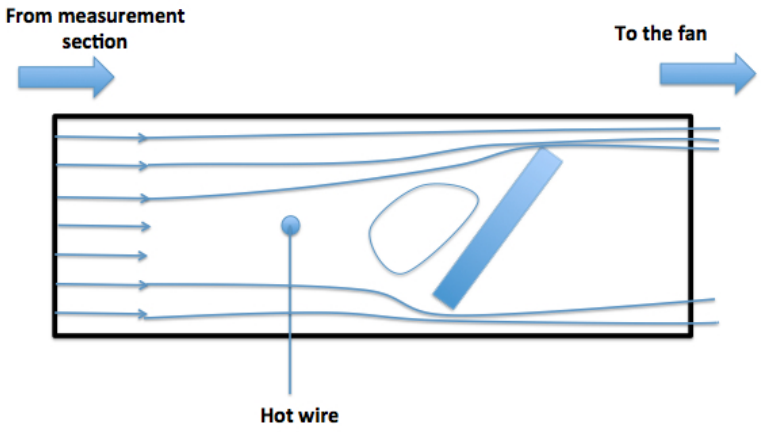

Figure 4.114: Schematic representation of the position of the hot wire during LIF measurements

Since the experimental set-up was moved from one test bench to the other, preliminaries PIV measurements were carried out in the second test bench in order to characterize the cross flow magnitude and to set the experimental conditions so that the cross flow magnitude was the same between the two set-ups. Despite of all these precautions, as it will be shown here, there is a possibility that the cross flow magnitude was different between the PIV and LIF measurements because of the high sensitivity of the control of the cross flow magnitude with respect to the position of the hot wire, and also because a relatively long time was required to adjust the LIF setup. This long time separated the preliminaries PIV measurements and the LIF measurements in the second test bench.

Fig. 4.115 to Fig. 4.122 show comparisons of the experimental temperature field with the dynamic Smagorinsky model and the σ-model.

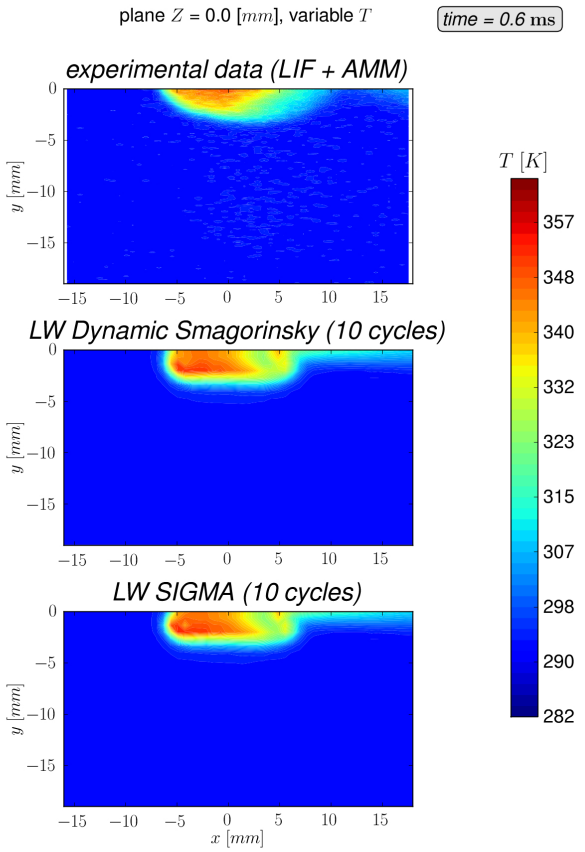

Figure 4.115: Temperature comparison: Influence of the SGS viscosity model at time $t = 0.6$ ms

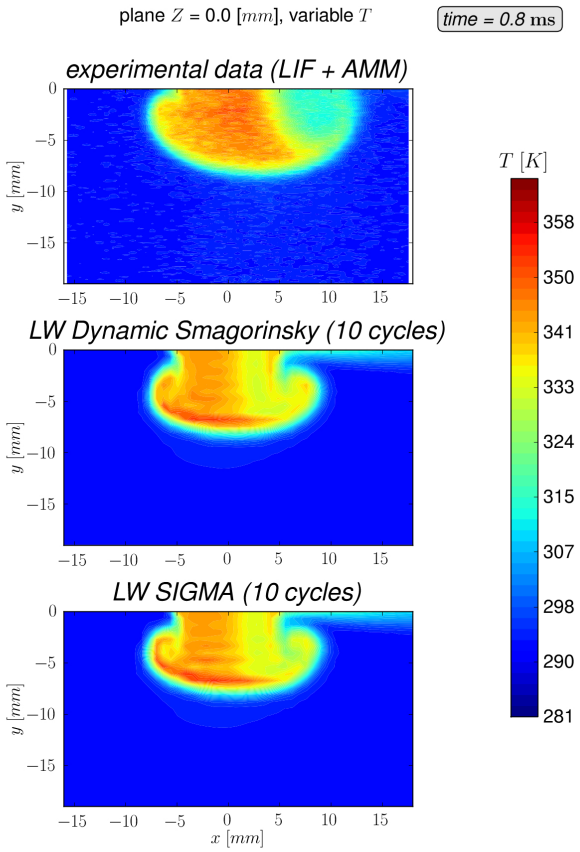

Figure 4.116: Temperature comparison: Influence of the SGS viscosity model at time $t = 0.8$ ms

Despite of the boundary conditions differences between the LIF measurements and the simulations, the experimental results are used here to perform initial comparisons, taking into account that the cross flow magnitude is not comparable. The results show that the temperature is effectively convected by vortices. The temperature field of the experiment shows a rapid cooling when the jet is penetrating in the cross flow compared to the simulations. This is very probably due to the mixing with ambient air that is more important in the experiment due to the cross flow.

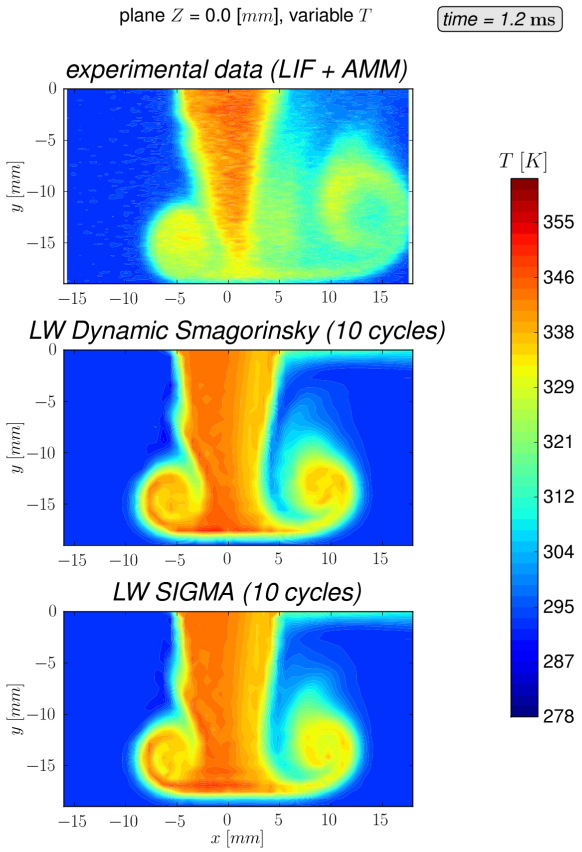

Figure 4.117: Temperature comparison on plane P5: Influence of the SGS viscosity model at time $t = 1.2$ ms

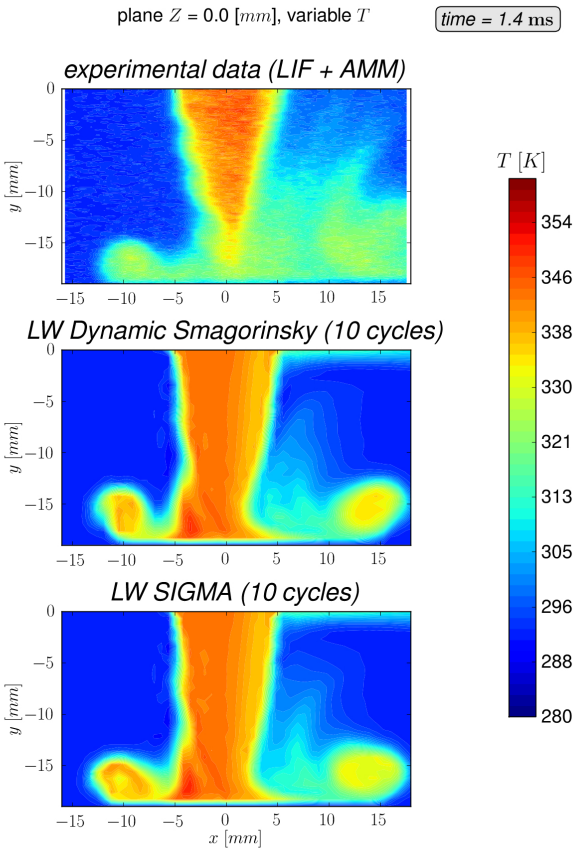

Figure 4.118: Temperature comparison on plane P5: Influence of the SGS viscosity model at time $t = 1.4$ ms

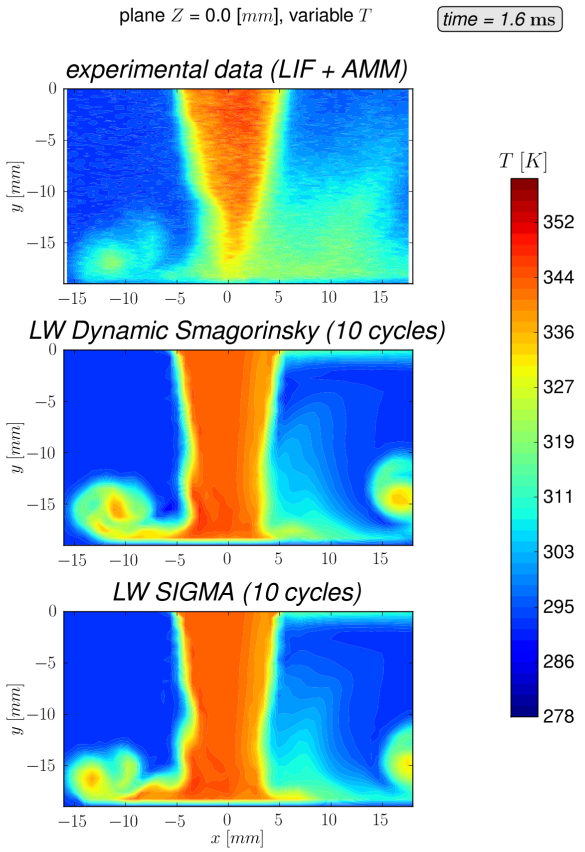

Figure 4.119: Temperature comparison on plane P5: Influence of the SGS viscosity model at time $t = 1.6$ ms

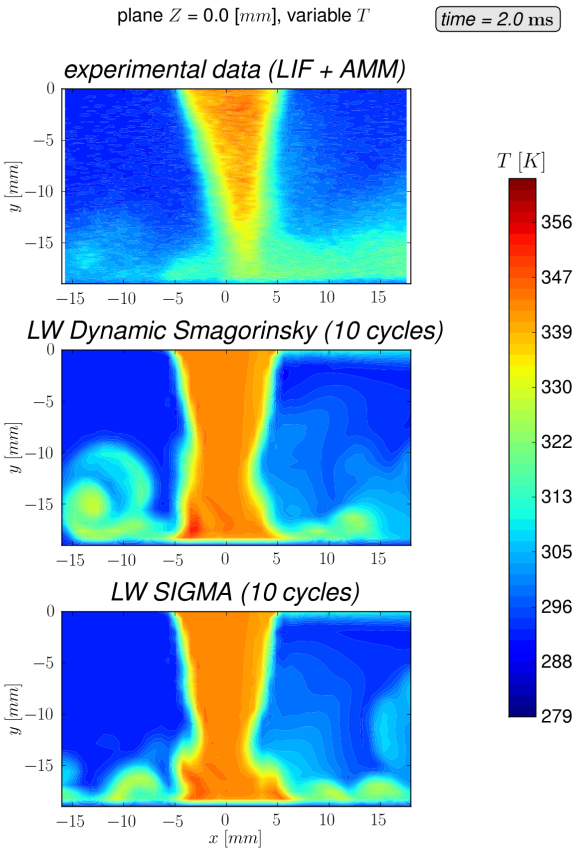

Figure 4.120: Temperature comparison on plane P5: Influence of the SGS viscosity model at time $t = 2.0$ ms

At early injection times, since the injection velocity is high (the effect of the cross flow is relatively less pronounced), they are little differences between the experiment and the simulations. One can observe that downstream convection of the vortex is more important (see Fig. 4.116) in the experiment than in the simulation in particular during the impingement with the bottom wall (see Fig. 4.117). After the impingement, because the cross flow is lower near the bottom wall, we can see that the vortices propagation is still badly predicted by the dynamic Smagorinsky model (see Fig. 4.120).

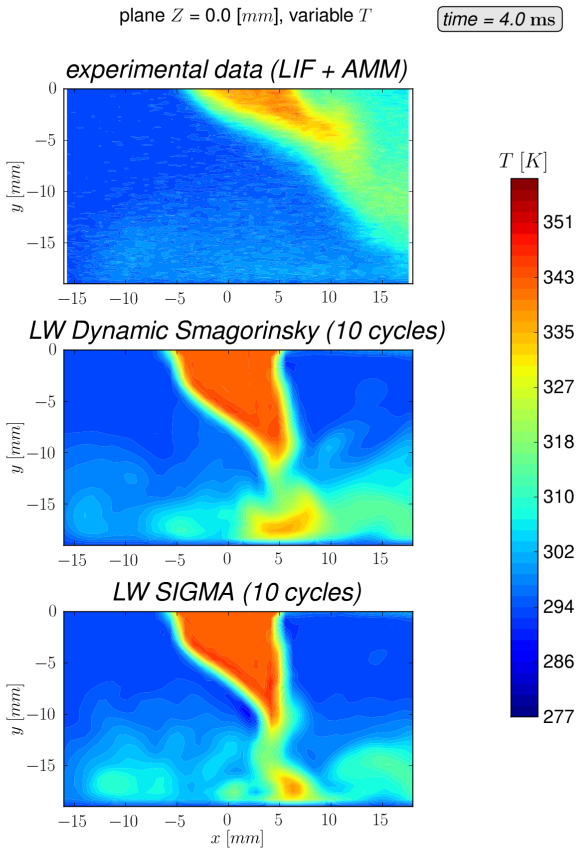

Figure 4.121: Temperature comparison on plane P5: Influence of the SGS viscosity model at time $t = 4.0$ ms

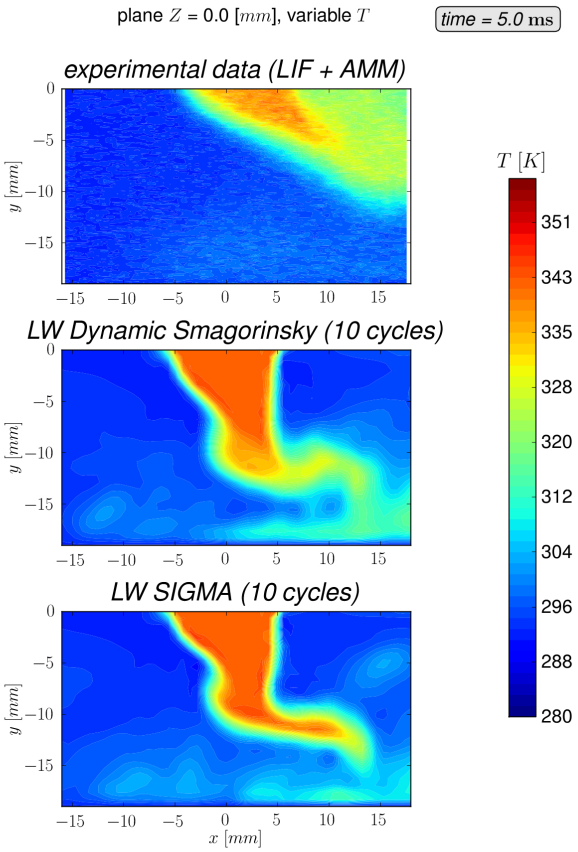

Figure 4.122: Temperature comparison on plane P5: Influence of the SGS viscosity model at time $t = 5.0$ ms

At late injection times when the jet velocity is small the influence of the cross flow is very important. Fig. 4.122 strongly suggests that the cross flow intensity is not the same in the experiment during the LIF compared to the cross flow during the LIF measurements Temperature profile (not shown here) at different sections confirmed the trend observed on the temperature field: the temperature in the experiment rapidly decreases due to the mixing with the cross flow that is more important.
Concerning the influence of the conductivity model, no major differences were observed on the temperature filed as it was the case on the velocity field. It confirms the fact that the low temperature gradients in the experimental set-up does not allow to highlight the differences between the hypothesis of a constant Prandtl number and a dynamic conductivity.

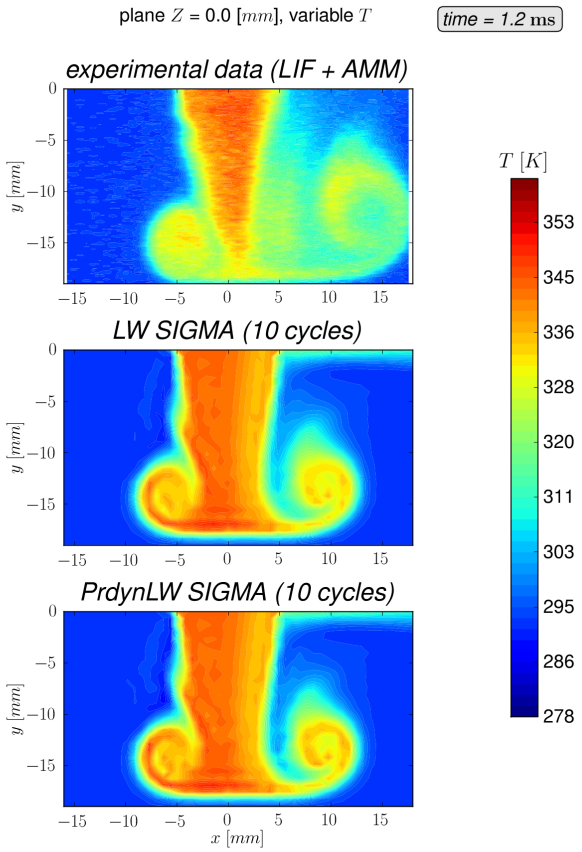

Figure 4.123: Temperature comparison on plane P5: Influence of the SGS conductivity model at time t = 1.2 ms

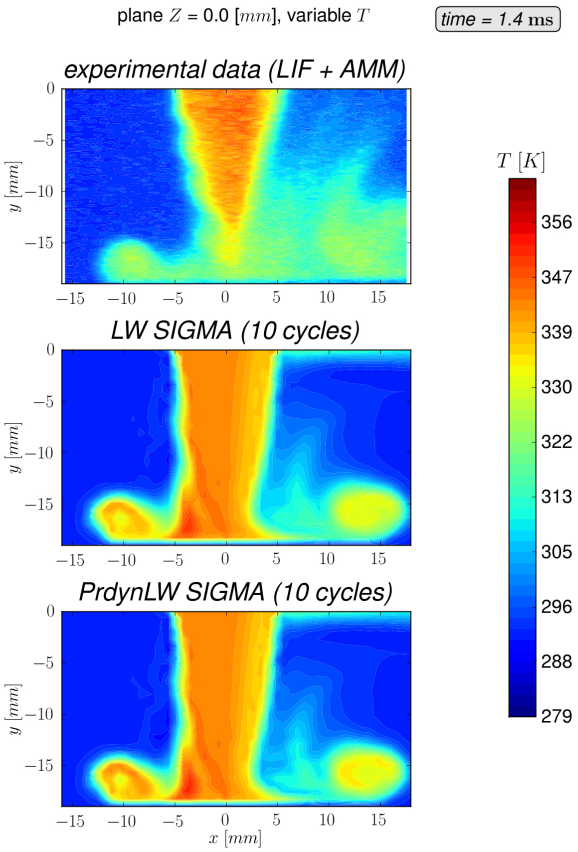

Figure 4.124: Temperature comparison on plane P5: Influence of the SGS conductivity model at time t = 1.4 ms

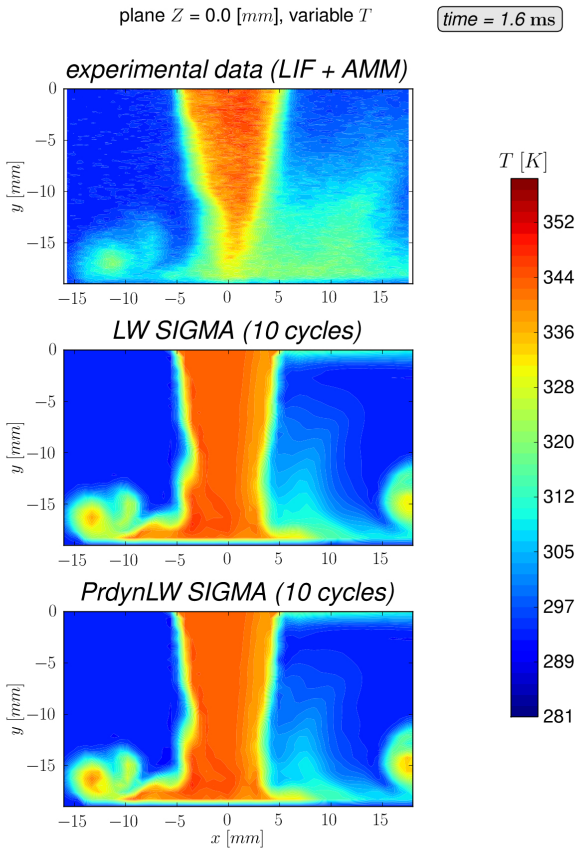

Figure 4.125: Temperature comparison on plane P5: Influence of the SGS conductivity model at time t = 1.6 ms

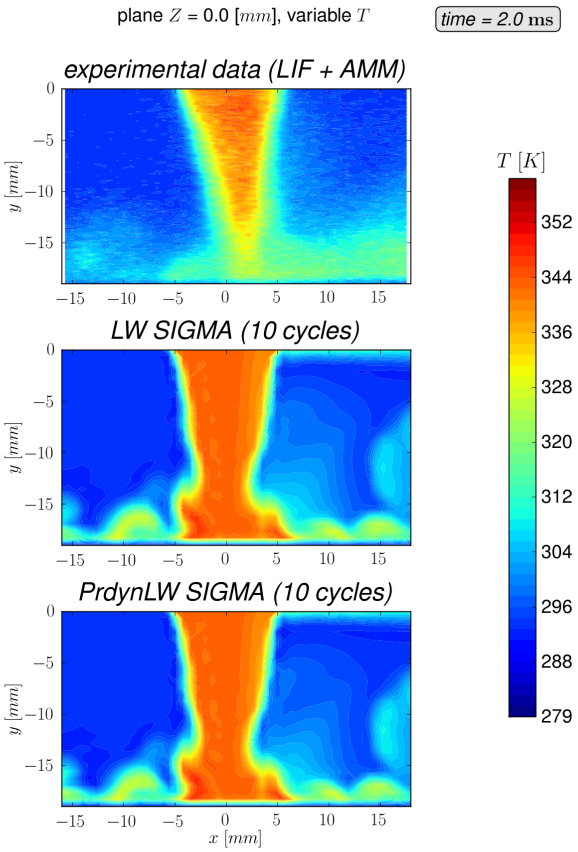

Figure 4.126: Temperature comparison on plane P5: Influence of the SGS conductivity model at time t = 2.0 ms

The overestimation of the SGS conductivity on the bottom wall of the dynamic SGS conductivity does not affect the velocity propagation of the vortices (see Fig. 4.128). It can be seen on the temperature profiles that they are only little differences between results obtained with the two formulations of the SGS conductivity (see Fig. 4.127 Fig. 4.128).

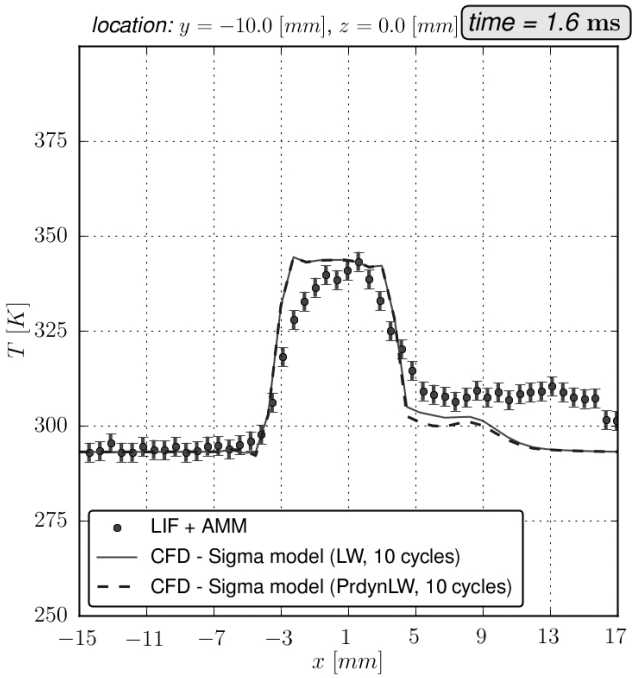

Figure 4.127: Temperature profile on plane P5 at $Y = -10$ mm: Influence of the SGS conductivity model at time $t = 1.6$ ms

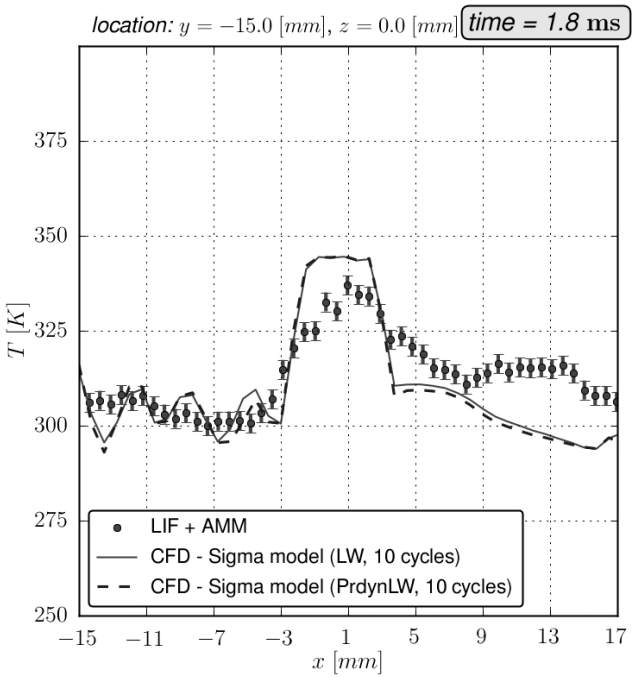

Figure 4.128: Temperature profile on plane P5 at $Y = -15$ mm: Influence of the SGS conductivity model at time $t = 1.8$ ms

Temperature results show significant differences between the experimental and simulation results. In the experimental case the jet deviation by the cross flow is much more significant. This result is very probably due to an increased cross flow magnitude in the experimental conditions. This is further confirmed by the comparisons of the PIV and LIF measurements. The jet deviation is more pronounced in the LIF images compared to the PIV, showing that the cross flow magnitude was higher in the LIF measurement compared to the PIV measurement campaign. These results show that despite of all the precautions taken to minimize experimental uncertainties when moving from one test bench to the other, the LIF measurements were not performed under the same cross flow conditions than the PIV measurements. The consequence is that the LIF measurements can not be used directly to validate the LES simulations performed under the same conditions than the PIV measurements in particular during the steady phase of the jet (when the jet is completely deflected).
A possible way to overcome the lack of knowledge of the cross flow intensity in the LIF measurements is to tune the cross flow intensity in the LES simulations(with the σ-model that gives bets match in term of velocity filed) in order to have the similar results in term of temperature profile. The tuning of the cross flow could be performed in such a way that the late time deflection of the jet as observed in the experiment (Fig. 4.122) is well recovered by the computation, assuming that the shape of the cross-flow velocity profile remains changed. The latter hypothesis was verified during the characterization of the cross flow campaign. Of course, this will not validate our temperature measurements but at least will provide a useful unknown quantity for other researchers interested in the temperature database. Besides, the experiment/LES comparison during the vortex shedding and impingement would be meaningful since the tuning is done once the interaction is finished

Chapter 5

Conclusion and Outworks

5.1 Conclusions

The work presented in this manuscript was motivated by three objectives: the development/improvement of LES turbulence models, the set-up of a LES-dedicated experimental database and the assessment of different models on the experimental database. Conclusions are presented with respect to each of these objectives:

1. **Models development:**

   The σ-model: During the past years, since the Smagorinsky model, the development of static models focused on vanishing the SGS viscosity model in near wall regions which was its main drawback. In the frame work of this thesis, this requirements was further extended to other canonical laminar flows. Indeed, predicting turbulence is a very complex issue but making sure that a turbulence model vanishes in laminar regions is more accessible and is mandatory to avoid altering the large resolved scales in LES. In opposite to the dynamic Smagorinsky model, this was achieved without additional filter. The σ-model is rather based on singular values of the velocity gradient tensor. The strategy of using information from the velocity gradient tensor ([106, 149]) has proved to be a good alternative for extending the applications of models to industrial applications no matter the complexity of the geometry. Results on academic cases and in different solvers showed that the σ-model gives equivalent or even better results than the dynamic Smagorinsky model.

   The global dynamic procedure: The development of the already mentioned advanced models has leaded to an unexpected paradox. It was considered that the difficulty to have a good local dynamic Smagorinsky model was because of the drawbacks of the Smagorinsky time scale. It was found during this thesis that, the problem is getting worse when an advanced time scale model is used. Indeed, it leads to a ill conditioned constant that highly fluctuates near solid boundaries where the model time scale vanishes. The alternative to the local formulation was then to calculate the model globally as suggested in [81]. This was applied to the σ-model. Simulations in different solvers has proved to lead to good prediction in unbounded flows such as Homogeneous Isotropic Turbulence and the turbulent periodic jets. However the extension to wall-bounded flows is not straightforward. The large values of the terms near solid boundaries seems to alter the evaluation of the global constant which is too high leading to an overestimation of the overall dissipation. An alternative has been suggested that consists in damping those terms with a sensor based on a singular value so that they can also be used in complex geometries. The resulting model has been successfully tested in the turbulent channel but additional tests need to be performed in other solvers to completely validate this formulation.

The alternative to the clipped version of the dynamic Smagorinsky model: When used in complex geometries the dynamic Smagorinsky model is generally applied locally with a stabilization procedure that consists in performing a volume weighted averaging over the node that surround the node of interest and to clip if necessary negative values. It was found in the simple turbulent channel test case that the clipping can reach 35% of the total constant. Meaning that around 4 out of 10 values of the constant obtained with the Germano-identity are not used. It was also found that this clipping may lead to an overestimation of the global dissipation since clipped negative values does not contribute to the overall dissipation. An alternative to this clipping was then proposed that consists in two steps. The first one is to calculate a global constant that could lead to the same global dissipation equivalent to the dynamic Smagorinsky model with the local constant. Once the global constant found, the second step consists in redistributing the global constant on each node. Results obtained in two solvers show respectively that it leads to equivalent results than the dynamic Smagorinsky model with averaging over homogeneous directions for unbounded flows (the test case was the periodic free jet) and to better results than the formulation with the clipping in wall-bounded flows (the test case was the turbulent channel). Additional tests should be performed on wall-bounded and other solvers to assess performances of this formulation.

2. **The experimental data base:** An experimental data base was developed during this thesis. It was designed so as to be easily reproduced with LES simulations. The boundary and initial conditions were also well characterized. The inlet flow rate, the inlet temperature and the cross flow were characterized and are available. Optical diagnostics technics such as PIV and LIF were used in order to measure the velocity and the temperature fields in a non intrusive way. The experimental set-up reproduced several interesting flow features that can be described in two phases: a first unsteady phase characterized by the formation of a vortex pair and the impingement with the bottom surface. The second phase which is more steady is characterized by the deviation of the jet due to the cross flow velocity. Results of the experimental database are available.

3. **LES simulations of the experimental database:** The impact of the SGS viscosity model and the SGS conductivity were assessed on the experimental data base. Preliminary tests were performed which have shown the low impact of the numerical scheme on the LES simulations of the experimental set-up.
   Concerning the impact of the SGS viscosity model, two models were compared: the local dynamic Smagorinsky model and the σ-model. The differences between the two models appear during the interaction of the vortices with the bottom wall. During this phase the propagation velocity of the vortices is under-predicted by the local dynamic Smagorinsky model. It is due to an overestimation of the SGS viscosity during impingement leading to a too fast dissipation of vortices. At the same time, the σ-model which is based on invariants automatically vanishes on the bottom wall and leads to a good prediction of the propagation velocity. The bad predictions of the dynamic Smagorinsky model can be explained by different reasons: the model is not applied as recommended with a stabilization over homogeneous directions, the systematic clipping leads to an over-estimation of the total SGS dissipation and finally the hypothesis of taking the constant out of the test filter when using the Germano-identity leads to bad predictions of the constant in coarse meshes and inhomogeneous flows. We are expecting that conclusions obtained on this experimental data base will be similar in IC engines where the confinement of the flow enhances the impact of the solid boundaries and also where the flow is particularly inhomogeneous.
   As for the impact of the hypothesis of constant SGS Prandtl number, the low temperature gradient in the experimental set-up has not allowed to analyze the impact of a SGS dynamic conductivity or a SGS conductivity deduced from the constant SGS Prandtl number. However comparison of the formulation of the two conductivities shows that the risk when assuming a constant SGS Prandtl number is that it predicts a systematic enhancement of the heat flux as long as the flow is turbulent. The consequence of the latter has not been assessed on the data base because of the low temperature gradients. At the same time, the SGS dynamic conductivity predicts a heat flux enhancement only in regions where there is effectively some temperature and velocity fluctuations. However, since this formulation is derived from the Germano-identity and it is applied similarly to the dynamic Smagorinsky model, it shares the same drawbacks. During impingement the level of the dynamic conductivity strongly increases. This can lead to a bad prediction of the heat flux on the solid boundary.

5.2 Outworks:

Throughout this thesis work, different tests were performed to validate the model in academic cases and also in a more complex database. Still they are some aspects discussed below that should be further tested or investigated:

1. It was decided to restrict the model development to the SGS viscosity. But this formulation implies an alignment of the SGS tensor and the strain rate tensor. This hypothesis is not always verified [7, 27, 128]. In addition, only forward energy transfer which is probably the most dominant in IC engines can be predicted with a SGS viscosity model. It would be interesting to combine the σ-model and a scale similarity model in order to account for the two mentioned phenomena. This was proved to improve the prediction of the WALE model in recent works [87].

2. Although the Germano-identity is a very powerful an largely used expression, it was proven to have some limitations when applied to advanced models. It can not be applied to advanced models to calculate their constant and when applied to a crude model like the Smagorinsky model, the hypothesis of taking the constant out of the filter might not hold. This is notably true in coarse and inhomogeneous flows which are typical in complex geometries.

3. Concerning the SGS conductivity, the hypothesis of constant SGS Prandtl number can lead to some risks of over-estimation of the heat flux. This enhancement is probably limited when it is used with a SGS model like the σ-model because it vanishes in different laminar flows. Still, alternative models based on invariant should be investigated to have models that predicts an heat flux enhancement only in regions where the temperature and the velocity fluctuate.

4. As for the improvements of the experimental set-up, it would be interesting to develop similar experiments but with higher temperature gradients between the injected gas and the bottom wall temperature. A 2D LIPT measurement technique should also be applied on the impingement surface in order to have a precise estimation of the spatial heat flux induced by the vortices propagation. This will allow to assess and compare predictions of SGS conductivity and heat fluxes models.

Bibliography

[1] Avbp code. *www.cerfacs.fr/cfd/avbp code.php and www.cerfacs.fr/cfd/cfdpublications.html.*

[2] A. A. Aldama. Lecture notes in engineering. *Springer-Verlag, New-York*, 29, 1990.

[3] S.W. Allison and G.T. Gillies. Remote thermometry with thermographic phosphors: Instrumentation and applications. *Rev. of Sc. Instr.*, 68(7), 1997.

[4] S. Andreas and E. W. Christian. *Particle Image Velocimetry: New Developments ans Recent Applications*. Springer-Verlag Berlin and Heidelberg GmbH & Co. K, 2008.

[5] R. Anthony. *Simulation aux Grandes Echelles d'un statoréacteur*. PhD thesis, Université de Toulouse: Institut National Polytechnique de Toulouse, 2009.

[6] M. Ashish and D.I. Pullin. A vortex-based subgrid stress model for large-eddy simulation. *Phys. Fluids*, 18, 1997.

[7] C. Bailly and G. Comte-Bellot. *Turbulence*. CNRS ÉDITIONS, 2003.

[8] G. Balarac, H. Pitsch, and V. Raman. Development of a dynamic model for the subfilter scalar variance using the concept of optimal estimators. *Phys. Fluids*, 20, 2008.

[9] J. Bardina, Ferziger J. H., and W. C. Reynolds. Improved turbulence models based on large-eddy simulations. *AIAA Paper. Fluid and Plasma Dynamics Conference* 13^{th}*, Snowmass, Colo., July 14-16*, pages 80–194, 1980.

[10] J. Bardina, Ferziger J. H., and W. C. Reynolds. Imroved turbulence models based on les of homogeneous incompressible turbulent flows. *Thermosciences Division, Dept. Mechanical Engineering, Stanford University*, Report TF-19, 1984.

[11] Y. Bazilevs, V.M. Calo, T.J.R. Hughes, A. Reali, and G. Scovazzi. Variational multiscale residual-based turbulence modeling for large eddy simulation of incompressible flows. *Computer Methods in Applied Mechanics and Engineering*, 193, 2003.

[12] J. H. Bell and P. Bradshaw. Contraction design for small low-speed wind tunnels. Technical report, Stanford University, 1988.

[13] J. H. Bell and P. Bradshaw. Boundary-layer predictions for small low-speed contractions. *American Institute of Aeronautics and Astronautics*, 27:372–374, March, 1989.

[14] M. Boger, D. Veynante, H. Boughanem, and A. Trouve. Direct numerical simulation analysis of flame surface density concept for large eddy simulation of turbulent premixed combustion. *Symposium (International) on Combustion*, 27(1):917–925, 1998.

[15] J. P. Boris, F. F. Grinstein, E. S. Oran, and R.L. Kolbe. New insights into large eddy simulation. *Fluid Dynamics Research*, 10:199–228, 1992.

[16] H. Boughanem and A. Trouve. Validation du code de simulation ntmix3d pour le calcul des ecoulements turbulents reactifs. Technical report, IFP, TAE, 1996.

[17] D. Brassard. Transformation of a polynomial for a contraction wall profile. Technical report, Lakehead University, 2003.

[18] L. Bricteux, M. Duponcheel, and G. Winckelmans. A multiscale subgrid model for both free vortex flows and wall-bounded flows. *Phys. Fluids*, 21, 2009.

[19] G. Brillant, S. Husson, and F. Bataille. Subgrid-scale diffusivity: Wall behavior and dynamic method. *J. of Appl. Mechs.*, 73, 2006.

[20] G. Bruneaux, K. Akselvoll, T. Poinsot, and J.H. Ferziger. Flame-wall interaction simulation in a turbulent channel flow. *Combust. Flame*, 107:27–36, 1996.

[21] O. Cabrit. *Modélisation des Flux pariétaux sur les tuyères des moteurs à propergol solide.* PhD thesis, Université de Montpellier II, 2009.

[22] O. Cabrit and F. Nicoud. Direct simulations for wall modeling of multicomponent reacting compressible turbulent flows. *Phys. Fluids*, 21, 2009.

[23] I. Calmet. *Analyse par simulation des grandes échelles des mouvements turbulents et du transfert de masse sous une interface plane.* PhD thesis, Institut National Polytechnique de Toulouse, 1995.

[24] I. Calmet and J. Magnaudet. Large-eddy simulation of high-schmidt number mass transfer in a turbulent channel flow. *Phys. Fluids*, 9, 1997.

[25] L.A. Catalano, P. D. Palma, M. Napolitano, and G. Pascazio. Cell-vertex adaptative euler method for cascadeflows. *AIAA Journal*, 33(12):2299–2304, 1995.

[26] D. Chapman and G. Kuhn. The limiting behavior of turbulence near a wall. *J. Fluid Mech.*, 170:256–292, 1986.

[27] P. Chassaing. *Turbulence en mécanique des fluides : Analyse du phénomène en vue de sa modélisation à l'usage de l'ingénieur.* Cépaduès-éditions, 2000.

[28] P. Chassaing, J. George, A. Claria, and S. Sanares. Physical characteristics of subsonic jet in a cross-stream (part1). *J. Fluid Mech.*, 17(9):1293–1313, 1974.

[29] R.A. Clark, J.H. Ferziger, and W.C. Reynolds. Evaluation of subgrid-scale models using an accurately simulated turbulent flow. *J. Fluid Mech.*, 91(1):1–16, 1979.

[30] O. Colin, F. Ducors, D. Veynante, and T. Poinsot. A thickened flame model for large eddy simulation of turbulent premixed combustion. *Phys. Fluids*, 12, 2000.

[31] G. Comte-Bellot and S. Corsin. Simple eulerian time correlation of full narrow-band velocity signals in grid generated "isotroppic" turbulence. *J. Fluid Mech.*, 48:273–337, 1971.

[32] C. B. Da Silva and O. Métais. On the influence of coherent structures upon interscale interaction in turbulent plane jets. *J. Fluid Mech.*, 473:103–145, 2002.

[33] E. David. *Modélisation des écoulements compressibles et hypersoniques: une approche instationnaire.* PhD thesis, Institut National Polytechnique de Grenoble, 1993.

[34] R. Dean. Reynolds number dependence of skin friction and other bulk flow variables in two dimensional rectangular duct flow. *J. of Fluids Eng.*, 100:215–223, 1978.

[35] J.W. Deardoff. A numerical study of three-dimensional turbulent channel flow at large reynolds numbers. *J. Fluid Mech.*, 41:1073–1091, 1970.

[36] J. E. Dec and W. Hwang. Characterizing the development of thermal stratification in an hcci engine using planar-imaging thermometry. *SAE International Journal of Engine*, 2(1):421–438, 2009.

[37] J. B. Donald, Y. Jing, and W. Bing-Chen. Les of turbulent heat transfer in couette channel flow using dynamic sgs models. *Progress in computational fluid dynamics*, 6:33–39, 2006.

[38] F. Ducros, V. Ferrand, F. Nicoud, C. Weber, D. Darracq, C. Gacherieu, and T. Poinsot. Large-eddy simulation of the shock/turbulence interaction. *J. Compt. Phys.*, 152:517–549, 1999.

[39] P. Ducros, F. an Comte and M. Lesieur. Large-eddy simulation of transition to turbulence in a boundary layer developing spatially over a flat plate. *J. Fluid Mech.*, 326:1-36, 1996.

[40] M. Duponcheel. *Direct and Large-eddy simulation of turbulent wall-bounded flows: further development of a parallel solver, improvement of multisacle subgrids models and investigation of vortex pairs in ground effect.* PhD thesis, Université catholique de Louvain, Ecole polytechnique de Louvain, 2009.

[41] M. M. El-Wakil, P. S. Meyers, and O. A. Uyehara. *SAE Trans*, 64:712–729, 1956.

[42] G. Erlebacher, M.Y. Hussaini, C.G. Speziale, and T.A. Zang. Toward the large-eddy simulation of compressible turbulent flows. Technical report, NASA CR178273, 1987.

[43] C. Espey, J. E. Dec, T. A. Litzinger, and D. A. Santavicca. Planar laser rayleigh scattering for quantitative vapor-fuel imaging in a diesel jet. *Combust. Flame*, 109:65–86, 1997.

[44] V. Eswaran and S. B. Pope. Direct numerical simulations of the turbulent mixing of a passive scalar. *Phys. Fluids*, 31, 1988.

[45] R.L. Fean and R.P. Weston. Induced velocity field of a jet in a crossflow. *NASA*, TP-1087, May 1978.

[46] J.P. Feist, A.L. Heyes, and S. Seefeldt. Thermographic phosphors for gas turbines: Instrumentation development and measurements uncertainties. *Proceedings symposium laser techniques, Lisbon*, July 2002.

[47] F. G. Fernando, G. M. Len, and J. R. William. *Implicit large eddy simulation: computing turbulent fluid dynamics.* Cambridge University Press, 2007.

[48] J. Ferziger. *Large eddy simulation: an introduction and perspective.* In Métais, O. and ferziger, J., editors, New tools in turbulence modelling, 29-37. Les editions de Physique - Springer Verlag, 1997.

[49] N. Franck. numerical study of a channel flow with variables properties. Technical report, Center for Turbulence Research, CTR Annual research Briefs, 1998.

[50] E. Garnier, M. Mossi, P. Sagaut, P. Comte, and M. Deville. On the use of shock-capturing schemes for large-eddy simulation. *J. Compt. Phys.*, 153:273–311, 1999.

[51] M. Germano. A proposal for redefinition of the turbulent stresses in the filtered navier-stokes equations. *Phys. Fluids*, 29:2323–2324, 1986.

[52] M. Germano, U. Piomelli, P. Moin, and W.H. Cabot. A dynamic subgrid-eddy viscosity model. *Phys. Fluids*, A3(7):1760–1765, 1991.

[53] S. Ghosal, T.S. Lund, P. Moin, and W.H. Cabot. A dynamic localization model for large-eddy simulation of turbulent flows. *J. Fluid Mech.*, 282:1–27, 1994.

[54] V. Giovangigli. Multicomponent flow modeling. *Modeling and Simulation in Science, Engineering and Technology. Birkhauser, Boston*, 1999.

[55] F. F. Grinstein and C. Fureby. Recent progress on miles for high reynolds number flows. *J. of Fluids Eng.*, 124(4), 2002.

[56] P. Guilbert, V. Modica, and C. Morin. Influence of pressure, temperature and gas phase composition on biacetyl laser-induced fluorescence. *Experiments in Fluids*, 40:245–256, 2006.

[57] M. G. Hall. Cell vertex multigrid solution of the euler equations for transonic flow past aerofoils. Technical report, Royal Aerospace Establishement, 1984.

[58] L. Hesselink. Digital image processing in flow visualization. *Annual Review of Fluid Mechanics*, 20:421–485, 1988.

[59] Heywood. *Internal Combustion Engine Fundamentals.* McGraw Hill, 1988.

[60] J. Hirschfelder, F. Curtis, and R. Bird. *Molecular theory of gases and liquids.* John Wiley and Sons, 1964.

[61] T.J.R. Hughes, L. Mazzei, and K.E. Jansen. Large eddy simulation and the variational multiscale method. *Computing and Visualization in Science*, 3:47–59, 2000.

[62] T.J.R. Hughes, A.A. Oberai, and L. Mazzei. Large eddy simulation of turbulent channel flows by the variational multiscale method. *Phys. Fluids*, 13(6), 2001.

[63] S. Husson. *Simulations des grandes échelles pour les écoulement turbulents anisothermes.* PhD thesis, Ecole doctorale MEGA, INSA de Lyon,, 2007.

[64] Y. Kamotani and I. Greber. Experiments on a turnulent jet in a cross flow. *AIAA Journal*, 10(11):1424–1429, Nov 1972.

[65] H. S. Kang, S. Chester, and C. Meneveau. Decaying turbulence in active-grid-generated flow and comparisons with large-eddy simulation. *J. Fluid Mech.*, 480:129–160, 2003.

[66] J. Kashdan. Etude gsm db1 2007, phase1: Etude bibliographique, mise en place d'un système de calibrage et évaluation de mesure de température paroi, phase2: Développement de la technique de mesure de température paroi en moteur, phase3: Application de la technique pour différentes conditions moteur. *Rapport d'activité IFP E.n. L0459001*, 2008.

[67] H. Kawamura, A. Hiroyuki, and Y. Matsuo. Dns of turbulent heat transfer in channel flow with respect to the reynolds and prandtl number effects. *Int. J. of Heat and Fluid FLow*, 20:196–207, 1999.

[68] K. C. Kays. Turbulent prandtl number. where are we ? *J. of Heat Transfer*, 116, 284, 1994.

[69] W.M. Kays, M.E. Crawford, and B. Weigand. *Convective Heat and Mass Transfer, Fourth Edition.* McGraw-Hill International Edition, 2005.

[70] J. Kim and P. Moin. Transport of passive scalar in a turbulent channel flow. *International Symposium on Turbulent and Shear Flow 6th, Toulouse, France*, 1987.

[71] J. Kim, P. Moin, and R. Moser. Turbulent characteristics in fully developed channel flow at low reynolds number. *J. Fluid Mech.*, 177:133–166, 1987.

[72] M. Klein, A. Sadiki, and J. Janicka. A digital filter based generation of inflow data for spatially developping direct numerical or large eddy simulations. *J. Compt. Phys.*, 186:652–665, 2003.

[73] M. Klein, A. Sadiki, and J. Janicka. Investigation of the influence of the reynolds number on a plane jet using direct numerical simulation. *Int. J. of Heat and Fluid Flow*, 6:785–794, 2003.

[74] W. Koban, J.D. Koch, R.K. Hanson, and C. Schulz. Oxygen quenching of toluene fluorescence at elevated temperatures. *Applied Physics B: Lasers and Optics*, 85:777–784, 2005.

[75] B. Koobus and C. Farhat. A variational multiscale method for the large eddy simulation of compressible turbulent flows on unstructured meshes -application to vortex shedding. *Computer Methods in Applied Mechanics and Engineering*, 193, 2003.

[76] R. H. Kraichman. Inertial ranges transfer in two-dimensional turbulence. *Phys. Fluids*, 10:1417–1423, 1967.

[77] R. H. Kraichman. Eddy viscosity in two and three dimensions. *J. of Atmospheric Sciences*, 33, 1976.

[78] R. H. Kraichman and D. Montgomery. Two-dimensional turbulence. *Report on Progress in Physics*, 43:547–619, 1980.

[79] D. S. Kyle and K. E. John. Preferential concentration of particles by turbulence. *Phys. Fluids*, A3(5), 1991.

[80] M. N. Lamarque. *Schémas numériques et conditions limites pour la simulation aux grandes échelles de la combustion diphasique dans les foyers d'hélicoptère*. PhD thesis, Institut National Polytechnique de Toulouse, 2007.

[81] J. Lee, H. Choi, and N. Park. Dynamic global model for large eddy simulation of transient flow. *Phys. Fluids*, 22, 2010.

[82] J.H. Lee, R. Knystautas, and C.K. Chan. Tubrulent flame propagation in obstacle-filled tubes. *Symp. (Int.) on Combust.*, 20(1):1663–1672, 1985.

[83] S. Lee, S. K. Lele, and P. Moin. Interaction of isotropic turbulence with shock waves: effect of shock strength. *J. Fluid Mech.*, 340:225–247, 1997.

[84] D.K. Lilly. A proposed modification of the germano subgrid-scale closure method. *Phys. Fluids*, A4(3):633–635, 1991.

[85] S. Liu, C. Meneveau, and J. Katz. On the properties of similarity subgrid-scales models as deduced from measurements in a turbulent jet. *J. Fluid Mechanics*, 275, 1994.

[86] G. Lodato. *Conditions aux limites tridimensionnelles pour la simulation directe et aux grandes échelles des écoulements turbulents. Modélisation de sous-maille pour la turbulence en région de proche paroi*. PhD thesis, Institut National des Sciences Appliquées de Rouen, 2008.

[87] G. Lodato, L. Vervisch, and P. Domingo. A compressible wall-adapting similarity mixed model for large-eddy simulation of the impinging round jet. *Phys. Fluids*, 21, 2009.

[88] M. Luong, W. Koban, and C. Schulz. Novel strategies for imaging temperature distribution using toluene lif. *J. of Phys.*, 45:133–139, 2006.

[89] K. Mahesh and N. Park. Reduction of the germano-identity error on the dynamic smagorinsky model. *Phys. Fluids*, 21, 2009.

[90] R.J. Margason. Fifty years of jet in crossflow research i. *n Computational and Experimental Assessment of Jets in Crossflow, AGARD-CP-534, Winchester UK*, 1993.

[91] R. D. Mehta. Turbulent boundary layer perturbed by a screen. *American Institute of Aeronautics and Astronautics*, 23, September, 1985.

[92] R. D. Mehta and P. Bradshaw. Design rules for small low speed wind tunnels. *The aeronautical Journal of the Royal Aeronautical Society*, November, 1979.

[93] C. Meneveau, T.S. Lund, P. Moin, and W.H. Cabot. A lagrangian dynamic subgrid-scale model of turbulence. *J. Fluid Mech.*, 319:233–242, 1996.

[94] O. Métais and M. Lesieur. Spectral large-eddy simulation of isotropic ans stably stratified turbulence. *J. Fluid Mech.*, 256:157–194, 1992.

[95] P. Moin. Advances in large eddy simulation methodology for complex flows. *Heat and Fluid Flow*, 2002.

[96] P. Moin and J. Kim. Numerical investigation of turbulent channel flow. *J. Fluid Mech.*, 118:341–377, 1982.

[97] P. Moin, K. Squires, W. Cabot, and S. Lee. A dynamic subgrid-scale model for compressible turbulence and scalar transport. *Phys. Fluids*, A3(11), 1991.

[98] K.W. Morton. Finite volume and finite element methods for the steady euler equations of gas dynamics. *In the Mathematics of Finite Elements Applications VI: MAFELAP 1987*, J.R. Whiteman. 79:353–378, 1988.

[99] R. D. Moser, J. Kim, and N. N. Manssour. Direct numerical simulation of turbulent channel flow up to $re_\tau = 590$. *Phys. Fluids*, 11(4), 1999.

[100] V. Moureau, P. Domingo, and L. Vervisch. Studying swirling flames using highly resolved simulations of an industrial premixed burner. *V European Conference on CFD. J.C.F. Pereira and A. Sequeira (Eds), Lisbon, Portugal, 14-17 June*, 2010.

[101] V. Moureau, G. lartigue, Y. Sommerer, C. Angelberger, O. Colin, and T. Poinsot. High order methods for dns and les of compressible multicomponent reacting flows on fixed and moving grids. *J. Compt. Phys.*, 202(2):710–736, 2005.

[102] M. Namazian, S. Hansen, E. Lyford-Pike, J. Sanchez-Barsse, J. Heywood, and J. Rife. Schlieren visualization of the flow and density fields in the cylinder of a spark-ignition engine. *SAE*, (800044), 1980.

[103] R.-H. Ni. A multiple grid scheme for solving the euler equations. *American Institute of Aeronautics and Astronautics*, 20:1565–1571, 1982.

[104] F. Nicoud. *Application of modern tools for the acoustic study of Application of modern tools for the acoustic study of annular combustion chambers.* University Montpellier II and I3M-CNRS UMR 5149, France, Von-Karman Institute Octobre 2010.

[105] F. Nicoud, J. Bagget, P. Moin, and W. H. Cabot. Les wall-modeling based on optimal control theory. *Phys. Fluids*, 13(10):1629 –1632, 2001.

[106] F. Nicoud and F. Ducros. Subgrid-scale stress modelling based on the square of the velocity gradient tensor. *Flow, Turb. and Combust.*, 62:183–200, 1999.

[107] M. Oberlack. Invariant modeling in large-eddy simulation turbulence. Technical report, Center for Turbulence Research, 1997.

[108] N. Park, S. Lee, J. Lee, and H. Choi. A dynamic subgrid-scale eddy-viscosity model with a global model coefficient. *Phys. Fluids*, 18, 2006.

[109] N. Park and K. Mahesh. A velocity-estimation subgrid model constrained by subgrid scale dissipation. *J. Compt. Phys.*, 227:4190–4206, 2008.

[110] M.A. Patrick. Experimental investigations of the mixing and penetraton of a round turbulent jet injected perpendicurlarly into a transverse stream. *Trans. Institute of Chemical Engineers*, 45, 1967.

[111] B. S. Petukhov. Heat transfer and friction in turbulent pipe flow with variable physical properties. *Advances in Heat Transfer*, 6, 1970.

[112] L.M. Pickett, S. Kook, and T. C. Williams. Visualization of diesel spray penetration, cool-flame, ignition, high-temperature combustion, and soot formation using high-speed imaging. *SAE*, 01-0658, 2009.

[113] U. Piomelli, W. H. Cabot, P. Moin, and S. Lee. Subgrid-scale backscatter in turbulent and transitional flows. *Phys. Fluids*, A3, 1991.

[114] T. Poinsot, C Angelberger, F.N. .Egolfopoulos, and D. Veynante. Large eddy simulations of combustion instabilities. *In International Symposium on Turbulence and Shear Flow Phenomena, Santa Barbara*, 1999.

[115] T. Poinsot and D. Veynantes. *Theoritical and Numerical Combustion.* R.T. Edwards, 2005.

[116] S. B. Pope. Self-conditioned fields for large-eddy simulations of turbulent flows. *J. Fluid Mech.*, 652:139–169, 2010.

[117] S.B. Pope. *Turbulent Flows.* Cambridge University Press, Cambridge, 2000.

[118] R. Radespiel. A cell-vertex multigrid method for the navier-stokes equations. Technical report, NASA: Technical Memorandum, 1989.

[119] P. Raffel, W. Christian, S. Wereley, and J. Kompenhans. *Particle Image Velocimetry.* Springer-Verlag Berlin and Heidelberg GmbH & Co. K, 2007.

[120] Rajaratnam. *Turbulent jets*. Cambridge University Press, 1976.

[121] M. Ricchiuto. *Construction and analysis of compact residual discretizations for conservation laws on unstructured meshes*. PhD thesis, Université Libre de Bruxelles, 2005.

[122] R. S. Rogallo. Numerical experiments in homogeneous turbulence. Technical report, NASA (National Aeronautics Space Administration, 1981.

[123] M. Rudgyard. *Cell Vertex methods for compressible gas flows*. PhD thesis, Oxford University Computing Laboratory, 1990.

[124] G. Saerner, M. Richter, M. Aldén, A. Vressner, and B. Johansson. Cycle resolved wall temperature measurements using laser- induced phosphorescence in an hcci engine. *SAE*, 01-3870, 2005.

[125] P. Sagaut. *Simulations numériques d'écoulement décollés avec des modèles de sous maille*. PhD thesis, Université de Paris VI, 1995.

[126] P. Sagaut. *Large eddy simulation for Incompressible flows*. Springer-Verlag Berlin and Heidelberg GmbH & Co. K, 1998.

[127] P. Sagaut and C. Cambon. *Homogeneous Turbulence Dynamics*. Cambridge University Press, 2009.

[128] P. Sagaut, P. Comte, and F. Ducros. Filtered subgrid-scale models. *Phys. Fluids*, 12(1), 2000.

[129] P. Sagaut, E. Garnier, and N. Adams. *Convective Heat and Mass Transfer*. Springer Science Science + Business Media B. V., 2009.

[130] P. Sagaut, E. Garnier, and N. Adams. *Large eddy simulation for compressible flows*. Springer Science Science + Business Media B. V., 2009.

[131] T. Schoenfeld and M. Rudgyard. Steady and unsteady flows simulations using the hybrid flow solver avbp. *AIAA Journal*, 37(1):1378–1385, 1999.

[132] C. M. Schulz and Sick. Tracer-lif diagnostics: quantitative measurement of fuel concentration, temperature and fuel/air ratio in practical combustion systems. *Progress Energy and Combustion*, 31:75–121, 2005.

[133] A. Scotti and C. Meneveau. A fractal model for large eddy simulation of turbulent flow. *Physica D*, 127, 1998.

[134] C.A. Sleicher and M.W. Rouse. Convenient correlation for heat transfert to constant and variable property fluids in turbulent pipe flow. *Int. J. Heat Mass Transfer*, 18(5):677–683, 1975.

[135] J. Smagorinsky. General circulation experiments with the primitive equations. *Month. Weather*, 93:99–165, 1963.

[136] M. Sommerfeld. Validation of a stochastic lagrangian modelling approach for inter-particles collisions in homogeneous isotropic turbulence. *Int. J. of Multiphase Flow*, 27:1829–1858, 2001.

[137] C. G. Speziale. Galilean invariance of subgrid-scale stress models in the large-eddy simulation. *J. Fluid Mech.*, 156:55–62, 1985.

[138] C.G. Speziale, Erlebacher, Zang T.A. G., and M.Y. Hussaini. The subgrid-scale modelling of compressible turbulence. *Phys. Fluids*, 31:940–942, 1988.

[139] G. Staffelbach, G. Boudier, N. Lamarque, C. Sensiau, L.Y.M. Gicquel, and T. Poinsot. Azimuthal thermo-acoustic stability of a full gas turbine combustion chamber using large-eddy simulations. In *11th CEAS-ASC Worshop of X3-Noise*, 1999.

[140] C. Strozzi, J. Stotton, Mura A., and M. Bellenoue. Characterization of a two-dimensional temperature field within a rapid compression machine using a toluene planar laser-induced fluorescence imaging technique. *Measurment Science and Technology*, 20(12), 2009.

[141] D. Stull and H. Prophet. janaf thermochemical tables, 2nd edition. Technical report, US National Bureau of Standards, 1971.

[142] P. Tabeling. Two-dimensional turbulence: a physicist approach. *Physics reports*, 362:1–62, 2002.

[143] J. Taine and P. Petit. *Cours et donées de base. Transferts thermiques. Mécaniques des fluides anisothermes*. Ed. Dunod, 1995.

[144] G. Tea, G. Bruneaux, J.T. Kashdan, and C. Schulz. Unburned gas temperature measurements in a surrogate diesel jet via two-color toluene-lif imaging. *Proceedings of the Combustion Institute*, 33:780–783, 2011.

[145] K.W. Tobin, S.W. Allison, M.R. Cates, G.J. Capps, D.L. Beshears, M. Cyr, and B.W. Noel. High-temperature phosphor thermometry of rotating turbine blades. *AIAA journal*, 28(8), 1990.

[146] K. Truffin. *Simulation aux grandes ćhelles et identification acoustique des turbines à gaz en régime partiellement prémélangé*. PhD thesis, Institut National Polytechnique de Toulouse, 2005.

[147] E.R. Van Driest. Turbulent boundary layers in compressible fluids. *J. Aero. Sci.*, 18(3):145–160, 1951.

[148] O.V. Vasilyev, Lund T.S., and P. Moin. A general class of commutative filters for les in complex geometries. *J. Compt. Phys.*, 146:82–104, 1998.

[149] A. Vreman. An eddy-viscosity subgrid-scale model for turbulent shear flow : Algebraic theory and applications. *Phys. Fluids*, 16(10), 2004.

[150] B. Vreman, B. Geurts, and H. Kuerten. On the formulation of the dynamic mixed subgrid-scale model. *Phys. Fluids*, 6, 1994.

[151] B.C. Wang, E. Yee, D.J. Bergstrom, and O. IIDA. New dynamic subgrid-scale heat flux models for large-eddy simulation of thermal convection based on the general gradient diffusion hypothesis. *J. Fluid Mech.*, 604:125–163, 2008.

[152] L. Wang, R. Martin, and Maxey. Setting velocity and concentration distribution of heavy particles in homogeneous isotropic turbulence. *J. Fluid Mech.*, 256:27–68, 1993.

[153] W-P. Wang. On the large eddy simulation of a turbulent channel flow with significant heat transfer. *Phys. Fluids*, 1996.

[154] F. A. Williams. *Combustion Theory*. Perseus Books, Reading,Massachussets 2nd edition, 1985.

[155] C. S. Yoo, Y. Wang, A. Trouve, and H. G. Im. Characteristic boundary conditions for direct simulations of turbulent counterflow flames. *Combustion Theory and Modelling*, 9:617 – 646, 2005.

[156] A. Yoshizawa, K. Kobayashi, T. Kobayashi, and N. Taniguchi. A nonequilibrium fixed-parameter subgrid-scale model obeying the near wall asymptotic constraint. *Phys. Fluids*, A9(12), 2000.

[157] D. You and P. Moin. A dynamic global eddy viscosity model for large-eddy simulation in complex geometries. *Phys. Fluids*, 19(06), 2007.

[158] R.B. Zang, T.A. andDahlburg and J.P. Dalburg. Direct and large-eddy simulations of three-dimensional compressible navier-stokes turbulence. *Phys. Fluids*, A4(1):127–140, 1992.

[159] Y. Zang, R.L. Street, and R.J. Koseff. A dynamic mixed subgrid-scale model and its application to turbulent recirculating flows. *Phys. Fluids*, A5, 1993.

APPENDICES

APPENDIX A

This extended abstract was submitted to the 7^{th} *Symposium on Turbulence and Shear Flow Phenomena, Ottawa, Canada 2011*. It is about the issue of the global dynamic procedure on wall-bounded flows.

A dynamic procedure for advanced subgrid-scale models and wall-bounded flows.
Baya Toda H, Cabrit O., Truffin K., Brunneaux G. and Nicoud F.
7^{th} *Symposium on Turbulence and Shear Flow Phenomena, Ottawa, Canada 2011*

A DYNAMIC PROCEDURE FOR ADVANCED SUBGRID-SCALE MODELS AND WALL-BOUNDED FLOWS

Baya Toda Hubert
Energy Applications Techniques
IFP Energie Nouvelles
Rueil - Malmaison, France
hubert.baya-toda@ifpen.fr

Olivier Cabrit
Department of Mechanical Engineering
University of Melbourne
Victoria 3010, Australia
o.cabrit@unimelb.au

Karine Truffin
Energy Applications Techniques
IFP Energie Nouvelles
Rueil - Malmaison, France
karine.truffin@ifpen.fr

Bruneaux Gilles
Energy Applications Techniques
IFP Energie Nouvelles
Rueil - Malmaison, France
gilles.bruneaux@ifpen.fr

Franck Nicoud
CNRS I3M 5149
University Montpellier II
Montpellier, France
franck.nicoud@univ-montp2.fr

ABSTRACT

Large Eddy Simulations (LES) in complex geometries require advanced models able to take into account the properties of the turbulence, variations of the mesh resolution and the accuracy of numerical schemes. In this study, a recently developed subgrid scale (SGS) model that takes into account several properties of the turbulence is used and combined with a global dynamic procedure suitable for such an advanced SGS model. A modification is introduced into the global procedure to account for solid boundaries. Validations are first performed on academic cases: an homogeneous isotropic turbulence and a turbulent channel. In addition, the potential of this global dynamic formulation is investigated on a more complex experimental test case performed at IFPEn. This test case corresponds to an hot unsteady impinging jet in presence of a cold cross flow. The resulting model gives fairly good results on the different configurations and does not require any homogeneous directions nor clipping.

INTRODUCTION

One way to overcome the drawbacks of the Smagorinsky (Smagorinsky, 1963) model is to use the Germano-identity (Germano *et al.*, 1991) with Lilly correction (Lilly, 1992). The constant of the Smagorinsky model is evaluated dynamically in order to adapt the SGS dissipation to the numerics (mesh refinement/numerical scheme) and to the flow features. To avoid local negative values leading to numerical instabilities, the constant is averaged over homogeneous directions. This procedure was proved to give very good results in simple configurations like in homogeneous isotropic turbulence (HIT) or in turbulent channel flows but it is almost impossible to apply it to complex geometries like piston engines or wind turbines. The development of more advanced models like the WALE (Nicoud and Ducros , 1999) and the Vreman (Vreman, 2004) models gives now the possibility to evaluate the model's constant globally rather than locally. Because the operators which they are based on go to zero in multiple cases where the SGS activity is not expected to be present, it remains to estimate their global dissipation. A recent study (Lee *et al.*, 2010) showed that the most efficient and easy to implement global dynamic procedure consists in performing a volume weighted averaging of local values that are obtained through the Germano identity. However, this procedure does not take into account the effect of solid boundaries that can alter the predictions of the global procedure. The objective of this study is then to improve the global dynamic procedure in order to take into account the presence of solid boundaries. The procedure will be applied to the sigma model: σ-model (Nicoud *et al.*, 2011, Baya Toda *et al.*, 2010). In addition to have the proper cubic near wall behavior, it also vanishes for different type of laminar flows where no SGS activity is expected: 2D flows and isotropic contraction and expansion. Due to this properties, the σ-model is more suitable than the WALE and Vreman models for the global dynamic procedure. One can also expect that the proposed modification of the global procedure can be applied to the previously cited models.

The paper is organized as follows: in section 1, the governing equations and the different SGS models (dynamic/static) are presented. In section 2, validation tests are performed on the HIT of Comte-Bellot and Corsin (Comte-Bellot and Corsin, 1971) and on a turbulent channel flow (Moser *et al.*, 1999) at friction Reynolds number $Re_\tau = 395$. The later case illustrates that the volume averaging of the global constant is not appropriate for wall-bounded flows. Better results are then obtained thanks to improved averaging procedure where the near wall regions are automatically accounted for. In this view, the volume averaging is weighted by a dimensionless sensor which vanishes in regions where shear dominates rotation (Baya Toda *et al.*, 2010). The potential of the global procedure is further investigated on a more complex case that consists of an impinging hot jet in a cross flow presented in

section 3. The experiment is set up at IFP En. Numerical results are compared with PIV measurements. This section is followed by a general conclusion.

GOVERNING EQUATION AND SUBGRID-SCALE MODELS

The filtered compressible Navier-Stokes equations are solved in this study but their incompressible counterpart are presented here for simplicity since only low Mach number flows will be considered:

$$\frac{\partial u_j}{\partial x_j} = 0 \tag{1}$$

$$\frac{\partial u_i}{\partial t} + \frac{\partial (u_i u_j)}{\partial x_j} = -\frac{1}{\rho}\frac{\partial p}{\partial x_i} + \nu \frac{\partial^2 u_i}{\partial x_i \partial x_j} + \frac{\partial \tau_{ij}^{sgs}}{\partial x_j} + S_i \tag{2}$$

the grid based filter is omitted for clarity, u_i is the filtered velocity, t is the time, p the pressure, ρ the density, ν the kinematic viscosity, S_i a source term acting in i-direction and τ_{ij}^{sgs} the subgrid scale (SGS) tensor expressed as:

$$\tau_{ij}^{sgs} = u_i u_j - \overline{u_i u_j} \tag{3}$$

Eddy viscosity models will be considered only in this study to model the SGS tensor which then takes the form:

$$\tau_{ij}^{sgs} - \frac{1}{3}\tau_{kk}^{sgs}\delta_{ij} = 2\nu_{SGS} S_{ij} \tag{4}$$

where S_{ij} is the strain rate based on the filtered velocity u_i and ν_{SGS} the eddy viscosity.

The dynamic Smagorinsky model

The dynamic Smagorinsky model is based on the Germano-identity and is expressed as:

$$\nu_{\mathrm{SGS}} = (C_s\Delta)^2 \mathscr{D}_s \; ; \; \mathscr{D}_s = \sqrt{2 S_{ij} S_{ij}} \tag{5}$$

The model constant C_s is computed from:

$$(C_s\Delta)^2 = \max\left[-\frac{\langle L_{ij} M_{ij} \rangle_{\mathrm{loc}}}{2\langle M_{ij} M_{ij} \rangle_{\mathrm{loc}}}, 0 \right] \tag{6}$$

where $L_{ij} = \widetilde{u_i}\,\widetilde{u_j} - \widetilde{u_i}\,\widetilde{u_i}$ is the Leonard term based on the grid based filter and test filter $\widetilde{\cdot}$. Besides, M_{ij} is directly related to the differential of the model:

$$M_{ij} = \frac{\widetilde{\Delta}^2}{\Delta^2}\widetilde{\mathscr{D}_s}\widetilde{S_{ij}} \; - \; \widetilde{\mathscr{D}_s\, S_{ij}},$$

where $\widetilde{\Delta}$ stands for the test filter width. In addition, $\langle\cdot\rangle_{\mathrm{loc}}$ stands for an integral taken over a small volume (typically a few grid cells) surrounding the current grid point and the model constant depends on both space and time. The local dynamic Smagorinsky model is referred to as the SMD model in this paper.

Advanced static model

In the following, "advanced" models stands for static SGS models with the desirable property that they produce zero eddy-viscosity near solid-boundaries. Examples of such models are the Vreman (Vreman, 2004) and the WALE (Nicoud and Ducros , 1999) models that respectively vanish with a linear and cubic behavior in pure shear regions.

As emphasized in the introduction, the chosen advanced model is the σ-model. It is based on the singular values of the velocity gradient tensor. It has the interesting properties to vanish in 2D flows 2D axisymmetric and 3D isotropic expansion/contraction. These are examples of flows where no SGS activity is expected. In addition, it has the proper y^3 asymptotic behavior near solid boundaries. The σ-model eddy viscosity is expressed as:

$$\nu_{\mathrm{SGS}} = (C_\sigma\Delta)^2 \mathscr{D}_\sigma \; ; \; \mathscr{D}_\sigma = \frac{\sigma_3(\sigma_1-\sigma_2)(\sigma_2-\sigma_3)}{\sigma_1^2} \tag{7}$$

where $\sigma_1 \geq \sigma_2 \geq \sigma_3 \geq 0$ are the three singular values of g_{ij} the velocity gradient tensor. $C_\sigma = 1.5$.

Global dynamic procedure

The model eddy viscosity is expressed from Eq.7 and the model constant C_σ^{Gvol} is evaluated from:

$$\left(C_\sigma^{Gvol}\Delta\right)^2 = -\frac{\left\langle L_{ij} M_{ij}^\sigma \right\rangle_{\mathrm{vol}}}{2\left\langle M_{ij}^\sigma M_{ij}^\sigma \right\rangle_{\mathrm{vol}}}; \tag{8}$$

M_{ij}^σ is obtained by replacing $\mathscr{D}_s$ by $\mathscr{D}_\sigma$ in the expression of M_{ij}. $\langle\cdot\rangle_{\mathrm{vol}}$ stand for a volume averaging over the entire domain. The contribution of each cell in the average is weighted by its volume. The resulting constant is then homogeneous in space and varies only in time. This model is referred to as the GSIG model throughout this paper.

Modified global dynamic procedure

The basic idea behind this modification is to remove near wall regions from the evaluation of the global constant. Indeed, close to the wall, the terms $L_{ij}M_{ij}$ and $M_{ij}M_{ij}$ are high and can be even higher than their values in the center of the channel. Since only viscous effects are dominant near the wall, it is then necessary in order to have the appropriate estimation of the mean constant to keep only values that are not in the near wall region. This consist in weighting each contribution by a sensor that vanishes in those regions. The chosen sensor in our case is the SVS sensor inspired from the WALE model but one can suppose that another sensor that vanishes

in shear region could also be used (for example the dimensionless sigma operator $\frac{\mathscr{D}_\sigma}{\sigma_1}$). The SVS is expressed as :

$$SVS = \frac{(S_{ij}^d S_{ij}^d)^{3/2}}{(S_{ij}^d S_{ij}^d)^{3/2} + (S_{ij}S_{ij})^3} \tag{9}$$

where S_d^{ij} is the traceless part of the square of the gradient tensor. It can be easily demonstrated that the SVS takes the values one and zero respectively for pure rotating flows and for pure shear flow with a y^3 near wall behavior. The global constant can then be rewritten as followed:

$$\left(C_\sigma^{Gsvs}\Delta\right)^2 = -\frac{\left\langle L_{ij}M_{ij}^\sigma \right\rangle_{\text{svs}}}{2\left\langle M_{ij}^\sigma M_{ij}^\sigma \right\rangle_{\text{svs}}} \tag{10}$$

where $\langle\cdot\rangle_{\text{svs}}$ stands for a global averaging where each cell contribution is weighted by its SVS. The model is referred to as the GsvsSIG model throughout the paper.

All the results presented in this paper were obtained with the AVBP code (AVBP, 2011). The academic test cases were performed with a centered Galerkin finite element method 4^{th} order in space with a 3^{rd} order Runge-Kutta temporal integration.

Validation on academic test cases

Simulations of the HIT of CBC are first performed in order to validate the dissipative behavior of the two global models. This is a standard test case where three spectra at three different adimensionnal time 42, 98, 171 are known from the experiment. The objective is to reproduce the proper energy decay rate (as well as the spectra decay) when starting the simulation with the spectrum at time $t^* = 42$. Fig. 1 shows that both models correctly reproduce the energy decay. As expected, for flows without solid boundaries the predictions of the two global models are similar. This is confirmed by the time evolution of the two global constant shown on Fig. 2.

In order to assess the performance of the different models when dealing with solid boundaries, simulation of a turbulent channel flow are also performed at a friction Reynolds number equal to $Re_\tau = 395$. The reference case is the DNS of Moser *et al.* The mesh characteristics were twice larger than the advised minimum channel (Kim and Moin,1987) dimensions. The chosen dimensions were proved to be sufficient to well recover first order statistics (Cabrit and Nicoud, 2009). The later were accumulated over approximately 10 diffusion times. Fig. 3 shows that the results of the modified global dynamic procedure are in good agreement with the DNS. In contrary, the mean velocity predicted by the dynamic Smagorinsky model and the classical global dynamic procedure are overestimated. This is respectively due to the non averaging over the homogeneous direction and to the global volume averaging that is not appropriate when dealing with wall-bounded flows. The later overpredicts the constant that leads to an overprediction of the SGS viscosity as shown on Fig. 4. In contrary, by giving a low weight to pure shear regions that correspond to near wall regions in the global averaging, the predictions of the model are improved.

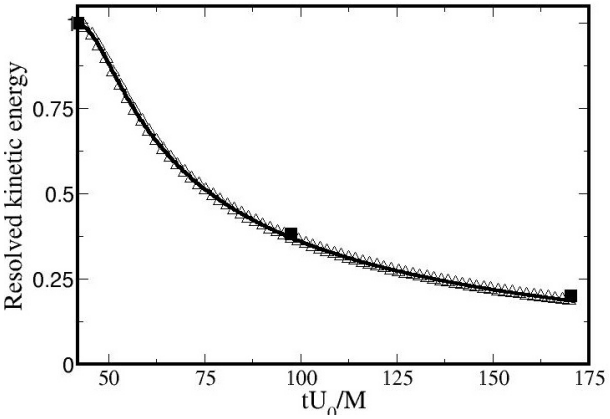

Figure 1. Resolved kinetic energy HIT of CBC on 64^3 nodes. Triangle up GSIG, thick line GsvsSIG and the squares are the experiment.

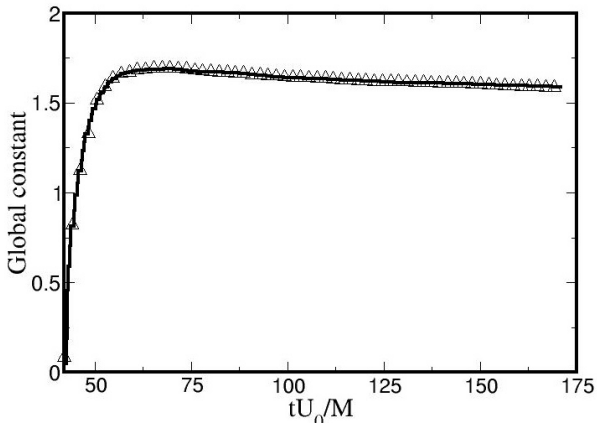

Figure 2. Global dynamic constant. Triangle up GSIG and solid line GsvsSIG.

TOWARDS THE APPLICATION ON AN IMPINGING HOT JET ON ISOTHERMAL WALL

Accurate results were obtained in standard validation cases but it is necessary to assess the performance of this procedure in a more complex configuration that involves different flow features such as shear flows, rotations, stagnation points and unsteadiness To this respect, an experiment that consists in a pulsed hot jet that impinges on a cold surface in presence of a cross flow (at ambient temperature) was performed. This experiment was specially design for comparison with LES results purposes: simple enough to enable accurate model validation, fully controlled boundary conditions (the cross flow profile and injector profile were well-defined) and representative enough to take into account the most important physical phenomena occurring in combustion chambers: transient interactions between hot vortices and a developed boundary

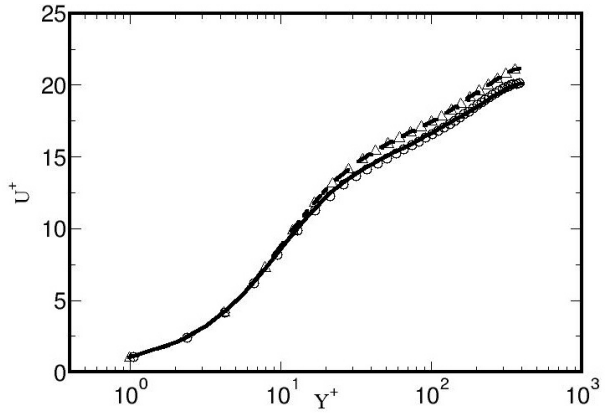

Figure 3. Mean velocity. Triangle up GSIG, solid line GsvsSIG, dashed line SMD and the circles are the DNS of Moser *et al.*

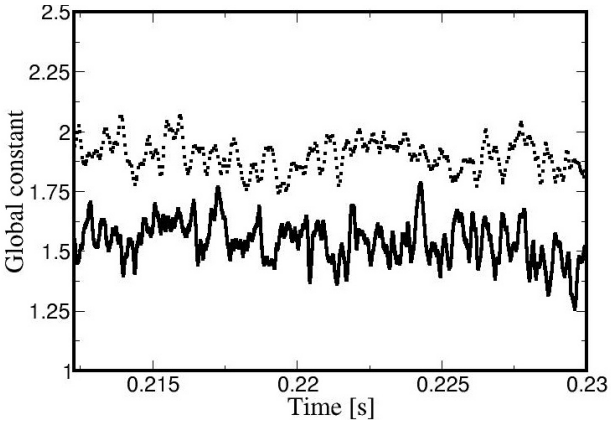

Figure 4. Global dynamic constant. Dotted line GSIG and solid line GsvsSIG.

layer. These guidelines led to the experimental set-up shown on Fig. 6 with the three main following characteristics: **1.** The global dimensions (nozzle hole, channel width) are consistent with the simulation constraints in order to allow full size computation of the geometry. In particular this led to the selection of the injector characterized by a large cross flow area together with a fast response time (of the order of 100 microseconds). **2.** The cross flow profile and turbulent characteristics are controlled by the use of inlet convergent and grid. The injector flow characteristics are also controlled by the use of a specific convergent profile, while the injection system is designed to control the upstream pressure. **3.** Wide optical access were provided by UV quality large quartz window in order to optimize the application of advanced optical diagnostics.

Experimental set-up and PIV measurements

The pulsed jet is generated by an electric injector (fast response time and large flow area Hoerbiger GV50 injector) and the opening duration is about 10ms. The injection frequency is 1Hz. The injection diameter is d = 1cm. The im-

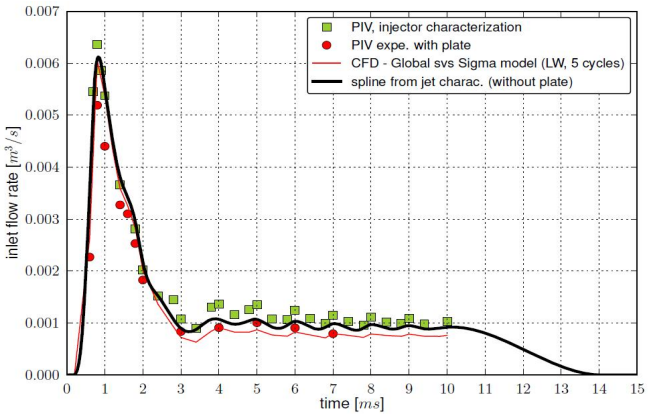

Figure 5. Flow rate. The plate corresponds to the impinging surface in presence of the cross flow.

pinging surface is situated at H = 2cm of the jet exit. The injector is supplied by a tank of volume V = 20l full of nitrogen. The nitrogen going to the injector is heated via an electric heater in order to keep it at the constant temperature. The nitrogen temperature at the exit of the jet was measured using a Two-color Toluene-LIF Imaging method (Tea *et al.*, 2011). The measured temperature at the jet exit is 343K. The air cross flow in the measuring section in which the mixing takes place is generated via a fan situated downstream. The cross flow is at ambient temperature. A convergent and a honeycomb situated upstream reduce significantly the fluctuation in the measurements section. The cross flow Reynolds number (based on the cross flow mean velocity and the channel width) is about 16000 and the jet flow Reynolds number (based on the mean inlet velocity and the injector's diameter) varies between 60000 and 12000.

PIV measurements were performed using a doubled frequency Nd:YAG-laser at 532nm. The signal was recorded with a CCD camera of 2048 X 2048 pixels resolution, equipped with a lens with the following characteristics: $f = 105mm$ and $f_{\#} = 2.8$. The time delay between the two pulses is 2 microseconds. Each pair of images was processed using cross correlation. Two preliminaries series of measurements were performed to get the initial conditions : a first one to characterize the injector flow rate (seeding inside the injector), the second one to characterize the cross flow turbulent intensity and mean profile (seeding only of the cross flow). The PIV measurements were performed on 3 plans in the streamwise direction (Z direction at $Z = 0mm$,$7mm$, $15mm$ where the injector center is the origin) and 3 in the spanwise direction (X direction at $X = -10mm$, $0mm$,$10mm$). For each plan, measurements were done at different times after the injection and the statistics were accumulated over 1000 snapshots.

Numerical procedure and results

The numerical set-up of the experiment consisted in two steps. The first step was the cross flow modeling. This was done by initializing the same mean flow obtained with the PIV measurements with 1% turbulent intensity. Depending on the number of injections to perform, different cross flows solutions were used as initial conditions before the injection. This

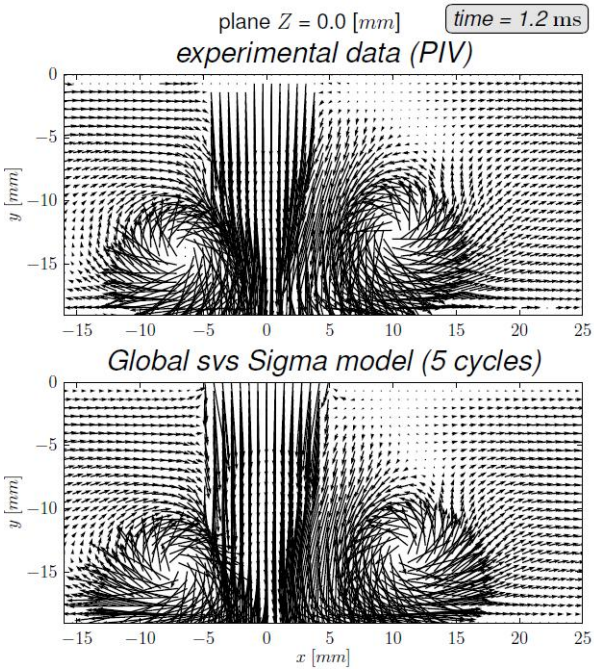

Figure 7. Velocity field at time 1.2*ms* after the beginning of the injection. The cross flow comes from the left hand side.

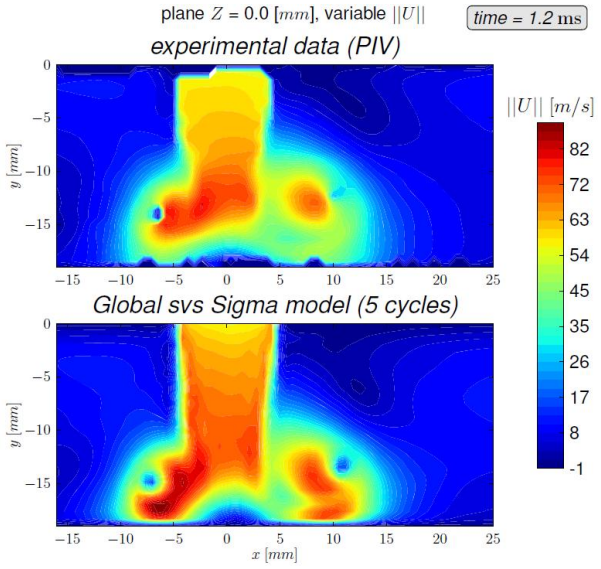

Figure 8. Velocity magnitude at time 1.2*ms* after the beginning of the injection. The cross flow comes from the left hand side.

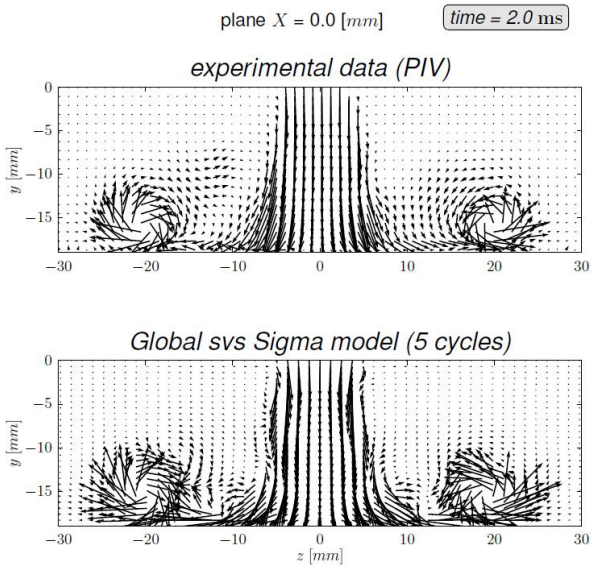

Figure 9. Velocity Field at time 2.0*ms* after the beginning of the injection. Plan $X = 0$ perpendicular to the cross flow.

allows to have a different cross flow at each injection and to perform ensemble average if necessary. The target flow rate of the injector was obtained from the PIV measurements with cross flow rate turned off. The nitrogen inside the injector was initialized at the temperature obtained via LIF measurement and the solid boundaries of the convergent were kept at this temperature during the simulation. The other solid boundaries were maintained at ambient temperature with a noslip isothermal boundary condition.

The simulations were performed with a Lax-Wendroff finite volume numerical scheme that is second order accurate in space with a single time step integration. It has the advantage to be fast and it is commonly used for industrial applications. Fig 5 shows the different flows rate with and without cross flow for the experiment and the simulation. As expected in the experiment the flow rate decreases in presence of the cross flow. We can also observe that the flow rate obtained in the simulation with the cross flow is quite in good agreement with the experiments. It is worth noting that the inlet conditions have a major impact on the quality of the results of the simulations. The predictions of the simulation (averaged over 5 cycles/injections) at the impinging time ($t = 1.2ms$) are quite in good agreement with the PIV measurements as it can be seen on Fig 7 and Fig 9. The position of the vortex after the impingement is also well predicted as shown on Fig 9. Further comparison at various section are required to compare more accurately PIV measurements and simulations. However the concept of a global constant that varies only in time seems to lead to quite good results even in a complex configuration.

CONCLUSION

The proposed modification for the global dynamic procedure allows to account for solid boundaries while keeping the interesting properties of the global approach. Indeed it does not require homogeneous directions nor clipping and it leads to same results in case of non wall bounded flows like an HIT. The combination with the σ-model provides accurate results on standard validation cases and on a more complex configurations that consists in a hot impinging unsteady jet with a cross flow. Although the constant is homogeneous in space and only varies in time, a first analysis shows that the

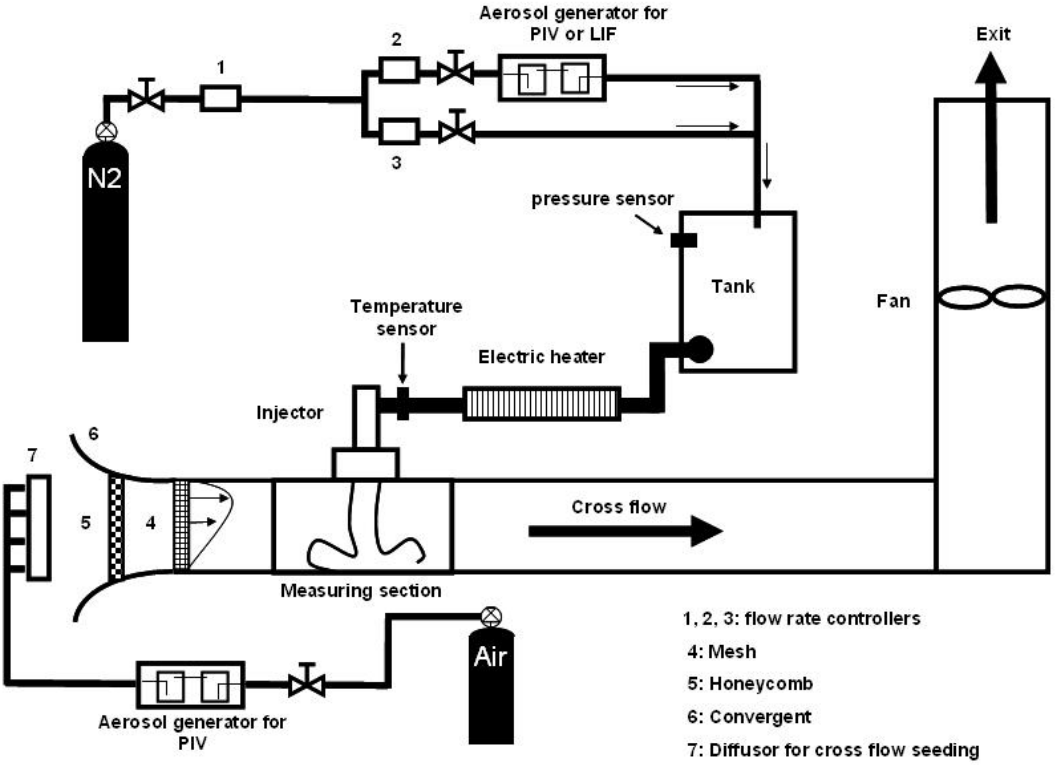

Figure 6. Schematic description of the experimental set-up of the hot impinging pulsed jet in presence of a cross flow.

simulation are in close agreement with the experiments. Further quantitative comparisons of the velocity field, the temperature stratification and rms still need to be done but the proposed procedure/model seems promising for extending the use of SGS models from simple academic cases to industrial applications.

REFERENCES

AVBP 2011 *http://www.cerfacs.fr/4-26334-the-avbp-code.php.*

Baya Toda, H., Cabrit, O., Balarac, G., Nicoud, F. 2011 A subgrid-scale model based on singular values for LES in complex geometries. *In. Proceedings Center for Turbulence Research* NASA Ames/Stanford University.

Baya Toda, H., Truffin K., Nicoud, F. 2010 Is the dynamic procedure appropriate for all sgs models ? *In V European Conference on Computational Fluid Dynamics, ECCOMAS (ed. J.C.F. Pereira & A. Sequeira).*

Cabrit, O., Nicoud, F. 2009 Direct simulations for wall modelling of multicomponent reacting compressible turbulent flows. *Physics of Fluids* **21**(055108).

Comte-Bellot, G., Corsin, S. 1971 Simple Eulerian time correlation of full narrow-band velocity signals in grid generated "isotroppic" turbulence. *Journal of Fluid Mechanics* **48**, 273-337.

Germano, M. and Piomelli, U. and Moin, P. and Cabot, W. 1991 A dynamic subgrid-scale eddy viscosity model *Physics of Fluids* **3** 1760-1765.

Kim, J., Moin, Moser, R. 1987 Turbulence statistics in fully developed channel flow at low Reynolds number *Journal of Fluid Mechanics* **177** 133-166.

Lee, J., Choi, H., Park, N. 2010 Dynamic global model for large-eddy simulation in transient flows. *Physics of fluids* **22, 075106**.

Lilly, D. K. 1992 A Proposed Modification of the Germano Subgrid-Scale Closure Method. *Physics of fluids* **A4(3)** 633-635.

Nicoud, F., Ducros, F. 1999 Subgrid-scale stress modeling based on the square of the velocity gradient tensor. *Flow, Turbulence and Combustion* **62** 183-200.

Nicoud, F., Baya Toda, H., Cabrit, O., Bose, S., Lee, J. 2011 Using singular values to build a subgrid-scale model for Large Eddy Simulations. *submitted to Physics of Fluids*.

R. D. Moser, J. Kim, Manssour, N. N. 1999 Direct numerical simulation of turbulent channel flow up to $Re_\tau = 590$. *Physics of fluids* **11(4)**.

Smagorinsky, J. 1963 General circulation experiments with the primitive equations. *Month. Weather* **93** 99-165.

Tea, G., Bruneaux, G., Kashdan, J.T., Schulz, C. 2011 Unburned gas temperature measurements in a surrogate Diesel Jet via Two-color Toluene-LIF imaging. *Proceeedings of the Combustion Institute* **33** 783-780.

Vreman, A. 2004 An eddy-viscosity subgrid-scale model for turbulent shear flow : Algebraic theory and applications. *Physics of fluids*. **16(10)**.

APPENDIX B

This article is the result of the works performed during the *Center for turbulence Research, Summer Program 2010* at Stanford University. It is about the development of the σ-model.

A subgrid-scale model based on singular values for LES in complex geometries.
Baya Toda H, Cabrit O., Balarac G., Bose S., Lee J., Choi H. and Nicoud F.
Proc. of the Summer Program. Stanford, Center for Turbulence Research,
NASA Ames/Stanford Univ., pp. 193-202, 2010

A subgrid-scale model based on singular values for LES in complex geometries

By H. Baya Toda†, O. Cabrit‡, G. Balarac¶, S. Bose, J. Lee‖, H. Choi‖ AND F. Nicoud ††

An eddy-viscosity based, subgrid-scale model for Large Eddy Simulations is derived from the analysis of the singular values of the resolved velocity gradient tensor. It is shown that the proposed σ-model has the property to automatically vanish as soon as the resolved field is two-dimensional, including the pure shear and solid rotation cases. In addition, the model generates no subgrid-scale viscosity when the resolved scales are in pure axisymmetric or isotropic contraction/expansion. At last, it has the appropriate cubic behavior in the vicinity of solid boundaries without requiring any ad-hoc treatment. Results obtained for different physical configurations (isotropic turbulence, channel flows, and periodic jet) are presented to illustrate the potential of the model. A dynamic version based on a volume averaged procedure is also proposed.

1. Introduction

When dealing with Large Eddy Simulations (LES), the eddy-viscosity assumption is by far the most used because it reduces the modeling effort considerably. In this view, the subgrid-scale (SGS) tensor is written as $\tau_{ij}^{\mathrm{SGS}} - \frac{1}{3}\tau_{kk}^{\mathrm{SGS}}\delta_{ij} = 2\nu_{\mathrm{SGS}}S_{ij}$, where $S_{ij} = \frac{1}{2}\left(g_{ij} + g_{ji}\right)$ and $g_{ij} = \partial u_i/\partial x_j$ is the velocity gradient tensor of the resolved scales. Note that the (implicit) filter $\bar{\cdot}$ is omitted throughout this paper for simplicity. From a simple dimensional analysis, it is natural to model the subgrid-scale viscosity as

$$\nu_{\mathrm{SGS}} = \left(C_m\Delta\right)^2 \mathcal{D}_m(\mathbf{u}), \tag{1.1}$$

where C_m is the model constant, Δ is the subgrid characteristic length scale (in practice the size of the mesh), and $\mathcal{D}_m$ is a differential operator associated with the model, homogeneous to a frequency and acting on the resolved velocity field $\mathbf{u} = (u_i)$. The most classical operator is by far the strain rate; this leads to the Smagorinsky (1963) model for which $\mathcal{D}_m = \mathcal{D}_s = \sqrt{2S_{ij}S_{ij}}$ and $C_m = C_s \approx 0.18$. This operator is known for not vanishing in near-wall regions. In the past, this major drawback (not the only one of the Smagorinsky operator) motivated the use of damping functions (Moin & Kim, 1982) and the development of the dynamic procedure by Germano *et al.* (1991). It is actually possible to overcome this weakness by using advanced models that naturally vanish in pure shear regions such as the WALE (Wall Adapting Local Eddy viscosity) and Vreman models (Vreman, 2004). However, all the models based on the eddy-viscosity assumption, Eq. 1.1, share the drawback that the model constant C_m must be adapted to the mesh refinement so that the proper amount of energy is drained from the resolved

† IFP Energie Nouvelles
‡ CERFACS
¶ LEGI
‖ Seoul National University
†† CNRS UMR 5149. Corr. author: franck.nicoud@univ-montp2.fr

scales. This issue is well addressed by the introduction of a dynamic procedure that can automatically adapt the model constant. In this view, the model constant C_m can be computed resorting to a least squares approach proposed by Lilly (1992),

$$(C_m\Delta)^2 = -\frac{L_{ij}M_{ij}}{2M_{ij}M_{ij}}, \tag{1.2}$$

where $L_{ij} = \widetilde{u_i}\,\widetilde{u_j} - \widetilde{u_i}\,\widetilde{u_j}$ is the (modified) Leonard term based on the grid-based filter (which is omitted for clarity, $\overline{u_i} = u_i$) and test filter $\widetilde{\cdot}$. In addition, M_{ij} is directly related to the differential operator and the eddy-viscosity model is based on

$$M_{ij} = \frac{\widetilde{\Delta}^2}{\Delta^2}\widetilde{\mathcal{D}_m}\widetilde{S_{ij}} \;-\; \widetilde{\mathcal{D}_m\,S_{ij}},$$

where $\widetilde{\Delta}$ stands for the test filter width. Unfortunately, the original dynamic procedure most often requires some averaging in order to reduce the constant variability over space and time. Several improved versions of the dynamic Smagorinsky model were proposed in order to make it more robust and suitable for complex configurations where no homogeneous directions are present (Ghosal, 1995; Meneveau *et al.*, 1996). Still, the common practice when dealing with complex geometries is to apply the least mean square formula over a small volume surrounding the current grid point and to clip the remaining negative values of the dynamically computed constant. This means replacing Eq. 1.2 by

$$(C_m\Delta)^2 = \max\left[-\frac{\langle L_{ij}M_{ij}\rangle_{\mathrm{loc}}}{2\,\langle M_{ij}M_{ij}\rangle_{\mathrm{loc}}}, 0\right], \tag{1.3}$$

where $\langle\cdot\rangle_{\mathrm{loc}}$ stands for an integral taken over a small volume (typically a few grid cells) surrounding the current grid point. Note that the model constant then depends on both space and time.

The main motivation of the local dynamic procedure was to adapt the constant to compensate the non-vanishing behavior of the Smagorinsky model in near-wall regions. Recently, Ghorbaniasl & Lacor (2008) proposed to extend the dynamic procedure to the WALE model. However, Baya Toda *et al.* (2010) reported that the combination of the classical dynamic procedure with any SGS model that has the proper near-wall cubic behavior leads to a paradox: the underlying differential operator rapidly goes to zero near solid boundaries, which favors unstable computations. For the sake of robustness while keeping an adaptation of the model coefficient to the grid resolution and numerical errors, two concepts of global dynamic procedure emerged from the properties of the Vreman model. The first one is based on the global equilibrium hypothesis (da Silva & Metais, 2002) and was proposed by Park *et al.* (2006) and was later improved by You & Moin (2007). The second one, based on the Germano identity, was also proposed by Park et al. (2006) and was proven to be better suited for transient flows (Lee *et al.*, 2010). This global dynamic procedure amounts to change Eq. 1.3 to

$$(C_m\Delta)^2 = -\frac{\langle L_{ij}M_{ij}\rangle_{\mathrm{dom}}}{2\,\langle M_{ij}M_{ij}\rangle_{\mathrm{dom}}}, \tag{1.4}$$

where $\langle\cdot\rangle_{\mathrm{dom}}$ stands for an averaging over the whole computational domain; the model constant is then uniform over space by construction. It has the advantage of producing mostly positive values for the dynamic constant, thus avoiding the clipping issue. The price to pay is that the differential operator $\mathcal{D}_m$ must behave appropriately in basic flow configurations because no compensation from the dynamic procedure can be ex-

pected (the constant of the model is uniform over space). For example, such formulation is not expected to provide good results if applied to the Smagorinsky model since the eddy-viscosity would then not vanish near solid walls. The differential operators used in the WALE and Vreman models are not very appropriate either. For example, it can be shown analytically that the latter is linear with respect to the distance to solid boundaries instead of having a cubic behavior in near-wall regions. Also, they both produce non zero eddy-viscosity in simple flow configurations such as solid rotation, and more generally two-dimensional and/or two-component (2C) flows, where no subgrid scale activity is expected to occur. Indeed, although two-dimensional turbulence has been evidenced experimentally and numerically (Lesieur, 2008), it is a phenomenon of fundamental interest that "might thus be viewed as just a toy model" (Frisch, 1995). Given that two- and three-dimensional turbulence are fundamentally different because of the absence of the vortex-stretching term in the former, it seems appropriate to make sure that any SGS model for three-dimensional turbulence switches off in the two-dimensional case. The alternative would be to switch to a SGS model appropriate for two-dimensional turbulence. Still, given the very little probability that a three-dimensional computation of a two-dimensional turbulent flow remains two-dimensional without any external action to maintain its two-dimensionality, this choice was not pursued. At the end, the main objective of this paper is to define and test a new static model for three-dimensional flows with better properties than the existing formulations. The analytical formulation is provided in section 2, numerical results are discussed in section 3.

2. A singular values-based model

Several properties are desirable for an improved differential operator, although establishing a definite list of such properties would be a very difficult task. Similar to the WALE and Vreman models, the operator should tend to zero in near-wall regions in order to mimic the turbulence damping due to the no-slip condition. It can be shown that the turbulent stress, thus the eddy-viscosity and the differential operator, would decay as the distance to the solid boundary to the third power (Chapman & Kuhn, 1986) (**Property P1**). At the same time, it would vanish in the case of a flow in solid rotation, like the Smagorinsky model, and in the case of a pure shear, like the WALE and Vreman models. More generally, the improved differential operator should be zero for any two-dimensional flow (**Property P2**). Indeed, such a situation for the resolved scales is not compatible with a subgrid-scale activity, which is presumably three-dimensional. The same reasoning leads to the conclusion that the SGS viscosity should be zero in the case where the resolved scales are either in pure axisymmetric or isotropic contraction/expansion (**Property P3**). The former case corresponds to the situation of a laminar round jet impinging on a solid plate for which turbulent effect should indeed not be present. The latter is representative of the velocity field near an acoustic monopole or a spherical premixed flame, which again are not phenomena of turbulent nature.

Analyzing the spectral content of the velocity gradient tensor proves to be a proper framework to investigate how these properties can be met by a single differential operator. Note, however, that the eigenvalues of $\mathbf{g}$ can be complex-valued in number of flow configurations (in the case of a solid rotation, for example). One way to avoid this difficulty is to consider the strain rate tensor instead of $\mathbf{g}$. In this case, the three eigenvalues are real-valued, although their sign is not known a priori. This route is explored in another paper in this volume (Verstappen & Bose, 2010). In the present study, one relies on

the singular value decomposition of $\mathbf{g}$ to build an improved differential operator for the SGS eddy viscosity. Specifically, let us introduce $\sigma_1 \geq \sigma_2 \geq \sigma_3 \geq 0$, the three singular values of $\mathbf{g} = (g_{ij})$. By definition, these values are always positive and equal the square root of the eigenvalues of the matrix $\mathbf{G} = \mathbf{g}^t\mathbf{g}$ (which are always positive because $\mathbf{G}$ is symmetric semi-definite positive). The smallest singular value, σ_3, is null if and only if one row or column of $\mathbf{g}$ is zero up to a rotation of the coordinate system. In other words, $\sigma_3 = 0$ is a marker for two-dimensional and/or 2C flows, and any operator proportional to this singular value would meet property **P2**. Similarly, the knowledge of the singular values of $\mathbf{g}$ helps to detect the case where the resolved velocity field is in axisymmetric contraction or expansion. Indeed, an appropriate rotation of the coordinate system then makes the velocity gradient tensor diagonal:

$$\mathbf{g} = \mathrm{diag}\,(\beta, -\alpha, -\alpha), \tag{2.1}$$

where α is positive for a contraction and negative for an expansion. Depending on the relative values of the parameters α and β, the singular values of $\mathbf{g}$ read either $\sigma_1 = |\beta| > \sigma_2 = \sigma_3 = |\alpha|$ or $\sigma_3 = |\beta| < \sigma_1 = \sigma_2 = |\alpha|$. In other words, the marker for such flow situations is either $\sigma_2 = \sigma_3$ or $\sigma_1 = \sigma_2$. Also a isotropic contraction/expansion corresponds to $\sigma_1 = \sigma_2 = \sigma_3$, thus any differential operator proportional to $(\sigma_1 - \sigma_2)(\sigma_2 - \sigma_3)$ would meet property **P3**. Note that the divergence-free assumption was not made to obtain the above results (β not necessary equal to 2α).

From the above analysis, a differential operator proportional to $\sigma_3(\sigma_1 - \sigma_2)(\sigma_2 - \sigma_3)$ would meet both properties **P2** and **P3**. By analyzing the asymptotic behavior of the singular values in the vicinity of a solid boundary, it is actually possible to show that

$$\sigma_1 = O(y^0) \quad ; \quad \sigma_2 = O(y^1) \quad ; \quad \sigma_3 = O(y^2). \tag{2.2}$$

The algebra that leads to this result is not given in this report for the sake of simplicity. Eqs. 2.2 indicate that the product $\sigma_3(\sigma_1 - \sigma_2)(\sigma_2 - \sigma_3)$ selected to meet properties **P2** and **P3** is of order $O(y^3)$ near solid boundaries and thus meets property **P1**. The derivation of the differential operator is finished by choosing a scaling factor so that it is a frequency scale. A natural choice is the use the largest singular value σ_1, which is nothing but the norm of $\mathbf{g}$, and which would not change the asymptotic behavior of the ratio. Finally, the proposed SGS model and associated differential operator read

$$\nu_{\mathrm{SGS}} = (C_\sigma \Delta)^2 \, \mathcal{D}_\sigma \quad ; \quad \mathcal{D}_\sigma = \frac{\sigma_3(\sigma_1 - \sigma_2)(\sigma_2 - \sigma_3)}{\sigma_1^2}. \tag{2.3}$$

This model will be referred to as the σ-model in the remaining of this paper.

Table 1 summarizes the properties of different differential operators and associated models. Contrary to what is often mentioned, the asymptotic behavior of the Vreman model is linear in y instead of being cubic. Thus, only the WALE and σ models comply with property **P1**. Note however that the first order behavior of the Vreman model is enough to make it more suitable for wall-bounded flows than the Smagorinsky model for which the eddy-viscosity does not tend to zero because $\mathcal{D}_s = O(y^0)$. Table 1 also shows that the σ-model meets properties **P2**-**P3**, contrary to the other formulations which all fail at some point. It also shares with the three other models the common property that involves only one-point velocity gradients; it is thus easy to implement in any general purpose LES code. The value reported for the model constant C_σ is a rough estimation generated by equating the averaged SGS dissipation obtained by feeding the Smagorinsky model and Eq. 2.3 with a large sample of random velocity gradient tensors. Of course, a more accurate assessment could be done by performing appropriate computations, for

Model	Smagorinsky Smagorinsky (1963)	WALE Nicoud & Ducros (1999)	Vreman Vreman (2004)	σ-model Present
Operator Model constant	$\sqrt{2S_{ij}S_{ij}}$ $C_s \approx 0.18$	Eq. 13 of above ref. $C_w \approx 0.50$	Eq. 35 of above ref. $C_v \approx 0.28$	Eq. 2.3 $C_\sigma \approx 1.5$
Asymptotic **P1**	$O(y^0)$ NO	$O(y^3)$ YES	$O(y)$ NO	$O(y^3)$ YES
Solid rotation Pure shear **P2**	0 1 NO	≈ 0.90 0 NO	≈ 0.71 0 NO	0 0 YES
Axisym Isotropic **P3**	≈ 3.46 ≈ 2.45 NO	≈ 0.15 0 NO	≈ 1.22 1 NO	0 0 YES

TABLE 1. Properties of the SGS models considered. Labels Axisym and Isotropic refer to axisymmetric and isotropic contraction/expansion respectively. The entries below the **P1** row are the values taken by the differential operators when all the velocity derivatives are zero except: Solid rotation: $du_1/dx_2 = -1$ and $du_2/dx_1 = 1$; Pure shear: $du_1/dx_2 = 1$; Axisym: $du_1/dx_1 = \pm 2$, $du_2/dx_2 = \mp 1$, $du_3/dx_3 = \mp 1$; Isotropic: $du_1/dx_1 = \pm 1$, $du_2/dx_2 = \pm 1$, $du_3/dx_3 = \pm 1$

example, of decaying isotropic turbulence cases. This task is not pursued here since the result of any tuning effort would depend on the grid resolution and numerics. Note, however, that the random procedure used to assess C_σ leads to fair estimates of the WALE and Vreman's constant [$C_w \approx 0.63$ and $C_v \approx 0.29$, to be compared with the values recommended by Nicoud & Ducros (1999) and Vreman (2004) and reported in Table 1]. The chosen value $C_\sigma = 1.5$ is thus sufficient to assess the potential of the static σ-model. The proper way to reduce the influence of the selected value for the model coefficient is to use some kind of dynamic procedure able to compensate, at least partly, for the grid resolution and numerical errors. Concerning this topic, a Germano-identity-based global dynamic procedure applied to the σ-model will be presented in section 3.

3. Numerical experiments

The σ-model was implemented in several numerical tools for LES and tested over a variety of academic flow configurations.

• **Solver A**: The general purpose AVBP code was developed at CERFACS and IFP Energies Nouvelles. It is based on a cell-vertex formulation and embeds a set of finite element/ finite volume schemes for unstructured meshes. In the present study a centered Galerkin finite element method (4^{th} order in space) with a 3^{rd} order Runge-Kutta temporal integration is retained for the investigation of two configurations: the decaying isotropic turbulence from the Comte-Bellot & Corsin (CBC) experiment and a turbulent channel flow at Reynolds number $Re_\tau = 395$. These flows were computed with the Dynamic Smagorinsky model and the present static σ-model. The dynamic procedure was applied locally, without averaging over homogeneous directions. Negative values of the

dynamically tuned constant of the Smagorinsky model were clipped to ensure stability (see Eq. 1.3).

- **Solver B**: a finite difference code dedicated to the computation of turbulent channels and developed at the Center for Turbulence Research. It is based on a kinetic energy conserving, 4^{th} order scheme in space as proposed by Morinishi *et al.* (1998). A 3^{rd} order Runge-Kutta scheme is used for the time integration, except for the diffusion terms in the direction normal to the wall that are integrated thanks to an Crank-Nicholson scheme. The divergence-free condition is met by a projection scheme. It was used to compute the turbulent channel flow case at $Re_\tau = 590$ with both the dynamic Smagorinsky model and the present static σ-model. Note that contrary to the implementation used in the general purpose AVBP solver, the dynamic procedure is not applied locally in this case. Instead, the Smagorinsky constant is computed as

$$(C_s\Delta)^2 = -\frac{\langle L_{ij}M_{ij}\rangle_{\text{plane}}}{2\,\langle M_{ij}M_{ij}\rangle_{\text{plane}}}, \tag{3.1}$$

where $\langle\cdot\rangle_{\text{plane}}$ stands for an integral taken over homogeneous planes parallel to the walls of the channel. This avoids clipping while keeping the favorable dependence of the model constant on the distance to the solid boundaries.

- **Solver C**: a dealiased spectral code developed at Seoul National University. It is based on a 2^{nd} order semi-implicit scheme for time integration: diffusion terms are treated implicitly using the Crank-Nicolson method, and a 3^{rd} order Runge-Kutta scheme is applied to convection terms. The decaying isotropic turbulence from the Comte-Bellot & Corsin (1971) experiment was computed with a dynamic version of the σ-model. The Germano-based global dynamic procedure (Park *et al.*, 2006; Lee *et al.*, 2010) was used (see Eq. 1.4), meaning that a single-model constant was computed for the whole domain at each iteration. A divergence-free initial field was generated using the re-scaling method proposed by Kang *et al.* (2003).
- **Solver D**: a pseudo-spectral code developed at the LEGI lab in Grenoble, France. With this tool, the viscous terms are treated exactly using a 2^{nd} order explicit Runge-Kutta time-advancement. A classical two-third rule is used for dealiasing the non-linear convection term. This tool was used to compute the case of a periodic plane jet as described in da Silva & Pereira (2008). Several SGS formulations were considered, including the global dynamic σ and Smagorinsky models (both based on the procedure of Eq. 1.4), a local dynamic Smagorinsky model with clipping (see Eq. 1.3), and a planewise dynamic Smagorinsky model without clipping (see Eq. 3.1).

3.1. *Isotropic decaying turbulence*

We first validate the behavior of the σ-model for the simple case of a freely decaying isotropic homogeneous turbulence. The experiment by Comte-Bellot & Corrsin (1971) on decaying turbulence behind a grid is simulated, where the mesh size of the grid turbulence is $M = 5.08$ cm and the free-stream velocity is $U_0 = 10$ m/s. The Taylor micro-scale Reynolds number is $Re_\lambda = u_{rms}\lambda/\nu = 71.6$ at time $tU_0/M = 42$ and decreases to 60.6 at $tU_0/M = 171$. In a reference frame moving with the average flow velocity the problem can be thought of as freely decaying isotropic turbulence. We model this by considering the fluid to be inside a cube-shaped box with periodic boundary conditions. The flow was first computed with the general purpose code AVBP (**Solver A**), where the static σ-model was implemented with $C_\sigma = 1.5$. The grid resolution was 61^3 and Fig. 1 shows that the computed spectra are in fair agreement with the experimental data. The

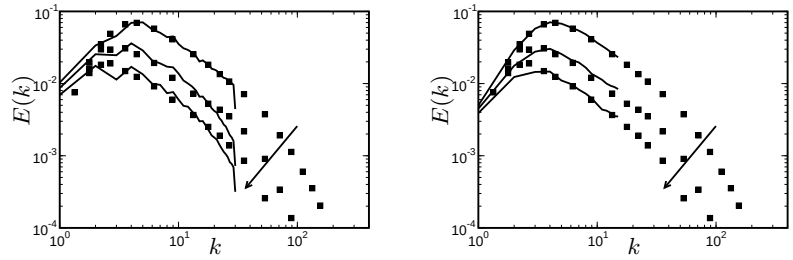

FIGURE 1. Time evolution of energy spectra for freely decaying isotropic turbulence with the σ-model. Symbols are experimental measurements corresponding to the three-dimensionless times $tU_0/M = 42$, 98 and 171. Left: Results from general purpose solver AVBP (**Solver A**) with grid 61^3. Static σ-model. Right: Results from spectral code (**Solver C**) with grid 32^3. Global dynamic σ-model.

biggest differences are obtained for the smallest scales; they are most probably from the large numerical errors that characterize finite volume/finite element methods for large wave numbers. This is confirmed by the results obtained from the spectral code **Solver C** which are essentially in good agreement with the measurements, although the grid is even coarser (32^3). Note that the global dynamic σ-model was used in this case; the constant (homogeneous in space) varied only weakly with time during the simulation with $C_\sigma \approx 1.5 - 1.7$, in close agreement with the value retained from the random procedure (see Table 1).

3.2. *Turbulent Channel flow*

The performance of the static σ-model for wall-bounded flows was investigated by computing LES of turbulent channel flows at friction Reynolds number $Re_\tau = 395$ and 590 with solvers **Solver A** (general purpose) and **Solver B** (channel solver), respectively. In both cases, the computed mean velocity profile is in good agreement with the DNS data from Moser *et al.* (1999), as displayed in Fig. 2. The results are in fact slightly better than what is obtained with the dynamic Smagorinsky model. The same trend is observed when looking at the velocity fluctuations (not shown). The theoretical asymptotic behavior of the σ-model near solid boundaries ($\nu_{\rm SGS} = O(y^3)$) is also well retrieved numerically, as shown in Fig. 3. Note that the amount of SGS eddy-viscosity is not negligible in front of the molecular viscosity, at least in the core region. This reflects the fact that the grid resolution is far from what is required to perform DNSs of the same flows: $\Delta x^+ \approx 48$, Δy^+ in the range 1-17, $\Delta z^+ \approx 10$ for the LES at $R_\tau = 395$ - **Solver A**; $\Delta x^+ \approx 58$, Δy^+ in the range 1-17, $\Delta z^+ \approx 29$ for the LES at $R_\tau = 590$ - **Solver B**. This figure also illustrates that the proper asymptotic behavior is obtained with the dynamic Smagorinsky model only when the plane-wise procedure (Eq. 3.1) is applied, as for the case $R_\tau = 590$ and **Solver B**. Recall that this procedure can be used only for simple cases with homogeneous directions. Conversely, the asymptotic behavior is built in the σ-model's differential operator itself and no specific dynamic procedure/homogeneous directions is required.

3.3. *Turbulent Plane jet*

Further LESs of a periodic planar jet configuration were performed in order to illustrate the potential of the global dynamic σ-model. The spectral code **Solver D** was used. The results from several 64^3 LESs are compared to 256^3 DNS data obtained by running the same spectral code. The configuration is close to the one studied in da Silva & Pereira (2008) except for the jet width-to-initial momentum thickness, which is 20 instead of 35. The

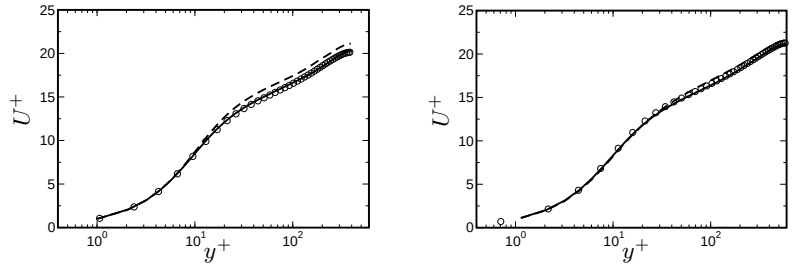

FIGURE 2. Mean velocity profile from the static σ-model (———) and the dynamic Smagorinsky model (- - - -). Symbols correspond to the DNS data of Moser *et al.* (1999). Some symbols of the DNS were removed for clarity. Left: Results from the general purpose solver AVBP (**Solver A**) at $Re_\tau = 395$. Right: Results from the channel code (**Solver B**) at $Re_\tau = 590$.

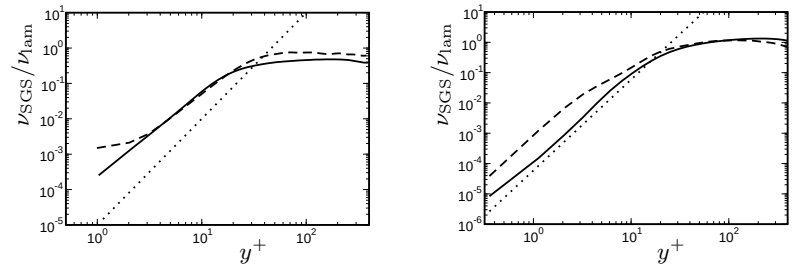

FIGURE 3. Scaled SGS eddy-viscosity from the static σ-model (———) and the dynamic Smagorinsky model (- - - -). The dotted lines correspond to the proper y^3 asymptotic behavior. Left: Results from general purpose solver AVBP (**Solver A**) at $Re_\tau = 395$. Right: Results from the channel code (**Solver B**) at $Re_\tau = 590$.

computational domain is periodic in the three spatial directions and its size is four times the initial jet width. The DNS initial field is generated by super-imposing divergence-free random fluctuations to the mean velocity profile. The LES initial condition is obtained from the DNS data by spectral interpolation. Because periodic conditions are imposed in both the streamwise and spanwise directions, the flow is not statistically steady and the jet keeps growing thicker and thicker as time increases. Figure 4 displays the resolved kinetic energy and SGS eddy-viscosity. from the different LES performed at time 12 h/U where h is the jet width and U is the maximum mean velocity. Note that the profiles are not symmetric because only plane-averaging over the homogeneous directions was applied and the flow is not statistically stationary. Regarding the dynamic Smagorinsky model, the best agreement with the filtered DNS is obtained when the dynamic procedure is applied planewise (see Eq. 3.1). This formulation permits the combination of accuracy (the model constant depends on the position in the plane jet) and robustness (the planar averaging stabilizes the procedure sufficiently to avoid clipping). When the dynamic procedure is applied locally to the Smagorinsky model, Eq. 1.3, a large amount of clipping is required to stabilize the pointwise model constant, and the overall accuracy degrades. On the other hand, when the global procedure, Eq. 1.4, is applied, the model constant is uniform over space and no clipping is required. However, a high level of eddy-viscosity is generated in the mean shear regions because the mean gradient contributes to the strain rate. As a consequence, the resolved scales are over-dissipated and their kinetic energy is under-estimated. Note that the over-estimation of ν_{SGS} does not appear in Fig. 4 because the amount of fluctuation is already way too small at the instant considered.

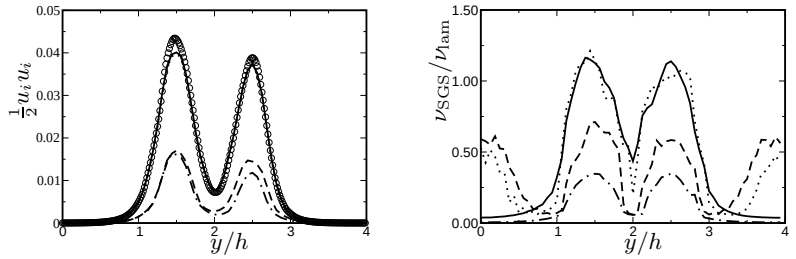

FIGURE 4. LES of a periodic plane jet with a 64^3 grid performed with the spectral code **Solver D**. The global dynamic σ-model (———) at time 12 h/U is compared with the local (– – – –), planewise (·····) and global (—·—) dynamic Smagorinsky models. Left: Resolved kinetic energy. Symbols correspond to the filtered 256^3 DNS. Right: SGS eddy-viscosity scaled by the molecular viscosity.

On the contrary, because the static σ-model produces zero eddy-viscosity for the mean shear associated with the jet, applying the same global dynamic procedure to this model leads to much better results, comparable to the planewise dynamic Smagorinsky model. Note, however, that the global dynamic σ-model can readily be extended to any complex geometry because neither averaging over homogeneous directions nor clipping are required.

4. Conclusions

A differential operator based on the singular values of the velocity gradient tensor is proposed as a basis for an improved SGS eddy-viscosity model. It is shown that the proposed static σ-model generates zero eddy-viscosity for any two-dimensional or 2C flows, as well as for axisymmetric and isotropic situations. It also has the proper cubic behavior in near-wall regions. Owing to its unique properties, this model is well suited for the global dynamic procedure, which adapts the overall coefficient to the grid resolution and numerical errors. The σ-model was implemented in several academic and general purpose CFD codes, under either its static or global dynamic version. The results presented in this report are promising because of the relative ease of implementation. It is anticipated that the σ-model could be useful in the current effort to make LES even more suitable for complex flow configurations.

Hubert Baya Toda gratefully acknowledges support from IFP Energies Nouvelles. CINES and IDRIS from GENCI are acknowledged for giving access to super-computing facilities. The authors also thank Prof P. Moin for fruitful discussions.

REFERENCES

AVBP 2006 Avbp code : www.cerfacs.fr/cfd/avbp_code.php and www.cerfacs.fr/cfd/ cfd-publications.html

BAYA TODA, H., TRUFFIN, K. & NICOUD 2010 Is the dynamic procedure appropriate for all SGS models? In V European Conference on Computational Fluid Dynamics, ECCOMAS (ed. J. C. F. Pereira & A. Sequeira).

CHAPMAN, D. & KUHN, G. 1986 The limiting behavior of turbulence near a wall. *J. Fluid Mech.* **170**, 265–292.

Comte-Bellot, G. & Corrsin, S. 1971 Simple Eulerian time correlation of full- and narrow-band velocity signals in grid generated, 'isotropic' turbulence flows. *J. Fluid Mech.* **48**, 273–337.

Da Silva, C. B. & Metais, O. 2002 On the influence of coherent structures upon interscale interaction in turbulent plane jets. *J. Fluid Mech.* **473**, 103-145.

da Silva, C.; & Pereira, J. 2008 Invariants of the velocity-gradient, rate-of-strain, and rate-of-rotation tensors across the turbulent/nonturbulent interface in jets. *Phys. Fluids* **20**, 055101.

Frisch, U. 1995 Turbulence: The Legacy of A.N. Kolmogorov. *Cambridge University Press*.

Germano, M. 1991 A dynamic subgrid-scale eddy viscosity model. *Phys. Fluids* **3** (7), 1760–1765.

Ghorbaniasl, G. & Lacor, C. 2008 Sensitivity of SGS models and of quality of LES to grid irregularity. In J. Meyers et al. (Eds), Quality and Reliability of Large-Eddy Simulations. Springer Science + Business Media B.V.

Ghosal, S., Lund, T., Moin, P. & Akselvoll, K. 1995 A dynamic localization model for large-eddy simulation of turbulent flows. *J. Fluid Mech.* **286**, 229–255.

Kang H. S., Chester S. and Meneveau C. 2003 Decaying turbulence in an active-grid-generated flow and comparisons with large-eddy simulation *J. Fluid Mech.* **480**, 129.

Lee, J., Choi, H. & Park, N. 2010 Dynamic global model for large eddy simulation of transient flow. *Phys. Fluids* **22**, 075106.

Lesieur, M. 1995 Turbulence in Fluids. *Springer Verlag - 4th Edition*.

Lilly, D. K. 1992 A proposed modification of the Germano subgrid-scale closure method. *Phys. Fluids* **4** (3), 633–635.

Meneveau, C., Lund, T. & Cabot, W. 1996 A lagrangian dynamic subgrid-scale model of turbulence. *J. Fluid Mech.* **319**, 353–385.

Moin, P. & Kim, J. 1982 Numerical investigation of turbulent channel flow. *J. Fluid Mech.* **118**, 341–377.

Morinishi Y., Lund T., Vasilyev O. & Moin P. 1998 Fully conservative higher order finite difference schemes for incompressible flow *J. Comp. Phys.* **143**(1), 90-124.

Moser, R., Kim, J. & Mansour, N. 1999 Direct numerical simulation of turbulent channel flow up to $Re_\tau = 590$. *Phys. Fluids* **11**, 943–945.

Nicoud, F. & Ducros, F. 1999 Subgrid-scale stress modelling based on the square of the velocity gradient. *Flow, Turb. and Combustion* **62** (3), 183–200.

Park, N., Lee, S., Lee, J. & Choi, H. 2006 A dynamic subgrid-scale eddy viscosity model with a global model coefficient. *Phys. Fluids* **18**, 125109.

Smagorinsky, J. 1963 General circulation experiments with the primitive equations: 1. the basic experiment. *Mon. Weather Rev.* **91**, 99–164.

Verstappen, R. & Bose, S. 2010 When does eddy-viscosity damp subfilter scales sufficiently? In Proceedings of the 13th Summer Program of the Center for Turbulence Research.

Vreman, A. 2004 An eddy-viscosity subgrid-scale model for turbulent shear flow: Algebraic theory and applications. *Phys. Fluids* **16** (10), 3670.

You, D. & Moin, P. 2007 A dynamic global-coefficient subgrid-scale eddy-viscosity model for large-eddy simulation in complex geometries. *Phys. Fluids* **19**, 065110/1–8.

APPENDIX C

This article was submitted to the *V European Conference on Computational Fluid Dynamics, Lisbon, Portugal 2010*. It is about the problem that arises when using the Germano-identity with advanced subgrid-scale models for developing local dynamic models.

Is the dynamic procedure appropriate for all sgs models ?
Baya Toda H., Truffin, K. and Nicoud, F
V European Conference on Computational Fluid Dynamics,
J. C. F. Pereira and A. Sequeira (Eds) Lisbon, Portugal,14-17 June 2010

V European Conference on Computational Fluid Dynamics
ECCOMAS CFD 2010
J. C. F. Pereira and A. Sequeira (Eds)
Lisbon, Portugal,14-17 June 2010

IS THE DYNAMIC PROCEDURE APPROPRIATE FOR ALL SGS MODELS ?

H. Baya Toda*, Karine Truffin* and Franck Nicoud†

*Institut Français du Petrole,
1-4 Avenue Bois preau 92852 Rueil-Malmaison
e-mail: hubert.baya-toda@ifp.fr
†I3M CNRS-Universite Montpellier 2
address
e-mail: franck.nicoud@univ-montp2.fr, karine.truffin@ifp.fr

Key words: Large eddy simulation, Germano-identity, Wall-bounded flows, Subgrid-scale model

Abstract. *The rapid growth of supercomputers will probably make the use of Large eddy simulations (LES) more accessible for industrial applications in a near future. It is then important to develop accurate models able to represent as well as possible the turbulence effects in very complex and wall-bounded flows. While the Smagorinsky model is known for its extradissipation in near wall regions, other models with the appropriate near wall behaviour are now available (e.g. WALE and Vreman model). Still, values of the constants proposed by the authors are expected to be not universal notably in complex geometries.*
In this study, a dynamic version of the WALE subgrid model has been developped based on the Germano-identity. The dynamic WALE, the dynamic Smagorinsky and the WALE models are first tested on the homogeneous isotropic turbulent (HIT) experiment of Comte-Bellot and Corsin (CBC). Large eddy simulations of an isothermal turbulent channel flow are then performed and results are compared with the DNS of Moser et al. at wall Reynolds number Re_τ 395 and 590. This last test illustrates how the dynamic procedure combined with the WALE fails to correctly model the mean velocity. It leads to very high values of the WALE constant near the wall and to an over prediction of the turbulent viscosity in the buffer-layer. It is then shown in the paper that the dynamic procedure might degrade any SGS model with the proper wall behaviour. Finally, a cure to this problem is proposed and used to built an appropriate dynamic WALE model which proves accurate in the channel flow and promising in an industrial like configuration.

1 INTRODUCTION

One of the most challenging aspect of LES modelling is certainly near wall effects. For industrial applications the knowledge of the latter is important for the optimisation of the energy consumption (heating or cooling); it is then necessary to develop accurate LES models able to represent as well as possible wall effects.
Since the Smagorinsky model[1], many attempts have been done to meet the requirements of modelling in presence of a solid wall. These requirements[2] are the y^3 asymptotic behaviour and the capability to represent laminar-to-turbulent transition. To this respect, the use of damping function[3] or of the Germano-identity[4] to dynamically adapt the model constant have been successfully used. This approach is most referred in the literature as an optimisation method and is more suitable for complex geometries where the knowledge of the distance to the wall is not straightforward. More recently the WALE model developed by Nicoud and Ducros[5] and the Vreman's[6] model have allowed to respect these requirements without using any damping functions or dynamic procedure. Still the value of the constant proposed by the authors is expected to vary depending on the flow and the geometry.
The present paper is organized as follows: in section 2, the governing equations and the different subgrid scales models are presented. In section 3, the models and their implementation are validated by considering the homogeneous isotropic turbulence configuration of Comte et Bellot[7]. In section 4, results by considering an isothermal turbulent channel computed with the different models are compared. The problem which arises when considering the WALE dynamic model based on the Germano-identity is also presented. A cure to the previous problem is presented in section 5 and the results with the improved dynamic WALE model are presented in the same section followed by a conclusion.

2 GOVERNING EQUATIONS AND SGS MODELS

The filtered compressible Navier-Stokes equations are solved in this study but their incompressible counterpart are presented here for simplicity since only low Mach number flows will be considered:

$$\frac{\partial \bar{u}_j}{\partial x_j} = 0 \tag{1}$$

$$\frac{\partial \bar{u}_i}{\partial t} + \frac{\partial (\bar{u}_i \bar{u}_j)}{\partial x_j} = -\frac{1}{\bar{\rho}} \frac{\partial \bar{p}}{\partial x_i} + \nu \frac{\partial^2 \bar{u}_i}{\partial x_i \partial x_j} + \frac{\partial \tau_{ij}^{sgs}}{\partial x_j} + S_i$$

where t is time, p the pressure, ρ the density, ν the kinematic viscosity, S_i a source term and τ_{ij}^{sgs} the subgrid scale (SGS) tensor expressed as:

$$\tau_{ij}^{sgs} = \bar{u}_i \bar{u}_j - \overline{u_i u_j} \tag{2}$$

An eddy viscosity approach has been chosen to model the SGS tensor which is then expressed as :

$$\tau_{ij}^{sgs} - \frac{1}{3}\tau_{kk}^{sgs}\delta_{ij} = 2\nu^{sgs}\bar{S}_{ij} \tag{3}$$

where $\bar{S}_{ij}$ is the strain rate based on the filtered velocity $\bar{u}_i$ and ν^{sgs} the eddy viscosity.

2.1 WALE model[5]:

Like the Vreman's model[6], the WALE model[5] does not generate SGS activity for pure shear flows and was built to recover the right asymptotic behaviour near solid walls and the eddy viscosity is expressed as follows:

$$\nu^{sgs} = C_w^2\bar{\Delta}^2|\bar{OP}| \tag{4}$$

where $C_w = 0.5$, $\bar{\Delta}$ is the filter size and $\bar{OP}$ an operator defined as follows:

$$|\bar{OP}| = \frac{(S_{ij}^d S_{ij}^d)^{3/2}}{(\bar{S}_{ij}\bar{S}_{ij})^{5/2} + (S_{ij}^d S_{ij}^d)^{5/4}} \tag{5}$$

where S_{ij}^d is the symmetric traceless part of the square of the strain rate, expressed as:

$$S_{ij}^d = \bar{S}_{ik}\bar{S}_{kj} + \bar{\Omega}_{ik}\bar{\Omega}_{kj} - \frac{1}{3}\delta_{ij}[\bar{S}_{mn}\bar{S}_{mn} + \bar{\Omega}_{mn}\bar{\Omega}_{mn}], \tag{6}$$

where $\bar{\Omega}_{ij}$ is the rotation rate based on the filtered velocity $\bar{u}_i$

2.2 Dynamic WALE model

To develop the dynamic WALE model, a second test filter $\hat{\Delta}$ bigger than the initial filter $\bar{\Delta}$ is first considered, the Navier-Stokes equations filtered at the test filter level are then expressed as follows:

$$\frac{\partial\hat{\bar{u}}_i}{\partial t} + \frac{\partial(\hat{\bar{u}}_i\hat{\bar{u}}_j)}{\partial x_j} = \frac{1}{\hat{\bar{\rho}}}\frac{\partial\hat{\bar{p}}}{\partial x_i} + \nu\frac{\partial^2\hat{\bar{u}}_i}{\partial x_i\partial x_j} + \frac{\partial T_{ij}^{sgs}}{\partial x_j}, \tag{7}$$

where T_{ij}^{sgs} is the sgs tensor at the test filter level. Using the Germano-identity, we have the following relationship between T_{ij}^{sgs} and τ_{ij}^{sgs} :

$$T_{ij}^{sgs} - \hat{\tau}_{ij}^{sgs} = L_{ij} \tag{8}$$

L_{ij} is the Leonard term expressed as:

$$L_{ij} = \widehat{\bar{u}_i\bar{u}_j} - \hat{\bar{u}}_i\hat{\bar{u}}_j \tag{9}$$

The WALE eddy viscosity model is used for the SGS tensors at the two level so that equation Eq.(8) becomes:

$$C_w^2 \hat{\Delta}^2 |\hat{\bar{O}P}| \hat{\bar{S}}_{ij} - (C_w^2 \widehat{\bar{\Delta}^2 |\bar{O}P|} \bar{S}_{ij}) = L_{ij} \tag{10}$$

If C_w is assumed constant over a distance at least equal to the testfilter width, its dynamic value can be expressed as follows using the least square method of Lilly[8]:

$$C_w^2 = \frac{1}{2} \frac{< L_{ij} M_{ij}^w >^+}{< M_{ij}^w M_{ij}^w >} \tag{11}$$

with

$$M_{ij}^w = \hat{\Delta}^2 |\hat{\bar{O}P}| \hat{\bar{S}}_{ij} - (\bar{\Delta}^2 \widehat{|\bar{O}P|} \bar{S}_{ij}) \tag{12}$$

The superscript + in the expression Eq.(11) denotes a positive clipping of all negative values to zero and the sign <> is a stabilisation method that consists in a local volume averaging. In contrary to what is often done for the dynamic Smagorinsky[4] model and recently for the WALE model[9], the stabilisation is not performed over homogeneous directions but locally; it is then well adapted to complex geometries.

2.3 Dynamic Smagorinsky model[4]

The dynamic Smagorinsky constant was calculated with the same consideration as for the dynamic WALE constant. The only difference is the operator $|\bar{OP}|$ in the expression of M_{ij}^s :

$$M_{ij}^s = \hat{\Delta}^2 |\hat{\bar{O}P^s}| \hat{\bar{S}}_{ij} - (\bar{\Delta}^2 \widehat{|\bar{O}P^s|} \bar{S}_{ij}) \tag{13}$$

with $|\bar{OP^s}|$ the second invariant of the strain rate based on the filtered velocity $\bar{u}_i$ expressed as :

$$|\bar{OP^s}| = \sqrt{2 \bar{S}_{ij} \bar{S}_{ij}} \tag{14}$$

and the dynamic Smagorinsky constant is expressed as :

$$C_s^2 = \frac{1}{2} \frac{< L_{ij} M_{ij}^s >^+}{< M_{ij}^s M_{ij}^s >} \tag{15}$$

The WALE[5] , the dynamic WALE and the dynamic Smagorinsky[4] models will be denoted respectively as WA, WAD and SMD.

2.4 Numerical solver

The calculations were carried out with AVBP, the CFD solver developed at CERFACS. This parallel solver offers the capability to handle unstructured and structured grids in order to solve the 3D compressible reacting Navier-Stokes equations with a cell-vertex formulation. A centered Galerkin finite element method with a three step Runge-Kutta temporal method has been used. The numerical solver is fourth order accurate in space and third order in time. The efficiency of the numerical method used and the AVBP code has already been successfully tested in the past years by Colin and Rudgyard[10], Moreau et al.[11] and recently by Cabrit and Nicoud[12].

3 HOMOGENEOUS ISOTROPIC TURBULENCE

The SGS models are first tested on the HIT experiment of Comte-Bellot and Corsin[7]. This experiment has already been widely [4,13,14,15] used either to validate purely eddy-viscosity models or to find their constant values. The characteristics of the CBC experiment are summarised in table.1.

$t* = \frac{U_o t}{M}$	$u_{rms}(cm.s^{-1})$	$\epsilon(cm^2.s^{-3})$	$\eta(cm)$	$\lambda(cm)$	R_λ
42	22.2	4740	0.029	0.484	71.6
98	12.8	633	0.048	0.764	65.3
171	8.95	174	0.066	1.02	60.7

Table 1: Characteristics of the HIT of CBC where $U_o = 10m/s$ is the convective velocity, ϵ is the kinetic energy dissipation, η is the kolmogorv scale, $M = 5.08cm$ is the grid size, λ the Taylor micro scale and R_λ the Reynolds number based on λ.

The experimental validation consists in initialising in a computation with a velocity field whose spectrum matches the first spectum at time $t^* = 42$ and comparing the experimental and the spectra at times $t^* = 98$ and $t^* = 171$. The reference length and the reference velocity are respectively $L_{ref} = \frac{L_B}{2\pi}$ and $U_{ref} = \sqrt{3/2}u_{rms}(t* = 42)$. $L_B = 11M$ is the length of the computation box. The simulations are performed over a 61^3 mesh. Since the experimental evolution of the kinetic energy is not available, the results will be compared with the data of the EQDNM simulations of Park and Mahesh[16].

Figure 1 shows the evolution of the spectra predicted by the static WALE model[5] and the dynamic WALE described in section 2.2 compared with the experiment.

The first spectrum corresponds to the initialisation at time $t^* = 42$. As expected, the spectra obtained with WALE[5] and the dynamic WALE models are very similar at the following time and in good agreement with the experiment for wavelengths smaller than $K < \frac{K_c}{2}$. In fact, for greater wavelengths the energy is under predicted. But those wavelengths are resolved with least than 4 points. The discrepancies observed are probably due to numerical errors rather than SGS model limitations. Nevertheless, the global energy

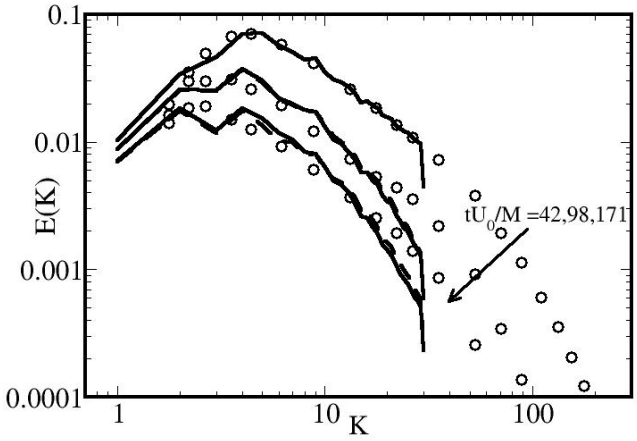

Figure 1: Three spectra at 3 times $t^* = 42, 98, 171$: ∘ Experiment of CBC; — WAD; ··· WA

prediction will not be affected since the under resolved wavelengths represent only 1% of the maximum energy. On figure 2, the spectra predicted by the dynamic Smagorinsky[4] and WALE[5] models are compared. The spectra are very similar at the different time and also in good agreement with the measurements.
The underprediction of the energy spectrum for $K > \frac{K_c}{2}$ is also observed for the dynamic Smagorinsky[4] model, supporting the fact that this issue is due to limitations of the numerical method at very high wavelengths.

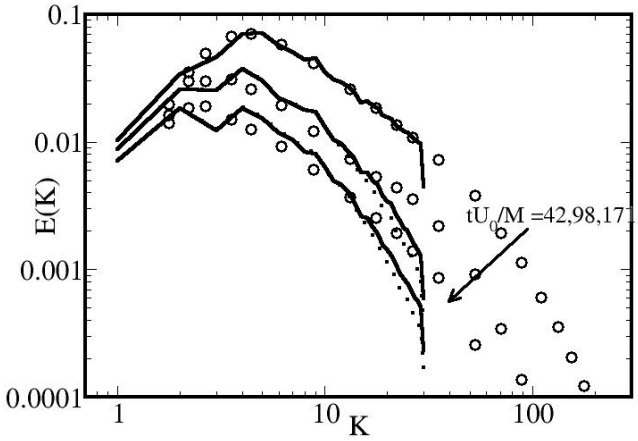

Figure 2: Three spectra at 3 times $t^* = 42, 98, 171$: ∘ Experiment of CBC; — WAD; ··· SMD

The temporal evolution of the resolved kinetic energy is also well predicted by the different models as shown in figure 3. The energy is normalised with the initial kinetic energy at time $t^* = 42$. The simulations are in good agreement with the experiment data and with the EDQNM simulations, the dynamic Smagorinsky[4] slightly underpredicts the resolved energy but still, remains in good agreement with the EDQNM results.

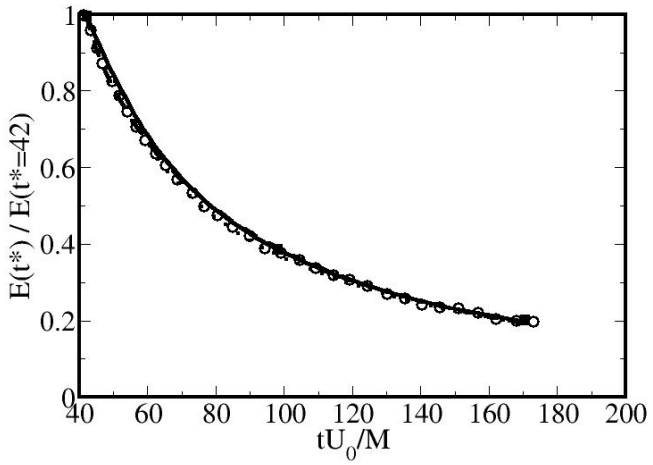

Figure 3: Temporal evolution of the resolved kinetic energy: ∘ EDQNM; — WAD; ··· WA; ··· SMD

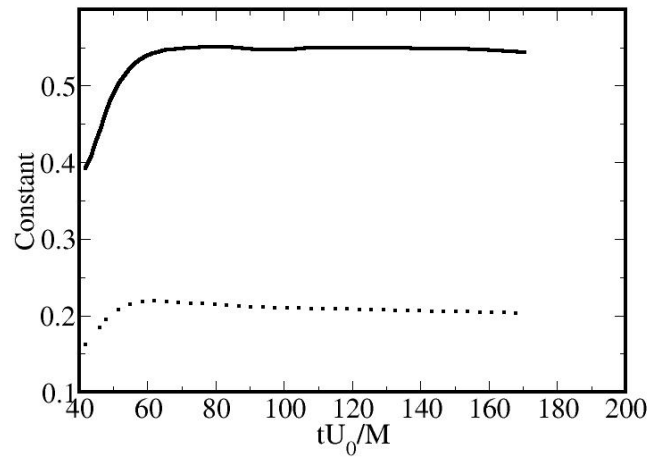

Figure 4: Temporal evolution of the dynamic constants: — WAD; ··· SMD

The temporal evolution of the dynamic constants is shown in figure 4. The dynamic

WALE constant converges to 0.55 a value closed to the one proposed by Nicoud and Ducros[5]. In the same way, the dynamic Smagorinsky constant converges to 0.2 that is closed to the canonical value, $C_s = 0.2$ performed by Clark et al.[17] for a HIT.

4 TURBULENT CHANNEL

4.1 Numerical set up

The periodic turbulent channel configuration is appropriate for testing the near wall behaviour of SGS models. It consists in a flow between two parallel planes (as shown in figure 5) which is driven by a source term imposed dynamically to reach a target bulk velocity:

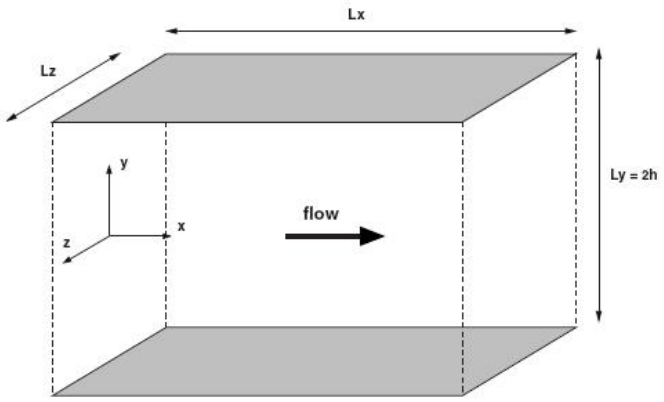

Figure 5: Turbulent channel

$$S_x = \frac{\rho U_{bulk} - \frac{1}{V}\int\int\int \rho u_x dV}{\tau_{relax}} \tag{16}$$

V is the volume of the computational domain and τ_{relax} is a relaxation time whose expression is:

$$\tau_{relax} = \frac{1}{5}\frac{h}{u_\tau}, \tag{17}$$

where u_{tau} is the friction velocity and h the channel half height. The reference data for this case are the DNS of Moser at al.[18]. The characteristics of the mesh for the friction Reynolds case $Re_\tau = 395$ are summarised in table 2. They were chosen in order to meet the requirement of the minimum turbulent channel dimensions advised by Jimenez and Moin[19].

Re_τ	$n_x \times n_y \times n_z$	$\frac{L_x}{h}$	$\frac{L_z}{h}$	Δx^+	Δz^+	Δy_w^+	Δy_c^+
395	$31 * 139 * 51$	3.5	1.3	46	10	1	17

Table 2: Characteristics of the mesh

4.2 Results

The friction Reynolds number, the friction coefficient and the error on this coefficient compared to the Petukhov[20] correlation as obtained with the different models are summarised in the table 3.

Case	$Re_\tau = 395$	C_f	% Error
WA	413	$6.55 * 10^{-3}$	9.9
SMD	396	$6.03 * 10^{-3}$	1.2
WAD	387	$5.75 * 10^{-3}$	-3.6
SVS WAD	396	$6.03 * 10^{-3}$	1.2

Table 3: Comparison of the different friction values

The main results is that the WALE model[5] over estimates the friction velocity while the dynamic WALE model slightly under estimates the friction velocity. However the dynamic Smagorinsky[4] model is in good agreement with the correlation and the expected friction velocity.

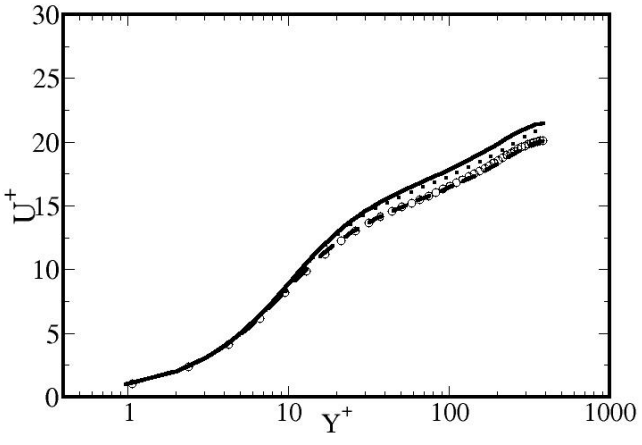

Figure 6: Mean velocity in the channel: ∘ DNS Moser et al.[18] $Re_\tau = 395$ — WAD; ··· WA; ••• SMD

Mean velocity profiles in wall units are displayed in figure 6 which shows that the dynamic Smagorinsky computation is in good agreement with the DNS data of Moser et al.[18] with a slight overprediction of the mean velocity in the buffer-layer. The dynamic

WALE model does not improve the WALE[5] model and its velocity profile is not better than the dynamic Smagorinsky[4] model. The mean velocity is clearly overestimated from the buffer-layer to the centre of the channel. This is due to the overestimation of the viscosity as depicted in figure 7 due to high value of the constant near the wall as shown in figure 8. The WALE computations are in good agreement with the DNS but it is certainly due to the overprediction of the friction veolicty as shown in table 3. Considering the eddy viscosity, figure 7 shows that the dynamic Smagorinsky model[4] does not have a y^{+3} asymptotic behaviour in contrary to what was obtained by Germano et al.[3]. This is due to the stabilisation method that is not performed over the homogeneous directions, as already mentionned in section 2.
The cubic asymptotic behaviour is better retrieved by the WALE[5] and the dynamic WALE models because they are built with the spatial operator of Eq.5. However, the eddy viscosity from WALE is substantially smaller than the values obtained by both dynamic models in the turbulent region ($y^+ > 30$). On the other hand, the dynamic WALE produces too large eddy-viscosity in the buffer-layer ($5 < y^+ < 30$). These behaviours are better understand by considering the profiles of the model constant, as depicted in figure 7. It strongly decreases in the near wall region for the dynamic Smagorinsky[4] model since the dynamic procedure is required to damp the eddy viscosity, if the Smagorinsky[1] model is used. The opposite is observed for the dynamic WALE model for which the model constant is 40 times larger than the value proposed by Nicoud and Ducros[5] (10 against 0.25). Note that even in the core region, the dynamic procedure generates a constant which is approximatively 3 times larger than its static counter part. This situation is different from what is observed for the dynamic Smagorinsky[4] model; in this case the dynamic constant (0.18^2) in the core region is close to the classical model constant as shown in figure 8.

The dynamic version of the WALE model leads to very high value of the constant near the wall and to a bad prediction of the mean velocity. It rises the question of the effectiveness of the Germano-identity when developping a dynamic version of a model that has a right asymptotic behaviour. This was already observed by Park et al.[21] in their attempt to develop a dynamic version of the Vreman's model[6] based on the Germano-identity. They observed a low correlation between the SGS tensor predicted by the dynamic model with the true SGS tensor specially near the wall. They then developed a global dynamic model improved by You and Moin[22] where a global equilibrium instead of the local equilibrium was assumed. The final constant was homogeneous in space but time dependent. The main drawback of such a global dynamic procedure is that it relies on the SGS model to ensure that the spatial variations in the eddy viscosity are properly obtained. Notably, one could expect that ν_{sgs} goes to zero with the appropriate y^{+3} behaviour near solid wall and at the same time vanishes in region of pure rotation. However, it can be easily demonstrated that the latter condition is not met for both the Vreman's[6] nor the WALE[5] models. It is then still necessary to investigate if a local version of those dynamic models can be developed. This is discussed in the next section.

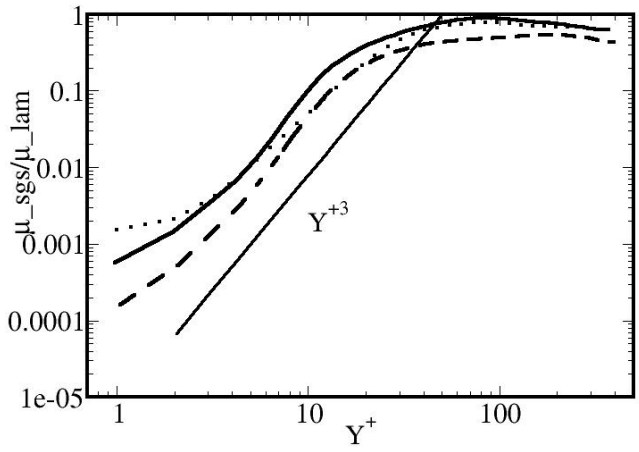

Figure 7: Mean viscosity in the channel: — WAD; -- WA; ··· SMD

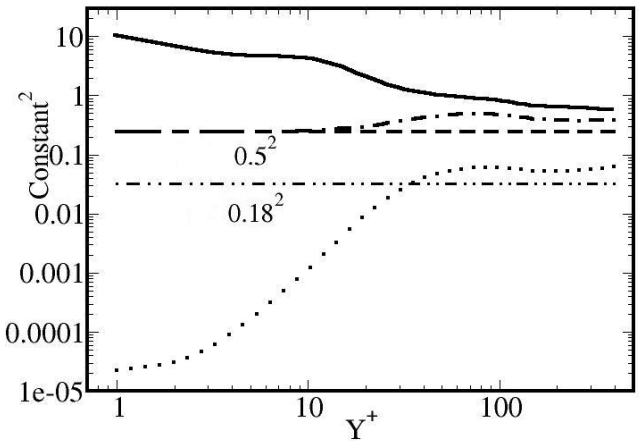

Figure 8: Square of the constant in the channel: — WAD; ··· SMD; – · – SVS WAD

5 MODIFIED DYNAMIC WALE MODEL

5.1 Theoretical study

The behaviour of the eddy viscosity and the constant in the channel shown respectively in figure 7 and 8 point out that the main problem of the model is near the wall. In fact for $Y^+ > 30$ the eddy viscosity predicted by the dynamic WALE and Smagorinsky[4] models are almost similar but the high values of the constant near the wall have an impact on

the viscosity in the buffer-layer.
In order to better understand this behaviour, we have first carried out a theoretical study of the asymptotic behaviour of the numerator and denominator of expression (11).

Considering a filtered incompressible velocity field $\bar{u}_1, \bar{u}_2, \bar{u}_3$ the asymptotic behaviour of the different components of the velocity are expressed as :

$$\begin{aligned} \bar{u}_1 &= ay + by^2 + O(y^3) \\ \bar{u}_2 &= cy^2 + O(y^3) \\ \bar{u}_3 &= dy + ey^2 + O(y^3) \end{aligned} \tag{18}$$

where a, b, c, d and e depend on x, z and time. We only consider the components that are most important near the wall. Then M_{ij}^w and L_{ij} will be simplified to M_{12}^w and L_{12} and we have the following behaviour:

$$\begin{aligned} M_{12}^w &= \hat{\Delta}^2 |\hat{\bar{O}P}| \hat{\bar{S}}_{12} - (\widehat{\bar{\Delta}^2 |\bar{O}P| \bar{S}_{12}}) \\ L_{12} &= \widehat{\bar{u}_1 \bar{u}_2} - \hat{\bar{u}}_1 \hat{\bar{u}}_2 \end{aligned} \tag{19}$$

From the expression 18, we have:

$$\begin{aligned} S_{12} &= a + O(y) \\ \bar{u}_1 \bar{u}_2 &= acy^3 + O(y^4) \end{aligned} \tag{20}$$

and the operator $|\bar{O}P|$ that is based on the WALE model[5] has a y^3 behaviour.

$$|\bar{O}P| = fy^3 + O(y^4) \tag{21}$$

With the relation Eq.20 and Eq.21 the terms L_{ij} and M_{ij} have the following behaviour:

$$\begin{aligned} M_{12}^w &= \hat{\Delta}^2 fay^3 - (\widehat{\bar{\Delta}^2 fay^3}) + O(y^4) \\ L_{12} &= \widehat{acy^3} - \widehat{ay}\widehat{cy^2} + O(y^4) \end{aligned} \tag{22}$$

Then near the wall, the dynamic constant converges to the following expression:

$$C_w = \frac{< \widehat{acy^3} - \widehat{ay}\widehat{cy^2} >}{< \hat{\Delta}^2 fay^3 - (\widehat{\bar{\Delta}^2 fay^3}) >} + O(y) \tag{23}$$

This relation shows that the dynamic constant formally behaves like y^0 near the wall. However, the leading order term in Eq.23 is the ratio of two very small quantities (behaving like y^{+3}) whose numerical assessment strongly depends on the details of the test filter application and stabilisation procedure. This situation is obviously ill-posed numerically and can lead to very large value of the dynamic constant, as observed in fig 8. Note that the situation is drastically different when the dynamic procedure is applied to the Smagorinsky[1] model. In this case, the spatial operator $|\bar{O}P|$ behaves like y^0 and the denominator of Eq.23 also. A model with a proper asymptotic behaviour seems to be more sensitive to the choice of the filters and the stabilisation, specially near the wall.

5.2 Proposed solution

The analysis conducted in section 5.1 suggests that the SGS models that have the correct behaviour near the wall could be very sensitive to the filtering procedure and the stabilisation method. This could be a real drawback to the development of any dynamic version based on the Germano-identity for those models. Since the laminar viscosity is dominant in the vicinity of the wall, there is no need, if one considers a SGS model with the proper wall behaviour, to adapt its constant dynamically in the near wall region. Still, it remains necessary to evaluate the constant in fully developed turbulent parts of the flow.
A simple way to achieve this is to identify the "near wall region". In other words, to have a sensor able to detect the presence of the wall without a priori knowledge of the geometry which can be arbitrary complex. Such a sensor is not unique. Here we propose to make use of an invariant similar to the one involved in the WALE model[5] (see Eq.5) More precisely, we have selected the following dimensionless parameter:

$$SVS = \frac{(S^d_{ij}S^d_{ij})^{3/2}}{(S^d_{ij}S^d_{ij})^{3/2} + (S_{ij}S_{ij})^3} \tag{24}$$

which has the following properties :

- the SVS behaves like y^{+3} since it shares the same numerator than the WALE operator (Eq.5),
- the $SVS = 0$ for pure shear flows for the same reason,
- the $SVS = 1$ for pure rotating flows since $S_{ij} = 0$ in this case

This last property indicates that SVS is bounded by $0-1$, its lower value corresponding to pure shear flows, its larger value corresponding to pure rotating flows. This also justifies the acronym SVS (Shear and Vortex Sensor) we have chosen for this sensor.

Figure 9 shows the SVS in the channel as a function of y^+ for the $Re_\tau = 395$.

It illustrates that this quantity can be used to divide the simulated geometry into two zones: a zone far from the wall where the model constant should be estimated dynamically using the Germano-identity and a zone close to the wall where the constant should be fixed to 0.5, suggested by Nicoud and Ducros[5]. The value 0.09 is considered here as the value below which the SVS behaves nearly y^{+3} and was thus chosen as threshold value (see figure 9).
The modified dynamic WALE model is then expressed as follows:
if $SVS > 0.09$

$$C^2_{wsvs} = \frac{1}{2}\frac{< L_{ij}M^w_{ij} >^+}{< M^w_{ij}M^w_{ij} >} \tag{25}$$

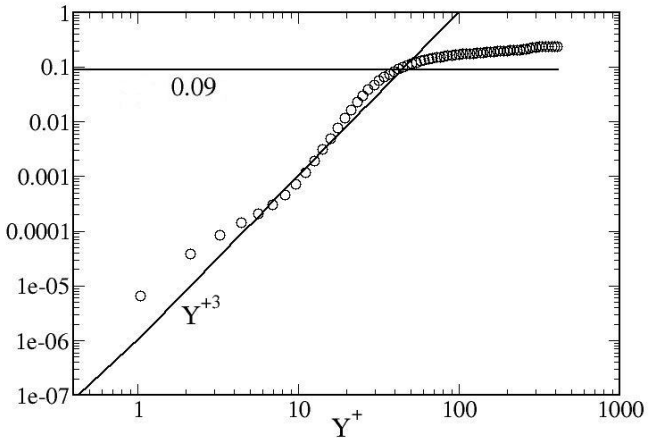

Figure 9: SVS in the channel at $Re_\tau = 395$

and if $SVS < 0.09$

$$C^2_{wsvs} = 0.25 \tag{26}$$

5.3 Results of the dynamic WALE with SVS at $Re_\tau = 395$

The modified model has been validated on the HIT of Comte-Bellot and Corsin[7] and the results are similar to those obtained with the normal dynamic WALE model. We will then only focus on results obtained in the turbulent channel.
Results of the friction value obtained with the SVS dynamic WALE (see table 3) show that the model has improved the prediction of the the static WALE model[5] and are similar to those obtained with the dynamic Smagorinsky model[4].

Figure 10 compares the mean velocity predicted by the modified dynamic WALE, the dynamic Smagorinsky[4] and the WALE[5] models. The mean velocity obtained with SVS dynamic WALE is in good agreement with the experiment. Figure 11 indicates that the viscosity in the channel is no longer affected by the high values near the wall. This is also illustrated in fig 8.

The figure 8 compared the prediction of the square of the dynamic WALE constant obtained with the normal and the modified dynamic WALE model. The introduction of the SVS helps to controlling the value of the constant near the wall while keeping the dynamic computation of the constant in the core region of the channel. This combination leads to a better results than the WALE model[5].

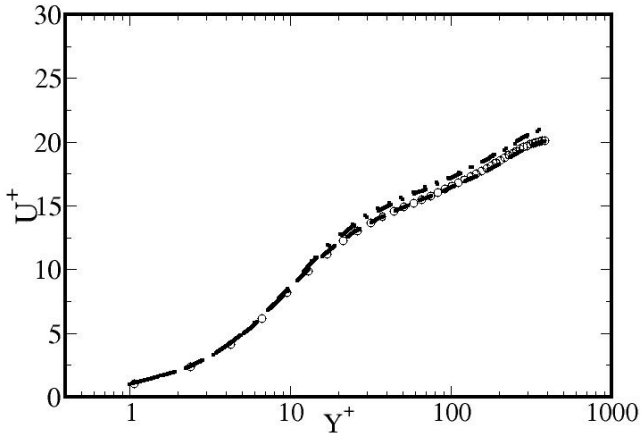

Figure 10: Mean velocity in the channel at $Re_\tau = 395$: ∘ DNS Moser et al.[17] $Re_\tau = 395$; ··· SMD; – · – SVS WAD

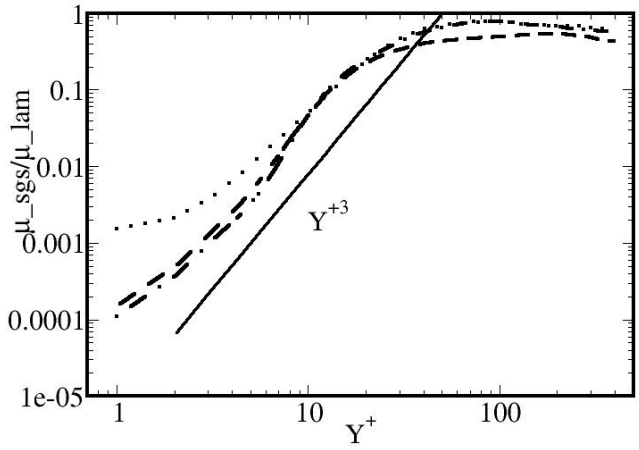

Figure 11: Eddy viscosity in the channel at $Re_\tau = 395$: ··· SMD; – · – SVS WAD

5.4 Results of the dynamic WALE with SVS at $Re_\tau = 590$

In an attempt to assess the adaptability of the procedure, we have kept the same mesh to compute the $Re_\tau = 590$ channel flow, also computed by Moser et al.[18] The characteristics of the mesh in wall units are summarised in the table 4.

Re_τ	$n_x \times n_y \times n_z$	$\frac{L_x}{h}$	$\frac{L_z}{h}$	Δx^+	Δz^+	Δy_w^+	Δy_c^+
590	$31 * 139 * 51$	3.5	1.3	65	14	1.4	24

Table 4: Characteristics of the mesh for the case $Re_\tau = 590$

Figure 12 shows the mean velocity in channel obtained with the modified dynamic WALE model. The velocity is slightly overestimated in the centre of the channel probably due to the resolution but results are still in good agreement with the DNS.

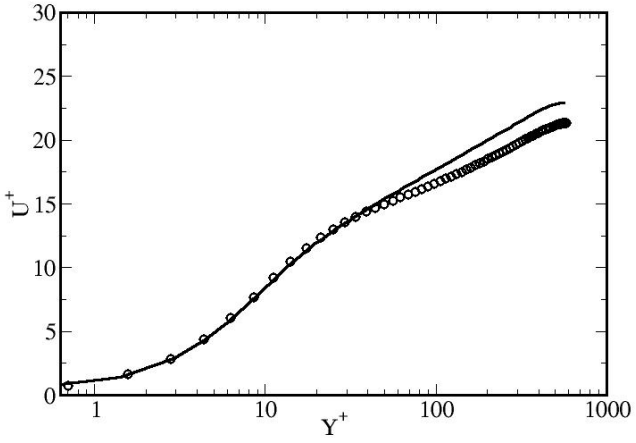

Figure 12: Mean velocity in the channel at $Re_\tau = 590$: ∘ DNS Moser et al.[17] ; — SVS WAD

Figure 13 shows the rms velocity. Although the maximum of the axial velocity is overestimated, the location of the maximum is reasonably well predicted by the simulations. The poor resolution of the mesh in the streamwise and spanwise directions is certainly the main cause of the discrepancies observed in figure 13.

The eddy viscosity is represented in figure 14. Even at this high wall Reynolds number the near wall behaviour of the model is preserved.

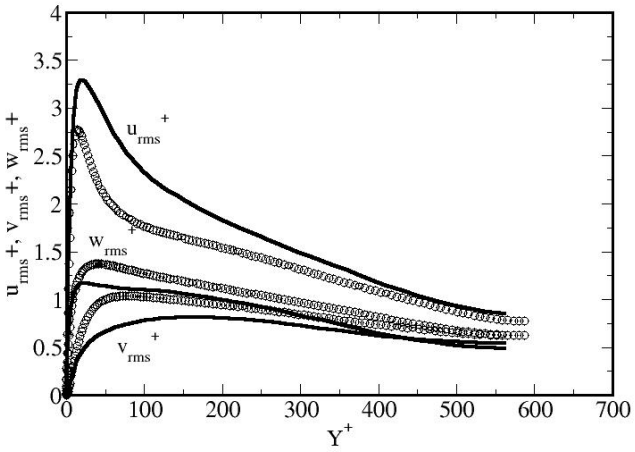

Figure 13: Root mean square of velocity in the channel at $Re_\tau = 590$: ∘ DNS Moser et al.[18]; — SVS WAD

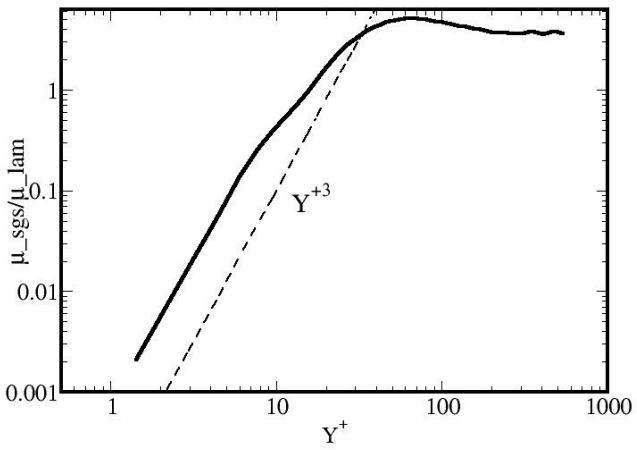

Figure 14: Sgs viscosity in the channel at $Re_\tau = 590$

The dynamic constants of the SVS WALE model are represented in figure 15 for the two friction Reynolds numbers. The constants clearly adapt their value to the flow in the turbulent part of the channel while the SVS keeps the same behavior (see figure 16). The only difference is due to the y^+ resolution that increased from the low to the high friction Reynolds number case when using the same mesh.

It is worth nothing that even by adding high level of artificial viscosity during the

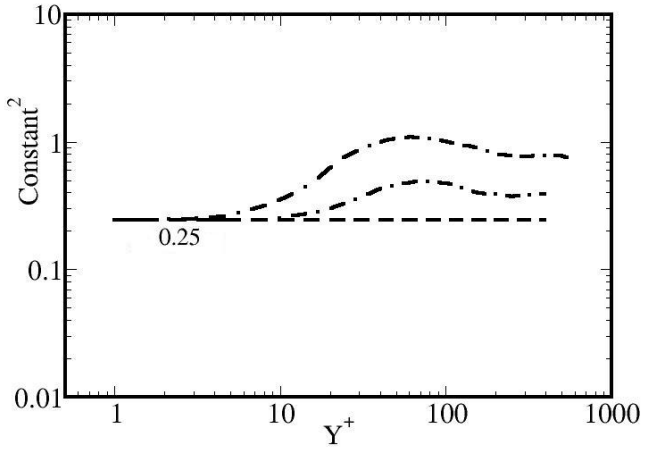

Figure 15: Constants of the SVS WAD for the two friction Reynolds number: $- \cdot - \; Re_\tau = 395$; $\cdot - - \; Re_\tau = 590$

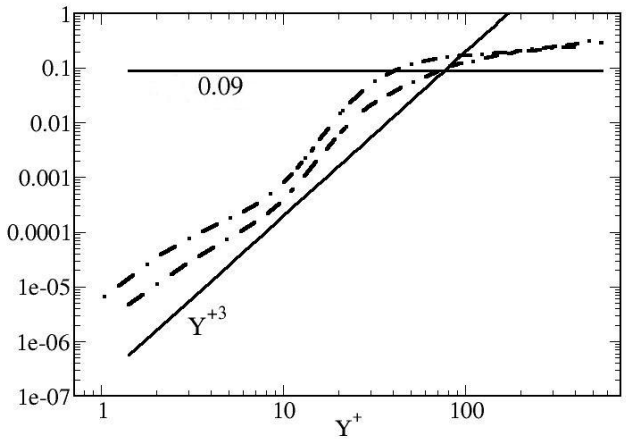

Figure 16: SVS for the two friction Reynolds number: $- \cdot - \; Re_\tau = 395$; $\cdot - - \; Re_\tau = 590$

runs, no satisfying results were obtained with the dynamic Smagorinsky model[4]. This is probably due to the fact that no averaging on homogeneous directions as discussed in section 2. This indicates that the SVS dynamic WALE model has greater potential than the dynamic Smagorinsky model[4] for complex/high Reynolds configurations while leading to equivalent results in simple/moderate Reynolds situations.

6 CONCLUSIONS

A dynamic version of the WALE model[5] with a Shear and Vortex Sensor has been proposed. The model was succefully implemented and tested on the HIT experiment of CBC[7]. The model gives equivalent results than the dynamic Smagorinsky model[4] at low friction Reynolds number and better results at high Reynolds number in an isothermal turbulent channel configuation. In contrary to the dynamic Smagorinsky constant, the dynamic WALE constant does not need to be averaged over homogeneous direction and is then more suitable for very complex flows and geometries. In order to avoid highest values of the viscosity in the laminar zone of the boundary layer due to the use of the Germano-identity and the small value of the WALE operator near the wall, the SVS has been introduced to divide the flow in two regions. A first one, close to the wall where the constant keeps the value advised by Nicoud and Ducros[5] and a second one corresponding to the fully developped parts of the flow where the constant is dynamically evaluated and can adapt to the mesh resolution and the turbulent flow level. The resulting viscosity still has the proper y^{+3} behavior near the wall. The SVS dynamic WALE model seems promising for modelling turbulent flow in very complex geometries without important additional CPU cost and control strategies with equivalent or even better results than the dynamic Smagorinsky model[4] and static constant SGS models.

REFERENCES

[1] J. S. Smagorinsky, General circulation experiments with the primitive equations, *Mon. Weather Rev.*, **Vol. 91**, 99-164 (1963).

[2] P. Sagaut, Large eddy simulation for Incompressible flows, *Springer-Verlag Berlin and Heidelberg GmbH & Co. K*, (1998).

[3] P. Moin and J. Kim, Numerical investigation of turbulent channel flow, *J. Fluid Mech.* , **Vol. 118**, 341-377 (1982).

[4] M. Germano, U. Piomelli , P. Moin,W. H. Cabot, A Dynamic Subgrid-Scale Eddy Viscosity Model, *Physics of Fluids*, **No. A3**, 1760-1765 (1991).

[5] F. Nicoud, F. Ducros, Subgrid-scale stress modelling based on the square of the velocity gradient tensor, *Flow, Turbulence and Combustion*, **Vol. 62** 183-200 (1999).

[6] A. W. Vreman , An eddy-viscosity subgrid-scale model for turbulent shear flow: Algebraic theory and applications, *Physics of Fluids*, **Vol. 16 No. 3**, 3670 (2004).

[7] G. Comte-Bellot, S. Corrsin, Simple Eulerian time correlation of full- and narrow-band velocity signals in grid generated, isotropic turbulence, *J. Fluid Mech.* **Vol. 48**, pp.273-337 (1971).

[8] D. K. Lilly, A proposed modification of the Germano subgrid scale closure model, *Physics of Fluid*, **A 4** (633).

[9] G. Ghorbaniasl and C. Lacor., Sensitivity of sgs models and of quality of les to grid irregularity, *In J. Meyers et al. (Eds), Quality and Reliability of Large-Eddy Simulations. Springer Science + Business Media B.V.* (2008).

[10] V. Moreau, G. Lartigue, Y. Sommerer, C. Angelberger, O. Colin and T. Poinsot, High order methods for DNS and LES of compressible multicomponent reacting flows on fixed and moving grids S. *J. Comp.Phys.* **Vol. 202 (2)**, pp.710-736 (2005).

[11] O. Colin and M. Rudgyard, Development of high-order Taylor-Galerkin schemes for unsteady calculations, *J. Comput. Phys.*, **162**, 338 (2000).

[12] O. Cabrit and F. Nicoud, Direct simulations for wall modeling of multicomponent reacting compressible turbulent flows, *Physics of Fluids*, **21**, (2009).

[13] A. Scotti, C. Meneveau, A fractal model for large eddy simulation of turbulent flow *Physica D* **127**, (1998).

[14] N. Park, K. Mahesh, A velocity-estimation subgrid model constrained by subgrid scale dissipation *J. Comp. Phys.*, **227**, 4190-4206, (2008).

[15] N. Park, K. Mahesh, Reduction of the Germano-identity error in the dynamic Smagorinsky model, *Physics of fluids*, **21**, (2009).

[16] N. Park, K. Mahesh, Analysis of numerical errors in large eddy-simulation using sattistical closure theory, *J. Comp. Phys.*, **222**, (2007).

[17] R. A. Clark, J. H. Ferziger, W.C.A. Reynolds, Evaluation of subgrid-scale models using an accurately simulated turbulent flow, *Journal of Fluid Mechanic*, **91(1)**, (1979).

[18] R. D. Moser, J. Kim and N. N., Direct numerical simulation of turbulent channel flow up to $Re_\tau = 590$, *Physics of Fluids*, **Vol. 11, No. 4**, pp. 943-945 (1999).

[19] Jiménez and P. Moin, The minimal flow unit in near-wall turbulence, *J. Fluid Mech*, **225** (1991).

[20] M. W. Kays, M. E. Crawford and B. Weigand, B. Convective Heat and Mass Transfer, Fourth Edition, *McGraw-Hill International Edition* .

[21] N. Park, S. Lee, J. Lee, and H. Choi. A dynamic subgrid-scale eddy viscosity model with a global model coefficient. *Physics of Fluids*, **18**, (2006).

[22] D. You and P. Moin. A dynamic global-coefficient subgrid-scale eddy-viscosity model for large-eddy simulation in complex geometries. *Physics of Fluids*, **19** (2007).

APPENDIX D

This section gives more precision on the parameters used regarding the boundary conditions for the LES simulations of the experimental set-up. The different patches are recalled in Fig. 5.1. The explanations on the boundary conditions are taken from the AVBP Handbook [1].

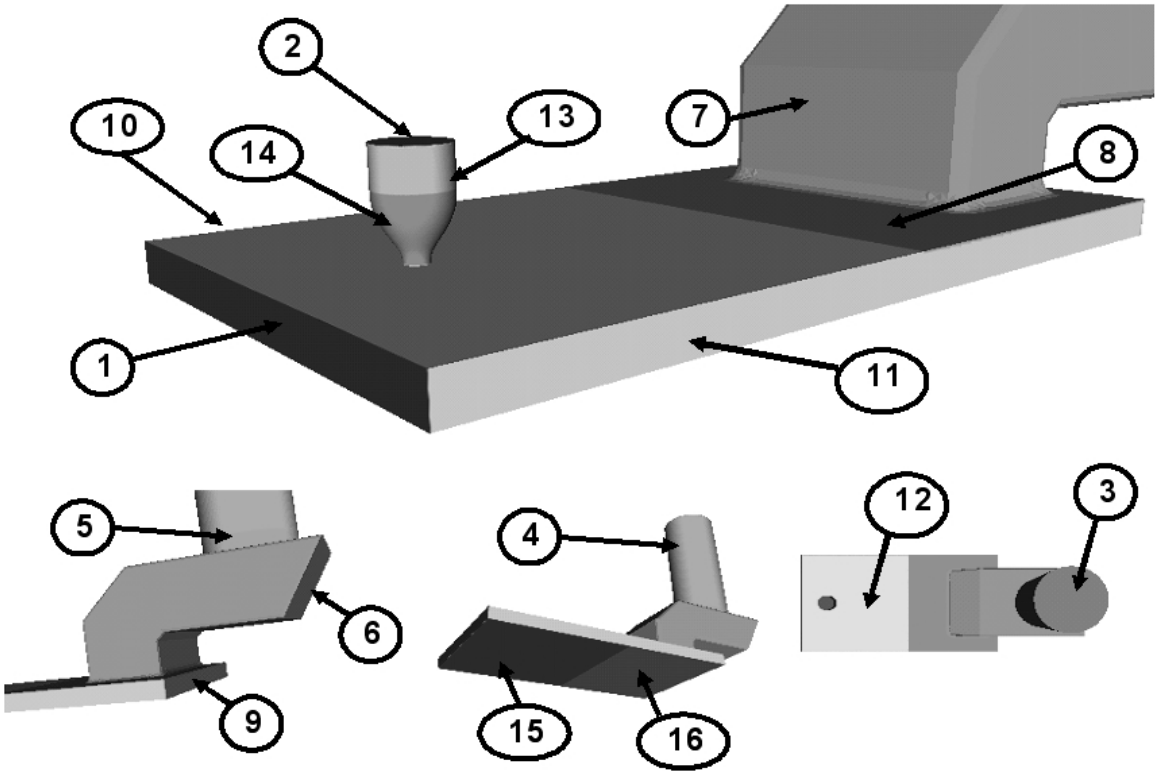

Figure 5.1: Different patches for the LES simulation of the experimental set-up

Patch1: INLET RELAX UVW T Y TURB
This characteristic boundary condition allows to impose the velocity components the static temperature and the mass fraction at an inlet in a soft way. This means that the ingoing waves are taken proportional to the difference between the actual state at the boundary nodes and the reference velocity and temperature. Three integer parameters allow to fix the way the waves are calculated in AVBP, the way the reference state is defined and the type of relaxation that is performed. It also allows a turbulent perturbation to enter the domain. The different values of the parameters used are given below:

- wave: 2
  The variations of the conservative variables are assessed from their time derivative and the strength of the i^{th} wave using Thompson's approach.
- ref type: 2
  The velocity and temperature are given through the user defined subroutines.
- relax type: 1
  The ingoing waves are computed pointwise so that the relaxation tends to drive the velocity components and temperature towards the exact profiles given in the reference state
- relax on Un: 500
- relax on T: 500
- relax on Y: 500
- inject type : 1
  It defines the type of turbulence injected: CERFACS approach (Taylor hypothesis)
- turb param1: 2
- turb param2: 1000
- turb param3: 0.0050
- turb param4: 0.0010
- turb param5: 6.68

Patch2: INLET RELAX RHO UVW T Y
This characteristic boundary condition allows to impose the components of the surfacic mass flow rate, the static temperature and the mass fraction at an inlet in a soft way. This means that the ingoing waves are taken proportional to the difference between the actual state at the boundary nodes and the reference flowrate, temperature and species. Three integer parameters allow to fix the way the waves are calculated in AVBP, the way the reference state is defined and the type of relaxation that is performed. The different values of the parameters used are given below:

- wave: 2.
  The variations of the conservative variables are assessed from their time derivative and the strength of the i^{th} wave using Thompson's approach.
- ref type: 1
  The flowrate components, temperature and species are given in their user defined subroutines
- relax type: 1
  The ingoing waves are computed pointwise so that the relaxation tends to drive the flowrate components and temperature towards the exact profiles given in the reference state.
- relax on rhoUn: 0
- relax on rhout: 0

- relax on T: 8000
- relax on Y: 8000

Patch3: OUTLET RELAX P 3D
This characteristic boundary condition allows to impose the static pressure at an outlet in a soft way. This means that the ingoing wave is taken proportional to the difference between the actual state at the boundary nodes and the reference static pressure. Three integer parameters allows to fix the way the waves are calculated in AVBP, the way the reference state is defined and the type of relaxation that is performed. In addition, there are transverse terms in the expression of the incoming wave's amplitude. This boundary conditions is aimed to substantially reduce spurious acoustic wave reflections. Based on the work of Yoo *et al.* [155] due to numerical instabilities, a damping coefficient β may be needed while using these transverse terms. In [155] the damping coefficient has to be equal to the local, normal to the boundary patch, mach number of the form (please note that $0 \leq \beta < 1$): $Ma = Un/c$ where Ma is the local mach number, n is the number of node on the boundary patch, Un is the velocity component normal to the boundary patch and c is the speed of sound. The different values of the parameters used are given below:

- wave: 3
- ref type: 1
  The static pressure is given in the used defined subroutine.
- relax type: 2
  The ingoing wave is computed from the difference between the mean value (over the patch) of the pressure at the outlet and the reference pressure (which should be constant over the patch in this case, although there is no consistency check coded in AVBP). As a result, the boundary treatment tends to drive the mean (over the patch) pressure towards the target value given in the reference state and the shape of the profile is the result of other non boundary terms (such as the swirl).
- damping type: 2
  The damping coefficient β applied is equal to the mean (in space over the boundary patch), normal to the boundary patch, mach number Ma
- relax on P: 500

Patch4, Patch8, Patch9, Patch10 and Patch11: WALL LAW COUPLED ADIAB
It is an improved velocity/temperature wall-model is used. It is notably able to take into account significant density/temperature variations and molecular Prandtl number effects. It is thus strongly recommended to use this wall-model when simulating anisothermal configurations. It is based on the Van Driest transformation [147] that introduces a new scaling for the velocity profile.

- free corner: 0.75

Patch5, Patch6 and Patch7: WALL NOSLIP ADIAB
Defines an adiabatic wall with zero normal velocity. No additional parameters are needed:

Patch13, Patch14: WALL SLIP RELAX T
Defines a zero mass-flux boundary condition with zero normal velocity (useful for DNS computations). The wall temperature is controlled by a relaxation coefficient that acts on the wall heat flux. The different values of the parameters used are given below:

- ref type: 1 The temperature is given in the user defined subroutine.
- relax coeff: 0.9

Patch16: WALL NOSLIP ISOT
Defines an isothermal wall with zero velocity. The only parameter used to describe the patch is an integer to define the reference temperature to impose at the wall:

- ref type: 1. The Temperature is given in the user defined subroutine.